

Charge-Exchange Collision Dynamics and Ion Engine Grid Geometry Optimization

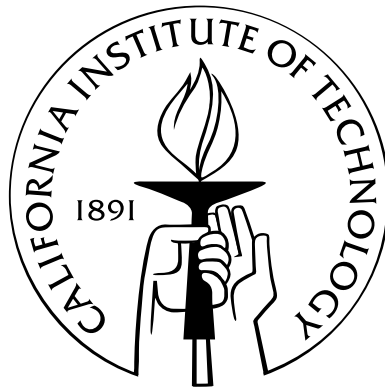
Thesis by

Brad Morris

In Partial Fulfillment of the Requirements

for the Degree of

Doctor of Philosophy



California Institute of Technology

Pasadena, California

2007

(Defended September 22, 2006)

© 2007

Brad Morris

All Rights Reserved

Acknowledgements

How do I even begin to express gratitude for all the support, encouragement, and technical assistance I have received from everyone during this time? I owe many thanks to my JPL advisor and friend, Lee Johnson, who has taught me so much about not only the world of ion propulsion science and technology, but also about myself, and given me a greater view of the world in general. I wish to thank Joseph Shepherd, my Caltech advisor, who took me as a student and was invaluable in offering assistance, insight, and encouragement. Thanks to Michael Ortiz and Fehmi Cirak for offering the use of the shell code and for their invaluable assistance in implementing it into my work. To the rest of my committee members, Fred Culick, Anthony Leonard, and Guruswami Ravichandran, thanks for your time reviewing and helping me to polish the final work. I am in great debt to Julian Cummings, Michael Rubel, and Chad Schmutzer for their technical assistance in computer and network issues, and in getting the codes operational. Lastly, to Jorge Garrido, Chris Mouton, Amy Lam, Alfredo Martinez, David Conroy, Anita Sengupta, my friends, and my family, thanks for standing by me and supporting me throughout this time. This work would not have been possible without each and every one of you. Thank you.

Abstract

The development of a new three-dimensional model for determining the absolute energy distribution of ions at points corresponding to spacecraft surfaces to the side of an ion engine is presented. The ions resulting from elastic collisions, both charge-exchange (CEX) and direct, between energetic primary ions and thermal neutral xenon atoms are accounted for. Highly resolved energy distributions of CEX ions are found by integration over contributions from all points in space within the main beam formed by the primary ions.

The sputtering rate due to impingement of these ions on a surface is calculated. The CEX ions that obtain significant energy (~ 10 eV or more) in the collision are responsible for the majority of the sputtering, though this can depend on the specific material being sputtered. In the case of a molybdenum surface located 60 cm to the side of a 30 cm diameter grid, nearly 90% of the sputtering is due to the 5% of ions with the highest collision exit energies. Previous models that do not model collision energetics cannot predict this. The present results agree with other models and predict that the majority of the ion density is due to collisions where little to no energy is transferred.

The sputtering model is combined with a grid-structure model in an optimization procedure where the sputtering rate at specified locations is minimized by adjustment of parameters defining the physical shape of the engine grids. Constraints are imposed that require that the deflection of the grid under a specified load does not exceed a maximum value, in order to ensure survivability of the grids during launch. To facilitate faster execution of the calculations, simplifications based on the predicted behavior of the CEX ions are implemented. For diametrically opposed sputtering locations, a rounded barrel-vault shape reduces the expected sputtering rate by up to 30% in comparison to an NSTAR-shaped grid.

Contents

Acknowledgements	iii
Abstract	iv
Nomenclature	xii
1 Introduction	1
1.1 The Ion Engine	3
1.2 Modeling the CEX Process	5
1.3 Limitations to Ion Engine Grid Design	7
1.4 Thesis Overview	9
2 Mathematical Formulation of the General Problem	12
2.1 Derivation of the Objective Function: Sputtering Rate	13
2.1.1 Energy- and Angle-Dependent Rate	13
2.1.2 Angle-Independent Sputtering Rate	22
2.2 Description of an Optimization Problem	25
3 Neutral Density Distribution Determination	29
3.1 Rarefied Flow through Holes of Varying Depth	30
3.2 DSMC Calculation of Neutral Distribution for an NSTAR Two-Hole Aperture	34
3.2.1 Single Aperture in an Infinite Grid	35
3.2.2 Single Aperture with a Pseudo-Periodic Hole Pattern	39
3.3 NSTAR Aperture Density Function and Clausing Factor	42

3.4	Neutral Distribution Due to Multiple Holes	43
3.4.1	Pseudo-Code: Calculating the Neutral Density	44
3.4.2	Neutral Density Downstream of an NSTAR Grid	45
4	Computation of CEX-Ion Flux and Sputtering Rate	48
4.1	Obtaining the Electrostatic Potential	49
4.2	The Charge Density: Computing the Electric Potential	52
4.2.1	Main Beam Ions	53
4.2.2	CEX Ions	58
4.2.3	Pseudo-Code: Calculating the Electric Potential	62
4.3	Computing Ion Trajectories Through the Electric Field	63
4.3.1	The Velocity-Verlet Method	64
4.3.2	Pseudo-Code: Time-Adaptive Velocity-Verlet Algorithm	65
4.4	The Differential Cross-Section	66
4.5	The Sputter Yield	71
4.6	Ion Behavior: Scattering Angle Solutions and Streamtube Divergence	73
4.6.1	A 2D Example	74
4.6.2	Extension to a 3D Example	83
4.6.3	Pseudo-Code: Scattering Angle Partial Gauss-Newton Search Algorithm	91
4.7	Computing the Ion Flux and Sputtering Rate	93
4.7.1	The Beamlet Shell	93
4.7.2	Example: Computing Quantities for One NSTAR Beamlet Shell	96
4.7.3	Example: Sputtering Rate Contribution from One NSTAR Beamlet	104
4.8	Chapter Summary	112
5	Approximation Technique	115
5.1	LOS Approximation Method	115
5.1.1	Description of the Approximation	115

5.1.2	Comparison of Results with the Full Trajectory Analysis	120
5.1.3	Pseudo-Code: Adjusting the Scattering Angle	127
5.2	In the Case of Grid-Shape Asymmetry	128
6	Perforated Shell Structure Analysis	135
6.1	Previous Results	135
6.2	Shallow Shells vs. Flat Plates	139
6.3	The Loading	140
7	Optimization Procedure and Results	144
7.1	Control Mesh and Limit Surface Construction	145
7.2	Setting Up the Problem	150
7.2.1	The Optimization Routine	150
7.2.2	The Load and Constraints	151
7.3	Optimization Results	153
7.3.1	Sensitivity: <i>param_init</i>	153
7.3.2	Sensitivity: Evaluation Points	158
7.3.3	Sensitivity: <i>Options</i>	160
7.3.4	Sensitivity: Neutral-Density Effects	162
7.3.5	Sensitivity: Sputter-Yield Effects	163
7.3.6	Thickness Effects	165
8	Discussion of Results and Conclusions	167
8.1	Summary of Work Done and Discussion of Results	167
8.2	Future Work	180
	References	182

List of Figures

1.1	Schematic of an ion engine	3
2.1	Primary-ion flux through a surface	14
2.2	CEX ions scattering from a small volume	16
2.3	Dynamics of an elastic charge-exchange collision	19
2.4	Velocity distribution of CEX ions passing through $S(\tilde{\mathbf{x}})$	20
3.1	An effusing infinitely-thin hole	31
3.2	Triangular hole pattern for NSTAR grids	35
3.3	Simulation domain for a single aperture in an infinite plane	36
3.4	Non-dimensional angular density distribution of a single aperture in an infinite plane	38
3.5	Simulation domain for a pseudo-periodic aperture pattern	39
3.6	Effective pseudo-periodic hole pattern	40
3.7	Non-dimensional angular density distribution of a pseudo-periodic aperture pattern	41
3.8	Non-dimensional far-field angular density distributions	42
3.9	NSTAR neutral density distribution	46
4.1	Sputtering source processes	49
4.2	Example of scattering solutions	50
4.3	Primary-ion beamlet emission source and cone	54
4.4	Beamlet current	56
4.5	NSTAR main beam ion density	57
4.6	Charge-exchange ion density	60

4.7	NSTAR plume potential	61
4.8	CEX neutrals scattered from a small volume	67
4.9	Elastic charge-exchange collision angles in the lab frame	69
4.10	Xe-Xe ⁺ charge-exchange differential cross-section	70
4.11	Sputter yield for xenon on molybdenum	72
4.12	Transformation coordinates of scattered-ion initial conditions	74
4.13	2D trajectories of ions from one scattering event	75
4.14	Downstream location at $x = 60$ cm for ions scattered at different angles	76
4.15	CEX-ion flux contribution as a function of scattering angle	81
4.16	CEX-ion contribution as a function of downstream location	82
4.17	Definition of the azimuthal and inclination scattering angles	84
4.18	Scattering target interception sphere	86
4.19	Chord-length surfaces and contours for the scattering event at $P_I(\mathbf{x}) = (12, 6, 2)$. . .	87
4.20	Chord-length surfaces and contours for the scattering event at $P_{II}(\mathbf{x}) = (5, 6, 2)$. . .	88
4.21	Chord-length surfaces and contours for the scattering event at $P_{III}(\mathbf{x}) = (0.95, 6, 2)$. .	89
4.22	Chord-length surfaces and contours for the scattering event at $P_{IV}(\mathbf{x}) = (-14, 6, 2)$. .	90
4.23	A beamlet shell	94
4.24	Beamlet-shell mesh-scattering solution quantities	98
4.25	Beamlet-shell summand quantities	102
4.26	Beamlet-shell contribution to the CEX-ion flux distribution	103
4.27	Beamlet contribution to the CEX-ion flux distribution	105
4.28	Spatially integrated beamlet contribution to the flux distribution	106
4.29	Beamlet contribution to the sputtering rate	109
4.30	Integrated beamlet sputtering contribution	110
5.1	Beamlet-shell mesh-scattering solution quantities: LOS approximation method	116
5.2	Beamlet-shell contribution to the CEX-flux distribution: Approximations	120
5.3	Sputtering-rate-distribution contribution comparison	121

5.4	Full-beamlet approximation comparison: Hole $(x, y)_k = (-0.111, 5.96)$ cm	123
5.5	Full-beamlet approximation comparison: Hole $(x, y)_k = (5.994, 0)$ cm	124
5.6	Full-beamlet approximation comparison: Hole $(x, y)_k = (0, 11.92)$ cm	125
5.7	Barrel-vault grid shape	129
5.8	Barrel-vault plume potentials	130
5.9	Full-beamlet 3D approximation comparison: Hole $(x, y)_k = (-0.111, 5.96)$	132
5.10	Full-beamlet 3D approximation comparison: Hole $(x, y)_k = (5.994, 0)$	133
5.11	Full-beamlet 3D approximation comparison: Hole $(x, y)_k = (0, 11.92)$	134
6.1	Effective moduli as a function of open-area fraction	137
6.2	Effective moduli as a function of plate thickness	138
6.3	Theoretical- and FEM-deflection comparison	142
7.1	Control mesh and imposed symmetry	146
7.2	Creating the finite-element mesh	148
7.3	Sample of a control mesh and resulting limit surface	149
7.4	Optimization procedure flowchart	151
7.5	Sample optimization results for Run 67	157
7.6	Original and constructed low/high energy emphasis sputter yields	165

List of Tables

4.1	Coefficients for piecewise continuous curve fit of the Xe ⁺ -Mo sputter yield	73
6.1	Effective properties for simulated NSTAR grids of different thickness: Obtained from interpolation from Figure 6.2	143
7.1	Optimization procedure (<i>fmincon</i>) input and output arguments	150
7.2	Optimization results demonstrating dependence on <i>param_init</i>	154
7.3	Optimization results demonstrating dependence on evaluation point location	159
7.4	Optimization results demonstrating dependence on algorithm parameters	161
7.5	Comparison of optimization results from different neutral densities	163
7.6	Coefficients for low-energy emphasis sputter yield	164
7.7	Coefficients for high-energy emphasis sputter yield	164
7.8	Comparison of optimization results for different grid thickness	166

Nomenclature

χ	Angle between hole normal $\hat{\mathbf{n}}_h$ and vector ℓ pointing to the position to determine the neutral atom density
δ_{\max}	Maximum grid/plate deflection under the static load Q
δA	Scattering center volume cross-section area
$\delta \tilde{A}$	Cross-section area of the CEX ion streamtube at the target point $S(\tilde{\mathbf{x}})$
$\delta \tilde{A}'$	Projected area of the CEX ion streamtube on the plane, with normal vector $\hat{\mathbf{n}}$, at the target point $S(\tilde{\mathbf{x}})$
$\delta a_{k,j}$	Area associated with point j in the beamlet mesh of hole k
δF	CEX ion flux from δV at $P(\mathbf{x})$ through the area $\delta \tilde{A}$ at the target point $S(\tilde{\mathbf{x}})$
$\delta F'$	CEX ion flux from δV at $P(\mathbf{x})$ through the projected area $\delta \tilde{A}'$ at the target point $S(\tilde{\mathbf{x}})$
δn_s	Contribution from δV at $P(\mathbf{x})$ to the CEX ion density at the target point $S(\tilde{\mathbf{x}})$
δN_0	Number of thermal neutral atoms within the scattering volume δV
δN_p	Number of primary ions of class \mathbf{u} located within δV
δN_s	Number of CEX ions scattered from the scattering volume δV
$\delta N_s(\tilde{\mathbf{x}}, E)$	Number of CEX ions of class E located within the volume $\delta \tilde{V}$ at the target point
$\delta N_s(\tilde{\mathbf{x}}, E, \tilde{\psi})$	Number of CEX ions of class $E_{\tilde{\psi}}$ located within the volume $\delta \tilde{V}$ at the target point
$\Delta \omega_k$	Solid angle subtended by the emission cone of hole k
$\delta \Omega$	Solid angle about the scattering angle θ^+
$\Delta \Phi$	Electrostatic potential difference between the scattering center at $P(\mathbf{x})$ and the target point at $S(\tilde{\mathbf{x}})$

$\delta\Upsilon'$	Sputtering rate, per unit area, of material due to impingement of CEX ions of class $E_{\tilde{\psi}}$ at the target point $S(\tilde{\mathbf{x}})$
δV	Scattering center volume element ($\delta V = \delta A \delta x$)
$\delta\tilde{V}$	Volume swept out at $S(\tilde{\mathbf{x}})$ by the CEX ions
δx	Scattering center volume length
Γ	Number flux of CEX ions of class E
$\Gamma'(E, \tilde{\psi})$	Number flux of CEX ions of class $E_{\tilde{\psi}}$
λ	Mean free path
$\boldsymbol{\lambda}$	Vector of Lagrange multipliers applied to the equality constraints
$\boldsymbol{\mu}$	Vector of Lagrange multipliers applied to the inequality constraints
ν^*	Effective Poisson's ratio
Φ	Electrostatic potential
$\bar{\varphi}_k \hat{\mathbf{u}}$	Monochromatic number flux of primary ions
ϕ^+	Azimuthal CEX ion scattering angle
ψ	Intersection angle of primary ion velocity vector with the scattering center cross-section at $P(\mathbf{x})$ ($\cos \psi = \hat{\mathbf{u}} \cdot \hat{\mathbf{n}}$)
$\tilde{\psi}$	Intersection angle of CEX ion velocity vector with the plane, with normal vector $\hat{\mathbf{n}}$, at the target point $S(\tilde{\mathbf{x}})$ ($\cos \tilde{\psi} = \hat{\mathbf{v}} \cdot \hat{\mathbf{n}}$)
$\varphi \hat{\mathbf{u}} \delta \mathbf{u}^3$	Number flux of primary ions of class \mathbf{u}
ϕ_u	Primary ion velocity azimuthal angle
ρ_k	Distance to hole k from the grid axis
ρ_0	Upstream neutral atom density (inside discharge chamber)
σ_0	Total charge-exchange scattering cross-section
Θ	Grid open-area fraction
θ^+	Inclination or colatitude scattering angle of CEX ions
θ^0	Inclination or colatitude scattering angle of CEX neutral atom
θ_{LOS}	Line-of-sight inclination scattering angle

ϑ_k	Divergence angle of the primary ion emission cone for hole k
θ_u	Primary ion velocity inclination angle
$\boldsymbol{\xi}$	Vector of optimizing parameters
A_h	Grid hole area
$\mathbf{a}(\boldsymbol{\xi})$	Equality constraints; vector valued function of the optimizing parameters
$\mathbf{b}(\boldsymbol{\xi})$	Inequality constraints; vector valued function of the optimizing parameters
D	Chord length between CEX ion interception point and target point on interception sphere
$\frac{d\tilde{A}}{d\Omega}$	CEX ion streamtube area expansion at the target point
$\frac{d\sigma^+}{d\Omega}$	Charge-exchange differential cross-section of CEX ions
$\frac{d\sigma^0}{d\Omega}$	Charge-exchange differential cross-section of CEX neutrals
E	CEX ion kinetic energy
E^*	Effective Young's modulus
E^+	CEX ion kinetic energy immediately following a CEX collision
E^0	CEX neutral atom kinetic energy following a CEX collision
E_0	Primary ion kinetic energy
\hat{E}	Logarithmic CEX ion energy
$f(\chi)$	Angular neutral atom density distribution function
$F(\tilde{\mathbf{x}})$	Total CEX ion flux through a spherical surface at the target point $S(\tilde{\mathbf{x}})$; <i>non-directional</i> CEX ion flux
$F'(\tilde{\mathbf{x}}, \hat{\mathbf{n}})$	Total CEX ion flux through the projected area $\delta\tilde{A}'$ at the target point $S(\tilde{\mathbf{x}})$; <i>directional</i> CEX ion flux
$f_p(\mathbf{u})$	Primary ion velocity distribution function
$f_s(E)$	CEX ion energy distribution function
$f_s(E, \tilde{\psi})$	CEX ion angular energy distribution function
I_k	Primary ion current through hole k
I_{SP}	Specific impulse

I_0	Neutral atom flow rate through a grid hole
J	Total number of points in the mesh of a beamlet shell
j	Mesh point index in a beamlet shell
K	Total number of holes in the grid
J_b	Total engine beam current
k	Hole index
k_B	Boltzmann's constant
Λ	Streamtube area expansion coefficient
m_i	Ionic mass
m_e	Electron mass
n_{CEX}	CEX ion density
$\hat{\mathbf{n}}_k$	Normal vector of hole k
$\hat{\mathbf{n}}$	Unit normal vector to cross-section area δA of the scattering center volume δV
$\dot{N}_s^0(\theta^0)$	Production rate of CEX neutrals scattered at an angle θ^0
n_0	Thermal neutral atom density
n_e	Electron density
n_i	Total ion density
$\dot{N}_s^+(\theta^+)$	Production rate of CEX ions scattered at an angle θ^+
$n_p(\mathbf{x})$	Number density of primary ions at \mathbf{x}
$n_s(\tilde{\mathbf{x}})$	Total CEX ion density at the target point $S(\tilde{\mathbf{x}})$
p	Grid hole-to-hole pitch
$P(\mathbf{x})$	Label of the scattering center located at \mathbf{x}
\bar{Q}	Normalized static load $\bar{Q} = Q R_g^4 / E^* t^4$
Q	Static load (kPa)
q_e	Electronic charge
R	Grid hole radius
r	Beamlet shell radius

R_g	Engine grid radius
$\hat{\mathbf{R}}$	Line-of-sight scattering trajectory unit vector
\mathbf{r}_k	Vector pointing from the emission point of hole k to the scattering center at \mathbf{x} ; $\mathbf{r}_k = \mathbf{x} - \mathbf{y}'_k$
R_s	CEX ion target interception sphere radius
$S(\tilde{\mathbf{x}})$	Label of the target point located at $\tilde{\mathbf{x}}$
t	Grid thickness
T_e	Electron temperature
Υ	Total sputtering rate, per unit area, of material due to impingement of CEX ions at the target point $S(\tilde{\mathbf{x}})$; <i>non-directional</i> sputtered flux; Objective Function
Υ'	Total sputtering rate, per unit area, of material due to impingement of CEX ions at the target point $S(\tilde{\mathbf{x}})$; <i>directional</i> sputtered flux
\mathbf{u}, u	Primary ion velocity, speed
$\hat{\mathbf{u}}$	Primary ion velocity unit vector
u_0	Thermal neutral atom speed
\mathbf{u}_e	Electron velocity
\mathbf{v}, v	CEX ion velocity, speed
$\hat{\mathbf{v}}$	CEX ion velocity unit vector
W	Clausing factor
$\tilde{\mathbf{x}}$	Spatial coordinates of the target point
$\underline{\mathbf{x}}$	Location to determine the neutral atom density in local hole centered coordinates
\mathbf{x}	Spatial coordinates of the scattering center
$Y(E)$	Energy dependent sputter yield
$Y(E, \tilde{\psi})$	Angular and energy dependent sputter yield
\mathbf{y}'_k	Spatial coordinates of the emission point for hole k
\mathbf{y}_k	Spatial coordinates of the center of hole k

Chapter 1

Introduction

Electric propulsion (EP) devices provide significantly more thrust than their chemical thruster counterparts, given a fixed amount of propellant. This advantage allows electrically propelled spacecraft to accelerate to large velocities, maneuver for significantly longer lifetimes, and operate for prolonged missions that are impossible for chemical rockets. And while conventional rockets currently require boosts, such as gravity assists, to reach far-flung destinations such as the outer planets or beyond, EP engines can potentially achieve the same mission goals without such maneuvers, greatly increasing the flexibility of such missions [1].

Despite the fact that electric propulsion technology has been in existence for more than four decades and has been successful with providing north-south station keeping on satellites [2], until recently — with the successful Deep Space One (DS1) [3] and SMART-1 [4] missions — EP engines have served limited propulsion roles on spacecraft. However, upcoming missions such as the Laser Interferometer Space Antenna (LISA), Terrestrial Planet Finder (TPF-1), and the soon-to-be-launched Dawn spacecraft indicate that electric propulsion is gaining recognition as a viable alternative to chemical thrusters as a main source of propulsion [1]. We refer the reader to other available works for a more complete discussion of the advantages and drawbacks of using electric propulsion [1, 5, 6].

A crucial factor to be considered when choosing to use electric propulsion for any mission is the effects that the exhaust plume may have on the successful long-term operation of the spacecraft. Since the exhaust products of an electric engine are charged particles accelerated to high velocities

by imposed electric fields, it is possible that the intended trajectory of the ions can be corrupted due to various processes and result in collisions of the ions with spacecraft surfaces. Such collisions can erode critical components, which may severely limit the operable lifetime of the spacecraft. A thorough understanding of the processes which lead to undesirable collisions is required in order for one to have confidence in the survivability of a craft long enough to successfully complete its mission.

In this chapter, we present a brief description of the operation of an ion engine (Section 1.1). This discussion will lead to an introduction of the charge-exchange (CEX) collision process and its effect on the design and building of engines. The current models used to predict and examine the plume behavior behind an ion engine, and specifically how these models deal with the CEX process, will be discussed in Section 1.2.

The limitations of the current models, imposed by the assumptions made, provide the motivation for the work presented here. Our primary objective is the development of an ion engine plume model that accounts for the dynamics of charge-exchange collisions and predicts the extent of sputtering, or erosion, of spacecraft surfaces that result from impingement of the ion products of these collisions. In Section 1.3, we introduce the way in which the results of the model developed here can be directly applied to the design of future ion engines, as well as the restrictions they impose. The second objective of this work is then to define and solve an optimization problem in which the application of the model to designing an ion engine is subjected to certain design conditions and structural constraints. We conclude this chapter in Section 1.4 with an overview of the organization of this thesis.

The work presented here was initially begun under the auspice of the now-cancelled NASA Jupiter Icy Moons Orbiter (JIMO) mission [7]. The proposed primary propulsion for JIMO was to be supplied by a cluster of ion and Hall-effect engines. The ion engines to be used were of the same family as the NSTAR engine used on the Deep Space One mission. However, they were to be much larger in physical size, as well as operate at significantly higher power. The NSTAR engine was designed to operate at a peak power of 2.3kW with an I_{SP} (change in momentum due to consumption of a unit mass of propellant) equal to 3100s; the specifications for the JIMO engines

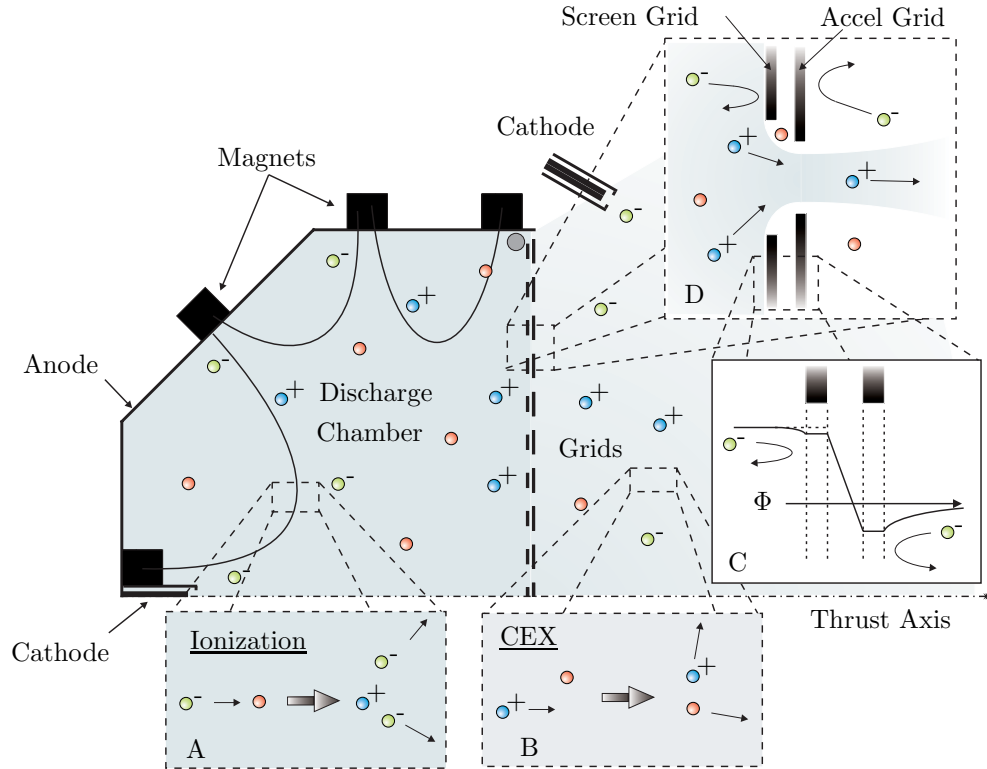


Figure 1.1: Schematic of an ion engine. Electrons confined by the magnetic fields collide with and ionize xenon atoms (inset A). The ions are accelerated out of the chamber through grid apertures (inset D). The grids are held at different potentials to prevent loss of electrons to the screen grid and backstreaming of neutralizing electrons into the discharge chamber (inset C). Collisions between the ions and neutral atoms that have diffused through the apertures result in charge-exchange (inset B). [1]

called for peak powers up to 30 kW and an I_{SP} greater than 6000 s. While many of the processes discussed here broadly apply to most electric engines, this work deals exclusively with the ion-engine class of thruster.

1.1 The Ion Engine

The operation of an ion engine begins with the injection of neutral propellant atoms into a discharge chamber (refer to Figure 1.1). Here the atoms collide with energetic electrons emitted from a cathode. Magnets surrounding the chamber create cusped magnetic fields which confine the electrons and increase the probability of a collision between an electron and an atom before the electron is collected at the anode [1]. Upon collision there is some probability that the electron will ionize the

neutral atom (inset A). At the aft end of the engine is a set of extraction grids designed to allow the ions to accelerate downstream, providing thrust to the craft, while preventing the neutral propellant from drifting out of the engine (inset D).

In a two-grid system, such as that on NSTAR, the upstream (screen) grid is kept at an elevated potential with respect to the spacecraft exterior, but slightly less than that of the rest of the chamber; while the downstream (accel) grid is maintained at a potential less than that of the exterior (Figure 1.1, inset C). Each grid has a pattern of holes which are precisely aligned to create apertures that allow unobstructed acceleration of the ions out of the engine. These are referred to as primary ions. The purpose of the screen grid is to protect the negatively charged accel grid from attracting the accelerating ions. Electrons emitted by a neutralizing cathode downstream of the engine combine with, and neutralize, the ions, preventing the spacecraft from building up a negative charge.

The accel grid is kept at a negative potential to prevent the neutralizing electrons from accelerating upstream into the discharge chamber. The effect of the differing potentials placed on the two grids creates a focussing effect on the ions being extracted, much like that found with an optic lens. This “ion optics” mechanism results in small ion beamlets emerging from each aperture [8]. The grid apertures and operating potentials are designed to make the effective transparency to the primary ions as high as possible while minimizing the transparency to the neutralizing electrons and neutral atoms [9].

Inevitably, however, some ions are lost to collisions with the grids and some neutral atoms still manage to diffuse through the holes. The loss of both ions and atoms results in a waste of propellant, since no thrust is obtained from these particles. Propellant is wasted when neutral atoms diffuse through the apertures; further, these atoms can cause an undesirable charge-exchange process leading to ions moving slowly on highly divergent trajectories from the thrust axis (Figure 1.1, inset B) [10].

There are two possible outcomes to a beamlet-ion/neutral atom collision. The first is the transfer of energy and momentum between the ion and neutral atom. In such an instance the ion and atom will scatter at angles such that the total momentum and kinetic energy in the collision system is conserved, and there is a certain probability associated with the incoming ion (projectile) scattering

within any specific range of angles quantified by the differential cross-section [11]. The second possible outcome is that an electron will transfer from the neutral atom to the ion in what is referred to as a charge-exchange (CEX) collision. Similar to the sole case of energy and momentum transfer, there is a charge-exchange differential cross-section associated with the probability of the CEX ion (target) scattering within any specific range of angles [12].

Wherever there are charges present, we can expect to find electromagnetic potentials and fields. Downstream of the engine grids an electromagnetic field forms due to the presence of both the charged grids as well as the moving charges in the form of neutralizing electrons, primary ions, and CEX ions. In turn, the movement of the electrons and ions is affected by this electromagnetic field [13]. Measurements made both in the lab and on operating engines have shown that there is a highly divergent population of ions at large angles from the thrust axis, which collide with surfaces far removed from direct interaction with the main exhaust. These ions are primarily slow-moving CEX ions, created by glancing charge-exchange collisions, which evolve on the electromagnetic field that has developed downstream of the thruster [14].

1.2 Modeling the CEX Process

In this work there are two types of ions which we treat. The first type consists of the energetic ions emerging from the apertures in the form of beamlets. These are the ions that we consider to be “projectiles” in charge-exchange collisions, and we refer to them as the primary ions. The second type of ion is created from “target” atoms as a result of charge-exchange collisions. These ions begin as neutral atoms and then each lose an electron to a primary ion during collision. We refer to these newly created ions as CEX ions.

When we discuss the charge-exchange differential cross-section in Chapter 4, we will find that the vast majority of CEX collisions involve only a transfer of an electron, but very-little-to-no energy or momentum transfer from the primary ion to the CEX ion. Based on this observation, current models of ion and Hall thruster plumes are based on the assumption that *all* CEX collisions occur with no transfer of energy or momentum, and that the newly created CEX ions emerge from the

collision with the same thermal velocity that the neutral atoms had before encountering the primary ion [15, 16]. Once ionized as a result of the charge-exchange process, the CEX ions are subjected to the electric field downstream of the engine. As we will also see in Chapter 4, there is a significant radial component to the electric field — especially near the edge of the main beam of primary ions. In addition, the axial component of the electric field is directed *upstream* at the edge of the main beam. Under this assumption of no energy or momentum transfer, the CEX ions are completely under the influence of the electric field and are accelerated outwards in a radial direction from the beam, in addition to back towards the spacecraft [17].

While the assumption used in the current models is well founded and applicable to most of the CEX ions created, a question still remains. What happens when a CEX collision occurs during which there is also a transfer of energy? We have stated, without evidence for the moment, that the differential cross-section highly favors those collisions that transfer little to no energy. Let us assume, for argument's sake, that for every one thousand CEX collisions involving no energy transfer there is one collision where five percent of the energy of the primary ion, 50 eV, is transferred to the neutral atom in addition to the electron transfer. Let us also assume that these collisions occur at points in space that are at an elevated potential, say 20 eV, with respect to the surface of the spacecraft.

Imagine all of the CEX ions accelerating through the electric field and colliding with the spacecraft surface that was at a potential 20 eV lower than the point where the ions were created. The one thousand ions will collide with an energy of 20 eV and the single ion initially imparted with 50 eV will collide with the surface with an energy of 70 eV. In this situation the question of which does more damage to the surface arises. Is it possible that the collision of one ion with 70 eV of energy results in more damage than the cumulative effect of one thousand ions with 20 eV? The models which assume there is no energy transfer during the charge-exchange process cannot answer this question.

This is the primary motivation for the work in this dissertation. The goal set forth for the work contained herein is to develop a model for the plume of an ion engine that accounts for the energy

and momentum transfer process during charge-exchange collisions, and more specifically, a model that can predict the amount of sputtering that one would expect at any particular point around the engine due to impacts from the CEX ions.

For reasons that are dictated by elastic collision dynamics and will be made apparent in Chapter 4, models that do not account for energy or momentum transfer only require total CEX ion production rates. The production rate at any particular point in space does not depend on the direction of motion of the primary ions; the rate depends only on the total current passing through the point [13]. In contrast, inclusion of energy and momentum dynamics in a charge-exchange plume model allows the direction of the primary ions to have a direct impact on the trajectory that a CEX ion will take after the collision. Since the source of primary ions determines the trajectories of these ions, the ion source itself has influence over the behavior of the CEX ions. This implies that, if one were to change the ion source, one could potentially increase or decrease the amount of sputtering that occurs at any particular surface due to CEX ion impacts.

If we can define the ion engine grids to be the source of ions, an immediate application of a model incorporating charge-exchange collision dynamics is to the design of these grids. Any spacecraft designer concerned about sputtering of surfaces on his craft can of course take the approach of building it such that nothing of importance is anywhere near the engine. This is the simple and uninteresting solution, and due to possible limitations, such as available space, may not be a viable option. The ability to design the engine to fit with the specific craft and mission could be extremely valuable; however, we understand that the grids on an ion engine can not be redesigned with complete impunity. In the next section we will discuss restrictions on the design of ion engine grids and how this leads to the second goal of this thesis — a constrained optimization of ion engine grid shapes.

1.3 Limitations to Ion Engine Grid Design

Before any spacecraft to be launched by NASA is even inserted into the launch vehicle or placed on the launch pad, it must undergo and pass a rigorous regimen of tests. One of these tests is called a “vibe test” where the craft is subjected to a period of intense vibration similar to that which it

would experience during launch before being released from the launch vehicle and inserted into its final orbit or trajectory [18]. During this test it must be shown that the craft has the structural integrity to survive the launch. The ion engine grids, critical to the operation of the entire engine, could easily fracture if not designed carefully, and cause catastrophic failure that could endanger the success of the entire mission of the spacecraft.

For perspective, the grids on the NSTAR engine that flew on Deep Space One were 30 cm in diameter, 0.38 mm (screen) and 0.51 mm (accel) thick, and separated by a scant 0.66 mm [9]. Had the launch environment proven to be too much for the grids such that they collided with each other, or simply fractured due to too much stress, the entire Deep Space One mission would have been in jeopardy. To prevent this possibility as well as to provide thermal-mechanical stability to the grids so that they wouldn't thermally expand and come into contact with each other during operation, the NSTAR ion engine grids were spherically dished [9].

A useful tool in the design of ion engine grids would permit reshaping of the grids to mitigate the amount of sputtering of critical spacecraft components, while meeting the thermal and structural constraints imposed for a high probability of successful engine operation. This is the second goal of the work in this thesis. We wish to combine the model that incorporates both charge-exchange dynamics and structural strength analysis into an optimization problem based on the shape of the grid. The optimized solution to this problem would minimize the amount of sputtering predicted at certain points, while meeting the constraints imposed by maintaining the structural strength required to survive launch. It must be understood that the intention of this work is not to develop robust structural analysis software, nor to develop a superlative optimization routine. The greatest scientific advancement, discovery, and interest of this work is found in developing the CEX ion model. For the structural analysis and optimization methods, we defer to those with more expertise in these areas and accept our role as simply a user of their products.

1.4 Thesis Overview

The general mathematical foundation for the work to follow is presented in Chapter 2. In Section 2.1 we derive the equations to be solved by the CEX ion model. The equations of primary importance are the CEX ion energy distribution at a specific point, and the sputtering integral. The energy distribution will quantify the number of CEX ions within any specific energy range that pass through the specified point. The sputtering integral will predict the total sputtering rate of a surface at the specified point due to collisions of the CEX ions described by the energy distribution. A brief discussion of the theory behind constrained optimization problem solving will follow in Section 2.2.

Chapter 2 will introduce a series of different quantities that must be found in order to solve the equations presented. Chapter 3 will follow with the discussion of the first of these quantities — the neutral atom density field. A frequently used model for finding the density of neutral atoms as a result of diffusion through a set of holes or apertures is a modified cosine, or Lambertian, distribution. In Section 3.1 we present the foundation and reasoning behind the use of such a model and from where the modifiers, including the Clausing factor, originally come. Comparison of the modified cosine distribution, with results from computations of rarefied gas flow through two hole apertures, using the direct simulation Monte Carlo (DSMC) method, are presented in Section 3.2. Simulations of both a single aperture in an infinite plane and a pseudo-periodic aperture pattern are shown. The farfield distribution will be emphasized in Section 3.3, where we present the distributions obtained from the simulations for each aperture and determination of the equivalent Clausing factor for each. Chapter 3 concludes with a demonstration of how the results obtained can be applied for determining the density of neutral atoms at any point downstream of an ion engine grid. The final neutral atom density field obtained in this way will be compared to that obtained by using the common modified cosine distribution.

In Chapter 4 we delve into finding the remaining quantities needed to solve the equations presented in the second chapter: the primary ion flux, the charge-exchange differential cross-section, the CEX ion scattering angle and energy, and the sputter yield. In order to integrate the equations of motion for CEX ions, the electric field through which they pass must be known. Section 4.1

presents a model for determining the electric potential from the ion charge density. In turn, the model for determining the ion charge density is presented in Section 4.2. The method for integrating the equations of motion, the velocity Verlet algorithm, will be shown in Section 4.3. The definitions and experimental data used for evaluating the charge-exchange differential cross-section and sputter yield follow in Sections 4.4 and 4.5. The behavior exhibited by CEX ions that scatter at different angles, and correspondingly with different initial energies, are analyzed in Section 4.6. Behavior in a two-dimensional system will be examined first, which will introduce principles useful for interpreting the results from a three-dimensional system. Every scattered CEX ion is found to apply to one of four distinct cases, and the implications of each case on the measured energy flux distribution of CEX ions through a particular point are discussed. Among these four cases, the interesting discovery, that from any scattering event there are two unique possible scattering angles a CEX ion can scatter into and end up passing through the same point is discussed. A physical explanation for this phenomena is given, as well as the method used to determine the two unique scattering angles. Having by that point determined methods for finding all the required quantities laid out in Chapter 2, Section 4.7 introduces the concept of the beamlet shell by which computational integration of all quantities is facilitated. Through integration, the full CEX ion energy flux distribution and sputtering integral at any particular point can be computed. An example of the implementation of this beamlet shell into the computation of the flux distribution and the sputtering rate, for both one individual shell as well as for an entire beamlet, will be presented.

While completely accurate — insofar as the assumptions made are correct — the model developed in Chapter 4 is found to be rather unwieldy for application to the optimization problem set before us as our second goal. Chapter 5 presents the simplifying assumptions made to reduce the complex problem to one that can be solved quickly and efficiently, while still yielding reasonably accurate results. In Section 5.1 we show a method for removing the majority of the ion trajectory computations required in the full model presented in Chapter 4 by assuming modified line-of-sight ion trajectories. A comparison between the full model results and those obtained using the simplification is given. Section 5.2 presents the effects of assuming that the electric field downstream of

the grid is symmetric, even if it is, in fact, asymmetric due to an asymmetric grid shape.

Discussion of how the structural component of the optimization problem is handled is given in Chapter 6. Section 6.1 presents the issues dealt with when working with perforated shell or plate-like structures. The results of theoretical and experimental work dealing with such structures are presented and summarized. In Section 6.2 we discuss the assumptions and limitations made in applying the knowledge gained from Section 6.1 to our specific optimization problem, where we deal with shaped shells instead of flat plates. The chapter ends in Section 6.3 with a demonstration of how we determine the effective properties for any grid; and the results from application of the finite-element software to a flat plate and the NSTAR grids.

The method by which the optimization was carried out and the results of some sample cases are presented in Chapter 7. In Section 7.1 we present the control mesh and how a parameterized limit surface is obtained from this mesh, which conforms to the grid shape under investigation. A brief description of the Matlab optimization algorithm is given in Section 7.2, where we set up our particular problem and determine the constraints on our optimization. Section 7.3 follows with results of sample optimization cases performed to demonstrate the sensitivity to different elements of the model, as well as to determine some general trends that arise, which tend to lead to more optimal grid shapes.

This thesis concludes in Chapter 8, where we discuss the results of both the model developed and the optimization procedure. Advancements made in the understanding of CEX collision processes within ion engine plumes, and electric propulsion devices in general, are presented. A discussion of both the advantages and disadvantages of the new model is given, from which follows suggestions for further improvements that could be made to both this model and others.

Chapter 2

Mathematical Formulation of the General Problem

The main problem to be solved in this work, as presented in Chapter 1, is to incorporate the charge-exchange collision dynamics into a model of the plume downstream of an ion engine. We intend to use this model to obtain the energy distribution of CEX ions from which we can predict the amount of sputtering at specified spacecraft surfaces. The second problem to be solved is the constrained optimization of the ion engine grid shape, such that the predicted sputtering at specified locations is minimized, while the strength and survivability of the grids is maintained. This chapter sets forth the general mathematical theory and concepts needed to accomplish the intended goals. Section 2.1 covers the derivation of the equations (employed in Chapter 4) that determine the energy distribution of CEX ions that are scattered to a specified location, and the amount of material sputtered as a result of these ions impacting that surface. A brief description of the terminology used in optimization problems is discussed in Section 2.2, followed by an introduction to the *Karush-Kuhn-Tucker* conditions. The *Karush-Kuhn-Tucker* conditions use the theory of Lagrange multipliers and application of constraints in a general mathematical framework by which optimization problems may be generally solved.

2.1 Derivation of the Objective Function: Sputtering Rate

In this section we present the derivation of the expressions that model the expected sputtering rate of material from a surface due to impingement of CEX ions. In Section 2.1.1 a sputtering rate is derived based on the observation that sputtering is dependent both on the ion energy and angle of impingement. Similar expressions are derived in Section 2.1.2 for situations when the assumption of angle-independent sputtering may be suitable. Justification for this assumption is presented.

Kinetic theory is a well established field and extensive discussions of the subject can be found in works by Jeans [19], Chapman and Cowling [20], Guggenheim [21], and Kennard [22], to name a few. The derivation presented here will begin with some fundamental concepts pertaining to kinetic theory, such as the velocity distribution function and the differential scattering cross-section. Jeans [19] and Chapman and Cowling [20] give thorough discussions of the velocity distribution function, and Guggenheim [21] gives an excellent explanation of the differential cross-section. Through manipulation of the equation defining the differential cross-section and through detailed balance, we will derive an integral expression that describes the expected flux of scattered CEX ions through a specified volume of space due to collisions between primary ions and cold neutral atoms throughout the entire region downstream of an ion engine. This integral expression will be equivalent to a modified and simplified version of the Boltzmann equation which is used extensively in kinetic theory. For further discussion of the Boltzmann equation, refer to texts by Kennard [22], Chapman and Cowling [20], or Reif [23].

2.1.1 Energy- and Angle-Dependent Rate

Let the primary ions of class \mathbf{u} be defined to be those ions with velocities between \mathbf{u} and $\mathbf{u} + \delta^3\mathbf{u}$, where $\hat{\mathbf{u}}$ is the unit vector in the direction of motion. By the definition of the velocity distribution function [20], $f_p(\mathbf{u})$, the number of primary ions of class \mathbf{u} located within a volume δV located at $P(\mathbf{x})$ is

$$\delta N_p(\mathbf{x}, \mathbf{u}) = n_p(\mathbf{x}) f_p(\mathbf{u}) \delta^3\mathbf{u} \delta V, \quad (2.1)$$

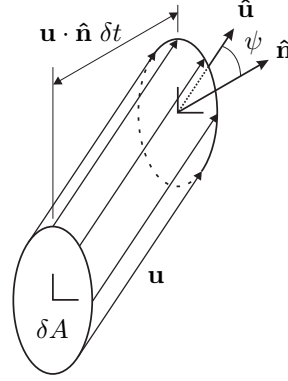


Figure 2.1: Primary ion flux through a surface. Primary ions with speed u and vector of motion $\hat{\mathbf{u}}$ pass through an area element δA with normal vector $\hat{\mathbf{n}}$. In the time δt , the ions passing through the area element sweep out a volume $\delta V = (\mathbf{u} \cdot \hat{\mathbf{n}} \delta t) \delta A$. The angle between the vector of motion and normal vector is $\psi = \cos^{-1}(\hat{\mathbf{u}} \cdot \hat{\mathbf{n}})$.

where

$$\int_{\mathbf{u}} f_p(\mathbf{u}) d^3\mathbf{u} \equiv 1, \quad (2.2)$$

and $n_p(\mathbf{x})$ is the total number density of primary ions within δV [24]. In the time δt , the ions of class \mathbf{u} that pass through the area δA with the normal vector $\hat{\mathbf{n}}$ sweep out the volume

$$\delta V = \delta x \delta A = (\mathbf{u} \cdot \hat{\mathbf{n}} \delta t) \delta A \quad (2.3)$$

(see Figure 2.1). Therefore, the number flux of ions of class \mathbf{u} passing through δA into the volume δV is

$$\frac{\delta N_p(\mathbf{x}, \mathbf{u})}{\delta A \delta t} = n_p(\mathbf{x}) f_p(\mathbf{u}) \mathbf{u} \cdot \hat{\mathbf{n}} \delta^3\mathbf{u} = \varphi \hat{\mathbf{u}} \cdot \hat{\mathbf{n}} \delta^3\mathbf{u}, \quad (2.4)$$

where we have defined the quantity

$$\varphi \equiv u n_p(\mathbf{x}) f_p(\mathbf{u}). \quad (2.5)$$

In the case of the NSTAR engine, the primary ions are accelerated to a speed of $u \approx 40$ km/s [9]. In contrast, the neutral atoms diffusing through the grid are expected to be in thermal equilibrium with the engine walls (~ 500 K), with speeds of $u_0 \approx 300$ m/s [15]. The thermal velocity of the atoms is significantly less than that of the primary ions, so we assume that the neutral atoms are stationary

scattering centers. Let us assume that contained within δV are stationary neutral particles with a number density of n_0 . The total number of CEX ions scattered, per unit time, into a small solid angle $\delta\Omega$ about an angle θ^+ , measured with respect to the flow direction $\hat{\mathbf{u}}$, *per scattering center or neutral particle*, due to a charge-exchange collision with a primary ion of class \mathbf{u} is

$$\frac{1}{\delta N_0} \left. \frac{\delta N_s}{\delta t} \right|_{\theta} = \frac{\delta N_p(\mathbf{x}, \mathbf{u})}{\delta A \delta t} \left. \frac{d\sigma^+}{d\Omega} \right|_{\theta^+} \delta\Omega = (\varphi \hat{\mathbf{u}} \cdot \hat{\mathbf{n}}) \left. \frac{d\sigma^+}{d\Omega} \right|_{\theta^+} \delta\Omega \delta^3\mathbf{u} \quad (2.6)$$

(see Figure 2.2) [23]. The differential charge-exchange scattering cross-section, for CEX ions, $d\sigma^+/d\Omega$, is defined to be such that,

$$\sigma_0 = \int_{\Omega} \frac{d\sigma^+}{d\Omega} d\Omega \quad (2.7)$$

where the integration is carried over the entire solid angle, and σ_0 is the total CEX scattering cross-section [23]. For xenon ions with energies of 1200 eV colliding with xenon neutrals, this value is approximately $53 \times 10^{-20} \text{ m}^2$ [25]. The differential cross-section is discussed further in Section 4.4.

The number of scattering centers located within the volume is $\delta N_0 = n_0 \delta V$. Therefore, from Equation 2.6, the total number of CEX ions scattered from δV , per unit time, into a small solid angle $\delta\Omega$ about an angle θ^+ , measured with respect to the flow direction $\hat{\mathbf{u}}$, is

$$\left. \frac{\delta N_s}{\delta t} \right|_{\theta^+} = n_0 (\varphi \hat{\mathbf{u}} \cdot \hat{\mathbf{n}}) \left. \frac{d\sigma^+}{d\Omega} \right|_{\theta^+} \delta\Omega \delta V \delta^3\mathbf{u}. \quad (2.8)$$

Note that this expression is identical to that which appears on page 35 of Kennard [22] if one of the gases is cold ($u_0 = 0$).

The ions scattered into this small solid angle can be thought of as forming a streamtube. As these ions move through space they may be subjected to forces, e.g., electric fields, which alter their trajectories, causing the streamtube to enlarge or contract and distort. Let us assume that these scattered ions arrive at $S(\tilde{\mathbf{x}})$ with a velocity \mathbf{v} , and the cross-sectional area of this streamtube at

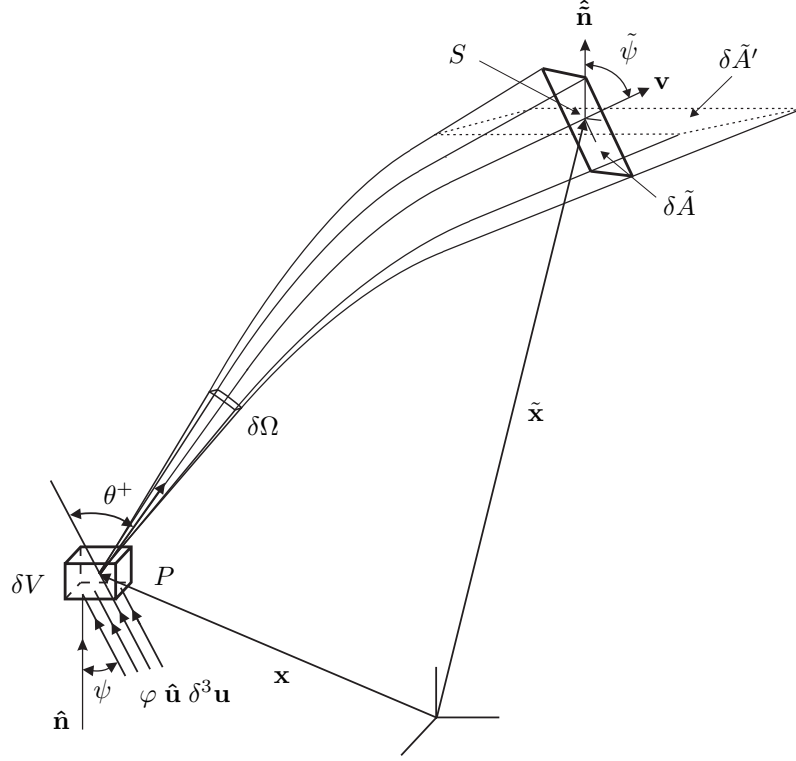


Figure 2.2: CEX ions scattering from a small volume. A flux of primary ions of class \mathbf{u} , $\varphi \hat{\mathbf{u}} \delta^3 \mathbf{u}$, pass through a volume δV centered around a point $P(\mathbf{x})$. CEX ions scattered into a solid angle $\delta\Omega$ about an angle θ^+ , with respect to the primary vector of motion $\hat{\mathbf{u}}$, form a streamtube with a cross-sectional area $\delta\tilde{A}$ at the target point $S(\tilde{\mathbf{x}})$. The curvature of the streamtube is due to the influence of the electric field on the ion trajectories. The same ions subtend an area $\delta\tilde{A}'$ on the plane, containing the point $S(\tilde{\mathbf{x}})$, with normal $\hat{\tilde{\mathbf{n}}}$. At the target point, the CEX ions have a velocity \mathbf{v} and pass through $S(\tilde{\mathbf{x}})$ at an angle $\tilde{\psi}$ with respect to $\hat{\tilde{\mathbf{n}}}$.

$S(\tilde{\mathbf{x}})$ is equal to $\delta\tilde{A}$ with a normal vector, $\hat{\tilde{\mathbf{v}}}$ (Figure 2.2). Therefore, the flux of ions through $\delta\tilde{A}$ is

$$\delta F(\tilde{\mathbf{x}}, \mathbf{v}; \mathbf{x}, \mathbf{u}) = \frac{\delta N_s}{\delta\tilde{A} \delta t} = n_0 \varphi \cos \psi \left. \frac{d\sigma^+}{d\Omega} \right|_{\theta^+} \frac{\delta\Omega}{\delta\tilde{A}} \delta V \delta^3 \mathbf{u}. \quad (2.9)$$

By the same reasoning that led to Equation 2.3, the volume swept out by these ions in a time δt is

$$\delta\tilde{V} = |\mathbf{v}| \delta t \delta\tilde{A}. \quad (2.10)$$

Substituting δt into Equation 2.9 yields the CEX-ion density contribution to the volume $\delta\tilde{V}$, at the target point $S(\tilde{\mathbf{x}})$, from collisions between neutral atoms and primary ions of class \mathbf{u} in the volume

δV at $P(\mathbf{x})$:

$$\delta n_s(\tilde{\mathbf{x}}, \mathbf{v}; \mathbf{x}, \mathbf{u}) = \frac{\delta N_s}{\delta \tilde{V}} = \frac{n_0 \varphi \cos \psi}{|\mathbf{v}|} \frac{d\sigma^+}{d\Omega} \bigg|_{\theta^+} \frac{\delta \Omega}{\delta \tilde{A}} \delta V \delta^3 \mathbf{u}. \quad (2.11)$$

The streamtube subtends an area $\delta \tilde{A}'$ on the plane, with a normal vector $\hat{\mathbf{n}}$, passing through $S(\tilde{\mathbf{x}})$ where

$$\delta \tilde{A} = \hat{\mathbf{v}} \cdot \hat{\mathbf{n}} \delta \tilde{A}' = \cos \tilde{\psi} \delta \tilde{A}'. \quad (2.12)$$

Thus the flux of ions scattered at an angle θ^+ , with respect to $\hat{\mathbf{u}}$, from δV through the plane, with normal vector $\hat{\mathbf{n}}$, at the point $S(\tilde{\mathbf{x}})$ is

$$\delta F'(\tilde{\mathbf{x}}, \hat{\mathbf{n}}, \mathbf{v}; \mathbf{x}, \mathbf{u}) = \frac{\delta N_s}{\delta \tilde{A}' \delta t} = n_0 \varphi \cos \psi \cos \tilde{\psi} \frac{d\sigma^+}{d\Omega} \bigg|_{\theta^+} \frac{\delta \Omega}{\delta \tilde{A}} \delta V \delta^3 \mathbf{u}. \quad (2.13)$$

The total flux of CEX ions through a plane with normal vector $\hat{\mathbf{n}}$ at the specified target point $S(\tilde{\mathbf{x}})$ is obtained by integrating over all space from which scattered ions can originate, $P(\mathbf{x})$, and all possible primary ion velocities, \mathbf{u} . In the limit as $\delta \Omega \rightarrow 0$, $\delta V \rightarrow dV$, and $\delta^3 \mathbf{u} \rightarrow d^3 \mathbf{u}$,

$$F'(\tilde{\mathbf{x}}, \hat{\mathbf{n}}) = \int_{\text{a.s.}} \int_{\mathbf{u}} n_0 \varphi \cos \psi \cos \tilde{\psi} \frac{d\sigma^+}{d\Omega} \bigg|_{\theta^+} \left(\frac{d\tilde{A}}{d\Omega} \right)^{-1} d^3 \mathbf{u} dV. \quad (2.14)$$

Similarly, the total CEX ion density at the target point $S(\tilde{\mathbf{x}})$ is obtained from integrating Equation 2.11:

$$n_s(\tilde{\mathbf{x}}) = \int_{\text{a.s.}} \int_{\mathbf{u}} \frac{n_0 \varphi \cos \psi}{|\mathbf{v}|} \frac{d\sigma^+}{d\Omega} \bigg|_{\theta^+} \left(\frac{d\tilde{A}}{d\Omega} \right)^{-1} d^3 \mathbf{u} dV. \quad (2.15)$$

Note that these equations do not address the question of *how* one obtains the quantity, $d\tilde{A}/d\Omega$. The presence of this quantity within the equations merely reflects the principle of continuity where if the cross-sectional area of a streamtube containing a specified number of ions increases, the flux must correspondingly go down. To obtain the actual value of the quantity $d\tilde{A}/d\Omega$, one must follow the trajectories of ions that scatter within a small solid angle, and find how the streamtube formed by this ensemble of ions contracts, bends, or distorts as the ions respond to the plasma's electric field. Also note that this streamtube is not in any way similar to a streamtube that one may encounter

when studying a fluid. Whereas in a fluid, the definition of a streamtube precludes any mass passing into or out of the region of space bounded by the streamtube, this is not the case in our calculations. Ions scattered from a different location may very well pass through the region of space enclosed by the streamtube as we have defined here. We simply use it as the term as a convenient shorthand for the region of space swept out by ions with similar initial conditions.

Assuming the CEX ions do not undergo further collisions, Equations 2.14 and 2.15 specify the total flux (through a plane with a specific normal, $\hat{\mathbf{n}}$) and total density (at a target point $S(\tilde{\mathbf{x}})$) of CEX ions resulting from all possible collisions between primary ions and neutral atoms in all space. Justification for the assumption of collisionless CEX-ion trajectories will be made in Chapter 3 (Section 3.4) by application of the Beer-Lambert Law.

Sputtering is an energy-dependent process [26, 27, 28]. The momentum and energy of the particle colliding with a surface determines the total transferable momentum and energy available to surface atoms that enables them to be freed from surface binding forces. In addition to the dependence on collision energy, the angle at which a particle is incident with the sputtered surface may also determine the amount of sputtering damage done [29, 30, 31]. In order to calculate the rate at which material is removed from any surface, the energy- and angular-distribution of the colliding ions must be known. Though Equations 2.14 and 2.15 make no apparent accounting of it, the population of CEX ions at the target point will, in general, have a distribution of energies and velocity vectors. The following discussion explains how the CEX-ion population at any target point comes to have a distribution of energies, and how this distribution is obtained from Equations 2.14 and 2.15. The relationship between the flux and density energy distributions will be determined.

In an elastic charge exchange collision between partners of identical mass (positive xenon ion and neutral atom), conservation of energy and momentum analysis stipulates that the ion and atom initially leave the collision on trajectories separated by 90° in the lab frame. Both the projectile (primary ion, CEX neutral) and target atom (CEX ion) leave the collision with energies E^0 and E^+ , respectively. Each collision exit energy is proportional to the square of the cosine of the angle, as measured in the lab frame, by which each particle is respectively scattered from the original

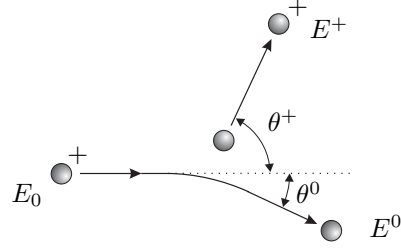


Figure 2.3: Dynamics of an elastic charge-exchange collision. A primary ion with energy E_0 collides with a stationary neutral atom. An electron is transferred from the atom to the primary ion creating a CEX ion and CEX neutral, respectively. The CEX ion scatters at an angle θ^+ with an energy $E^+ = \cos^2 \theta^+$. Similarly, the CEX neutral scatters at an angle θ^0 with an energy $E^0 = \cos^2 \theta^0$.

projectile vector of motion, $\hat{\mathbf{u}}$, i.e.,

$$\frac{E^+}{E_0} = \cos^2 \theta^+, \quad \text{and} \quad \frac{E^0}{E_0} = \cos^2 \theta^0, \quad (2.16)$$

where E_0 is the kinetic energy of the primary ion of class \mathbf{u} (see Figure 2.3) [32]. In general, the scattering angle required to place an ion on a trajectory passing through the target point depends both on the primary-ion flux velocity vector, $\hat{\mathbf{u}}$, and the location of the scattering center, $P(\mathbf{x})$. If the scattering occurs at a point with a potential Φ_P and the target point is at a different potential Φ_S , by conservation of energy, the kinetic energy of the scattered particle must gain the difference in potential between the two points as it arrives at $S(\tilde{\mathbf{x}})$, i.e.,

$$\Delta E^+ = -\Delta\Phi = \Phi_P - \Phi_S. \quad (2.17)$$

The combined result of each of these factors results in the expression for the energy of any particular CEX ion scattered by ions of class \mathbf{u} , at an angle θ^+ from a point $P(\mathbf{x})$, at the target point $S(\tilde{\mathbf{x}})$:

$$E = E_0 \cos^2 \theta^+ - \Delta\Phi = \frac{m_i |\mathbf{v}|^2}{2}, \quad (2.18)$$

where henceforth it will be understood that E refers to the kinetic energy of the CEX ion at the target location $S(\tilde{\mathbf{x}})$, and m_i is the mass of the ion.

From Equation 2.18, the two factors that contribute to the development of a distribution of

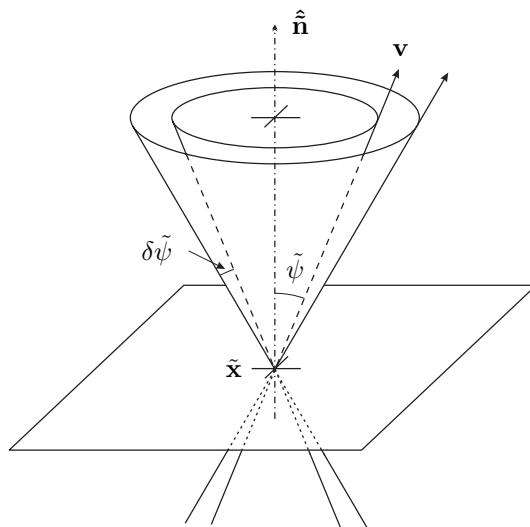


Figure 2.4: Velocity distribution of CEX ions passing through $S(\tilde{\mathbf{x}})$. CEX ions passing through $S(\tilde{\mathbf{x}})$ with energies between E and $E + \delta E$ (or speeds between v and $v + \delta v$) and at angles between $\tilde{\psi}$ and $\tilde{\psi} + d\tilde{\psi}$, with respect to the plane normal $\hat{\mathbf{n}}$, are classified to be of class $E_{\tilde{\psi}}$.

energies of CEX ions at the target point are: (1) the diverse range of values the potential difference, $\Delta\Phi$, can have due to the variation in electric potential at all the different possible scattering centers, $P(\mathbf{x})$, and (2) the range of primary ion energies, E_0 , and scattering angles, θ^+ , required to set an ion on a path through $S(\tilde{\mathbf{x}})$ due to the variation in primary ion velocities, \mathbf{u} . Later we will see that, depending on the location of the target point and the actual plume potential, the varying values of the potential difference, $\Delta\Phi$, can account for an energy spread of up to approximately 20 eV. The range of primary-ion velocities and resulting scattering angles can account for a much larger spread in energies.

Of all the CEX ions passing through $S(\tilde{\mathbf{x}})$ (see Equations 2.14 and 2.15), let us define those ions passing through the target point with energies between E and $E + \delta E$ (corresponding to speeds between v and $v + \delta v$) and at angles between $\tilde{\psi}$ and $\tilde{\psi} + d\tilde{\psi}$, with respect to the plane normal $\hat{\mathbf{n}}$, to be of class $E_{\tilde{\psi}}$ (see Figures 2.2 & 2.4). In a manner similar to how we defined the velocity distribution function of primary ions at $P(\mathbf{x})$ in Equation 2.1, let us define the angular energy distribution function of CEX ions to be such that the number of CEX ions of class $E_{\tilde{\psi}}$ located in a volume $\delta\tilde{V}$ at $S(\tilde{\mathbf{x}})$ is

$$\delta N_s(\tilde{\mathbf{x}}, E, \tilde{\psi}) = n_s(\tilde{\mathbf{x}}) f_s(E, \tilde{\psi}) \delta E \delta\tilde{\psi} \delta\tilde{V}, \quad (2.19)$$

where

$$\int_{\tilde{\psi}} \int_E f_s(E, \tilde{\psi}) \, dE \, d\tilde{\psi} \equiv 1. \quad (2.20)$$

In the limit as $\delta E \rightarrow 0$, $\delta \tilde{\psi} \rightarrow 0$, and $\delta \tilde{V} \rightarrow 0$,

$$n_s(\tilde{\mathbf{x}}) f_s(E, \tilde{\psi}) = \frac{\partial^2 n_s}{\partial E \partial \tilde{\psi}}. \quad (2.21)$$

Similar to Equation 2.4, the number flux of CEX ions of class $E_{\tilde{\psi}}$ passing through $\delta \tilde{A}'$ into the volume $\delta \tilde{V}$ is

$$\frac{\delta N_s(\tilde{\mathbf{x}}, E, \tilde{\psi})}{\delta \tilde{A}' \delta t} = v n_s(\tilde{\mathbf{x}}) f_s(E, \tilde{\psi}) \hat{\mathbf{v}} \cdot \hat{\mathbf{n}} \delta E \delta \tilde{\psi} = \Gamma'(E, \tilde{\psi}) \cos \tilde{\psi} \delta E \delta \tilde{\psi}, \quad (2.22)$$

and, by definition, is also

$$\frac{\delta N_s(\tilde{\mathbf{x}}, E, \tilde{\psi})}{\delta \tilde{A}' \delta t} = \frac{\partial^2 F'}{\partial E \partial \tilde{\psi}} \delta E \delta \tilde{\psi}. \quad (2.23)$$

Combining Equations 2.21 through 2.23 yields

$$\Gamma'(E', \tilde{\psi}) = v \frac{\partial^2 n_s}{\partial E \partial \tilde{\psi}} = \left(\cos \tilde{\psi} \right)^{-1} \frac{\partial^2 F'}{\partial E \partial \tilde{\psi}}, \quad (2.24)$$

where F' and n_s are those quantities obtained from Equations 2.14 and 2.15, respectively.

The sputter yield, $Y(E, \tilde{\psi})$, is a measure of the average number of atoms sputtered from a surface by an ion, with an energy equal to E , colliding with the surface at an angle $\tilde{\psi}$ with respect to the surface normal $\hat{\mathbf{n}}$ [33]. The rate, per unit area, at which atoms are removed from a surface, due to a flux of ions with energy E colliding with the surface at an angle $\tilde{\psi}$, is (using Equations 2.23 and 2.24)

$$\delta \Upsilon' = Y(E, \tilde{\psi}) \frac{\partial^2 F'}{\partial E \partial \tilde{\psi}} \delta E \delta \tilde{\psi} = Y(E, \tilde{\psi}) \Gamma'(E', \tilde{\psi}) \cos \tilde{\psi} \delta E \delta \tilde{\psi}. \quad (2.25)$$

The total sputtering due to all possible collisions with the surface, and all possible ion energies is

obtained by integration [34]:

$$\Upsilon' = \int_0^{\pi/2} \int_0^{E_{max}} Y(E, \tilde{\psi}) \Gamma'(E', \tilde{\psi}) \cos \tilde{\psi} dE d\tilde{\psi}. \quad (2.26)$$

The quantity in Equation 2.26 is referred to as the *directional* sputtered flux. It is referred to as a directional flux since this quantity, by means of the incident angle $\tilde{\psi}$, is dependent on the orientation of the normal of the surface being sputtered, $\hat{\mathbf{n}}$.

2.1.2 Angle-Independent Sputtering Rate

The quantities in Section 2.1.1 were derived under the assumption that the sputtered surface at the target location $S(\tilde{\mathbf{x}})$ had a preferred or specified direction of orientation, $\hat{\mathbf{n}}$. The model developed in this work has no particular project or spacecraft for which it is to be applied. With no specification of the design of the spacecraft to be used, there is no preferential direction for which the surfaces sensitive to sputtering are oriented. Since we have no reason to prefer one orientation over another, different measures, similar to those derived in Section 2.1.1 but independent of direction, will be used.

Instead of defining a planar surface with a normal unit vector $\hat{\mathbf{n}}$ at the target point $S(\tilde{\mathbf{x}})$, let us define a spherical surface, with a cross-sectional area $\delta\tilde{A}$, surrounding the target point. The flux of CEX ions *into* the sphere originating from collisions involving primary ions of class \mathbf{u} in δV is the same quantity derived in Equation 2.9, i.e.,

$$\delta F(\tilde{\mathbf{x}}, \mathbf{v}; \mathbf{x}, \mathbf{u}) = \frac{\delta N_s}{\delta\tilde{A} \delta t} = n_0 \varphi \cos \psi \left. \frac{d\sigma^+}{d\Omega} \right|_{\theta^+} \frac{\delta\Omega}{\delta\tilde{A}} \delta V \delta^3 \mathbf{u}. \quad (2.27)$$

This flux is referred to as the *non-directional* CEX-ion flux since there is no specified direction from which it can be measured. The density remains unchanged from that calculated in Equation 2.11:

$$\delta n_s(\tilde{\mathbf{x}}, \mathbf{v}; \mathbf{x}, \mathbf{u}) = \frac{\delta N_s}{\delta\tilde{V}} = \frac{n_0 \varphi \cos \psi}{|\mathbf{v}|} \left. \frac{d\sigma^+}{d\Omega} \right|_{\theta^+} \frac{\delta\Omega}{\delta\tilde{A}} \delta V \delta^3 \mathbf{u}. \quad (2.28)$$

The total non-directional CEX-ion flux through $S(\tilde{\mathbf{x}})$ (analogous to the directional flux of Equation 2.14), or the total flux of CEX ions entering the sphere, is obtained through integration over all space and all primary ion velocities:

$$F(\tilde{\mathbf{x}}) = \int_{\text{a.s.}} \int_{\mathbf{u}} n_0 \varphi \cos \psi \left. \frac{d\sigma^+}{d\Omega} \right|_{\theta^+} \left(\frac{d\tilde{A}}{d\Omega} \right)^{-1} d^3\mathbf{u} dV. \quad (2.29)$$

Again, we define an energy distribution function, $f_s(E)$, where the number of CEX ions of class E located in $\delta\tilde{V}$ at $S(\tilde{\mathbf{x}})$ is

$$\delta N_s(\tilde{\mathbf{x}}, E) = n_s(\tilde{\mathbf{x}}) f_s(E) \delta E \delta\tilde{V}, \quad (2.30)$$

where

$$\int_E f_s(E) dE \equiv 1. \quad (2.31)$$

In a manner by which Equations 2.21 through 2.24 were obtained, the non-directional flux of CEX ions of class E is

$$\frac{\delta N_s(\tilde{\mathbf{x}}, E)}{\delta\tilde{A} \delta t} = v n_s(\tilde{\mathbf{x}}) f_s(E) \delta E = \Gamma \delta E, \quad (2.32)$$

where

$$\Gamma = v \frac{dn_s}{dE} = \frac{dF}{dE}. \quad (2.33)$$

It was established in the previous section that the sputter yield is generally a function of both the energy and angle of incidence of the colliding ion. The fact that we have no preferential direction in which to orient the sputtered surface makes implementing the angle dependence of the sputter yield difficult at best. If we were to assign an arbitrary preferred direction, the expected sputtering rates predicted by our model would be particular only to that case and might not be at all accurate for a surface oriented otherwise. Though it is relatively simple in the model presented in this work to account for it, we assume that there is no angular dependence of the sputter yield.

With no angular dependence on the sputter yield, the sputtered flux of Equation 2.26 reduces to

$$\Upsilon = \int_0^{E_{max}} Y(E) \Gamma \, dE. \quad (2.34)$$

The purpose of this work is to develop a method for solving the equations (especially Equation 2.34) laid out in this chapter for any point in the region surrounding the exit of an ion engine thruster. Specifically, the following procedure will be followed. First, we must develop the ability to compute all of the individual quantities required to solve Equation 2.29. The neutral density, n_0 , is dealt with in Chapter 3. Methods for computing the remaining quantities, the primary-ion flux $\varphi \hat{\mathbf{u}} \, d^3\mathbf{u}$, differential cross-section $d\sigma^+/d\Omega$, and the streamtube expansion $d\tilde{A}/d\Omega$, are presented in Chapter 4, in Sections 4.2, 4.4, and 4.7, respectively. Second, the non-directional energy flux distribution (Equation 2.33) must be found, and is discussed in Section 4.7. The sputter yield is discussed in Section 4.5, which, in conjunction with the flux distribution, may then be used to solve for the sputter rate from Equation 2.34. This last step is discussed in Section 4.7.

The second purpose of this work is to use the model developed in an optimization procedure to find the best grid shape that minimizes the sputtering rate at specified points, and maintains the required structural integrity needed to survive a launch environment. The next section presents a brief overview of optimization theory using the *Karush-Kuhn-Tucker* conditions. The results of various optimization calculations performed are presented in Chapter 7.

2.2 Description of an Optimization Problem

The description here is a brief summary of the more complete discussion found in Papalambros [35]. As with any optimization problem, there are three key components required. The first is the *objective function*, a scalar function which defines that quantity which we wish to minimize. The second requirement is the set of any and all *parameters* which directly influence the value of the objective function. These parameters must completely define a configuration from which the objective function can be directly found. The third component to this problem is that of the *constraints* on either the values of the parameters themselves, or on any functions of the parameters. The constraints can be divided into two distinct types: (1) *equality* and (2) *inequality* constraints.

Let us form the n -dimensional configuration space, Π , spanned by all possible values of all the n pre-determined parameters. Each point in this space, denoted by a vector, $\boldsymbol{\xi}$, of specific values for each parameter, defines a specific configuration for which a unique value can be found for the objective function, $\Upsilon(\boldsymbol{\xi})$. Let us assume the constraints are represented by vector-valued functions of the subset of parameters, $\boldsymbol{\xi}$, such that

$$\mathbf{a}(\boldsymbol{\xi}) = \mathbf{0} \quad \text{and} \quad \mathbf{b}(\boldsymbol{\xi}) \leq \mathbf{0}. \quad (2.35)$$

The first constraint condition defines an $(n - m)$ -dimensional hypersurface that is a subset of Π , on which the minimizing solution, $\Upsilon(\boldsymbol{\xi}^*)$, must lie, where m is the number of equality constraint conditions contained in $\mathbf{a}(\boldsymbol{\xi})$. The second constraint condition defines a set of n -dimensional regions that are subsets of Π , and are bounded by the set of $(n - 1)$ -dimensional hypersurfaces defined by $\mathbf{b}(\boldsymbol{\xi}) = \mathbf{0}$.

The problem posed can be stated as follows:

$$\text{minimize} \quad \Upsilon(\boldsymbol{\xi}) \quad (2.36a)$$

$$\text{subject to} \quad \mathbf{a}(\boldsymbol{\xi}) = \mathbf{0}, \quad (2.36b)$$

$$\mathbf{b}(\boldsymbol{\xi}) \leq \mathbf{0}. \quad (2.36c)$$

If we can assume that the Objective Function, Υ , is continuous and differentiable, a solution to the problem, $\boldsymbol{\xi}^*$, must satisfy the *Karush-Kuhn-Tucker* conditions:

$$\mathbf{a}(\boldsymbol{\xi}^*) = \mathbf{0}, \mathbf{b}(\boldsymbol{\xi}^*) \leq \mathbf{0}; \quad (2.37a)$$

$$\nabla\Upsilon(\boldsymbol{\xi}^*) + \boldsymbol{\lambda}^T \nabla\mathbf{a}(\boldsymbol{\xi}^*) + \boldsymbol{\mu}^T \nabla\mathbf{b}(\boldsymbol{\xi}^*) = \mathbf{0}^T, \quad \text{where } \boldsymbol{\lambda} \neq \mathbf{0}, \boldsymbol{\mu} \geq \mathbf{0}, \boldsymbol{\mu}^T \mathbf{b} = \mathbf{0}, \quad (2.37b)$$

where $\nabla\mathbf{a} = [\nabla a_1, \nabla a_2, \dots, \nabla a_m]^T$ is the Jacobian of \mathbf{a} , and ∇ is the gradient with respect to the parameters $\boldsymbol{\xi}$. The first condition simply reiterates that the solution must meet all conditions defined by the constraints. Some may recognize the second condition to be simply that found in the theory of Lagrange multipliers which states that the gradients of the function and the constraining surfaces must be linear combinations of each other.

While the constraints must always be met, the inequality constraints can be further subdivided into two types: (1) *active* and (2) *inactive* constraints. Active inequality constraints are those which actually play a part in determining the location of the minimizing solution; the solution lies on these constraining surfaces ($\mathbf{b}(\boldsymbol{\xi}^*) = 0$) for, in the absence of these surfaces, the solution would be located at a point located within the volume excluded by the active constraint. Inactive equality constraints are those which could be removed from the list of constraints as they have no impact on the solution, since the minimizing solution is located neither on the constraining surface ($\mathbf{b}(\boldsymbol{\xi}^*) = 0$), nor within the volume excluded by the constraint ($\mathbf{b}(\boldsymbol{\xi}^*) > 0$). In the simplest sense, the number of degrees of freedom (design parameters) is equal to the total number of parameters, n , minus the number of equality constraints, m , minus the number of active inequality constraints, s . In theory, each equality constraint and active inequality constraint could be used to eliminate one of the parameters in terms of the others until there were no constraints, and a new function to minimize, $\tilde{\Upsilon}$, that is only dependent on the $m - n - p$ parameters left; in practice this may be impossible to do.

The vector $\boldsymbol{\lambda}$ is a vector of *Lagrange multipliers*, and is restricted to all non-zero values; by nature, equality constraints are always active — a Lagrange multiplier with a value of zero would effectively remove the constraint and render it inactive. The vector $\boldsymbol{\mu}$ is another vector of Lagrange

multipliers applied to the inequality constraints. Permitting elements of $\boldsymbol{\mu}$ to be equal to zero is simply a combination of the active and inactive constraints; any zero value corresponds to an inactive constraint, which reflects that fact that it has no effect on the solution.

These conditions are *necessary*, however they are *insufficient* to guarantee that $\Upsilon(\boldsymbol{\xi}^*)$ is a local constrained minimum. In order for the point $\boldsymbol{\xi}^*$ to be a minimizing solution, the Hessian of the Lagrangian must be positive-definite in the local vicinity of the solution point $\boldsymbol{\xi}^*$, where the Lagrangian is defined to be

$$L(\boldsymbol{\xi}, \boldsymbol{\lambda}, \boldsymbol{\mu}) \equiv \Upsilon(\boldsymbol{\xi}) + \boldsymbol{\lambda}^T \mathbf{a}(\boldsymbol{\xi}) + \boldsymbol{\mu}^T \mathbf{b}(\boldsymbol{\xi}), \quad (2.38)$$

and the Hessian is the gradient of the gradient with respect to the parameters $\boldsymbol{\xi}$. This is akin to stating that any small step in *any* allowable direction away from the solution point results in an increase in the value of the objective function.

In this specific problem, we have created a model for which we can define a set of parameters that determine the trajectories of ions as they exit the engine and collide with neutrals. The subsequent evolution of each resulting CEX ion may result in a collision with some portion of the spacecraft and sputtering of material from the surface. It is this sputtering of sensitive areas of the spacecraft that we wish to minimize, and so defines what the Objective Function is. In Section 2.1 we derived the equations for which Chapters 3 and 4 are devoted to developing a method to solve. The end result is a model that computes the sputtering rate, per unit area, due to CEX ion collisions with a surface, based on a number of parameters chosen. It is this sputtering flux that we define to be the objective function.

The parameters $\boldsymbol{\xi}$ chosen to determine the value of the sputtered flux Υ will determine how sophisticated the model will need to be. A small, but by no means exhaustive list of possible quantities that could be chosen to be parameters are: physical geometry of the grid set, grid hole pattern, grid thickness, and beamlet structure. Due to the extensive previous work studying the ion optics for the NSTAR grid set, for this project we will use the NSTAR grid hole pattern, grid thickness, and beamlet structure as given conditions, and only parameters defining the physical shape of the grid set will be used as optimizing (design) parameters, $\boldsymbol{\xi}$.

Further, the constraints imposed on the proposed optimization will be those physical constraints on the shape of the grid set such that there is a high confidence that the grids will survive the launch into space. While such quantities could include both the maximum tolerable stresses and displacements, we will consider only the maximum displacements in this study.

After developing the sputtering rate model in the following three chapters, the method by which we determine the displacements of any grid under a specified load is detailed in Chapter 6. The optimization procedure and results are presented in Chapter 7.

Chapter 3

Neutral Density Distribution Determination

There has been previous work in modeling the plume downstream of not only ion engines, but other electric propulsion devices. The different exit-plane conditions, through which ions are accelerated and neutral atoms diffuse in the various types of engines, place different restrictions and limits on the behavior of these species. For example, for configurations involving ion grids, the ions and atoms can only exit through well-defined apertures formed by the ion optics holes, whereas Hall thrusters have no such barrier at the exit plane, and neutrals can diffuse out from any point in the channel. Despite the different conditions encountered in modeling the different thrusters, a common assumption is made to model how the neutrals diffuse and spread from the engine exit. This assumption is that the neutrals spread out according to a modified cosine distribution. This chapter examines the validity of using such a distribution for modeling the neutral density downstream of an ion engine, through comparison with computer simulations of gas diffusion through ion grids. In Section 3.1 the origin of and rationale for choosing the cosine distribution is discussed. In Section 3.2, we present the procedure followed to model gas diffusing through both a single and a pseudo-periodic aperture in an infinite grid. In Section 3.3, we calculate the far-field density distribution functions of the simulations performed, from which we calculate the Clausing factor for each. Finally, in Section 3.4, using the results from the simulations, the density of neutral atoms downstream of an NSTAR grid is computed and compared to that using the cosine distribution assumption.

3.1 Rarefied Flow through Holes of Varying Depth

Rarefied gas flow is defined to occur when the Knudsen number is much larger than unity, i.e., $Kn = \lambda/d \gg 1$, where λ is the mean free path of the atoms and d is a characteristic dimension of the region through which the gas is flowing [36]. The first question to answer when determining the neutral density downstream of an ion engine is whether the state of the gas is in the rarefied regime or not. The discharge chamber of the NSTAR engine operates with a neutral xenon density of the order of 10^{18} m^{-3} [9], yielding a mean free path of approximately $\lambda = 22 \text{ cm}$ for an atomic radius of 2 \AA . The screen and accel grid thickness, separation, and hole radii are all of the order of 1 mm [9], yielding a Knudsen number much larger than unity, and placing the flow firmly in the rarefied regime.

Previous models that required the determination of the neutral density around Hall thrusters [17, 37] have used a modified cosine, or Lambertian, distribution law for the particles emitted from a point located one thruster radius, R_g , behind the thruster exit:

$$n_0(\ell, \chi) \approx W \rho_0 \cos \chi \left[1 - \frac{1}{\sqrt{1 + (R_g/\ell)^2}} \right], \quad (3.1)$$

where ρ_0 is the neutral number density at the thruster exit; χ is the angle between the thruster axis and the vector originating from the emission source and directed to the point where we wish to compute the density; ℓ is the distance between the emission source and the computation point; and W is a correction factor. The use of this distribution is motivated by the result of gas effusing from a region filled with neutral gas in thermal equilibrium through an infinitely thin hole to a region of empty space. Assuming thermal equilibrium allows a Maxwellian distribution of atoms in the gas to be used. Imagine that the center of the hole is located at the position \mathbf{y} . Let us construct a local coordinate system such that $\underline{\mathbf{x}} = 0$ is located at the center of the hole, and the coordinate system is oriented such that the hole lies in the $\underline{z} = 0$ plane. The density at any point $P(\underline{x}, \underline{y}, \underline{z})$ can be found by integrating the flux of atoms through the hole passing through the point in question. The result

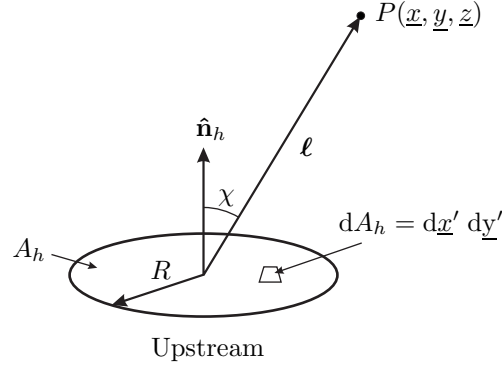


Figure 3.1: An effusing infinitely-thin hole. The density of neutral atoms at a point P is obtained by integrating the flux of effusing atoms through the hole over the entire hole area, A_h . The local coordinate system, \underline{x} , is centered on the center of the hole, and oriented such that \underline{z} is measured along the hole normal, $\hat{\mathbf{n}}_h$.

for a hole of arbitrary shape is exactly expressed by the following integral (Figure 3.1):

$$n_0(\underline{x}, \underline{y}, \underline{z}) = \frac{\rho_0}{4\pi} \int_{A_h} \frac{\underline{z} d\underline{x}' d\underline{y}'}{[(\underline{x} - \underline{x}')^2 + (\underline{y} - \underline{y}')^2 + \underline{z}^2]^{3/2}}, \quad (3.2)$$

where ρ_0 is the density of the gas upstream, and A_h is the area of the hole. The full derivation can be found in many textbooks on kinetic theory [23].

Two specific cases allow for simple evaluation of the integral. The first case applies when the point in question P is any point on the axis of the hole, ($\underline{x} = \underline{y} = 0$), and the hole is circular. In this case, the integral simplifies to

$$n_0(\underline{z}) = \frac{\rho_0}{2} \left[1 - \frac{1}{\sqrt{1 + (R/\underline{z})^2}} \right] \quad (\underline{x} = \underline{y} = 0), \quad (3.3)$$

where R is the radius of the hole. The second case is a far-field asymptotic solution, valid when the distance between the point in question and the hole, ℓ , becomes large. In the limit of $\ell/R \gg 1$, the integral approaches the value

$$n_0(\ell, \chi) = \frac{\rho_0 \cos \chi}{4\pi \ell^2} A_h \quad \left(\frac{\ell}{R} \gg 1 \right), \quad (3.4)$$

where χ is the angle between the hole axis and the vector directed to the point in question. Both

specific cases allow for rapid evaluation of the density of gas at any point within their respective regions of validity.

Unfortunately, other than on the axis of the hole, there is no exact expression for the density in the immediate vicinity of the hole. If one were to assume that the second case is “good enough”, regardless of the distance from the hole, an immediate problem arises upon evaluation of the density very close to the hole, as ℓ gets very small and the density rapidly increases. Since the first case does not have this problem of predicting a density approaching infinity for points very close to the hole, and is finite regardless of distance from the hole, we will use this case as a starting point for deriving an equation that models the density near the hole, but not on the thrust axis. The first modification is to take the cosine factor from the second case and append it to the first, then replace \underline{z} with ℓ to approximate the density at any point around the hole:

$$n_0(\ell, \chi) \approx \frac{\rho_0 \cos \chi}{2} \left[1 - \frac{1}{\sqrt{1 + (R/\ell)^2}} \right] \quad \left(\frac{\ell}{R} \text{ unrestricted} \right). \quad (3.5)$$

In the limit as $R/\ell \rightarrow 0$ (large ℓ) this expression approaches the far-field limit of Equation 3.4.

The expression for the far-field limit (Equation 3.4) can be viewed as describing anisotropic emission from a point source, for as the distance from the hole gets large the distance to any area element of the hole, dA_h , becomes constant. By continuity, the integrated flux normal to any surface enclosing the hole must be constant, and thus the density must decrease with ℓ^2 . As an anisotropic source, the flux measured can depend on the angle. We can expect that this same argument applies at a sufficient distance from any hole or aperture. Thus, regardless of the shape or complexity of the aperture, in the limit of $\ell/R \gg 1$, we can define a far-field density distribution function:

$$n_0(\ell, \chi) = \frac{\rho_0}{4\pi} \frac{f(\chi)}{\ell^2} A_h, \quad (3.6)$$

where $f(\chi)$ is some function expressing the anisotropy of the emission source; in the case of the infinitely flat hole (see Equation 3.4), $f(\chi) = \cos(\chi)$.

If a hole has any finite depth, the atoms in the gas begin to interact with the surface inside the hole

through adsorption, desorption, and reflection [38]. The assumption of a Maxwellian distribution for the atoms becomes no longer valid since the atoms bouncing off the hole walls alter the distribution. In his work with vacuum system tubes, Knudsen [36] formulated the cosine law which describes the pattern, for many surfaces, in which atoms diffusively reflect after contacting the surface. The significant impact of such a re-emission distribution is that atoms which otherwise would have passed through a thin hole may be re-emitted back in the direction from which they originally came. This back reflection results in a reduced total flow rate of atoms through the hole, and thus a reduction of the density at any point downstream of the hole.

The presence of a hole of finite length also effectively screens atoms from passing through, and causes a beaming effect of the angular distribution of atoms downstream, due to the depletion of atoms at the larger angles. Clausing [39, 40] developed integral relationships which not only predict the reduction in flow rate as a function of the ratio of the hole depth to radius, L/R , but also found the angular distribution, $f(\chi)$, as a function only of this same ratio. The resulting angular distribution in the back-reflecting direction was found by Dayton [41] by extending Clausing's original work.

The reduction in flow rate through a hole due to a finite depth is commonly referred to as the Clausing factor, W , or "probability of passage", and is the ratio of the resulting flow rates for two identical gases under the same conditions through two different holes: (1) flow through a hole with a specific depth-to-radius ratio to the flow, and (2) flow through an infinitely thin hole [41]. This Clausing factor can be found from Equation 3.6 in the following way. By conservation of mass,

$$I_0 = \int_{\partial\Omega} \mathbf{F} \cdot d\mathbf{a} = \int_{\partial\Omega} n_0 \mathbf{u}_0 \cdot d\mathbf{a}, \quad (3.7)$$

where I_0 is the flow rate of atoms through the hole, $\partial\Omega$ is any surface enclosing the hole, \mathbf{F} is the flux, and \mathbf{u}_0 is the velocity of the atoms. Substituting for the density from Equation 3.6 into the expression, and arbitrarily letting the enclosing surface be a hemisphere of radius ℓ , yields

$$I_0 = 2\pi \int_0^{\pi/2} \left(\frac{\rho_0 A_h \bar{u}_0}{4\pi} \frac{f(\chi)}{\ell^2} \right) \ell^2 \sin \chi \, d\chi = \frac{\rho_0 A_h \bar{u}_0}{2} \int_0^{\pi/2} f(\chi) \sin \chi \, d\chi. \quad (3.8)$$

In the case of the infinitely thin hole, $I_0^* = \rho_0 A_h \bar{u}_0/4$. We have implicitly assumed the use of a mean velocity, \bar{u}_0 , which results in no loss of generality, since we require that both gases flowing through the aperture and the infinitely thin hole are under the exact same conditions. By definition of the Clausing factor,

$$W = \frac{I_0}{I_0^*} = 2 \int_0^{\pi/2} f(\chi) \sin \chi \, d\chi. \quad (3.9)$$

Though Clausing provided integral relationships for determining the angular distribution of the flux through a hole of finite depth, statistical computation methods are typically required for more complex systems [38]. This difficulty in determining the angular distribution, $f(\chi)$, for complex geometries, such as those encountered with electric propulsion devices, has led to the common use of the modified cosine distribution (Equation 3.5), adjusted by a Clausing-type correction factor, W [17].

3.2 DSMC Calculation of Neutral Distribution for an NSTAR Two-Hole Aperture

For this work, we desire to obtain an angular distribution function, $f(\chi)$, for the neutral atoms effusing from the two-hole aperture created by the alignment of the ion engine grids. The holes on the NSTAR grids are patterned such that each hole is found at the vertex of an equilateral triangle (Figure 3.2). Each hole has six nearest neighbors equally spaced along a circle centered on the middle hole. The radius of this circle is equal to the hole pitch, p , and is equal to 2.22 mm for the NSTAR grids. The NSTAR screen and accel grids are 0.38 mm and 0.51 mm thick, respectively. The holes in the screen grid have a radius of 0.955 mm, and the accel grid holes have a radius of 0.57 mm. The grid separation is 0.66 mm [9].

Computational simulations were performed to obtain the expected distribution function for two different aperture geometries representative of the NSTAR hole pattern. Our simulation was performed using DS2G, a Direct-Simulation Monte Carlo (DSMC) code developed by Dr. Graeme Bird [42]. This code is designed for use with two-dimensional or axisymmetric problems involving mole-

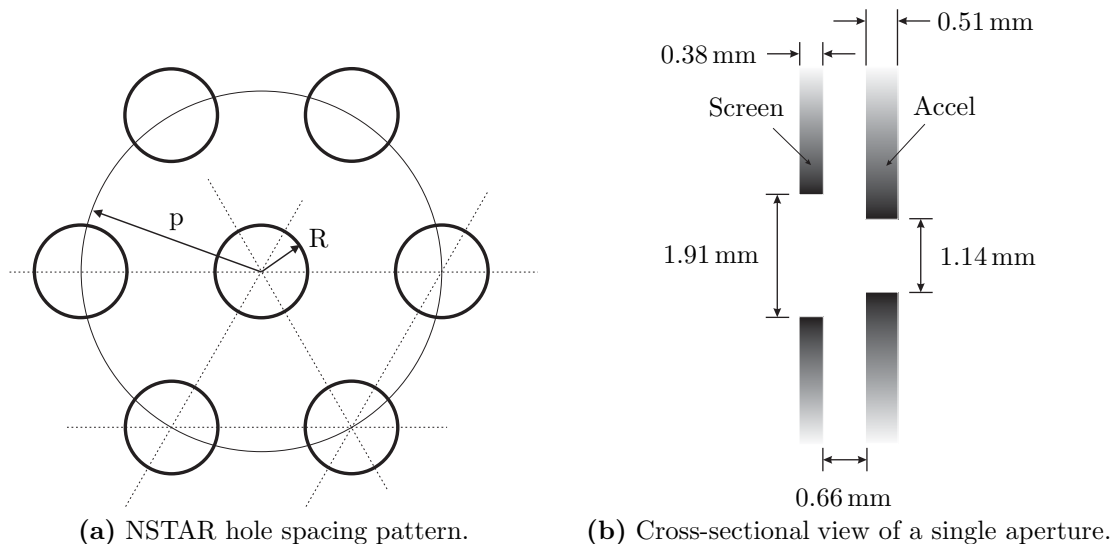


Figure 3.2: Triangular hole pattern for NSTAR grids. Both the screen and accel grids have the same hole-to-hole pitch, $p = 2.22\text{ mm}$. The hole radii are $R = 0.38\text{ mm}$ and $R = 0.57\text{ mm}$ for the screen and accel grid, respectively.

cular flow, such as those encountered when dealing with rarefied gases. A thorough explanation of the method can be found in [43].

3.2.1 Single Aperture in an Infinite Grid

Using the dimensions appropriate for the NSTAR hole pattern (see Figure 3.2), an axisymmetric simulation domain was created to model the effusion of gas through one aperture in an infinite plane, and is shown in Figure 3.3. The positions of the screen and accel grids are indicated by the shading. Simulating the entire domain at once was found to require too many simulated particles to obtain a sample of the downstream density without significant statistical error. To reduce the computational time required to obtain a statistical sample of the density downstream of the hole, the simulation was split into two phases. In the first phase the region extending from approximately eleven accel grid hole radii (6 mm) upstream from the screen grid to the aperture exit (5a in the figure) was simulated. There were a total of 16,600 cells that constituted the entire upstream domain used in the first phase. The second phase simulated only the downstream portion extending from the aperture exit (5b in the figure) to approximately 24 accel grid hole radii (14 mm) downstream. The downstream region was made up of 85,000 separate cells.

2,400 real atoms, were in the upstream domain at any time. The position and velocity of any particle that intercepted the surface at 5a, after steady state was achieved, were recorded; the particle was then removed from the domain. Simulation continued until the states of approximately 1.2 million atoms were recorded.

During the second phase, the record from the first was used as the input atom source file for the surface at 5b. The simulation of the particles downstream was started with no atoms in the domain. For this phase, the number of atoms each simulated particle represented was reduced to nine to increase the number of simulated atoms within the domain. As the simulation proceeded the program randomly selected atoms from the input file and added them to the flow at 5b such that the total flux from this surface was the same as that through 5a during the first phase. Once a steady state was achieved, approximately 160,000 simulated molecules were in the domain at any time. Any molecule intersecting boundary 4 was removed from the simulation. The total simulation took approximately nine days on a modern desktop computer.

During both simulation phases, after a steady state had been obtained, a sample of the atom density was recorded at periodic intervals. Each sample comprised a record of the density of atoms within each cell. Over one million samples were obtained during the second phase. The average density, over these one million samples, for each domain cell was provided as output at the conclusion of the simulation. Averaging over many samples reduced any statistical fluctuations that might be present at any particular time.

Measuring from the center of the accel grid hole (where 5b intersects the rotation axis in Figure 3.3), the density at points along curves of constant radius were interpolated from the data output from the simulation. The density for various radii ℓ , as a function of the angle χ measured from the rotation axis, is shown in Figure 3.4 in non-dimensional units. The non-dimensional density is the angular distribution function, $f(\chi)$, obtained by rearranging Equation 3.6:

$$f(\chi) = 4 \frac{n_0}{\rho_0} \left(\frac{\ell}{R} \right)^2. \quad (3.10)$$

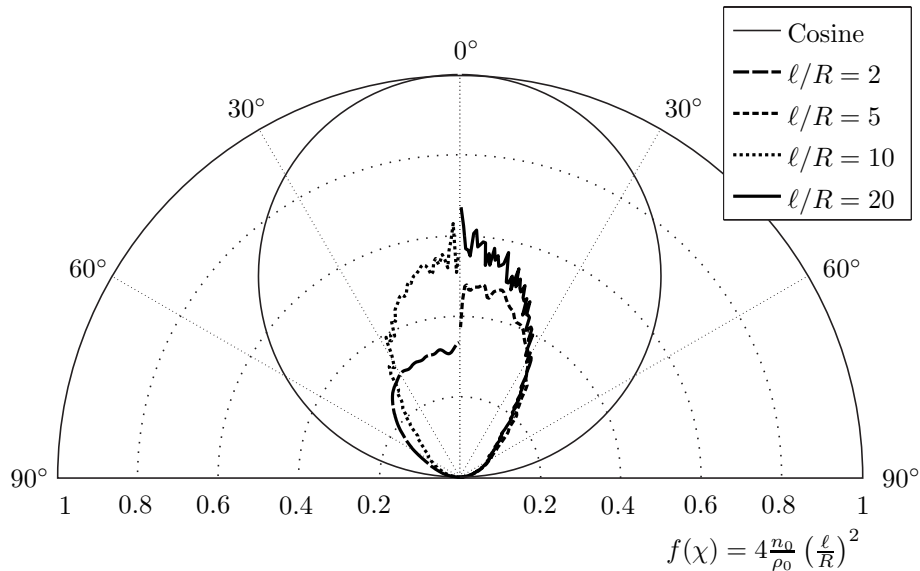


Figure 3.4: Non-dimensional angular density distribution of a single aperture in an infinite plane. The density at various points along curves of constant radius from the accel grid hole center were interpolated from the averaged data output at the conclusion of the simulation. The non-dimensional angular density distribution for each curve was computed from Equation 3.10 and plotted as a function of the angle measured from the rotation axis, χ . For clarity, axisymmetry allows for only half of each distribution to be shown. The cosine distribution is shown for comparison.

The cosine function, for an infinitely thin hole, is also shown for comparison.

The beaming effect, as a result of an aperture of finite depth, is immediately evident. Despite averaging over 10^6 time steps, fluctuations are still within 5-10% of the maximum. The fluctuations are seen to be greatest at small angles. This is not unexpected. In an axisymmetric case, the volume represented by each domain cell element is proportional to d^2 , where d is the distance to the cell from the axis. At small angles, the cells are close to the rotation axis, which means the volume of each is relatively small. As the volume of a cell decreases we can expect the probability of molecules to be found within the volume to decrease as well.

As anticipated, the angular distribution is found to approach a single far-field function as the distance from the hole increases. The resulting far-field distribution, from which the reduction in flow rate compared to an infinitely thin hole (Clausing factor) will be found, will be described in more detail in Section 3.3.

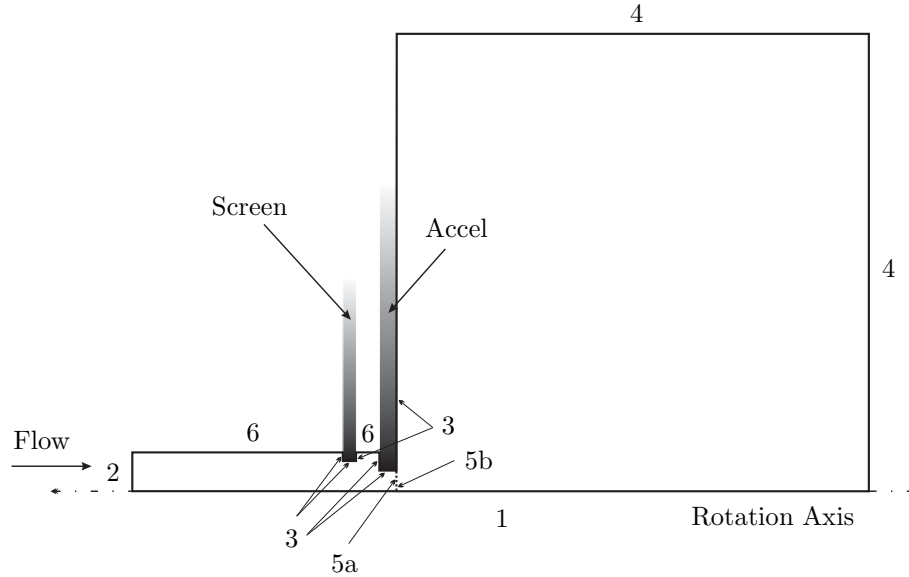


Figure 3.5: Simulation domain for a pseudo-periodic aperture pattern. Both the upstream (left of 5a) and downstream (right of 5b) domains started with zero molecules at the beginning of their respective simulation phases. The upstream flow conditions had a density of 10^{18} cm^{-3} , a temperature of 500 K, and zero mean velocity (molecules diffused in through sides 2). The positions and velocities of molecules intersecting 5a during the first phase were recorded, then the particle was removed from the domain. The recorded molecules from the first phase were used as a molecular input (at 5b) to the downstream domain in the second phase. Molecules intersecting sides 4 were removed from the simulation. The width of the upstream domain (distance between sides 1 and 6) is equal to one half of the NSTAR pitch, $p/2 = 1.11 \text{ mm}$.

3.2.2 Single Aperture with a Pseudo-Periodic Hole Pattern

The previous simulation predicted only the density downstream of a single NSTAR aperture, and did not include the possible influence that neighboring holes may have on the distribution. To estimate the effect of surrounding holes, the previous simulation was slightly modified. In an axisymmetric simulation, it is not possible to exactly model the periodic nature of the triangular pattern of holes found on the NSTAR (Figure 3.2). Instead, a simulation domain was created that modeled a series of concentric apertures which allow for influence by the adjacent holes on the density downstream of the center hole. Since this domain does not exactly model the periodic nature of the NSTAR hole pattern, we have termed this to be a pseudo-periodic hole pattern. The domain created is shown in Figure 3.5. The boundary conditions were similar to those used in the previous section to simulate a single hole, except for the addition of specularly reflecting surfaces in the upstream domain. The boundary conditions follow.

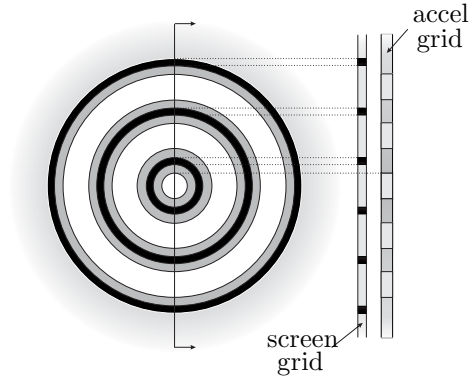


Figure 3.6: Effective pseudo-periodic hole pattern. The domain of Figure 3.5 models a series of concentric apertures. Though the simulation effectively allows atoms to exit through the apertures surrounding the center, only those exiting through the central aperture are recorded for the purpose of populating the downstream domain (right of 5b) during the second phase of the simulation.

Boundary 1: Axis of rotation

Boundary 2: Free stream boundary

Boundary 3: Diffuse reflecting surface at a temperature of 500 K

Boundary 4: Vacuum (intersecting molecules removed from domain)

Boundary 5a: Vacuum (Molecular output)

Boundary 5b: Molecular input

Boundary 6: Specularly reflecting surface

The specularly reflecting surfaces (Boundary 6) allow for atoms to pass from the vicinity of one hole to another. The concentric hole pattern modeled by this domain is shown in Figure 3.6. Though atoms are permitted to exit through the apertures surrounding the center, only the position and velocity of those exiting from the center aperture are recorded for the purpose of populating the downstream domain during the second simulation phase. Thus, the resulting neutral density distribution downstream of the aperture is a single-hole distribution, but the distribution of atoms upstream is influenced by the presence of other holes. The width of the upstream domain, i.e., the distance between surfaces 1 and 6, is equal to one half of the NSTAR pitch, $p/2 = 1.11$ mm.

As for the single aperture simulation detailed in the previous section, the simulation was split into two phases. The upstream domain extended from approximately eleven accel grid hole radii (6 mm) upstream from the screen grid to the aperture exit (5a in Figure 3.5), and had a total of

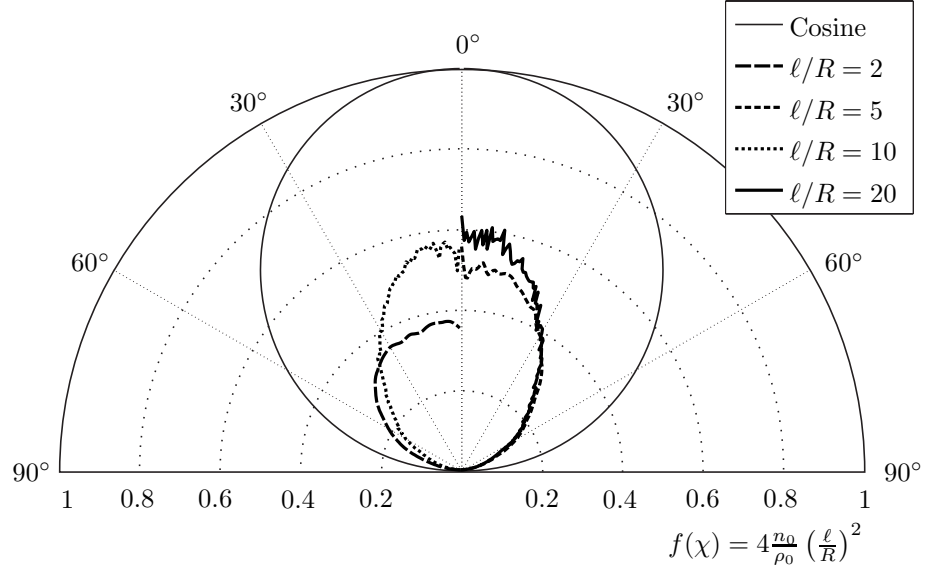


Figure 3.7: Non-dimensional angular density distribution of a pseudo-periodic aperture pattern. The density at various points along curves of constant radius from the accel grid hole center were interpolated from the averaged data output at the conclusion of the simulation. The non-dimensional angular density distribution for each curve was computed from Equation 3.10, and plotted as a function of the angle measured from the rotation axis, χ . For clarity, axisymmetry allows for only half of each distribution to be shown. The cosine distribution is shown for comparison.

15,160 cells. The free stream was specified to be a flow of argon gas with a density of 10^{18} cm^{-3} , a temperature of 500 K, and zero mean velocity. The simulation was started with no atoms present within the domain. Once a steady state was reached, there were a total of approximately 240,000 simulated molecules, each representing 250 real atoms, within the upstream domain at any time. The position and velocity of all molecules intercepting surface 5a during the first phase of the simulation were recorded, and then the molecules were removed from the domain. Simulation continued until approximately 2.5 million molecules were recorded. The simulation of the downstream domain in phase two was carried out identically to that described in Section 3.2.1.

The angular distribution function, $f(\chi)$, for various radial curves is shown in Figure 3.7. The cosine distribution is shown for comparison. As in the previous simulation, fluctuations are seen for the data at small angles, and are within about 5-10% of the maximum density. The function is less than the cosine at all angles. In the next section we will evaluate and compare the non-dimensional far-field distributions ($\ell/R \gg 1$) from both simulations to the cosine distribution, and obtain the appropriate Clausing factors for each.

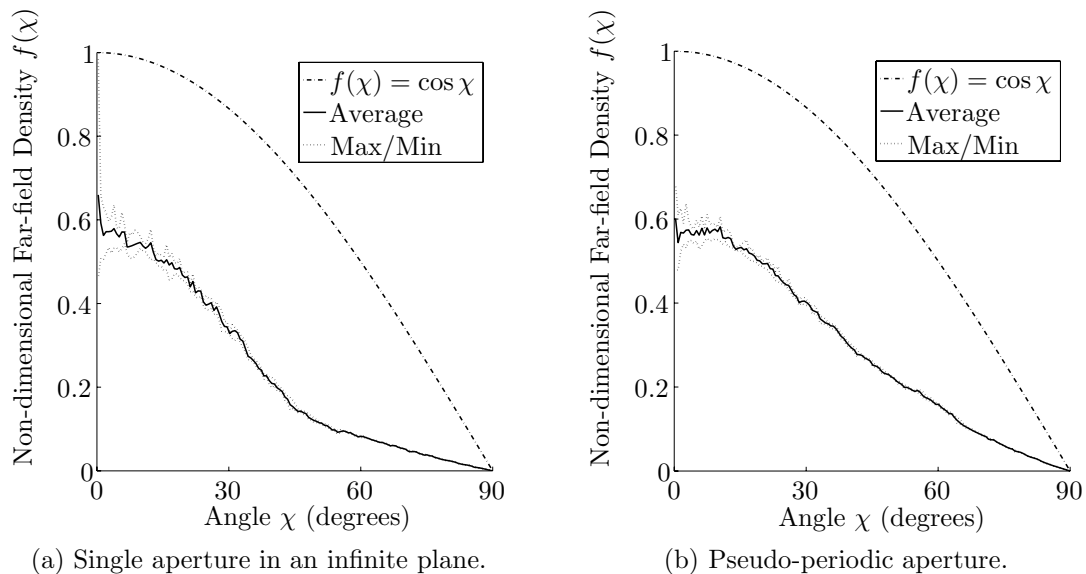


Figure 3.8: Non-dimensional far-field angular density distributions. Obtained from averaging the non-dimensional density, $f(\chi)$, obtained for $\ell/R = 9$ to $\ell/R = 22$ in increments of one. The maximum and minimum range about the mean of all functions used in the average is shown in the Max/Min curves. Cosine distribution is shown for comparison. The hole axis corresponds to $\chi = 0$. The Clausing factor for each is obtained by integrating $2f(\chi)\sin\chi$ over all angles (see Equation 3.9) yielding values of $W = 0.279$ and $W = 0.380$ for the single aperture and the pseudo-periodic aperture, respectively.

3.3 NSTAR Aperture Density Function and Clausing Factor

To obtain the far-field distributions from each of the simulations in Section 3.2, the non-dimensional density, $f(\chi)$, was found for radial curves starting with $\ell/R = 9$ up to $\ell/R = 22$, in increments of one and averaged together. The two averaged solutions are shown in Figure 3.8 in addition to the flat hole solution, $f(\chi) = \cos(\chi)$. In Section 3.1 the Clausing factor was defined to be (Equation 3.9)

$$W = \frac{I}{I^*} = 2 \int_0^{\pi/2} f(\chi) \sin \chi \, d\chi. \quad (3.11)$$

Numerical integration of the two functions (shown in Figure 3.8) yields Clausing factors for the single and pseudo-periodic apertures of $W_s = 0.279$ and $W_p = 0.380$ respectively.

The Clausing factor for the pseudo-periodic aperture is approximately 35% greater than that for the single aperture. This is evidenced by the higher density at large angles¹. The higher density

¹In this situation, discussion of the density is synonymous with a discussion of flux, since we have assumed a constant mean velocity; density and flux are related by a constant. See the discussion leading to the derivation of the Clausing factor in Equation 3.9.

at large angles can be explained by the fact that, in the pseudo-periodic aperture, atoms that pass through the screen grid through a hole adjacent to the center hole can then pass through the accel grid through the center hole. Such atoms will have trajectories inclined at large angles with respect to the hole axis. There are some atoms present at these high angles with the single hole, since some atoms that begin travelling down the channel between the screen and accel grids can collide with a wall and be reemitted back towards the hole.

Both aperture configurations permit less flow of atoms than an infinitely thin hole, and have distributions different than the cosine. Normalizing the conditions upstream of an infinitely thin hole, such as to match the flow rate with one of the apertures, would result in a lower density along the hole axis and a higher density at large angles, compared with the density distribution of the aperture. This is demonstrated in the next section, where we compute the total neutral atom density downstream of the NSTAR grid using both the cosine and the single-aperture density distributions.

3.4 Neutral Distribution Due to Multiple Holes

The DSMC simulations described in Section 3.2 only simulated the neutral density distribution resulting from atoms effusing downstream through an individual aperture. Earlier, the mean free path within the discharge chamber was found to be approximately 20 cm. The density downstream of an aperture is limited by the upstream density, so the mean free path downstream is, at a minimum, the same as in the discharge chamber. Since the mean free path is on the order of the size of the engine grids (30 cm), we expect very few collisions between atoms, and so it is reasonable to assume that the total density downstream of the engine grids can be found by superposition of the density contributions from all grid holes. The neutral density downstream of an NSTAR-shaped grid was computed using superposition of both the cosine distribution and the distribution resulting from a single hole in an infinite plane. The pseudo-code for the method is detailed in Section 3.4.1, and the results are discussed in Section 3.4.2.

3.4.1 Pseudo-Code: Calculating the Neutral Density

The following pseudo-code outlines the procedure used to determine the neutral atom density at any point. The density is computed at the desired point by superposition of the contributions from all grid holes. The code was implemented using Matlab.

1. Let \mathbf{x} be the location of the point at which to evaluate the density, N be the total number of holes, and R be the accel grid hole radius.
2. Let ρ_0 be the neutral density inside the engine discharge chamber.
3. $k = 0$.
4. $k = k + 1$.
5. Let \mathbf{y}_k be the coordinates of the center of hole k , and $\hat{\mathbf{n}}_k$ the normal vector to hole k .
6. Compute the vector between hole k and the evaluation point, $\boldsymbol{\ell}_k = \mathbf{x} - \mathbf{y}_k$.
7. Compute $\ell_k = \|\boldsymbol{\ell}_k\|$.
8. Compute $\chi_k = \cos^{-1}(\ell_k^{-1} \boldsymbol{\ell}_k \cdot \hat{\mathbf{n}}_k)$.
9. If $0 \leq \chi_k \leq 90^\circ$, go to step 10; otherwise $n_{0,k} = 0$, go to step 11.
10. Calculate the contribution to the density from hole k ,

$$n_{0,k} = \frac{\rho_0 f(\chi_k)}{2} \left[1 - \frac{1}{\sqrt{1 + (R/\ell_k)^2}} \right]. \quad (3.12)$$

11. If $k < N$, go to step 4; otherwise go to step 12.
12. Sum all contributions, $n_0(\mathbf{x}) = \sum_k n_{0,k}$.
13. Output $n_0(\mathbf{x})$.

3.4.2 Neutral Density Downstream of an NSTAR Grid

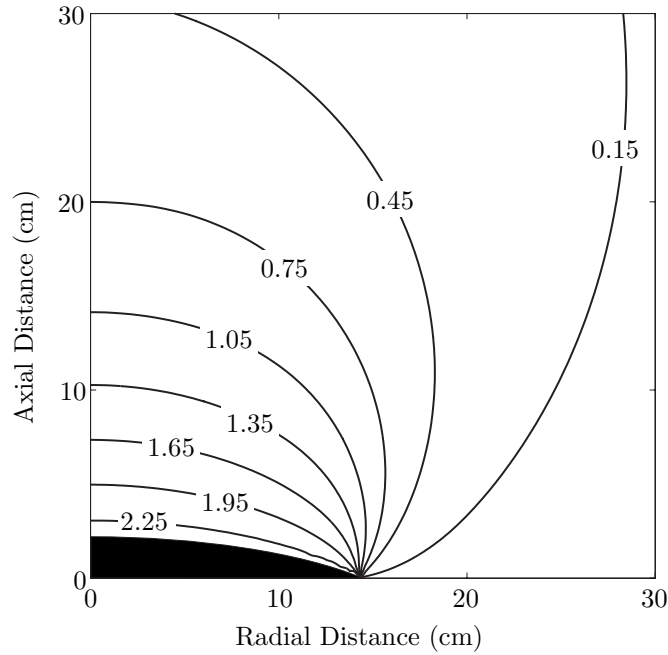
The total neutral density distribution downstream of an NSTAR-shaped grid was modeled using superposition of the contributions from all grid holes. In order to prevent near-infinite contributions at positions very close to the surface of the grid, the distribution contribution from each hole was calculated using the following (see Equations 3.5 and 3.6):

$$n_0(\ell, \chi) = \frac{\rho_0 f(\chi)}{2} \left[1 - \frac{1}{\sqrt{1 + (R/\ell)^2}} \right]. \quad (3.13)$$

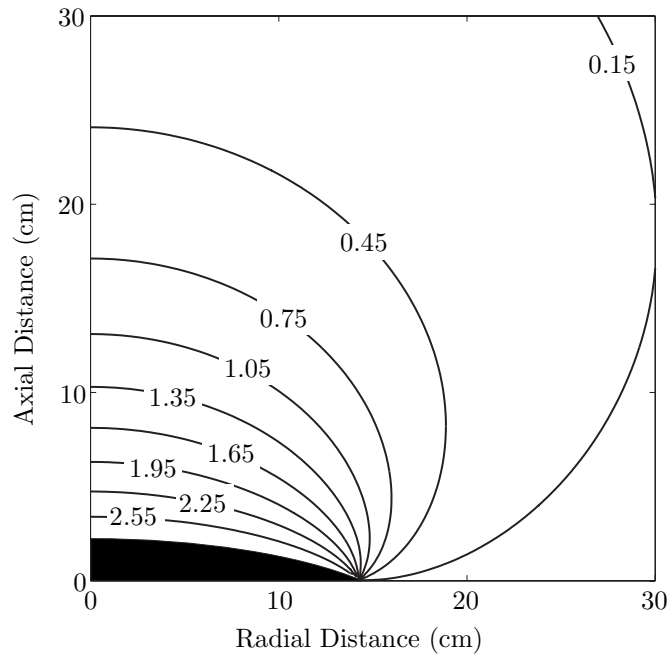
At large distances, $\ell/R \gg 1$, Equation 3.13 approaches that of Equation 3.6; at a distance of 0.5 cm ($\sim 10 R$), the density contributions computed from each relation differ by less than 1%.

The total density was computed using both the distributions resulting from a single aperture in an infinite plane, and from an infinitely thin hole (cosine distribution). The total flux from each hole was normalized by reducing the total flux through the infinitely thin hole, i.e., $f(\chi) = W_s \cos \chi$. The procedure for computing the density at any point downstream of the grid is detailed in Section 4.4.1. The resulting density distributions, using both the single aperture and infinitely thin hole, are shown in Figure 3.9.

Comparing the two resulting distributions yields the following conclusions. In the region near the grid axis and up to approximately 13 cm downstream, the expected neutral density is higher using the thin hole than using the single aperture, especially within the first couple of centimeters from the grid surface. Beyond approximately 13 cm in the region near the grid axis, the density drops off more rapidly for the cosine distribution than for the single aperture distribution. Also, at high angles with respect to the grid axis, the density drops off less rapidly using the thin hole than using the single aperture. As we develop the model in Chapter 4, we will find that the high energy CEX ions that reach points inclined at large angles, with respect to the grid axis (greater than $\sim 80^\circ$), predominantly originate from the region near the edge of the main beam. As a result, the differences in the neutral density in this region, due to the different neutral distribution models, could have a significant impact on the predicted sputtering rates.



(a) Density distribution resulting from modeling each hole as a single aperture in an infinite plane.



(b) Density distribution resulting from modeling each hole using the cosine distribution.

Figure 3.9: NSTAR neutral density distribution. The density at any individual point is obtained from superposition of the contributions from all grid holes. Each grid hole is modeled to have the density distribution of (a) a single aperture in an infinite plane, and (b) an infinitely thin hole (cosine distribution). In the case of the infinitely thin hole, the total flux through each hole was normalized to be the same as for the single aperture, i.e., $f(\chi) = W_s \cos \chi$. Contour line quantities are in terms of percentage of the upstream density, ρ_0 .

In the derivation of the model equations in Chapter 2, we assumed that the CEX ions do not undergo further collisions once they are created from a charge-exchange collision. Now that we have estimates to the neutral density distribution around an NSTAR grid, we are in a position to test whether this assumption is reasonable or not. According to the Beer-Lambert Law, the attenuated flux, F , of a beam passing through some medium (due to scattering collisions) is

$$F = F_0 \exp \left(- \int_0^d n_0 \sigma_0 ds \right), \quad (3.14)$$

where F_0 is the flux of the beam at the starting point, $s = 0$, d is the path length traversed through the medium, n_0 is the density of scattering centers, and σ_0 is the total scattering cross-section [23]. In Chapter 4, we will find that the total charge-exchange cross-section for xenon ion/atom collisions is approximately 55 \AA^2 for ion energies of 300 eV. Using this cross-section, integrating down the grid axis of both neutral distributions (Figure 3.9) yields an attenuation of less than 1% for a beam of ions travelling from the grid surface to a position 30 cm downstream. Though there are collisions between the CEX ions and the neutral atoms, in light of this small attenuation rate, we feel the assumption made in deriving the model equations is justified. The assumption of no collisions between CEX ions and neutral atoms may not be appropriate for describing the plume of an engine operating in a vacuum chamber, since the background pressure may significantly raise the neutral density and increase the number of scattering centers [37].

Now, having established a method for determining the neutral density at any point downstream of the engine grid, we proceed to develop a method for modeling the remaining quantities in the model equations of Chapter 2.

Chapter 4

Computation of CEX-Ion Flux and Sputtering Rate

The primary goal of this work was to develop a model of the plume of an ion engine that incorporates the momentum and energy-transfer process during elastic charge-exchange collisions and, how the resulting energy distribution of CEX ions affects the sputtering rate of specified surfaces (see Figure 4.1). In Chapter 2 we derived the equations (Equations 2.18, 2.29, 2.33, and 2.34) to be modeled using certain assumptions of collisionless CEX ions and angle-independent sputtering. It was found that — in order to compute the energy distribution of CEX ions at any point in space, and the resultant sputtering rate of a surface due to collisions with the CEX ions — there are certain quantities which we must be able to compute. The first quantity, the neutral atom density n_0 , was examined in Chapter 3, where we developed a method for computing the neutral density at any point by superposition of the contributions from all grid holes.

The quantities remaining to be computed are the primary ion flux $\varphi \hat{\mathbf{u}} \, d\mathbf{u}^3$, the charge-exchange differential cross-section $d\sigma^+/d\Omega$, the streamtube expansion $d\tilde{A}/d\Omega$, and the CEX-ion energy E . In this chapter we present a model for computing all these quantities, and how we perform the integration of Equation 2.29, in addition to further discussion of the sputter yield, $Y(E)$. We start with a discussion of how the electric fields present in the region downstream of the engine can affect the trajectories of the CEX ions, and how we compute these trajectories.

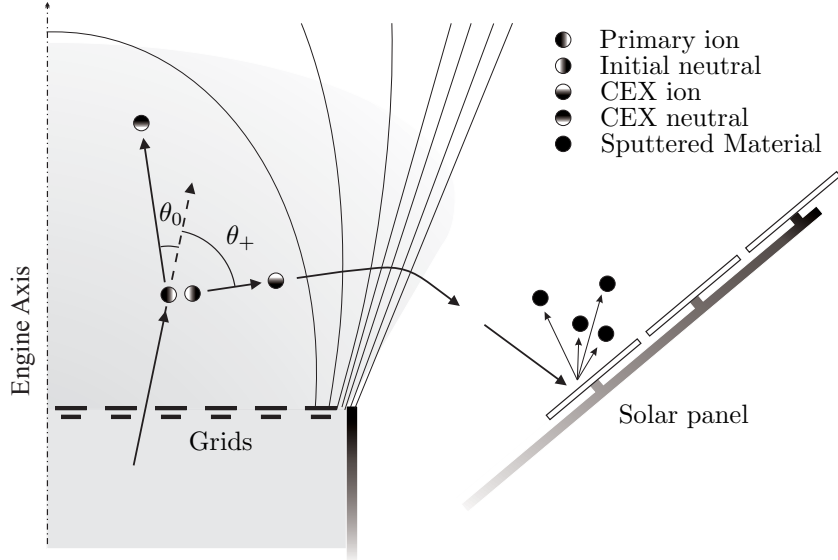


Figure 4.1: Sputtering source processes. A high-velocity primary ion collides with a slow atom downstream of the engine grids and experiences a charge-exchange collision. Scattering at the angle, θ^+ , the newly created CEX ion receives energy and momentum from the primary ion. Under the influence of the electric field formed by the charges downstream, the CEX ion is accelerated, possibly back upstream towards the spacecraft. Impingement of the CEX ion on a spacecraft surface results in sputtering of material from the craft.

4.1 Obtaining the Electrostatic Potential

Referring to Figure 4.2, let us assume that an ion scattered from P at the angle θ , with respect to the primary ion velocity vector, $\hat{\mathbf{u}}$, has a trajectory passing through S , in the absence of any external forces (Path 1). Under the influence of external forces, this same ion will, in general, follow a path that does not pass through S (Path 2). In order for an ion to scatter onto a path passing through S (Path 3), it must scatter at an angle θ^* .

The contribution to the density and energy distribution at S from ions scattering at θ^* will be different than the contribution from those scattering at θ . First, the number of ions scattered into a solid angle $\delta\Omega$ will be different for each angle, due to the different values of the differential cross-section $d\sigma/d\Omega$. Second, the area, $\delta\tilde{A}$, through which ions pass that are scattered into a solid angle $\delta\Omega$ will be different for each scattering angle, due to the effect the external forces have on distorting the streamtube formed by these ions. Third, the kinetic energy of the ions scattered into the two different angles will be different at the point S , due to the dependence of the initial scattered energy

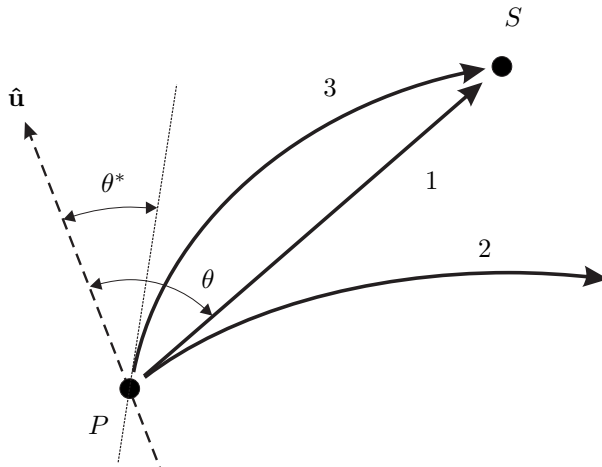


Figure 4.2: Example of scattering solutions. In the absence of any external forces, a CEX ion scattered at an angle, θ , with respect to the primary-ion velocity vector, will pass through the point S (Path 1). If external forces are present, the same ion will travel on a trajectory that does not pass through S (Path 2). The CEX ion must scatter at a different angle, θ^* , in order to travel on a trajectory that passes through S , if external forces are present (Path 3). Due to the different scattering angles, the energy of an ion that travels to S along Path 1 will be different than the energy of an ion that travels along Path 3.

on the scattering angle (Equation 2.18). In order to compute an accurate count of the CEX ions passing through S and their corresponding energies, the electric field (obtained from the electric potential Φ) influencing their trajectories must be known. In this section we present a model for determining the electric potential, Φ , from the ion density, n_i .

The small mass and resulting high mobility of electrons leads to the situation known as Debye shielding, in which the electrons move to nearly neutralize the electric field at distances larger than the Debye length from an ion [44]. We thus assume that the plasma is in a state of quasi-neutrality for length scales greater than the Debye length. Under the assertion of quasi-neutrality, the electron and ion charge densities are very nearly equal; $n_e \simeq n_i$ [12].

In molecular dynamics models it is typical to assume that the neutralizing electrons behave as a fluid [45], for which the conservation of momentum equation is

$$m_e \frac{D\mathbf{u}_e}{Dt} \equiv m_e \left(\frac{\partial \mathbf{u}_e}{\partial t} + \mathbf{u}_e \cdot \nabla \mathbf{u}_e \right) = \sum_i \mathbf{F}_i. \quad (4.1)$$

We assume that the only significant forces acting on the electrons are pressure and electrostatic

forces. Let us also assume that the electrons have reached a steady state in thermal equilibrium as an isolated population, and that they behave as an ideal gas [12]. With these assumptions, the momentum equation for the electrons yields

$$m_e \mathbf{u}_e \cdot \nabla \mathbf{u}_e = -\frac{\nabla p}{n_e} + q_e \nabla \Phi = -k_B T_e \frac{\nabla n_e}{n_e} + q_e \nabla \Phi, \quad (4.2)$$

where n_e is the electron number density, T_e is the electron equilibrium temperature, q_e is the electron charge, and k_B is Boltzmann's constant. It is common to assume that the inertial term is negligible, due to the small mass of the electrons, especially in comparison with the ions [14, 46]. Thus

$$\nabla \Phi = \frac{k_B T_e}{q_e} \frac{\nabla n_e}{n_e}, \quad (4.3)$$

for which integration yields the Boltzmann relation

$$\Phi - \Phi_0 = \frac{k_B T_e}{q_e} \ln \left(\frac{n_e}{n_{e,0}} \right), \quad (4.4)$$

where Φ_0 is a reference potential assigned to the reference density, $n_{e,0}$. The relation between the electrostatic potential and the electron density in Equation 4.4 is commonly referred to as the barometric potential law [12, 14, 47]. From the condition of quasi-neutrality, the electrostatic potential can be inferred if the density of either species is known. Assuming that the electric potential is the only source of any significant force acting on the ions [14], the equation of motion for any ion is

$$m_i \frac{d\mathbf{u}_i}{dt} = -q_e \nabla \Phi. \quad (4.5)$$

It is immediately evident that a problem arises if we attempt to use Equation 4.4 to compute the electric potential. In order to do so we must have *a priori* information about the ion density which is the quantity we are attempting to compute in the first place. Computational methods such as Particle-in-Cell (PIC) models approach this problem by solving for the ion trajectories and electrostatic potential self-consistently, through sequential time-integration of the equations of

motion [48]. At each time step the total charge density is computed, from which the potential is updated by Poisson’s equation or the barometric potential law [46] for the next step. The equations of motion (Equation 4.5) are then integrated through another time step, using the new potential, from which the total charge density can be updated. Self-consistent electric potentials and ion trajectories through the domain of interest are obtained by integrating through a sufficiently large number of time steps.

In this work we need to compute the electric field downstream of multiple grid shapes. The time required for a complete self-consistent computation of the electric field using time-integration methods, such as PIC, for multiple grids makes using these methods impractical. In Section 4.2 we present an alternate method to compute the electric field, which, though not strictly self-consistent, may be adequate for our purposes.

4.2 The Charge Density: Computing the Electric Potential

While the expression for computing the electric potential (Equation 4.4) is straightforward, computing the ion density required to determine the potential is, in general, not a trivial matter. To know the charge density at any point, it must be known from where these charges originated, and the processes by which they are transported to the location in question. Since the electric field affects the transport of these ions, the electric potential must be known beforehand. As mentioned in the previous section, other methods, such as PIC codes, resolve this issue by self-consistently solving for both the potential and charge distribution at sequential time steps. These methods are not suitable for optimization problems, since obtaining the solution requires multiple evaluations of the objective function corresponding to different combinations of parameter values ξ — in the present case, those defining the shape of the grid (see Section 2.2). Thus, each new combination of parameters defines a different grid shape, requiring a complete recalculation of the plume. As this process is computationally impractical, this section presents an alternative method.

4.2.1 Main Beam Ions

The plume can be viewed as composed of two distinct ion populations — primary-beam ions and CEX ions [12]. Primary-beam ions are those accelerated through the grids from the discharge chamber, and are highly energetic; NSTAR primary ions have energies of approximately 1100 eV for fourteen of the sixteen throttle levels used [9]. CEX ions are those that are created as a result of charge-exchange collisions, and typically have only a small fraction of the energy of the primary ions. The CEX ions — scattered at large angles with respect to the grid axis, and accelerated by the electric fields — make up the significant population of ions outside of the main beam [11]. These are the ions responsible for sputtering, and the population for which this model solves.

The primary ions originate from within the engine, and accelerate through the grid ion optics to form beamlets. Both physical observation and detailed computational modeling have shown these beamlets to have a divergent beam structure, and to merge to form the main beam downstream of the engine [16, 49].

Each ion beamlet is modeled as an isotropic emission cone, with a divergence half-angle, ϑ_k , originating from a point source, \mathbf{y}'_k , behind each hole (Figure 4.3). The position of the emission point is determined to be such that the cone fully encompasses the hole. If \mathbf{y}_k is the location of the hole center, $\hat{\mathbf{n}}_k$ is the normal vector of hole k , and R is the hole radius, then the emission point is specified to be located at

$$\mathbf{y}'_k = \mathbf{y}_k - \frac{R}{\tan \vartheta_k} \hat{\mathbf{n}}_k. \quad (4.6)$$

Let us define a single-hole primary ion velocity distribution function, $f_{p,k}(\mathbf{u})$, such that the number flux of primary ions from hole k through δA is (using Equation 2.4)

$$\frac{\delta N_{p,k}(\mathbf{x}, \mathbf{u})}{\delta A \delta t} = n_{p,k}(\mathbf{x}) f_{p,k}(\mathbf{u}) \mathbf{u} \cdot \hat{\mathbf{n}} \delta^3 \mathbf{u} = \varphi_k \hat{\mathbf{u}} \cdot \hat{\mathbf{n}} \delta^3 \mathbf{u}, \quad (4.7)$$

where $n_{p,k}(\mathbf{x})$ is the density contribution of primary ions at \mathbf{x} from hole k . The total primary-ion

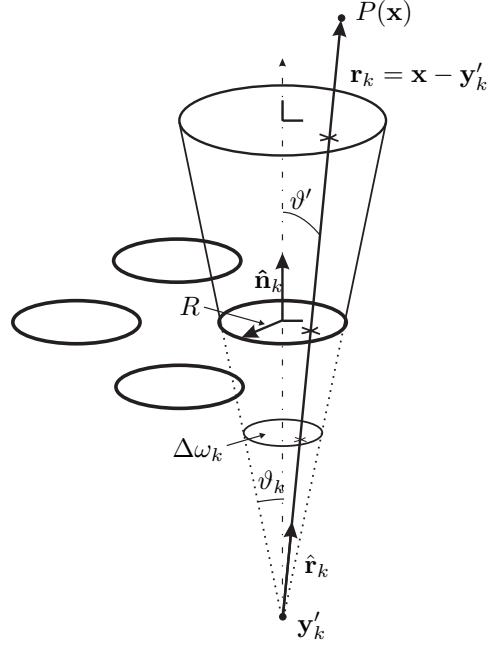


Figure 4.3: Primary-ion beamlet emission source and cone. All primary ions are assumed to originate from emitting source points located behind each hole. Ions are emitted isotropically within the cone with half-angle ϑ_k such that the respective hole is completely subtended by the cone. The velocity vector of any ion passing through a point P is defined to be the radial vector, $\hat{\mathbf{r}}_k$, pointing from the emission point of origin \mathbf{y}'_k .

density at \mathbf{x} is found from the superposition of the contributions from all holes:

$$n_p(\mathbf{x}) = \sum_k n_{p,k}(\mathbf{x}). \quad (4.8)$$

Since the emission is specified to be isotropic within the cone, the flux is independent of the angle measured with respect to the hole normal, $\hat{\mathbf{n}}_k$, and is directed along the rays, $\hat{\mathbf{r}}_k$, originating from the emission point \mathbf{y}_k . Thus, we can redefine the distribution of primary-ions originating from hole k in terms of a single-hole primary ion speed distribution function, $f_{p,k}(u)$, such that

$$f_{p,k}(\mathbf{u}) \hat{\mathbf{u}} \delta^3 \mathbf{u} = f_{p,k}(u) \hat{\mathbf{r}}_k \delta u. \quad (4.9)$$

Since all the primary ions were originally thermal neutrals located in the discharge chamber at an elevated potential (1100 eV in the case of NSTAR), it is reasonable to assume that the spread in primary ion speeds, upon exiting the chamber, is only on the order of the thermal velocity

(~ 300 m/s). In comparison with the final exit velocity of the ions, $u_p \approx 40$ km/s, the thermal velocity is so small that we assume the primary ions are monochromatic, with energy E_0 corresponding to speed u_p . The assumption of monochromaticity simplifies the single-hole primary-ion speed distribution function: $f_{p,k}(u) = \delta_D(u_p)$, where $\delta_D(u_p)$ is the Dirac delta function. Integrating Equation 4.7 over all speeds yields

$$\int_{\mathbf{u}} u n_{p,k}(\mathbf{x}) \delta_D(u_p) \hat{\mathbf{r}}_k \cdot \hat{\mathbf{n}} du = u_p n_{p,k}(\mathbf{x}) \hat{\mathbf{r}}_k \cdot \hat{\mathbf{n}} = \bar{\varphi}_k \hat{\mathbf{r}}_k \cdot \hat{\mathbf{n}}. \quad (4.10)$$

By continuity, integration of Equation 4.7 over any surface, \wp , fully enclosing the emission point, is constant and equal to the total beamlet current, I_k , from hole k . Integrating Equation 4.7 over a spherical shell, centered on and enclosing the emission point, yields

$$I_k = \int_{\mathbf{u}} \int_{\wp} q \varphi_k \hat{\mathbf{u}} \cdot d\mathbf{A} d\mathbf{u}^3 = q \bar{\varphi}_k \int_0^{2\pi} \int_0^{\vartheta_k} \hat{\mathbf{r}}_k \cdot (\|\mathbf{r}_k\|^2 \sin \vartheta' d\vartheta' d\phi' \hat{\mathbf{r}}_k) = q \bar{\varphi}_k r_k^2 \Delta\omega_k, \quad (4.11)$$

where the solid angle subtended by the emission cone is $\Delta\omega_k = 2\pi(1 - \cos \vartheta_k)$.

Computational models of the NSTAR engine and other ion engines, and physical observation have shown that neither the beamlet current nor the divergence angle is the same for all holes. For the NSTAR engine, it has been found that the beamlet current, I_k , decreases and the divergence angle, ϑ_k , increases with increasing radius from the grid center [50]. Measurements from the NSTAR engine operating at the TH15 throttle level have found that the beamlet current peaks at approximately 23 mA at the center, and decreases to approximately 6 μ A for the outermost holes in the grid. The computed beamlet current for the NSTAR engine, as a function of the distance from the grid center [50], along with the curve fit used for this study are presented in Figure 4.4. The functional form for the curve fit used is

$$I_k = 0.23 \exp \left[- \left(\frac{\rho_k}{7.9} \right)^2 \right] + 0.063 \exp \left[- \left(\frac{\rho_k - 9.5}{3} \right)^2 \right] \text{ mA} \quad (4.12)$$

where ρ_k is the distance, in cm, to hole k from the grid axis. The total beam current, $J_b = \sum I_k$,

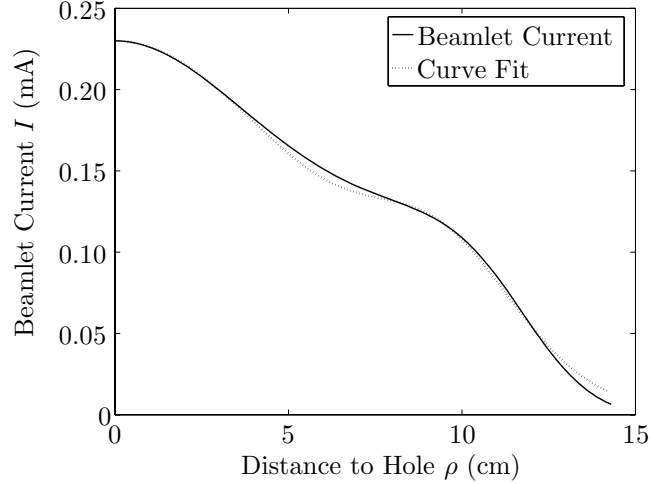


Figure 4.4: Beamlet current. The current from any particular grid hole is a function of the distance between the hole and the grid axis. The solid line indicates results from computations for the NSTAR done by others [50]. The dashed line represents a normalized curve fit to the data in the solid line, such as to yield the same total beam current, $J_b = 1.48$ A.

obtained from the computed data shown is equal to 1.48 A, and the fitting curve is normalized to yield the same.

Computations of individual beamlets have shown that the divergence angle varies from $\vartheta_k = 8.5^\circ$, for the higher-current beamlets near the center of the grid, to $\vartheta_k = 17^\circ$, for the holes near the edge [50]. Some computations have found the divergence angle for the low-current beamlets near the edge to be as high as $\vartheta_k = 30^\circ$ [51]. Since the divergence angle influences the vector of motion of the primary ions, and consequently the required CEX scattering angle, this parameter may have a significant influence on the CEX-ion energy distribution computed. The ability for the user to adjust the divergence angle was included in the code, however the effects of adjusting this parameter were not investigated in this work. To simplify our model, the divergence angle was assumed to be a constant equal to 11° for all holes.

Returning to Equation 4.11, due to isotropic emission within a cone and monochromaticity, the contribution from hole k to the primary ion flux at any point $P(\mathbf{x})$ is

$$\bar{\varphi}_k \hat{\mathbf{u}} = \begin{cases} \frac{I_k}{q\Delta\omega_k} \frac{\mathbf{x}-\mathbf{y}'_k}{\|\mathbf{x}-\mathbf{y}'_k\|^3} & \text{if } \cos^{-1}\left(\hat{\mathbf{n}}_k \cdot \frac{\mathbf{x}-\mathbf{y}'_k}{\|\mathbf{x}-\mathbf{y}'_k\|}\right) \leq \vartheta_k \\ 0 & \text{otherwise} \end{cases} \quad (4.13)$$

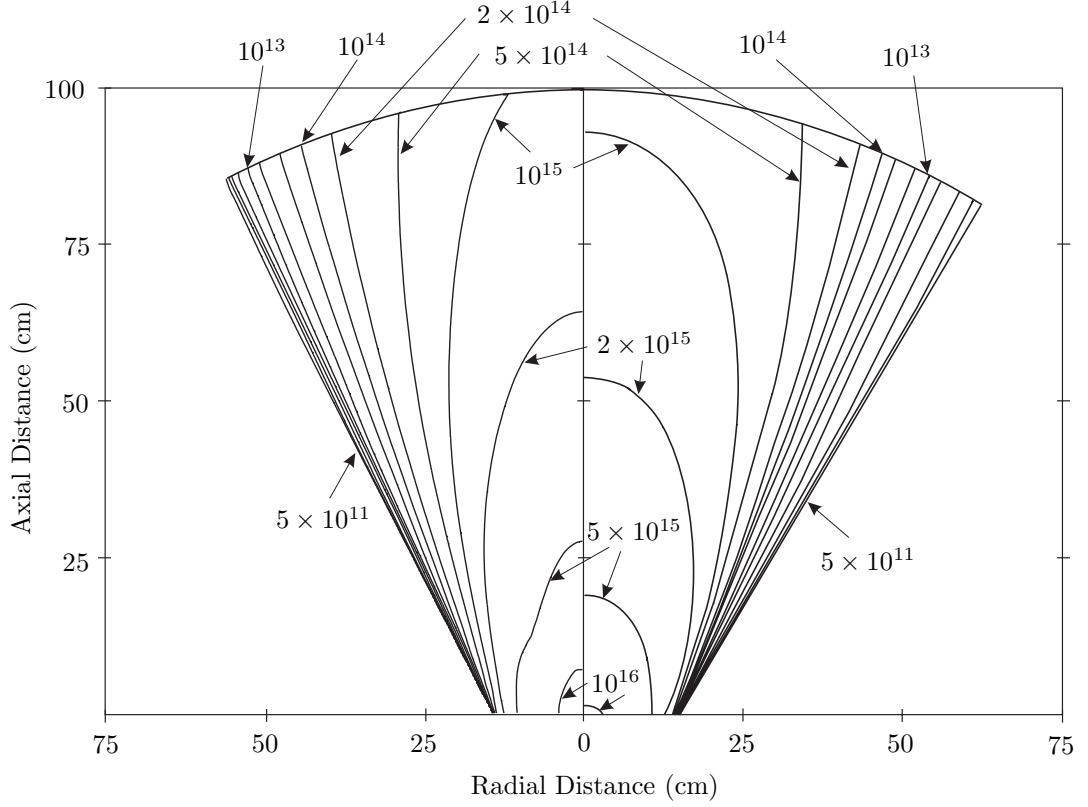


Figure 4.5: NSTAR main beam ion density. The left figure presents primary ion densities, in ions/m³, calculated for an NSTAR-shaped grid using the method presented in this work. The primary ions were assumed to have a speed of $u_p = 40$ km/s, and the total beam current was $J_b = 2.14$ A. The individual beamlet divergence angle was assumed to be constant, with a value $\vartheta = 11^\circ$. The beamlet current of each hole was calculated using the curve fit in Figure 4.4, and then scaled to yield the intended total beam current J_b . The right figure shows the primary ion densities, in ions/m³, calculated using a PIC method by others [52, 53]. The mean primary ion speed for these computations was 35 km/s, and the total beam current was 2.14 A.

Finally, the contribution to the primary-ion density at \mathbf{x} from hole k is obtained from Equation 4.10:

$$n_{p,k}(\mathbf{x}) = \frac{\bar{\varphi}_k}{u_p} = \begin{cases} \frac{I_k}{q\Delta\omega_k\|\mathbf{x}-\mathbf{y}'_k\|^2} \sqrt{\frac{m_i}{2E_0}} & \text{if } \cos^{-1}\left(\hat{\mathbf{n}}_k \cdot \frac{\mathbf{x}-\mathbf{y}'_k}{\|\mathbf{x}-\mathbf{y}'_k\|}\right) \leq \vartheta_k \\ 0 & \text{otherwise} \end{cases}, \quad (4.14)$$

where m_i is the ionic mass. Primary-ion density contours computed for the NSTAR grid configuration, using Equation 4.14, are compared in Figure 4.5 to computations conducted in previous studies [52, 53].

Now that we have a method for computing the primary ion density at any point downstream

of the grid, we have half of what is required in order to compute the electric field. In the next section we present how we calculate the CEX-ion density at any point which, when added with the main beam density, yields the total ion density, from which we can obtain the potential using the barometric law (Equation 4.4).

4.2.2 CEX Ions

As we have described, unlike the main-beam ions, obtaining the density of CEX ions at any point is not straightforward; it is the energy distribution of the CEX ions, after all, which we are attempting to compute in order to predict the sputtering rate at any specified location. Our lack of a priori information about the CEX-ion density hinders our ability to compute the potential, which, in turn, is needed to obtain the CEX-ion density to begin with. Within the main beam, where primary ions are present, this is of small concern, since we will find that the number of CEX ions is significantly less than the number of primary ions in this region. Due to the logarithmic dependence of the potential on the ion density (Equation 4.4), the small number of CEX ions (in comparison to the number of primary ions) makes only a small correction to the potential within the main beam. Outside of the main beam however, the plume potential is determined solely by the density of scattered ions, since they are the only positive charges present [11].

To obtain a first approximation to the CEX-ion density outside the main beam, for the sole purpose of determining the plume potential for an arbitrary grid, one could assume that the CEX-ion density is constant everywhere. This constant could be any reasonable value, such as an average from measurements or computational models. The value chosen is rather inconsequential, since the electric field is determined from the gradient of the potential and so will be zero regardless. This initial guess could then be improved upon by using it to compute a correction to the CEX-ion density which, in turn, could correct the potential. This process could be repeated iteratively until convergence is obtained. Obtaining the self-consistent density at a sufficient number of points from which an electric field can be found could take as long as a few days on a modern personal computer. For the final purpose of optimizing the grid shape, this method is impractical due to the immense

amount of time that would be required to obtain a self-consistent plume potential for each grid configuration.

According to Equation 4.4, the electric field is proportional to the gradient of the logarithm of the ion density. Therefore, even significant changes in the ion density may not result in large changes to the electric field. It will be shown later that the vast majority of CEX ions receive very little energy from the collision. Since the majority of the CEX ions move slowly, it is reasonable to assume that large gradients in the CEX-ion density (especially in comparison to the gradients formed at the edge of the main beam) do not have the opportunity to form. Based on the two assertions of the logarithmic dependence on density and the formation of only moderate gradients in the CEX-ion density, we will assume that moderate changes in the shape of the grid do not result in drastic changes to the total CEX-ion density at any point. Therefore, we will use the CEX-ion density computed previously by others (shown in Figure 4.6) [53] and assume that, for the sole purpose of computing the electric potential, the CEX-ion density is unchanging for all grid shapes.

Having established methods to obtain the main-beam primary-ion density (Section 4.2.1), and the CEX-ion density (Section 4.2.2), we are at the point that we can find the electric potential in the region surrounding any grid. The following section outlines the procedure followed in order to do so. The axisymmetric potential downstream of an NSTAR-shaped grid, as computed using this procedure, is shown in Figure 4.7. An ion temperature of 2 eV was used for this work, since measurements of the electron temperature during operation of the NSTAR thruster, at the TH15 throttle level, found temperatures between 1-2 eV [13, 15].

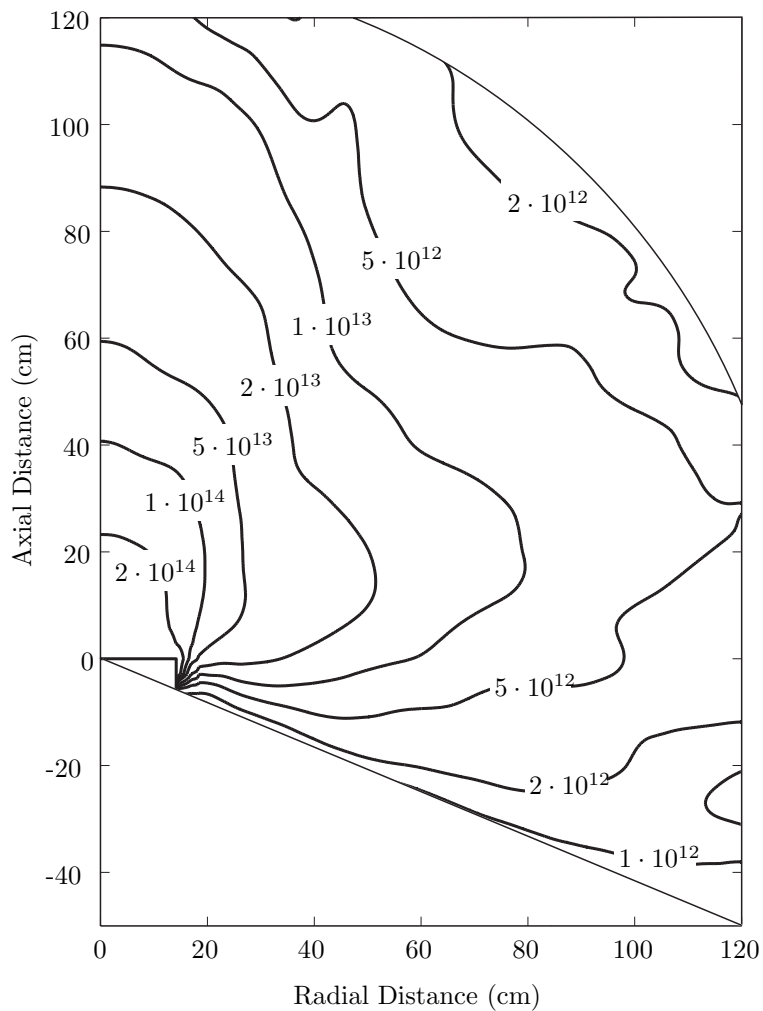


Figure 4.6: Charge-exchange ion density. Obtained from PIC computations performed previously by others [53] and complements the primary ion densities shown on the right side of Figure 4.5. The lack of large-density gradients (in comparison with the gradients at the edge of the main beam), and the logarithmic dependence of the potential on the density leads us to believe the total CEX-ion density changes relatively little with changing grid shape. For the sole purpose of computing the electric field, the CEX-ion density is assumed to be unchanging. Densities are in ions/m³.

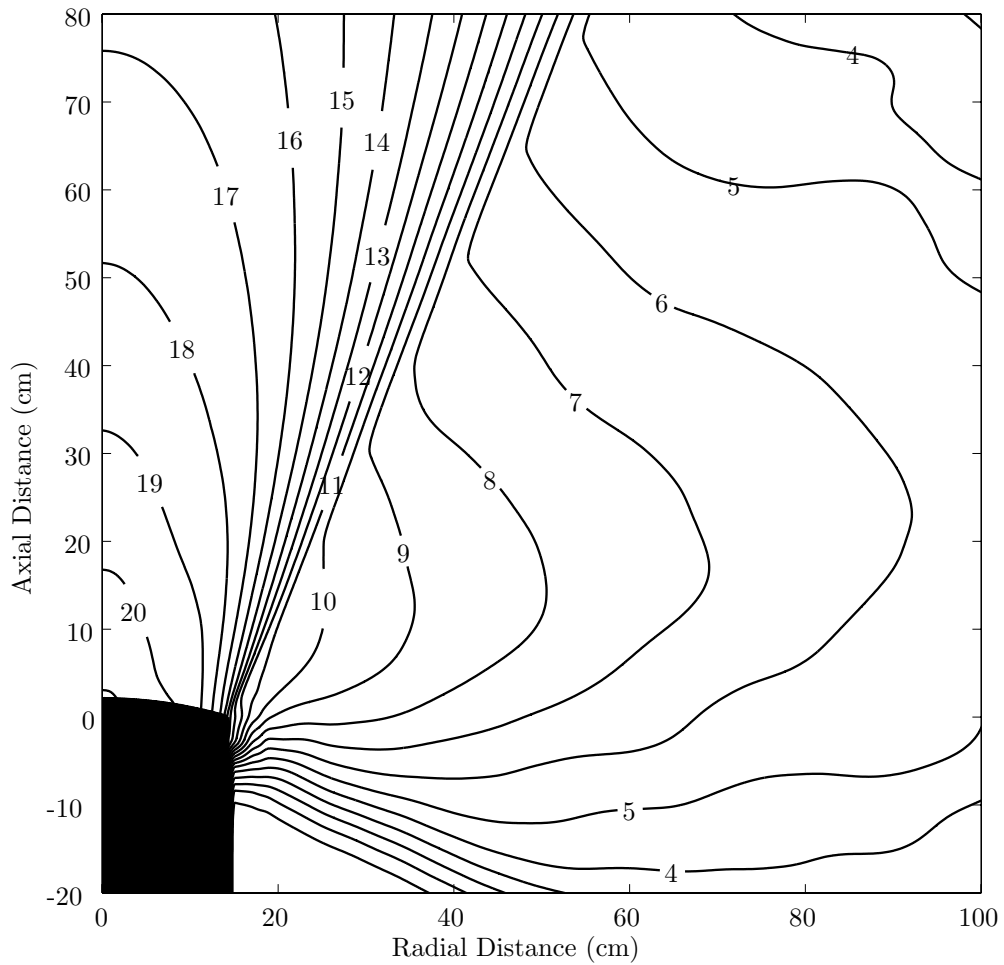


Figure 4.7: NSTAR plume potential. Main-beam ion densities for an NSTAR-shaped grid (Figure 4.5) were computed using the method outlined in Section 4.2.1, and added to the CEX-ion densities from Figure 4.6. The potential was calculated from the densities using the barometric law (Equation 4.4), and an electron temperature of $T_e = 2$ eV. Contour values are in volts.

4.2.3 Pseudo-Code: Calculating the Electric Potential

The following pseudo-code outlines the procedure used to determine the electric potential at any point. The ion density is computed at the desired point by superposition of the contributions of primary ions from all grid holes, as well as the CEX-ion density obtained using other PIC models. The potential is then calculated from the ion density by application of the barometric potential law. The code was implemented using Matlab.

1. Let \mathbf{x} be the location of the point at which to evaluate the electric potential, and T_e the electron temperature.
2. Let $\{\mathbf{y}'_1, \dots, \mathbf{y}'_N\}$ be the locations of the N hole emission points, $\{\hat{\mathbf{n}}_1, \dots, \hat{\mathbf{n}}_N\}$ be the normal vectors to the N holes, and $\{\vartheta_1, \dots, \vartheta_N\}$ the beamlet divergence angles.
3. Let Φ_0 be the reference potential at a reference density, $n_{e,0}$, and E_0 the primary ion kinetic energy.
4. $k = 0$.
5. $k = k + 1$.
6. Compute the vector between the emission point of hole k and the evaluation point, $\mathbf{r}_k = \mathbf{x} - \mathbf{y}'_k$.
7. Calculate the angle between the hole normal and \mathbf{r}_k , $\vartheta'_k = \cos^{-1} (\|\mathbf{r}_k\|^{-1} \mathbf{r}_k \cdot \hat{\mathbf{n}}_k)$.
8. If $\vartheta'_k \leq \vartheta_k$, go to step 9; otherwise $n_k = 0$, go to step 12.
9. Compute the distance to hole k from the grid axis, ρ_k , and the beamlet current (Equation 4.12),

$$I_k = 0.23 \exp \left[- \left(\frac{\rho_k}{7.9} \right)^2 \right] + 0.063 \exp \left[- \left(\frac{\rho_k - 9.5}{3} \right)^2 \right] \text{ mA.}$$

10. Compute the beamlet subtending solid angle, $\Delta\omega_k = \int_0^{2\pi} \int_0^{\vartheta_k} \sin \vartheta' d\vartheta' d\phi' = 2\pi(1 - \cos \vartheta_k)$.

11. Calculate the contribution to the primary-ion density from hole k (Equation 4.14),

$$n_{p,k} = \frac{I_k}{q\Delta\omega_k\|\mathbf{r}_k\|^2} \sqrt{\frac{m_i}{2E_0}}.$$

12. If $k < N$, go to step 5; otherwise go to step 13.

13. Find the CEX-ion density, n_{CEX} , at the evaluation point by interpolating from Figure 4.6.

14. Compute the total ion density at the evaluation point, $n_i = n_{\text{CEX}} + \sum_k n_{p,k}$.

15. Calculate the potential (Equation 4.4),

$$\Phi = \Phi_0 + \frac{k_B T_e}{q} \ln \left(\frac{n_i}{n_{e,0}} \right).$$

16. Output n_i and Φ .

4.3 Computing Ion Trajectories Through the Electric Field

Sections 4.1 and 4.2 were devoted to computing the electric field present downstream of an ion engine with arbitrarily shaped grids. This was due to the fact that the field exerts forces on the scattered CEX ions, and thus affects the computed CEX-ion energy distribution at any particular target point. The angle at which a group of CEX ions must be scattered from a small volume in order to pass through the target point is influenced by the electric field. This scattering angle affects the expected number of CEX ions, for any given primary ion flux, scattered to the target point, and affects the energy of the scattered ions through the momentum transfer which takes place during the collision. To determine the required scattering angle, the trajectories of the CEX ions through the electric field must be known. In this section we present the method chosen to calculate the trajectories of the CEX ions through integration of the equations of motion — the velocity-Verlet method.

4.3.1 The Velocity-Verlet Method

Ion particle trajectories were computed using a velocity-Verlet method, modified for time-step adaptation. In the form introduced for the original verlet method [54], the position and velocity of the particle at a specific time are found using a central difference scheme;

$$\mathbf{x}(t+h) = 2\mathbf{x}(t) - \mathbf{x}(t-h) + h^2\mathbf{f}(\mathbf{x}(t)), \quad (4.15)$$

$$\mathbf{v}(t) = \frac{\mathbf{x}(t+h) - \mathbf{x}(t-h)}{2h}. \quad (4.16)$$

At each time step, this algorithm requires only one evaluation of the force function, $\mathbf{f}(\mathbf{x}(t))$, and the storage of the $6N$ positions of the N particles at the times $t-h$ and t . The positions have an error of order h^4 , and the velocities have an error of order h^2 . In addition to the limited accuracy of the velocity in this algorithm, our knowledge of the velocity always lags behind the positions by one time step. The algorithm can be modified for better precision for the velocities; the new algorithm is commonly referred to as the velocity-Verlet algorithm [54]:

$$\mathbf{x}(t+h) = \mathbf{x}(t) + h\mathbf{v}(t) + \frac{h^2}{2}\mathbf{f}(\mathbf{x}(t)), \quad (4.17)$$

$$\mathbf{v}(t+h) = \mathbf{v}(t) + \frac{h}{2}[\mathbf{f}(\mathbf{x}(t)) + \mathbf{f}(\mathbf{x}(t+h))]. \quad (4.18)$$

Both the positions and velocities have an error of order h^4 , and both are known at the same time. Each time step only requires one function evaluation, $\mathbf{f}(\mathbf{x}(t+h))$, and storage of the $9N$ positions, velocities, and accelerations, $\mathbf{f}(\mathbf{x}(t))$, of the N particles at time t .

One issue encountered when computing ion trajectories is the possible large difference between the initial and final velocities of any particles. Since this algorithm is an explicit method, care must be taken to meet the Courant condition, which states that the time step, h , should be no greater than the time it takes for the particle to traverse adjacent grid points in the discrete grid domain of the function, $\mathbf{f}(\mathbf{x})$ [55]. If a particle starts initially with a very small or even zero velocity, a relatively large time step can be used, since the positions will change very little between each successive step.

However, as the particles are accelerated out of the main beam, the large time step appropriate for the initially small velocity of these ions may be too large to meet the Courant condition for the subsequent accelerated velocity. Unless a method to adapt the time step is used, a time step appropriate for the final velocity must be used throughout the entire computation. This can make the calculation computationally expensive when the final velocity is significantly larger than the initial velocity.

However, implementing a time-adaptive technique at each time step could substantially increase the number of computations required, since a new time increment, h , must be computed at each step. A compromise was made, and a routine was developed where the time increment is updated, but only periodically, after a specified number of time steps. Provision for the case when the velocity may be very small, allowing for a very large time increment, was made by introducing a maximum time increment, h_{\max} . In cases where the Courant condition would allow for time increments larger than this maximum value, we specify that $h = h_{\max}$. The pseudo-code for the routine follows.

4.3.2 Pseudo-Code: Time-Adaptive Velocity-Verlet Algorithm

The following pseudo-code outlines the procedure used to implement the velocity-Verlet method for computing the trajectory of an ion through an electric field. The method was modified to allow for time-adaptation by recomputing the time-step size h_k at regular intervals. The code was implemented using Matlab.

1. Let \mathbf{x}_0 and \mathbf{v}_0 be the initial position and velocity of the particle, and R to be the minimum distance to move the particle from \mathbf{x}_0 before terminating the computation.
2. Choose the maximum path length increment per time step, $\delta s < \delta x$, and the maximum time increment, h_{\max} , where δx is the grid point spacing of the function \mathbf{f} .
3. Choose the number of steps between each time increment update, N , and the maximum number of time steps to evaluate, K .
4. $k = 0$; $n = N$.

5. If $n = N$, evaluate $h_k = \min \left\{ \frac{\delta s}{\|\mathbf{v}_k\|}, h_{\max} \right\}$ and go to 6; otherwise $h_k = h_{k-1}$ and go to 7.
6. $n = 0$; If $\|\mathbf{x}_k - \mathbf{x}_0\| > R$ go to 11.
7. Evaluate $\mathbf{x}_{k+1} = \mathbf{x}_k + h_k \mathbf{v}_k + \frac{h_k^2}{2} \mathbf{f}(\mathbf{x}_k)$.
8. Evaluate $\mathbf{v}_{k+1} = \mathbf{v}_k + \frac{h_k}{2} [\mathbf{f}(\mathbf{x}_k) + \mathbf{f}(\mathbf{x}_{k+1})]$.
9. $k = k + 1$; $n = n + 1$.
10. if $k = K$, go to 11; otherwise go to 5.
11. Output \mathbf{x} , \mathbf{v} , and \mathbf{h} .

4.4 The Differential Cross-Section

Sections 4.1 through 4.3 laid out the details of how we compute the electric field and the individual ion trajectories through the field. However, to determine the flux of ions through a specific area of space, we must also know the average number of ions scattered into the trajectory passing through the area due to multiple similar collisions. This average quantity is determined by the differential cross-section $d\sigma/d\Omega$ [56].

During an elastic collision between a primary ion and a thermal-neutral atom, there are two possible outcomes, which are based on the end state of the outermost valence electron of the original neutral atom. One possible result is that the electron remains with the neutral atom and the collision is like any other elastic collision between two particles. The second possible outcome is for the valence electron to transfer from the neutral atom to the primary ion during the interaction, in what is called a charge-exchange collision. The trajectories of the two particles are no different than in any other elastic collision between two particles in the same state, however what was originally the neutral atom is now an ion. Referring to Figure 4.8, imagine a flux of collimated, monochromatic ions, $\bar{\varphi} \hat{\mathbf{u}}$, through a volume of space, $\delta V = \delta A \delta x$, containing some number of neutral atom targets, N_0 . The charge-exchange differential cross-section is defined to be such that the average number of CEX neutrals due to a charge-exchange collision, δN_s^0 , measured per unit time, at a large distance

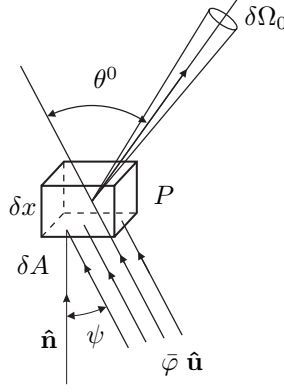


Figure 4.8: CEX neutrals scattered from a small volume. A flux of collimated, monochromatic ions, $\vec{\varphi} \hat{\mathbf{u}}$, pass through a small volume, δV , around the point P that contains some number of neutral atoms, N_0 . The number of CEX ions, δN_s^0 , scattered into a small solid angle $\delta\Omega_0$ about a scattering angle θ^0 is determined by the charge-exchange differential cross-section, $d\sigma^0/d\Omega$.

from the volume, within some solid angle, $\delta\Omega_0$, of the scattering angle, θ^0 , measured with respect to the direction of motion of the ions, $\hat{\mathbf{u}}$, is [23]

$$\dot{N}_s^0(\theta^0) = \frac{\delta N_s^0(\theta^0)}{\delta t} \equiv N_0 \vec{\varphi} \left. \frac{d\sigma^0}{d\Omega} \right|_{\theta^0} \delta\Omega_0 = n_0 (\vec{\varphi} \hat{\mathbf{u}} \cdot \hat{\mathbf{n}}) \left. \frac{d\sigma^0}{d\Omega} \right|_{\theta^0} \delta\Omega_0 \delta A \delta x. \quad (4.19)$$

Similarly, the number of CEX ions due to a charge-exchange collision, δN_s^+ , measured per unit time, at a large distance from the volume, within some solid angle, $\delta\Omega_+$, of the scattering angle, θ^+ , measured with respect to the direction of motion of the ions, $\hat{\mathbf{u}}$, is

$$\dot{N}_s^+(\theta^+) = \frac{\delta N_s^+(\theta^+)}{\delta t} \equiv N_0 \vec{\varphi} \left. \frac{d\sigma^+}{d\Omega} \right|_{\theta^+} \delta\Omega_+ = n_0 (\vec{\varphi} \hat{\mathbf{u}} \cdot \hat{\mathbf{n}}) \left. \frac{d\sigma^+}{d\Omega} \right|_{\theta^+} \delta\Omega_+ \delta A \delta x. \quad (4.20)$$

Since every collision results in one CEX ion and one CEX neutral, for every CEX ion measured there must be a corresponding CEX neutral scattered (see Figure 4.9). Therefore, from any specific volume, the two measured rates of CEX-ion and CEX-neutral production must be equal; i.e., the quantities in Equations 4.19 and 4.20 must be the same. Therefore

$$\left. \frac{d\sigma^+}{d\Omega} \right|_{\theta^+} \delta\Omega_+ = \left. \frac{d\sigma^0}{d\Omega} \right|_{\theta^0} \delta\Omega_0. \quad (4.21)$$

The quantities $\delta\Omega_0$ and $\delta\Omega_+$ are not independent, but are related to each other in a way such that the kinematic constraints of conservation of momentum and energy are met. In the infinitesimal limit:

$$d\Omega_0 = \sin\theta^0 d\theta^0 d\phi^0, \quad (4.22)$$

$$d\Omega_+ = \sin\theta^+ d\theta^+ d\phi^+, \quad (4.23)$$

since the elastic-collision dynamics between any individual ion and atom can be completely described in the plane of motion of the two particles, $d\phi^0 = d\phi^+$. Additionally, for elastic collisions involving identical species, conservation of momentum and energy dictate that the two particles scatter at right angles to each other, as measured in the lab frame [57];

$$\theta^0 + \theta^+ = \pi/2. \quad (4.24)$$

Therefore, in the case of charge-exchange collisions between identical species, Equation 4.21 reduces to

$$\sin\theta^+ \left. \frac{d\sigma^+}{d\Omega} \right|_{\theta^+} = \sin\theta^0 \left. \frac{d\sigma^0}{d\Omega} \right|_{\theta^0} = \cos\theta^+ \left. \frac{d\sigma^0}{d\Omega} \right|_{\pi/2-\theta^+},^1 \quad (4.25)$$

or

$$\left. \frac{d\sigma^+}{d\Omega} \right|_{\theta^+} = \frac{\cos\theta^+}{\sin\theta^+} \left. \frac{d\sigma^0}{d\Omega} \right|_{\pi/2-\theta^+}. \quad (4.26)$$

If the charge-exchange differential cross-section between identical species can be measured for either of the collision products (ion/neutral), the cross-section for the other product (neutral/ion) can be obtained from Equation 4.26.

Measurements of the charge-exchange differential cross-section were performed at JPL [25]. A monochromatic, collimated beam of singly charged xenon ions was passed through a target cell containing neutral xenon atoms at a known pressure and temperature. The density of the xenon

¹The pesky negative sign from the relation $d\theta^0 = -d\theta^+$ has been ignored, since we recognize that each quantity on either side of the equal sign must be positive. The negative sign only affects the order of the limits of integration.

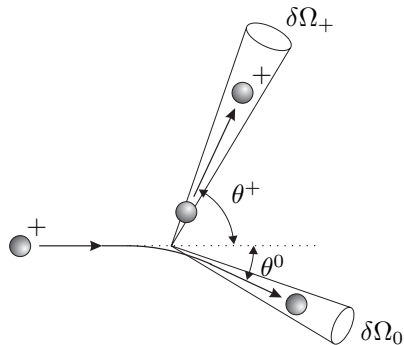


Figure 4.9: Elastic charge-exchange collision angles in the lab frame. The rate at which ions are scattered into $\delta\Omega_+$ must equal the rate at which neutral atoms are scattered into $\delta\Omega_0$. In a collision involving identical particles, the two particles must scatter at right angles to each other, $\theta^0 + \theta^+ = \pi/2$.

ions in the target cell was obtained from the ideal gas law. Located downstream of the target cell was a detector which collected the neutrals produced as a result of the charge-exchange collisions occurring in the target cell. The remaining ions left in the beam were deflected away from the collector plate using charged deflection plates. The detector had an active area of 16 cm^2 , with 256×256 pixel resolution. In order to differentiate between different scattering angles, the array of collecting pixels was divided into rings centered around the beam axis. The scattering angle to any ring was assumed to be the average of the angles to the inner and outer pixels that define the ring. The maximum measurable angle was 3.6° .

The results of measurements (black dots) made for beam ions with an energy of 1100 eV, and an extrapolated curve fit of the data (red line) up to a scattering angle of 90° , are shown in Figure 4.10. For identical species, no scattering events can occur at angles greater than 90° , thus requiring the differential cross-section to drop off to zero at 90° . The measurements did not extend up to scattering angles of 90° , and we have no further information as to what angle this drop off actually occurs. The curve fit neglects the presence of a drop off, so we anticipate the extrapolation of the data to be higher at larger angles than in reality.

The total charge-exchange cross-section is defined to be

$$\sigma_0 = \int_{\Omega} \frac{d\sigma}{d\Omega} d\Omega. \quad (4.27)$$

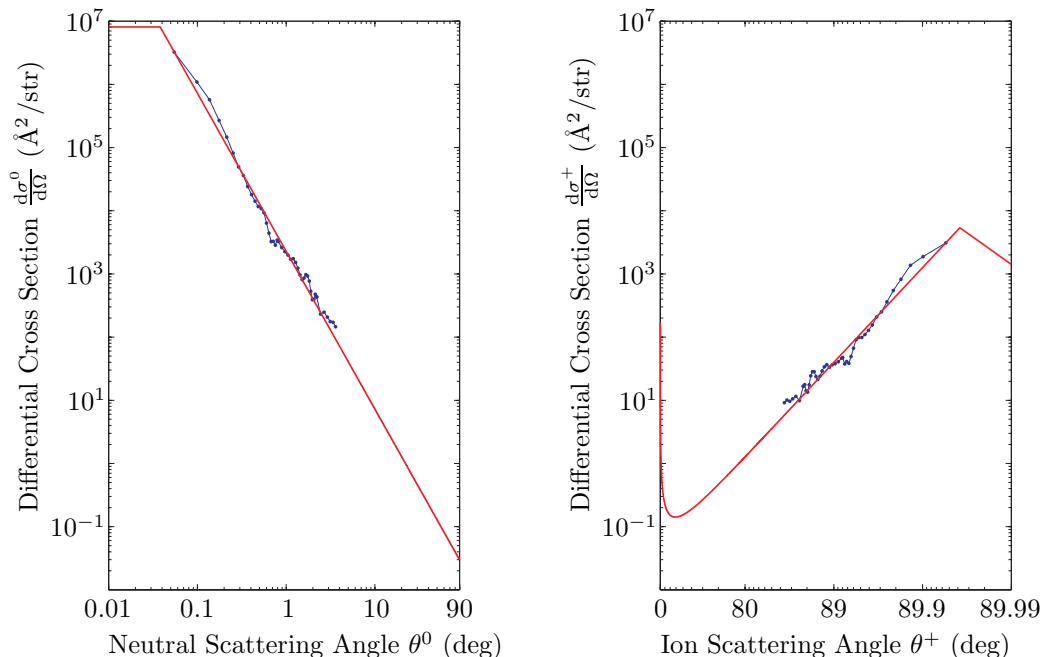


Figure 4.10: Xe-Xe⁺ charge-exchange differential cross-section. Black dots in the left figure show data taken from measurements of CEX neutrals from collisions involving primary ions with an energy of $E_0 = 1100$ eV. The red line in the left figure is a curve-fit to the measured data (black dots). The right figure is the corresponding differential cross-section for the CEX ions obtained by transformation of the data in the left figure, according to Equation 4.26.

For charge-exchange collisions between xenon ions and atoms, the total cross-section is finite and has a value of approximately 55 \AA^2 for ion energies of 300 eV [58]. A cut-off angle very close to zero, θ_c^0 , was imposed where the curve fit for the differential cross-section is constant for all angles less than this value. This was necessary in order to maintain a finite total cross-section. The extrapolating curve fit for the data has the functional form

$$\frac{d\sigma^0}{d\Omega} = 7.2 \left(\frac{\theta^0}{10^\circ} \right)^{-5/2} \text{ \AA}^2/\text{str}, \quad \theta_c^0 = 0.038^\circ. \quad (4.28)$$

The cut-off angle, θ_c^0 , was chosen such that the total cross section was equal to the measured value, $\sigma_0 = 55 \text{ \AA}^2$. Though this value for the total cross-section is the value for 300 eV ions, it has been found that at low energies, the total cross-section changes little [58]. The functional form for the differential cross-section can easily be modified to conform to accurate values of the total cross-section by adjusting the cut-off angle; however for modest changes in the total cross-section the

cut-off angle will change very little.

The differential cross-section for CEX ions is shown on the right of Figure 4.10. The rapid increase of the differential cross-section at angles $\theta^+ < \sim 30^\circ$ is due to both the $\sin^{-1} \theta^+$ conversion from Equation 4.26, and that, as mentioned earlier, the differential cross-section is artificially high as $\theta^0 \rightarrow 90^\circ$. The decrease in the differential cross-section as $\theta^+ \rightarrow 90^\circ$ is due to the $\cos \theta^+$ conversion from Equation 4.26, and the imposition of a constant value for $\theta^0 < \theta_c^0$. Charge-exchange ion quantities obtained from scattering angles near these two extremes may be suspect, however it will be shown later that the scattering angles of relevance to this work do not lie close to either extreme.

4.5 The Sputter Yield

Sputtering is the result of collisions of energetic particles with a surface. As these particles collide with the surface, any number of atoms may be ejected and, over time, erode the surface material. Originally thought to be a thermal evaporation-like process, it was later found to be the result of momentum-transfer cascades within the material being sputtered [30].

Experimental measurement confirms our intuition: Sputtering is a process dependent on the energy of the colliding particle [33, 30]. As it turns out, the average number of atoms removed by a collision from an energetic ion is also dependent on the angle at which the ion collides with the surface. Some models have been developed which predict sputter yields that are in reasonable agreement with experimental data from high-energy, normal-incidence measurements [28, 33]. However, significantly less research has been invested in sputter yields of materials involving low-energy (< 1 keV) ions or at angles other than normal-incidence. Largely motivated by sputtering issues of spacecraft surfaces, attempts at measurements of low-energy, oblique-incidence sputter yields have been made recently [26, 59].

As discussed in Chapter 2, for this work we make no assumption of orientation of the surface being sputtered. Since we have no reason to assume the surface to be facing in one direction over another, we will consider all collisions to be at normal incidence. This decision was also made partly due to the limited availability of angular-dependent sputter yield data. Possible inclusion of

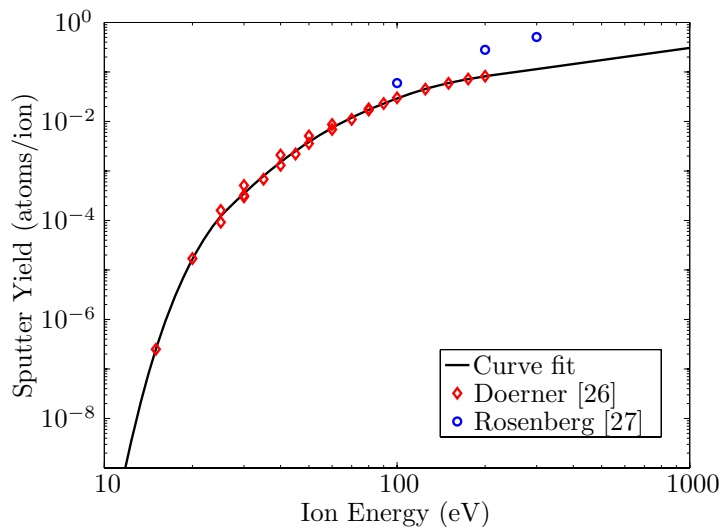


Figure 4.11: Sputter yield for xenon on molybdenum. Measurements indicate a dramatic drop-off of the sputter yield at ion energies less than approximately 20 eV. Both sets of measurement data were obtained for oblique-incidence sputtering. The curve-fit is a piecewise continuous, cubic polynomial.

angular-dependent sputter yields in the future is not made forfeit in this model, however instead of only computing the speed (or energy) of the ions as they reach the target point, calculation of the velocity vector would be required.

Measurements of the sputter yield of xenon ions colliding with a molybdenum surface have been made [26, 27], and are reproduced in Figure 4.11. As can be seen from the data, the amount of material sputtered drops off dramatically for ions with energies less than approximately 20 eV. The fact that the measured sputtering has been found to be significantly less for ions in this range than for ions with energies greater than approximately 20 eV, may have serious implications on the ranges of ion energies expected to do the most sputtering damage, and will be the basis for simplifications made in the calculations later on.

A piecewise continuous, cubic polynomial curve-fit was used to represent the data in our model. The functional form of the curve-fit is

$$\log_{10} Y(E) = \alpha \hat{E}^3 + \beta \hat{E}^2 + \gamma \hat{E} + \delta, \quad (4.29)$$

where $\hat{E} = \log_{10}(E/\text{eV})$. The coefficients of the polynomial are dependent on the energy \hat{E} , and are

Table 4.1: Coefficients for piecewise continuous curve fit of the Xe⁺-Mo sputter yield

	α	β	γ	δ
$\hat{E} < 1.384$	30.679	-144.55	231.39	-128.71
$1.384 \leq \hat{E} < 1.803$	0	-3.608	16.147	-19.432
$1.803 \leq \hat{E} < 2.3$	0	-2.236	11.105	-14.802
$2.3 \leq \hat{E}$	0	0	0.8203	-2.975

listed in Table 4.1. The extrapolating portion of the curve-fit was obtained by matching both the value and the slope of the curve at $\hat{E} = 2.3$. It is interesting to note that the slope of the curve-fit at $\hat{E} = 2.3$ is close to unity, which is equivalent to a linear relationship between the sputter yield Y and energy E . Some have suggested that this may be the case for low energies (< 1 keV) [34].

4.6 Ion Behavior: Scattering Angle Solutions and Stream-tube Divergence

It was stated at the beginning of this chapter that we wish to develop a method for solving the model equations (Equations 2.18, 2.29, 2.33, and 2.34). The neutral atom density, n_0 , was dealt with in Chapter 3. Our model for the primary ion flux, $\varphi \hat{\mathbf{u}} \, d\mathbf{u}^3$, was presented in Section 4.2. Given the required angle, θ^+ , into which the CEX ions are scattered, we can compute the CEX-ion energy, E , through application of the methods presented in Sections 4.1 through 4.3. In addition, if we are given the solid angle, $\delta\Omega_+$, into which the CEX ions are scattered, we can compute the number of CEX ions scattered through the target area $\delta\tilde{A}$ by using the charge-exchange differential cross-section discussed in Section 4.4. The question remains as to how we solve for these two required quantities, θ^+ and $d\tilde{A}/d\Omega$.

Some insight into how we determine these two quantities can be obtained by examining some representative trajectories of CEX ions passing through the electric field. Before proceeding to the full three-dimensional computation, in Section 4.6.1 we present a two-dimensional discussion based on trajectories of CEX ions scattered on a radial plane of an axisymmetric NSTAR potential. This discussion will qualitatively help us to interpret the behavior of CEX ions when we no longer restrict

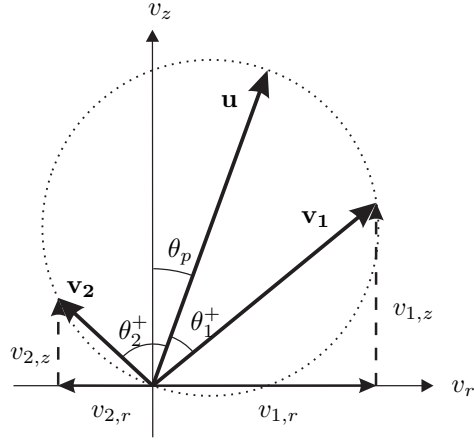


Figure 4.12: Transformation coordinates of scattered-ion initial conditions. The total speed of an ion scattered at an angle $\theta_{1,2}^+$ is equal to $u \cos \theta_{1,2}^+$. The initial velocity components are determined by the angle of scattering, $\theta_{1,2}^+$, as well as the direction of the primary ion flow, $\hat{\mathbf{u}}$.

their movement to two dimensions in Section 4.6.2.

4.6.1 A 2D Example

Imagine the *group* of CEX ions scattered from a specific volume in space as a result of collisions with the primary ions associated with a given flux vector, $\hat{\mathbf{u}}$. We call this a *scattering event*. Note that each scattering event produces a number of ions associated with all possible scattering angles. Further, note that the scattering angle is defined in relation to the primary-ion flux vector, and that the initial velocity of the scattered ion is dependent on both this scattering angle and the direction of motion of the primary ions (see Figure 4.12). Some representative scattered CEX-ion trajectories from a specific scattering event were computed, and are shown in Figure 4.13. The ions shown are those that originate from the scattering event that occurs at a scattering center located three centimeters downstream from the base plane of the grid, and two centimeters off the grid axis, $P(x, z) = (2, 3)$. The primary-ion flux vector from which the CEX ions scattered, $\hat{\mathbf{u}}$, was specified to be moving parallel to the thrust axis, $\hat{\mathbf{z}}$. All scattered ions were assumed to scatter in the same plane as the scattering center (x - z plane), and to only scatter in the positive x direction.

An important observation to be made from these sample trajectories is that the CEX ions may initially be swept downstream due to the nature of the electric field inside the main-beam region.

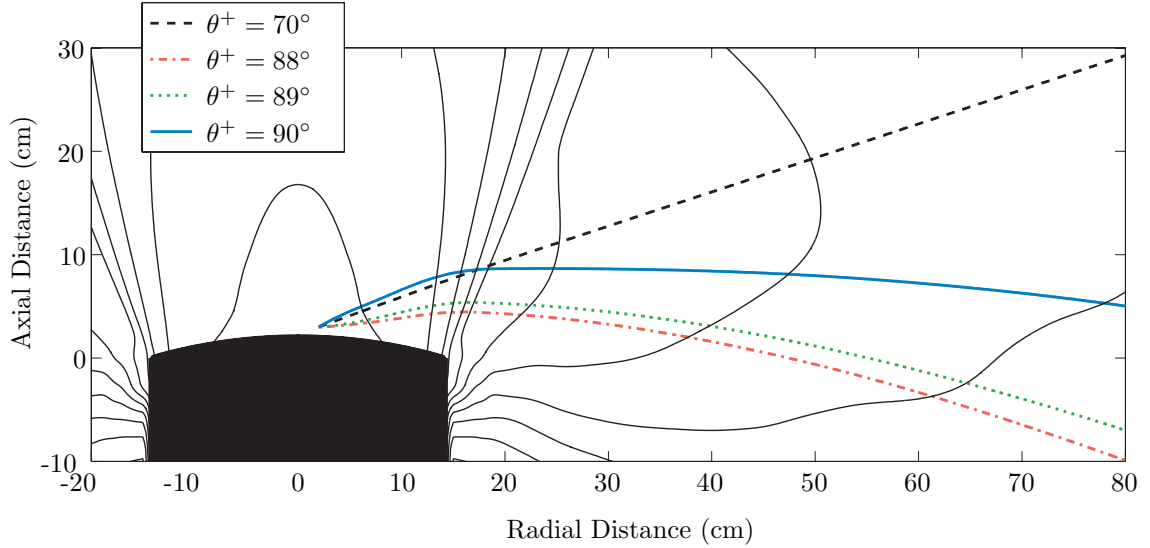


Figure 4.13: 2D trajectories of ions from one scattering event. The primary ion velocity vector, $\hat{\mathbf{u}}$, is specified to be moving parallel to the engine axis, $\hat{\mathbf{z}}$, through the scattering center, $P(x, z) = (2, 3)$. All ions are scattered into the same plane as the scattering center (x - z plane) and in the positive x direction. Note that the CEX ions with higher initial kinetic energy (eg. $\theta^+ = 70^\circ$) are affected little by the electric field while those with less initial kinetic energy (zero in the case of $\theta^+ = 90^\circ$) are affected considerably.

Once the ions reach the main-beam edge however, there is a significant gradient in the electric potential which turns the ion trajectories back towards the spacecraft. This effect is seen to be more prominent with the low-energy CEX ions that scatter at angles close to 90° (see Equation 2.18). This is the primary reason that CEX ions collide with spacecraft surfaces and cause the sputtering that we are concerned about. Another interesting observation to be made is that the ions swept farthest upstream are not necessarily the ions scattered with the minimum initial energy at the largest angle, i.e., $\theta^+ = 90^\circ$. A clearer demonstration of this can be seen by examining the downstream location of ions scattered in a range of angles as they reach a specified distance from the grid axis.

Let us assume that we are interested in the location of all scattered ions when they reach an off-axis distance of 60 cm. Figure 4.14 shows the downstream location of CEX ions scattered in a range of angles as they pass through the plane at this specified radius. Ions scattered from the four indicated scattering-center locations are shown. This demonstrates very clearly how there is a maximum distance that ions will be swept upstream for any particular scattering center and primary-ion flux direction. In general, the angle at which this maximum occurs is not 90° . This has

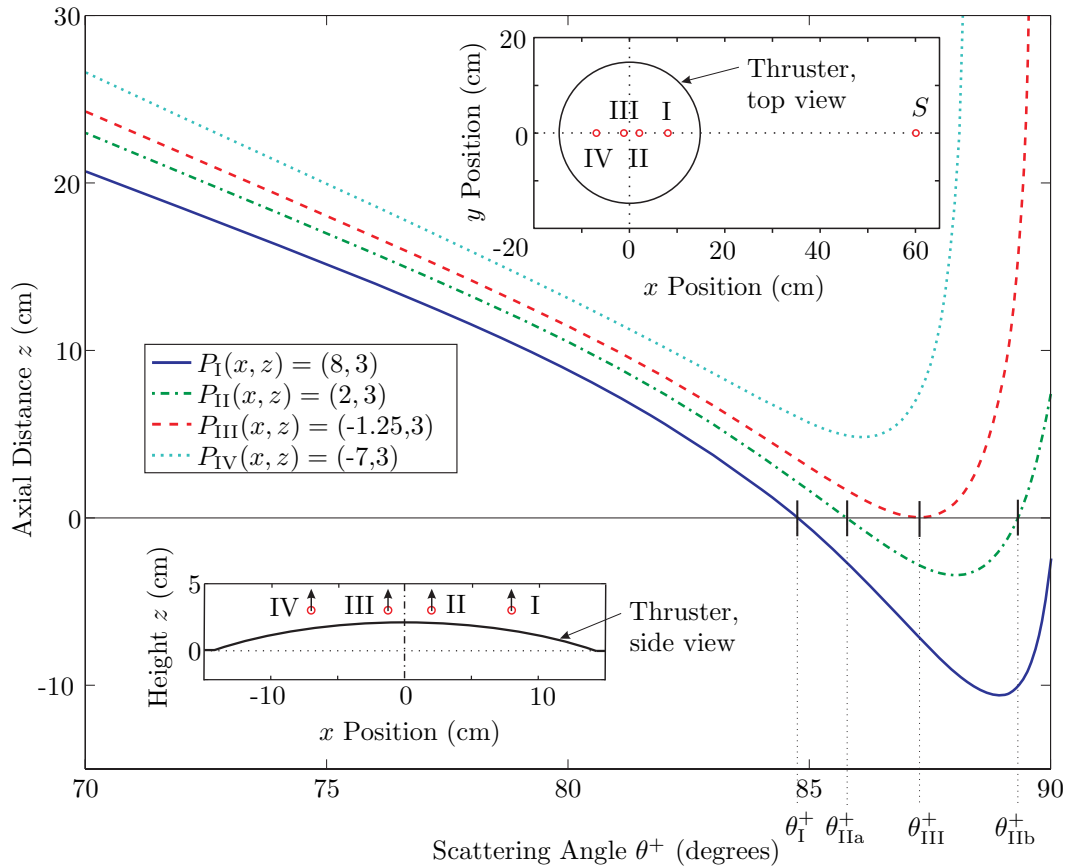


Figure 4.14: Downstream location at $x = 60$ cm for ions scattered at different angles. One line is for each of the scattering events occurring at four scattering locations, $P_{I-IV}(\mathbf{x})$. The trajectories of ions scattered at different angles from the primary-ion velocity vector, $\hat{\mathbf{u}} = \hat{\mathbf{z}}$, were computed. The downstream coordinate, z , of each ion as it passes through $x = 60$ cm is shown as a function of the scattering angle. The angles corresponding to an ion passing through the target point $S(\tilde{x}, \tilde{z}) = (60, 0)$ are indicated. **Top inset:** Top view of the thruster, x positions of the four scattering centers, and the location of the target point $S(\tilde{\mathbf{x}})$. **Bottom inset:** Side view of the thruster and z positions of the four scattering centers. Arrows indicate the primary-ion velocity vector, $\hat{\mathbf{u}}$.

a significant impact when determining the total flux of ions to a specific point.

For example, let us assume that we are concerned about the total flux of CEX ions through the target point at $S(\tilde{x}, \tilde{z}) = (60, 0)$. We find that one scattering angle from both of the scattering centers at $P_I(x, z) = (8, 3)$ and $P_{III}(x, z) = (-1.25, 3)$ will result in CEX ions passing through the target point, $\theta_I^+ = 84.7^\circ$ and $\theta_{III}^+ = 87.3^\circ$, respectively. From the scattering center located at $P_{II}(x, z) = (2, 3)$, we find that there are two scattering angles, $\theta_{IIa}^+ = 85.7^\circ$ and $\theta_{IIb}^+ = 89.3^\circ$. On the other hand, *no* ions from the scattering event occurring at $P_{IV}(x, z) = (-7, 3)$ will reach the target point.

The physical explanation for the behavior exhibited in Figure 4.14 is as follows: Scattering events with a relatively small scattering angle result in the ion emerging from the collision with a relatively large fraction of the total energy in the collision (see Equation 2.16). The effect of the electrostatic force from the plume on the ion is relatively small and the ion continues on a nearly straight trajectory from the scattering point. For this specific example, where the primary ions are moving parallel to the thrust axis, the limiting value of the downstream coordinate \tilde{z} of an ion scattered from $P(x, z)$ is

$$\tilde{z}_{\theta \rightarrow 0} = z + \frac{\tilde{x} - x}{\tan \theta}. \quad (4.30)$$

An example of this is seen in the first ion trajectory ($\theta^+ = 70^\circ$) pictured in Figure 4.13.

As the scattering angle increases, the scattered CEX ion receives a smaller fraction of the total collision energy and thus the effect of the electrostatic field on the trajectory of the ion increases. As the ion passes through the edge of the main beam, it experiences a significant force in the upstream direction which tends to decrease or even reverse the direction of the ion's velocity component parallel to the grid axis. The effect of this can be seen in the second and third ion trajectories ($\theta^+ = 88^\circ, 89^\circ$) from Figure 4.13. As the scattering angle continues to increase, and the initial energy of the scattered ion continues to decrease, the effect of the smaller electrostatic force in the beam interior — in comparison to the force at the beam edge — grows. The electrostatic field in the interior of the beam is generally directed downstream, and so begins to have an increasing impact on sweeping the ion downstream before it reaches the beam edge. Once the ion does reach the beam edge, it experiences an upstream force which once again sweeps it back upstream. However, at some critical scattering angle, it will be such that the ion is swept so far downstream within the beam before encountering the edge, that the force at the beam edge is insufficient to sweep the ion upstream as far as ions with a slightly smaller scattering angle. For scattering angles larger than this critical “turn around” angle, the resulting downstream coordinate \tilde{z} at the desired radial distance \tilde{x} (60 cm in this example) will be located increasingly further downstream. The net result of this is that it is possible for two unique scattering angles from the same scattering event to result in ions passing through the same target point, $S(\tilde{\mathbf{x}})$. The ions from the scattering point $P_{\text{II}}(x, z)$ in

Figure 4.14 demonstrate this possibility of multi-valued solutions.

At first glance, we may expect that, of the four cases presented in our example, the scattering event occurring at $P_{II}(x, z)$ would have the largest contribution of ions passing through our specified target point. Not only does this event have two contributing scattering angle solutions, θ_{IIa}^+ and θ_{IIb}^+ , but the largest scattering angle solution (associated with the largest cross-section) from all the events shown also occurs for this event. To know if this is truly the case, we must compare the total flux contribution, through some small area $\delta\tilde{A}$ about the target point, from each scattering event (Equation 2.27):

$$\delta F(\tilde{\mathbf{x}}, \mathbf{v}; \mathbf{x}, \mathbf{u}) = \frac{\delta N_s}{\delta\tilde{A} \delta t} = n_0 \varphi \hat{\mathbf{u}} \cdot \hat{\mathbf{n}} \left. \frac{d\sigma^+}{d\Omega} \right|_{\theta^+} \left(\frac{\delta\tilde{A}}{\delta\Omega} \right)^{-1} \delta V \delta \mathbf{u}^3. \quad (4.31)$$

For the moment, let us assume that the neutral density and primary-ion flux is the same for each scattering center. The two factors which influence the flux contribution from each scattering event are: (1) the charge-exchange differential cross-section, $d\sigma^+/d\Omega$, evaluated at the scattering angle solution, and (2) the streamtube divergence, $d\tilde{A}/d\Omega$, which describes the area enclosed by the streamtube formed by the ions scattered in some small solid angle. A large value of the streamtube divergence describes a situation where the scattered ions spread out due to the influence of the electric field, where, on the other hand, a small value indicates a focussing effect. Thus we see that the magnitude of the charge-exchange differential cross-section does not alone determine the amount of CEX- ion flux from each scattering event, for in cases where the streamtube divergence is very small, even a small number of scattered ions (small cross-section) can result in a very large flux due to focussing.

In this two-dimensional example,

$$\frac{d\tilde{A}}{d\Omega} \rightarrow \left| \frac{d\tilde{z}}{d\theta^+} \right|, \quad (4.32)$$

where we have taken the magnitude, since this must be a positive quantity. Referring back to Figure 4.14, we could expect the CEX-ion flux contribution to the target point $S(\tilde{x}, \tilde{z}) = (60, 0)$ from the scattering event at $P_{II}(x, z)$ to be substantial, since there is a focussing effect evidenced

by that fact that $d\tilde{z}/d\theta^+ = 0$ at the scattering angle solution, θ_{III}^+ .

Thus we see that Figure 4.14 demonstrates four different possible cases for the solutions which determine the CEX-ion flux contribution to any particular target point, $S(\tilde{\mathbf{x}})$, from a scattering event occurring at any scattering center, $P(\mathbf{x})$ with a primary-ion flux direction $\hat{\mathbf{u}}$:

- (I) One inclination scattering angle, θ^+ , results in the scattered ion passing through the target point; the streamtube area at the target point is greater than zero ($|d\tilde{z}/d\theta^+| > 0$).
- (II) Two unique scattering angles, “high” and “low” energy, result in a scattered ion passing through the target point.
- (III) One scattering angle results in the scattered ion passing through the target point; the streamtube area at the target point is equal to zero ($d\tilde{z}/d\theta^+ = 0$).
- (IV) No ion from this scattering event passes through the target point.

The differential cross-section applicable in this situation is the three-dimensional cross-section integrated over all azimuth angles, i.e.,

$$\frac{d\sigma}{d\theta} = 2\pi \sin\theta \frac{d\sigma}{d\Omega}. \quad (4.33)$$

Therefore, with all other quantities being equal, the CEX-ion flux contribution from each scattering event is proportional to the quantity

$$\delta F(\tilde{\mathbf{x}}, \mathbf{v}; \mathbf{x}, \mathbf{u}) \propto \left. \frac{d\sigma^+}{d\theta} \right|_{\theta^+} \left| \frac{d\tilde{z}}{d\theta^+} \right|^{-1}. \quad (4.34)$$

This quantity, for each of the example scattering events occurring at the four scattering centers $P_{\text{I-IV}}(x, z)$, is shown in Figure 4.15. The scattering angle solutions for the target point $S(\tilde{x}, \tilde{z}) = (60, 0)$ (determined from Figure 4.14) are indicated, and point to the relative CEX-ion flux contributions from each scattering event. Despite the fact that the largest scattering angle (and larger cross-section) is associated with $P_{\text{II}}(x, z)$, the largest contribution of CEX ions to the target

point seems to originate from $P_{\text{III}}(x, z)$. This is a direct result of the focussing effect of the electric field on the ions originating from this point ($d\tilde{z}/d\theta^+ = 0$).

Perhaps a clearer comparison of the contributions from each scattering center can be seen from a coordinate transformation. Though it is not a one-to-one mapping, Figure 4.14 provides the relationship between the scattering angle and the downstream distance, $z = h(\theta^+)$. The inverse of the function h , $g = h^{-1}$, yields a multi-valued function describing the scattering angle in terms of the downstream distance, i.e., $\theta^+ = g(z)$. Using this inverse function, we can perform a coordinate transformation of the abscissa of Figure 4.15. The result is shown in Figure 4.16, where the contribution from each scattering event is shown as a function of the downstream location of the target point S . The previous example for a target point located at $S(\tilde{x}, \tilde{z}) = (60, 0)$ is indicated.

The multi-valuedness of the ion contribution from any scattering event is apparent. For the specific example of a target point at $S(\tilde{x}, \tilde{z}) = (60, 0)$, we can see the significant contribution from the scattering event at $P_{\text{III}}(x, z)$, the double contribution from the event at $P_{\text{II}}(x, z)$, and the single contribution from the event at $P_{\text{I}}(x, z)$. It is also apparent that the event at $P_{\text{IV}}(x, z)$ makes no contribution to the CEX-ion flux to any points (along $\tilde{x} = 60$ cm) less than approximately $\tilde{z} = 4$ cm downstream.

The peaks in Figures 4.15 and 4.16 mathematically approach a value of infinity, for, at these points, $|dz/d\theta = 0|$. This may prove to introduce difficulty in dealing with the infinite flux predicted at these points. Physically, an infinite flux is impossible; for here we have assumed a continuum approach which eventually breaks down as the area through which the ions pass gets too small. In reality, we must find the average flux through some finite but small area in the vicinity of our target point. This average quantity can be found by integrating the quantities in Figure 4.16 over some small, but finite distance — for example, the flux between $z = 0$ cm and $z = 0.1$ cm. The only question that remains is whether the integral over any arbitrarily small but finite area of the curves is finite, especially in the regions where the values approach infinity. The answer to this is found by noting that the quantity computed is simply a coordinate transformation of the differential

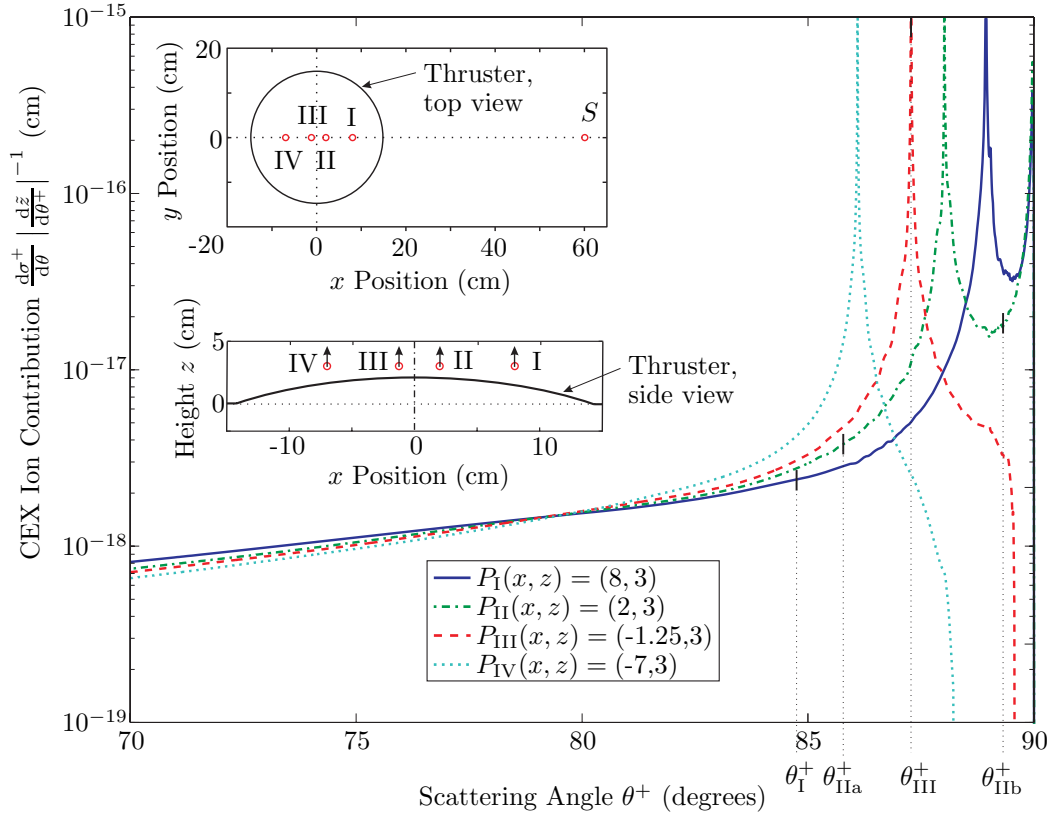


Figure 4.15: CEX-ion flux contribution as a function of scattering angle. With all other quantities equal, the CEX-ion flux from any scattering event is proportional to the differential cross-section, and inversely to the streamtube divergence. Values computed are for when ions reach a point $\tilde{x} = 60$ cm from the grid axis (refer to Figure 4.14). Infinite values occur when the streamtube becomes focussed by the electric field, $dz/d\theta = 0$. The scattering angle solutions for each scattering event, such that the ion passes through $S(\tilde{x}, \tilde{z}) = (60, 0)$, are indicated. **Top inset:** Top view of the thruster, x positions of the four scattering centers, and the location of the target point $S(\tilde{x})$. **Bottom inset:** Side view of the thruster and z positions of the four scattering centers. Arrows indicate the primary-ion velocity vector, $\hat{\mathbf{u}}$.

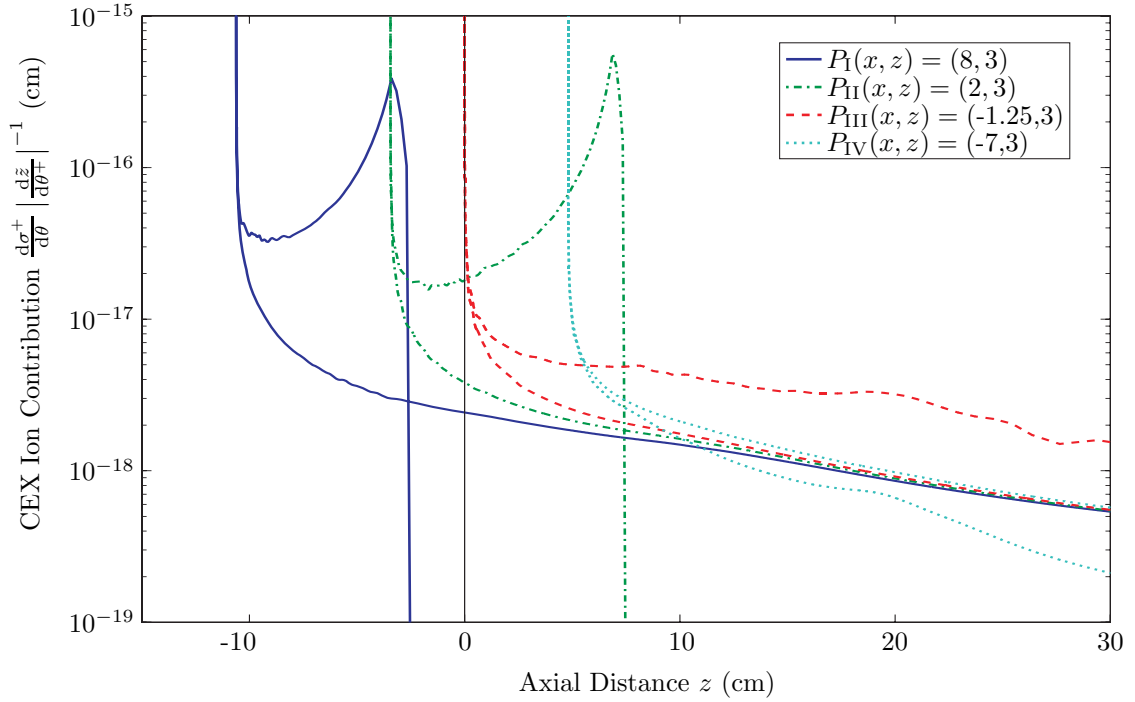


Figure 4.16: CEX-ion contribution as a function of downstream location. Obtained from Figure 4.15 by a coordinate transformation of $\theta^+ \rightarrow z$ using Figure 4.14. With all other quantities equal, the CEX-ion flux from any scattering event is proportional to the differential cross-section, and inversely to the streamtube divergence. Values computed are for when ions reach a point $\tilde{x} = 60$ cm from the grid axis (refer to Figure 4.14). Infinite values occur when the streamtube becomes focussed by the electric field, $dz/d\theta = 0$. The multi-valuedness of the functions indicates the possibility of multiple scattering angles from the same scattering event that contribute CEX ions to any particular target location. The contributions to the point at $S(\tilde{x}, \tilde{z}) = (60, 0)$ are indicated.

cross-section, ie.,

$$\sigma_0 = \int_0^{\pi/2} \frac{d\sigma}{d\theta} d\theta = \int_{-\infty}^{\infty} \frac{d\sigma}{d\theta} \left(\frac{dz}{d\theta} \right)^{-1} dz. \quad (4.35)$$

Since the integral over all z is bounded, the integral over any range of finite z will also be finite.

4.6.2 Extension to a 3D Example

In the previous discussion, we looked at only scattering events that (1) occurred in the radial plane, (2) scattered in the positive x direction, and (3) had a primary-ion flux directed parallel to the thrust axis. In general, not only are there multiple ion flux velocity directions through any scattering volume, but the scattering event is not restricted to the radial plane. Since in general the scattered ion will have an azimuthal velocity component (measured with respect to the grid axis), the scattering locations are also not restricted to the radial plane, but can, in general, be located at any point where there are primary ions present.

The two parameters fully defining the initial velocity vector for any scattered ion are defined with respect to the primary-ion velocity vector, $\hat{\mathbf{u}}$, as shown in Figure 4.17. The primary scattering angle, θ^+ , is the inclination angle and is measured from the initial primary ion velocity vector, $\hat{\mathbf{u}}$. The initial speed and energy of the scattered ion is directly impacted by this angle, for

$$v = u \cos \theta^+, \quad (4.36)$$

where v and u are the magnitudes of the initial velocity of the scattered ion and the velocity of the primary ion, respectively (see Equation 2.16 and Figure 4.12). The second scattering angle, ϕ^+ , has no influence on the energy of the particle and merely reflects the axisymmetric nature of the collision process. Where ϕ^+ is defined to be equal to zero is inconsequential—due to the 2π periodicity—so long as the choice is used consistently.

The initial state of the scattered ion is fully defined by these two scattering angles, θ^+ and ϕ^+ , if the primary-ion velocity vector $\hat{\mathbf{u}}$ is known. Let the primary-ion velocity unit vector have the three

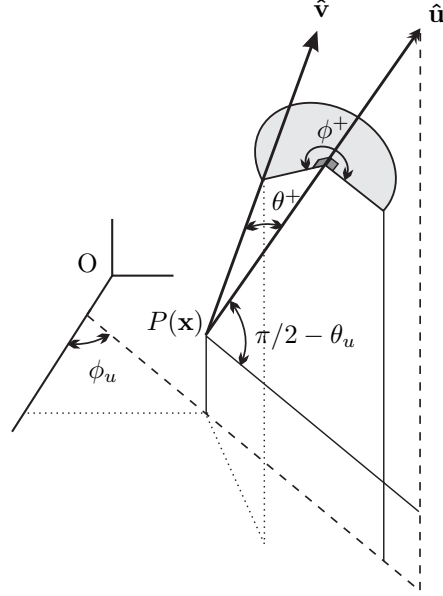


Figure 4.17: Definition of the azimuthal and inclination scattering angles. Both the azimuthal and inclination scattering angles, ϕ^+ and θ^+ , are measured with respect to the primary ion velocity vector, $\hat{\mathbf{u}}$. The zero-point for ϕ^+ is arbitrary, due to the averaged 2π azimuthal symmetry of the scattering process, and is of no consequence to the initial speed or energy of the scattered ion. The $\phi^+ = 0$ convention shown here was chosen due to the resulting simple rotation matrices (Equation 4.39). The initial speed of the scattered ion is $v = u \cos \theta^+$.

velocity components, $\hat{\mathbf{u}} = (\hat{u}_x, \hat{u}_y, \hat{u}_z)$. Let us then define the two angles θ_u and ϕ_u , such that

$$\sin \theta_u \equiv \sqrt{\hat{u}_x^2 + \hat{u}_y^2}, \text{ and} \quad (4.37)$$

$$\cos \phi_u \equiv \frac{\hat{u}_x}{\sqrt{\hat{u}_x^2 + \hat{u}_y^2}}. \quad (4.38)$$

The initial velocity unit vector, $\hat{\mathbf{v}} = (\hat{v}_x, \hat{v}_y, \hat{v}_z)$, of the scattered ion can then be found from the following rotation operation:

$$\hat{\mathbf{v}} = \begin{pmatrix} \hat{v}_x \\ \hat{v}_y \\ \hat{v}_z \end{pmatrix} = \begin{pmatrix} \cos \theta_u \cos \phi_u & -\sin \phi_u & \sin \theta_u \cos \phi_u \\ \cos \theta_u \sin \phi_u & \cos \phi_u & \sin \theta_u \sin \phi_u \\ -\sin \theta_u & 0 & \cos \theta_u \end{pmatrix} \begin{pmatrix} \sin \theta^+ \cos \phi^+ \\ \sin \theta^+ \sin \phi^+ \\ \cos \theta^+ \end{pmatrix} \quad (4.39)$$

It can be verified that $\hat{\mathbf{u}} \cdot \hat{\mathbf{v}} = \cos \theta^+$. The magnitude of the initial velocity of the scattered ion is described by Equation 4.36.

In Section 4.6.1 we examined the locations that scattered ions passed through a specified plane ($\tilde{x} = 60$ cm), and obtained sets of curves — one curve for each scattering event. A procedure similar to that used to construct the curves in Figures 4.14 through 4.16 can be used for the more general 3D case, however, instead of obtaining sets of curves, sets of surfaces will be obtained. Each point on these surfaces will represent some parameter defining the position of a CEX ion scattered with the pair of scattering angles, (θ^+, ϕ^+) .

In the 2D example, the downstream distance z at which the ion trajectory passed through the plane at $\tilde{x} = 60$ was the quantity of interest, however this is inadequate for the 3D case. It is very easy to imagine situations in which the scattered particle would never have a trajectory passing through the plane at $\tilde{x} = 60$; the value would not exist. Let us imagine a sphere that is centered on the scattering center, $P(\mathbf{x})$, and such that the target point, $S(\tilde{\mathbf{x}})$, lies on the surface of this sphere. The radius of this sphere is $R_s = |\tilde{\mathbf{x}} - \mathbf{x}|$. For any scattered ion with scattering angles (θ^+, ϕ^+) , there exists a point on this sphere, $T(\mathbf{x}')$, through which the ion will pass. We will make the 3D analogy of the downstream distance z , from the 2D example, to be the length of the chord, $D(\theta^+, \phi^+)$, joining the location that the trajectory passes through the surface of the sphere, $T(\mathbf{x}')$, and the target point, $S(\tilde{\mathbf{x}})$, i.e., $D(\theta^+, \phi^+) = |\mathbf{x}' - \tilde{\mathbf{x}}|$. By this definition, the minimum attainable value occurs when the ion passes through $S(\tilde{\mathbf{x}})$: $D_{\min} = 0$. The maximum value occurs when the ion passes through the point diametrically opposed to $S(\tilde{\mathbf{x}})$: $D_{\max} = 2R_s$. Figure 4.18 graphically depicts the definition described.

For any scattering location and primary-ion velocity vector, a surface can be constructed depicting the relationship between the two scattering angles, ϕ^+ and θ^+ , and the chord length described above, $D(\theta^+, \phi^+)$. For example, let us assume that now the scattering center is not located in the radial plane passing through the point of interest, but is instead located at the general cartesian coordinates, $P(x, y, z)$, and the target point is located, as before, at $S(\tilde{x}, \tilde{y}, \tilde{z}) = (60, 0, 0)$. In this example, rather than primary ions moving parallel to the thrust axis, we will assume that the primary ions have the velocity angles $\theta_u = 10^\circ$ and $\phi_u = 180^\circ$. The resulting surfaces and contours for scattering events occurring at four different scattering centers $P_{I-IV}(\mathbf{x})$ are shown in Figures 4.19 through

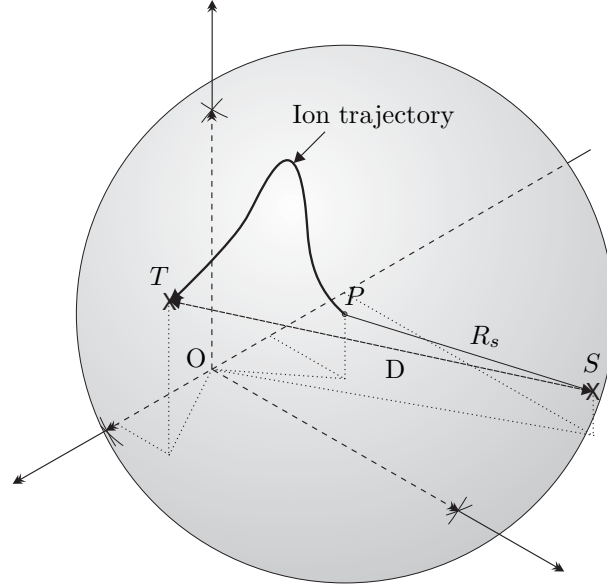


Figure 4.18: Scattering target interception sphere. A sphere is centered on the scattering center $P(\mathbf{x})$. The target point $S(\tilde{\mathbf{x}})$ is located on the surface of the sphere and defines the radius, $R_s = |\tilde{\mathbf{x}} - \mathbf{x}|$. An ion scattered from P with the scattering angles (θ^+, ϕ^+) passes through the surface of the sphere at the position $T(\mathbf{x}')$. The chord length, $D(\theta^+, \phi^+) = |\tilde{\mathbf{x}} - \mathbf{x}'|$, is computed.

4.22. The scattering-angle solutions (those pairs of scattering angles which result in an ion passing through the specified target point) for any scattering event are those angles for which $D(\theta^+, \phi^+) = 0$. For example, the scattering event at $P_{\text{II}}(\mathbf{x})$ has two solutions: (1) $(\theta_1^+, \phi_1^+) = (110.0^\circ, 89.1^\circ)$, and (2) $(\theta_2^+, \phi_2^+) = (159.5^\circ, 86.1^\circ)$. The scattering event at $P_{\text{IV}}(\mathbf{x})$, on the other hand, has no solutions that result in scattered CEX ions passing through the specified target point, $S(\tilde{x}, \tilde{y}, \tilde{z}) = (60, 0, 0)$. The 2π -periodicity in ϕ^+ is apparent.

The four cases shown present the analogous 3D extension of the four cases discussed in the 2D example:

- (I) One unique pair of scattering angles, (θ^+, ϕ^+) , results in the scattered ion passing through the target point; the streamtube area at the target point is greater than zero ($d\tilde{A}/d\Omega > 0$).
- (II) Two unique pairs of scattering angles result in a scattered ion passing through the target point.
- (III) One unique pair of scattering angles results in the scattered ion passing through the target point; the streamtube area at the target point is equal to zero ($d\tilde{A}/d\Omega = 0$).
- (IV) No ion from this scattering event passes through the target point.

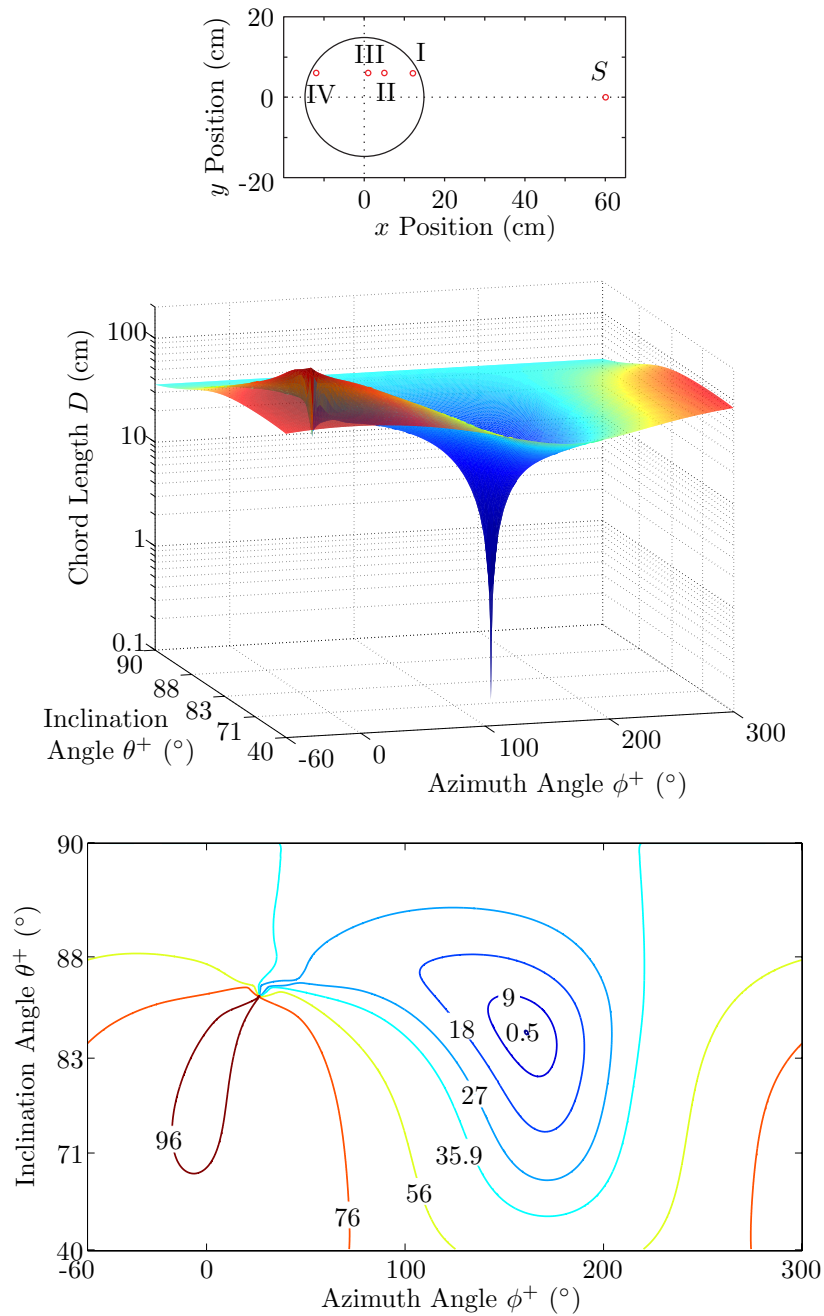


Figure 4.19: Chord-length surfaces and contours for the scattering event at $P_1(\mathbf{x}) = (12, 6, 2)$. The chord length between the target point $S(\tilde{\mathbf{x}})$ and the point $T(\mathbf{x}')$ that an ion passes through the target sphere, $D(\theta^+, \phi^+)$, is a function of the scattering angles of the ion, (θ^+, ϕ^+) . The primary-ion velocity vector angles are specified to be $\theta_u = 10^\circ$ and $\phi_u = 180^\circ$. **Top figure:** Top view of the thruster, indicating the relative position of the four example scattering centers $P_{I-IV}(\mathbf{x})$ and the target point $S(\tilde{\mathbf{x}}) = (60, 0, 0)$. **Middle figure:** Chord-length surface as a function of the pair of scattering angles (θ^+, ϕ^+) . **Bottom figure:** Constant value contours of the chord-length surface. One scattering solution (where $D(\theta^+, \phi^+) = 0$) exists for this scattering event.

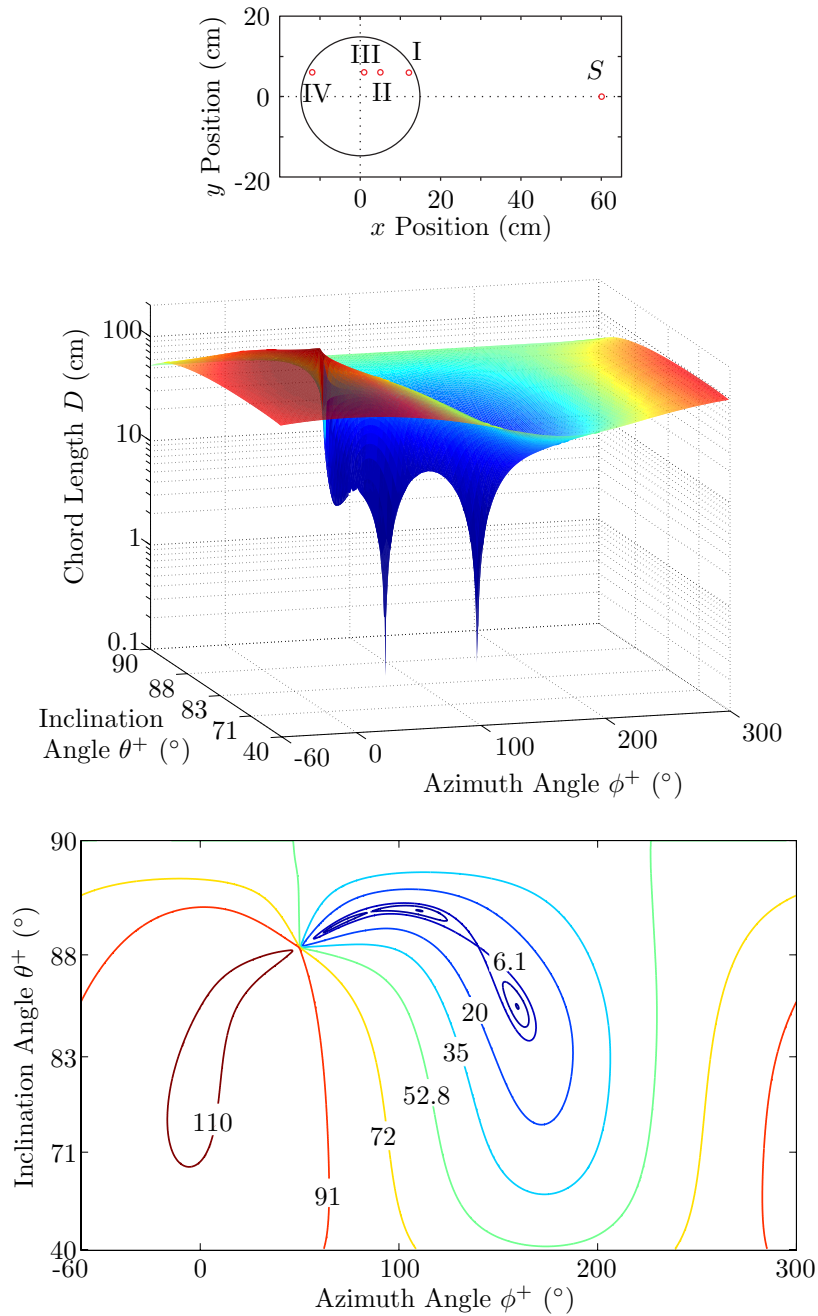


Figure 4.20: Chord-length surfaces and contours for the scattering event at $P_{II}(\mathbf{x}) = (5, 6, 2)$. The chord length between the target point $S(\bar{\mathbf{x}})$ and the point $T(\mathbf{x}')$ that an ion passes through the target sphere, $D(\theta^+, \phi^+)$, is a function of the scattering angles of the ion, (θ^+, ϕ^+) . The primary-ion velocity vector angles are specified to be $\theta_u = 10^\circ$ and $\phi_u = 180^\circ$. **Top figure:** Top view of the thruster, indicating the relative position of the four example scattering centers $P_{I-IV}(\mathbf{x})$ and the target point $S(\bar{\mathbf{x}}) = (60, 0, 0)$. **Middle figure:** Chord-length surface as a function of the pair of scattering angles (θ^+, ϕ^+) . **Bottom figure:** Constant value contours of the chord-length surface. Two scattering solutions (where $D(\theta^+, \phi^+) = 0$) exist for this scattering event.

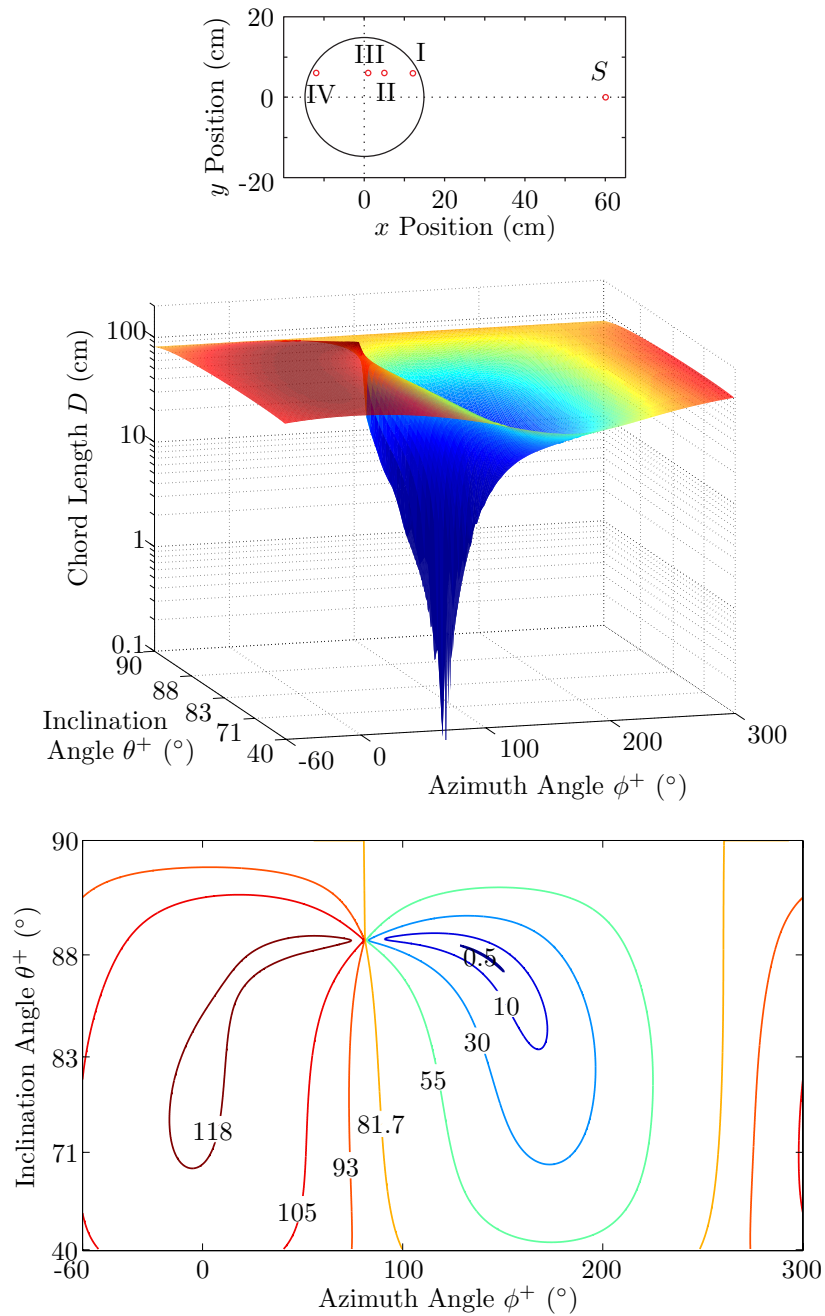


Figure 4.21: Chord-length surfaces and contours for the scattering event at $P_{\text{II}}(\mathbf{x}) = (0.95, 6, 2)$. The chord length between the target point $S(\bar{\mathbf{x}})$ and the point $T(\mathbf{x}')$ that an ion passes through the target sphere, $D(\theta^+, \phi^+)$, is a function of the scattering angles of the ion, (θ^+, ϕ^+) . The primary-ion velocity vector angles are specified to be $\theta_u = 10^\circ$ and $\phi_u = 180^\circ$. **Top figure:** Top view of the thruster, indicating the relative position of the four example scattering centers $P_{\text{I-IV}}(\mathbf{x})$ and the target point $S(\bar{\mathbf{x}}) = (60, 0, 0)$. **Middle figure:** Chord-length surface as a function of the pair of scattering angles (θ^+, ϕ^+) . **Bottom figure:** Constant value contours of the chord-length surface. One scattering solution (where $D(\theta^+, \phi^+) = 0$) exists for this scattering event.

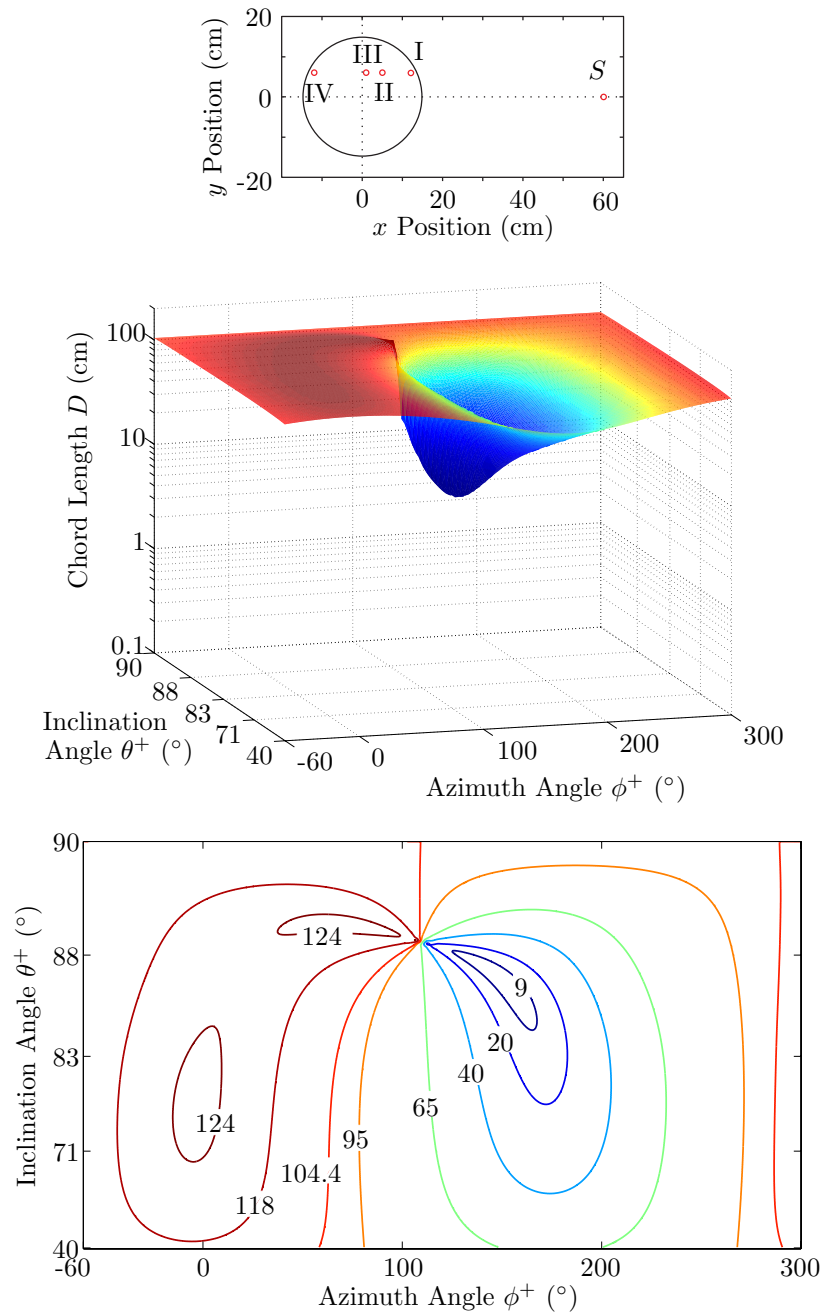


Figure 4.22: Chord-length surfaces and contours for the scattering event at $P_{IV}(\mathbf{x}) = (-14, 6, 2)$. The chord length between the target point $S(\bar{\mathbf{x}})$ and the point $T(\mathbf{x}')$ that an ion passes through the target sphere, $D(\theta^+, \phi^+)$, is a function of the scattering angles of the ion, (θ^+, ϕ^+) . The primary-ion velocity vector angles are specified to be $\theta_u = 10^\circ$ and $\phi_u = 180^\circ$. **Top figure:** Top view of the thruster, indicating the relative position of the four example scattering centers $P_{I-IV}(\mathbf{x})$ and the target point $S(\bar{\mathbf{x}}) = (60, 0, 0)$. **Middle figure:** Chord-length surface as a function of the pair of scattering angles (θ^+, ϕ^+) . **Bottom figure:** Constant value contours of the chord-length surface. No scattering solutions (where $D(\theta^+, \phi^+) = 0$) exist for this scattering event.

Given a particular scattering event with a primary-ion velocity, \mathbf{u} , a scattering center location, $P(\mathbf{x})$, and a target point location, $S(\tilde{\mathbf{x}})$, we must solve a boundary value problem in order to determine the solution angles, (θ^+, ϕ^+) . The goal is to locate all scattering angle pairs for which $D(\theta^+, \phi^+)$ is a minimum. Any pair for which $D(\theta^+, \phi^+) = 0$ is a solution. Computing the surfaces, of which Figures 4.19 through 4.22 are examples, for every possible scattering event is impractical. Instead, a Gauss-Newton with an inexact line search root-finding algorithm was developed [35]. The pseudo-code for the method is presented in the following section.

4.6.3 Pseudo-Code: Scattering Angle Partial Gauss-Newton Search Algorithm

The following pseudo-code outlines the procedure used to implement a Gauss-Newton root finding algorithm. Due to the presence of saddle points in the function for which we wish to find the locations of the minimum values, a steepest-descent method was also incorporated for use when the hessian is not positive-definite. The Gauss-Newton/steepest-descent method is used to compute the direction in which to search for the minimum, and also computes an estimate to the step size to take in that direction. An inexact line search was incorporated for obtaining an estimate to the actual location the minimum is found in the search direction. This algorithm is used in all cases when it is desired to compute the scattering angle at a certain location required to send CEX ions through the target point. The code was implemented using Matlab.

1. Let \mathbf{x}_0 and \mathbf{v}_0 be the scattering center position and primary-ion velocity vector, respectively.
2. Let coordinates of target point, S, be $\tilde{\mathbf{x}}$, and find the radius of the target sphere, $R = \|\tilde{\mathbf{x}} - \mathbf{x}_0\|$.
3. Choose threshold values to determine when to terminate iteration, ϵ^D , ϵ^ϕ , and ϵ^θ .
4. $k = 0$. Choose an initial guess for the azimuth and inclination scattering angles, $\Phi_0 = [\phi_0, \theta_0]$.
5. $k = k + 1$.

6. Find initial velocity vectors for nine sample ions, using all combinations of the scattering angles, $\hat{\Phi}_k^i = \{\phi_k - \delta\phi, \phi_k, \phi_k + \delta\phi\} \cup \{\theta_k - \delta\theta, \theta_k, \theta_k + \delta\theta\}$.
7. Integrate the equations of motion for the sample ions until all pass through the target sphere.
8. Locate coordinates for each ion where each trajectory intercepts the target sphere, $\mathbf{x}'_k{}^i$.
9. Compute the chord length between ion intercept points and target point, $\hat{D}_k^i = \|\mathbf{x}'_k{}^i - \tilde{\mathbf{x}}\|$.
10. If there is any $\hat{D}_k^i \leq \epsilon^D$, then go to step 22; otherwise go to step 11.
11. Determine the gradient, $\mathbf{g}_k = [g_k^\phi, g_k^\theta]^T = \nabla \hat{D}_k$, and hessian, $\mathbf{H}_k = \nabla \left(\nabla \hat{D}_k \right)^T$, using central difference; compute the eigenvalues of \mathbf{H}_k . ($\nabla \equiv [\partial/\partial\phi, \partial/\partial\theta]^T$).
12. If both eigenvalues are positive, go to step 13; otherwise go to step 15.
13. If $g_k^\phi \leq \epsilon^\phi$ and $g_k^\theta \leq \epsilon^\theta$, then go to step 22; otherwise go to step 14.
14. Compute the Newton step, $\mathbf{s}_k = -\mathbf{H}_k^{-1} \mathbf{g}_k$. Go to step 17.
15. Compute the Jacobian, $\mathbf{J}_k = \nabla (\mathbf{x}'_k - \tilde{\mathbf{x}})$, using central difference.
16. Solve for the Newton step, \mathbf{s}_k , such that $(\mathbf{x}'_k - \tilde{\mathbf{x}}) = -\mathbf{s}_k^T \mathbf{J}$.
17. Choose N equi-spaced scale lengths, $\hat{\alpha}_i$, such that $0 < \hat{\alpha}_i \leq 1$.
18. Find initial velocity vectors for N sample ions using the scattering angles, $\hat{\Phi}_k^i = \Phi_k + \hat{\alpha}_i \mathbf{s}_k^T$.
19. Repeat steps 7 through 9.
20. If there is any $\hat{D}_k^i \leq \epsilon^D$, then go to step 22; otherwise go to step 21.
21. Interpolate for α_k such that D_k is a minimum at $\Phi_{k+1} = \Phi_k + \alpha_k \mathbf{s}_k^T$. Go to step 5.
22. $D^* = \hat{D}_k^i$ and $\Phi^* = \hat{\Phi}_k^i$. Output Φ^* and D^* .

4.7 Computing the Ion Flux and Sputtering Rate

Sections 4.1 through 4.6 were devoted to developing methods for computing the individual quantities included in the CEX-ion flux integral of Equation 2.29. The remaining tasks are to (1) develop a method for evaluating the integral over all primary-ion velocity vectors and all space, (2) compute the ion flux energy distribution through differentiation (see Equation 2.33), and finally (3) evaluate the sputtering rate of a surface located at a specified target point (see Equation 2.34). The concept of a *beamlet shell* is introduced in Section 4.7.1. The beamlet shell enables simple evaluation of all the desired quantities by summing the contributions from each individual hole. An example of the implementation of the model is given in Section 4.7.2.

4.7.1 The Beamlet Shell

For any grid hole, k , let us construct a spherical beamlet scattering shell with a radius r_k and a thickness δr . In Section 4.2.1 we defined a hole beamlet to be the isotropic emission cone with a divergence half-angle ϑ_k , originating from a point source \mathbf{y}'_k behind the hole. We define the sphere from which this beamlet shell originates as centered on the emission point for the hole in question. We construct a square mesh of scattering centers that conforms to the surface of the shell, and has a width such that the mesh fully encompasses the perimeter of the shell. An example of a beamlet shell and scattering-center mesh is shown in Figure 4.23.

A small volume element of the shell contained within the subtending solid angle, $\delta\omega$, is equal to $\delta V = r^2 \delta\omega \delta r$. Any point on the shell has a normal vector $\hat{\mathbf{n}} = \hat{\mathbf{r}}$. Substituting Equation 4.13 into Equation 2.27 yields the flux of CEX ions from this volume element, due to collisions involving primary ions originating from hole k :

$$\delta F_k(\tilde{\mathbf{x}}, \mathbf{v}; \mathbf{x}, \mathbf{u}) = \frac{n_0 I_k}{q \Delta \omega_k} \frac{d\sigma}{d\Omega} \Big|_{\theta^+} \left(\frac{dA}{d\Omega} \right)^{-1} \frac{\mathbf{x} - \mathbf{y}'_k}{\|\mathbf{x} - \mathbf{y}'_k\|^3} \cdot \hat{\mathbf{r}} r^2 \delta\omega \delta r. \quad (4.40)$$

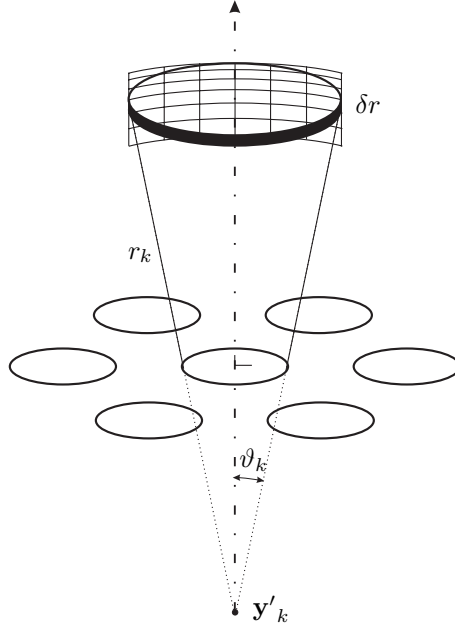


Figure 4.23: A beamlet shell. The shell is comprised of the portion of a sphere that is subtended by the beamlet cone with divergence angle ϑ_k . The sphere is centered on the emission point \mathbf{y}'_k , has a radius r , and a thickness δr . A square mesh of scattering centers is constructed on the surface and fully encompasses the perimeter of the shell.

Since the beamlet shell is centered on the emission point for the hole, $\mathbf{x} - \mathbf{y}'_k \equiv \mathbf{r}$, we obtain

$$\frac{\delta F_k}{\delta r} = \frac{n_0 I_k}{q \Delta \omega_k} \frac{d\sigma}{d\Omega} \Big|_{\theta_+} \left(\frac{dA}{d\Omega} \right)^{-1} d\omega. \quad (4.41)$$

To reiterate, this expression is equal to the non-directional flux, per unit beamlet-shell radius, through the target point $S(\bar{\mathbf{x}})$, due to scattering events occurring from a shell element subtended by $\delta\omega$, located on the shell at \mathbf{x} . The contribution from the whole beamlet shell is obtained by integrating over the entire solid angle, subtended by the emission cone, $\Delta\omega_k = 2\pi(1 - \cos\vartheta_k)$. Evaluating this integral and allowing $\delta r \rightarrow 0$ we obtain

$$\frac{dF_k}{dr} \Big|_r = \frac{I_k}{q \Delta \omega_k} \int_{\Delta \omega_k} n_0 \frac{d\sigma}{d\Omega} \Big|_{\theta_+} \left(\frac{dA}{d\Omega} \right)^{-1} d\omega. \quad (4.42)$$

The integral in Equation 4.42 is calculated numerically in the following manner: A mesh of J scattering points within the shell of radius r is constructed, where the coordinates of point j are $\mathbf{x}_{k,j}$. Each scattering point in the mesh is associated with a portion of the total surface area of the

shell, $\delta a_{k,j}$, where

$$\sum_{j=1}^J \delta a_{k,j} = r^2 \Delta \omega_k. \quad (4.43)$$

The solid angle enclosing the area associated with each scattering point is then computed to be

$$\delta \omega_{k,j} = \frac{\delta a_{k,j}}{r^2}. \quad (4.44)$$

The quantities within the integral of Equation 4.42 are then computed for the scattering events at each of the scattering points. The numerical integral is then equal to

$$\left. \frac{dF_k}{dr} \right|_r = \frac{I_k}{q \Delta \omega_k} \sum_{j=1}^J \left[n_{0,j} \left. \frac{d\sigma}{d\Omega} \right|_{\theta_{k,j}^+} \left(\frac{dA}{d\Omega} \right)_j^{-1} \delta \omega_{k,j} \right], \quad (4.45)$$

where $n_{0,j}$ is the neutral atom density at $\mathbf{x}_{k,j}$, $\theta_{k,j}^+$ is the scattering-angle solution obtained using the search algorithm from Section 4.6.3, and $(dA/d\Omega)_j$ is the streamtube expansion for the scattering-angle solution.

Other than how they influence the plume potential, we have to this point assumed that the primary ions are non-interacting, and so the contribution to the CEX-ion density at a specific target point from one hole is completely independent of the contribution from any of the other holes in the grid. Therefore, the total flux, per unit shell radius, through the target point $S(\tilde{\mathbf{x}})$ is found from the superposition of the contributions from all K grid holes:

$$\left. \frac{dF}{dr} \right|_r = \sum_{k=1}^K \sum_{j=1}^J \left[\frac{n_{0,j} I_k}{q \Delta \omega_k} \left. \frac{d\sigma}{d\Omega} \right|_{\theta_{k,j}^+} \left(\frac{dA}{d\Omega} \right)_j^{-1} \delta \omega_{k,j} \right]. \quad (4.46)$$

To compute the sputtering rate, we need to know the CEX-ion flux energy distribution, Γ (see Equations 2.33 and 2.34). Numerical differentiation of the CEX-ion flux is achieved by summing only those areas of the shell, $\delta \omega_{k,j}$ from which CEX ions with energies between E and $E + \delta E$

originate, i.e.,

$$\left. \frac{d\Gamma}{dr} \right|_{E,r} = \left. \frac{\partial^2 F}{\partial E \partial r} \right|_{E,r} = \sum_{k=1}^K \left\{ \sum_{\substack{j \\ E \leq E_j < E + \delta E}} \frac{1}{\delta E} \left[\left. \frac{n_{0,j} I_k d\sigma}{q \Delta \omega_k d\Omega} \right|_{\theta_{k,j}^+} \left(\frac{dA}{d\Omega} \right)_j^{-1} \delta \omega_{k,j} \right] \right\}, \quad (4.47)$$

where E_j is defined by Equation 2.18. The sputtering rate, per unit shell radius, is thus obtained from Equation 2.34:

$$\left. \frac{d\Upsilon}{dr} \right|_r = \left[\frac{d}{dr} \int_0^{E_{max}} Y(E) \Gamma dE \right]_r = \int_0^{E_{max}} Y(E) \left. \frac{d\Gamma}{dr} \right|_r dE. \quad (4.48)$$

The integral can be approximated by dividing the energy range into M increments:

$$\left. \frac{d\Upsilon}{dr} \right|_r = \sum_m^M \left(\sum_{k=1}^K \left\{ \sum_{\substack{j \\ E_m \leq E_j < E_{m+1}}} Y(E_m) \left[\left. \frac{n_{0,j} I_k d\sigma}{q \Delta \omega_k d\Omega} \right|_{\theta_{k,j}^+} \left(\frac{dA}{d\Omega} \right)_j^{-1} \delta \omega_{k,j} \right] \right\} \right). \quad (4.49)$$

4.7.2 Example: Computing Quantities for One NSTAR Beamlet Shell

For the purpose of demonstration, a beamlet shell with a radius of $r = 1.293$ cm was constructed for one hole on the NSTAR grid model. The center of the hole had coordinates, $\mathbf{y}_k = (3.11, 8.07, 1.34)$, and unit normal vector, $\hat{\mathbf{n}}_k = (0.061, 0.158, 0.986)$. The hole had a radius of $h = 0.057$ cm and a beamlet cone half-angle of $\vartheta_k = 11^\circ$. According to Equation 4.6, the emission point was located at $\mathbf{y}'_k = (3.09, 8.03, 1.05)$. Using the plume potential computed for the NSTAR grid model (see Figure 4.7), the scattering solution angles $(\theta_{k,j}^+, \phi_{k,j}^+)$ to scatter an ion to the point $S(\tilde{\mathbf{x}}) = (60, 0, 3)$ from each mesh point $P(\mathbf{x}_{k,j})$ were found using the Gauss-Newton algorithm (see Section 4.6.3).

The top figures in both columns of Figure 4.24 show the inclination angles $\theta_{k,j}^+$ corresponding to a minimum chord length $D(\theta^+, \phi^+)_{\min}$. The angles are plotted as a function of the local shell coordinates, such that the scattering point located at the center of the shell is specified to be $(x', y') = (0, 0)$. The multi-valuedness of the solution is evident for a majority of the scattering centers. Of the four different cases outlined in Section 4.6.2, Case II applies to those points with two solutions. The column of figures on the left graphically depict the quantities associated with

the lower branch of solutions, which, for reasons made apparent later, we will refer to as the “high-energy” branch. The right column of figures depict the quantities associated with the upper branch of solutions, which we will refer to as the “low-energy” branch.

It can be seen that there is a locus of points where the two solutions merge. The bottom figures in both columns present the chord length (on a logarithmic scale) used for determining if an ion passes through the target point. The scattering points with two solutions all have a chord length $D_{\min} < 10^{-4}$ cm, which was the maximum tolerance value, ϵ_D , used for evaluating whether an ion has passed through the target point. Along the locus of points where the two solutions merge it is seen that the chord length rapidly increases. Scattering points located beyond this locus have no solution resulting in an ion scattering through the target point (Case IV). It was found that the root-finding algorithm used for locating the angles corresponding to the minimum chord length did not operate optimally in cases where $D_{\min} \neq 0$, thus the data is significantly more noisy for those points, with no solution than for those points where $D_{\min} = 0$.

In both columns, the second figure from the top displays the corresponding azimuth angle solution, $\phi_{k,j}^+$. The large jump seen to occur for both the high- and low-energy branches is due to the 2π -periodicity of the azimuth angle and the specific branch cut chosen for displaying the results; while the azimuth solution may look discontinuous it is, in fact, continuous. An ion scattered from the scattering point at the center of the shell at an azimuth angle $\phi^+ = 0$ would be scattered parallel to the x' -axis.

In the absence of an electric field, the scattered ions would follow asymptotically straight trajectories. If this were the case, the cross-sectional area of a streamtube $\delta\tilde{A}$ subtended by a solid angle $\delta\Omega$, at a distance R_s from the scattering point, would be the area of the sphere, with a radius equal to R_s , subtended by $\delta\Omega$. Thus, for non-interacting ions on asymptotically straight trajectories,

$$\left(\frac{d\tilde{A}}{d\Omega}\right)^* = \frac{R_s^2 d\Omega}{d\Omega} = R_s^2, \quad (4.50)$$

where R_s is the distance between the scattering center $P(\mathbf{x})$ and the target location $S(\tilde{\mathbf{x}})$. With the

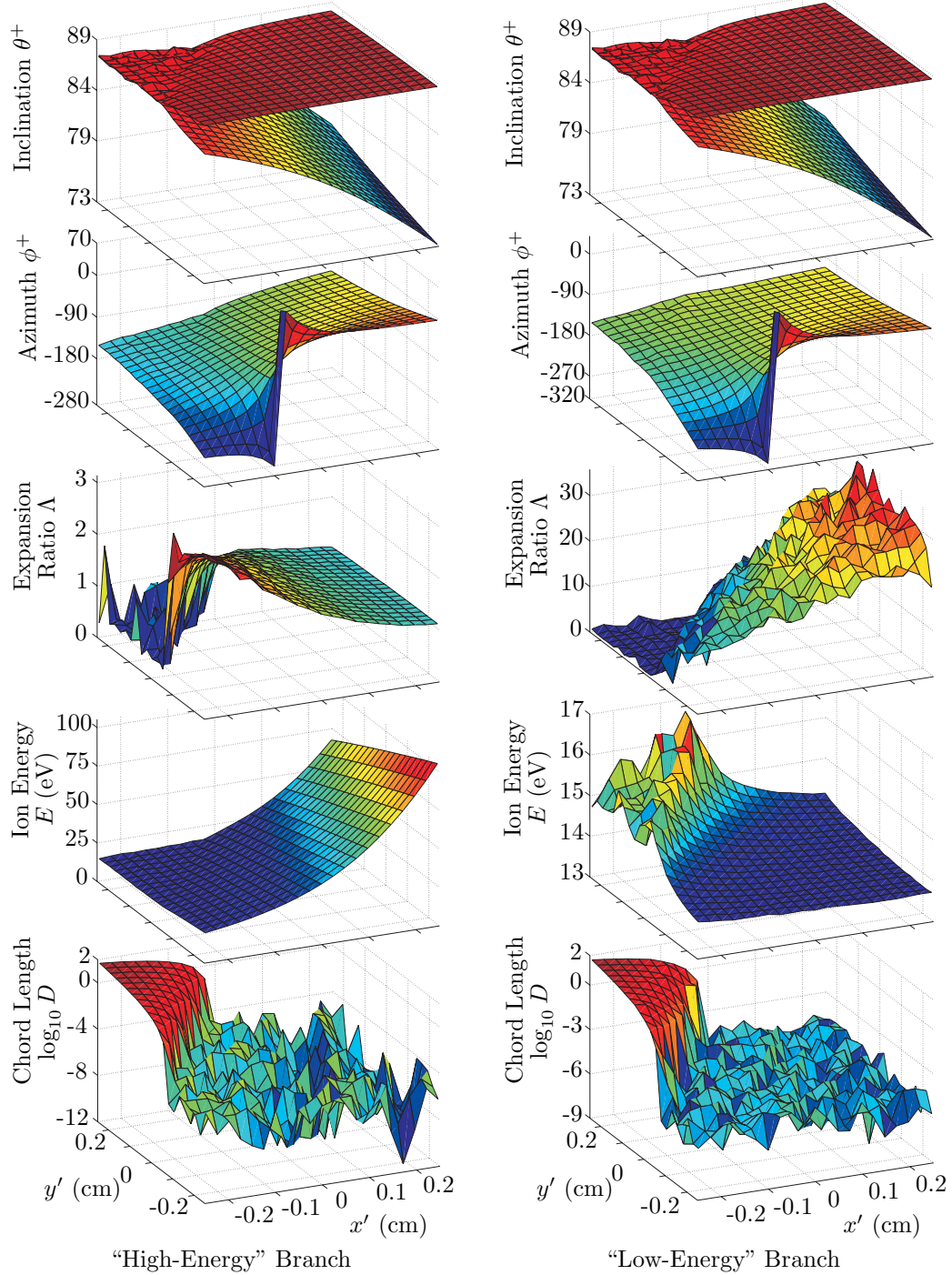


Figure 4.24: Beamlet-shell mesh-scattering solution quantities. Each point in the beamlet shell mesh (see Figure 4.23) has one or more inclination scattering angle solutions (top left and right figures) that minimize the interception sphere chord length D (bottom figures). The left and right columns correspond to the lower- and upper-solution branches, respectively. The apparent discontinuities in the azimuth scattering angle solutions (second figures from the top) are due to the branch-cuts chosen for display. A value of unity for the streamtube expansion coefficient (third figures from the top) indicates expansion identical to that of uniform divergence. The energies of the scattered ions, at the target point, are shown in the fourth figures from the top.

presence of the plume, this relation no longer holds in general. We define a streamtube expansion coefficient, which is a measure of how similar the streamtube expansion of ions scattered in an electric field is to that of those scattered without the presence of an electric field, Λ :

$$\Lambda \equiv \frac{d\tilde{A}/d\Omega}{(d\tilde{A}/d\Omega)^*} = \frac{1}{R_s^2} \frac{d\tilde{A}}{d\Omega}. \quad (4.51)$$

A coefficient value of unity would be interpreted to be that the streamtube, at that point, has expanded to the same cross-sectional area as if the ions had followed asymptotically straight trajectories. A value less than one would indicate a focussing effect on the ions, and a value greater than one indicates that the streamtube has diverged more than those on asymptotically straight trajectories. The third figure in both columns of Figure 4.24 shows the streamtube expansion coefficient, Λ , for ions scattered within a small solid angle of the solution inclination scattering angle, θ^+ .

In the case of the high-energy branch, it is seen that the coefficient approaches a value of unity as the scattering angle θ^+ decreases. This is not unexpected, for as the scattering angle decreases, the initial ion velocity and energy increases. As was seen with the trajectories in Figure 4.13, the electric field has a diminishing influence as the initial ion energy increases (e.g., $\theta^+ = 70^\circ$ vs. $\theta^+ = 90^\circ$). As the scattering angle increases it is seen that the coefficient increases up to a value of approximately three for the high-energy branch ions, and to even larger values for the low-energy branch where the scattering angle approaches 90° . It is also seen that the coefficient drops off quickly and obtains a zero value at the locus of points between the regions where there are multiple solutions and where there is no solution. The scattering points along the dividing locus correspond to Case III where there is one solution and $d\tilde{A}/d\Omega = 0$. From our analysis of the 2D example, this is to be expected, for Case III was found to be the solution at the transition between two solutions, and no solution, and $|dz/d\theta| = 0$.

The chaotic, noisy behavior of the streamtube expansion coefficient in the region where there is no solution is attributed to the non-optimum execution of the root-finding algorithm in this region. The values obtained in this region are inconsequential to our calculation since these points have no

scattering solution, and thus make no contribution to the CEX-ion flux. The significant noise in the coefficient values for the low-energy branch is attributed to the sensitivity of these ions to the plume potential; computational error from interpolation and finite difference methods is more evident with these ions.

The fourth figure in each column of Figure 4.24 shows the kinetic energy E (in electron-volts) of the ion, scattered at (θ^+, ϕ^+) , as it passes through the target point. It is clearly evident that as the inclination scattering angle increases, the energy decreases, as per Equation 2.18. In this example, the potential difference between the scattering point and the target point is $\Delta\Phi = 13.0$ eV, a value the ions scattered at the largest scattering angles are close to approaching. Though the definition of “high” energy is relative, all ions scattered according to the lower branch have a larger energy than those scattered according to the upper branch. Thus the lower branch is labeled as the “high-energy” branch since the energies of ions from this branch are higher than those of ions from the upper, or “low-energy” branch.

The plots in Figure 4.24 contain all the data needed in order to compute the contribution of CEX ions scattered to the target point, $S(\tilde{\mathbf{x}})$, from all scattering points, $P(\mathbf{x})$, contained within this beamlet shell. Figure 4.25 demonstrates how the summand of Equation 4.45 is constructed from the data shown in Figure 4.24. All points, $\mathbf{x}_{k,j}$, in the mesh which are not in the actual beamlet shell (i.e., not subtended by the beamlet), or for which there is no solution resulting in an ion passing through the target point (Case IV), are removed from the mesh, as shown in the topmost plot of Figure 4.25. Below this plot is shown the neutral density computed for each point remaining in the mesh. Below these figures, the data is again split into two columns, where the data associated with the lower branch of scattering angles are in the first column and the data associated with the upper branch of scattering angles are in the second column. The top figure in each column shows again the inclination scattering angles as from Figure 4.24. Following this figure is plotted the corresponding values of the differential cross-section, as computed from Equation 4.28. As expected, the differential cross-section for points in the “low-energy” branch have a larger value than for those in the “high-energy” branch. The third plot in each column shows the streamtube area expansion,

$d\tilde{A}/d\Omega$.

The contribution from mesh point j to the sum of Equation 4.45 is the product of the neutral atom density $n_{0,j}$, the differential cross-section $d\sigma^+/d\Omega$, and the inverse of the streamtube expansion $d\tilde{A}/d\Omega$ evaluated at that point. The contribution from each mesh point in this example is shown in the last plot of Figure 4.25. As in the 2D example, we see that the largest contributions come from those points for which Case III applies ($d\tilde{A}/d\Omega = 0$).

The CEX-ion flux energy distribution contribution to the target point from the shell of this example is obtained by evaluating the quantity within the braces of Equation 4.47, i.e.,

$$\left. \frac{d\Gamma_k}{dr} \right|_{E,r} = \frac{I_k}{q\Delta\omega_k \delta E} \sum_{\substack{j \\ E \leq E_j < E + \delta E}} \left[n_{0,j} \left. \frac{d\sigma}{d\Omega} \right|_{\theta_{k,j}^+} \left(\frac{dA}{d\Omega} \right)_j^{-1} \delta\omega_{k,j} \right]. \quad (4.52)$$

If there is a relatively small number of points in the beamlet shell from which to compute the energy distribution, a large amount of numerical noise may arise. With a small number of beamlet-shell points, very few of these points may contribute ions within any particular energy range. To increase the probability of finding shell points contributing ions to any specific energy range, either the energy range δE or the number of shell points must be increased. While increasing the energy range is a viable option it reduces the resolution of the energy distribution; it is more desirable to increase the number of shell points so that we can have a statistically significant number of points contributing to each energy range from each shell.

Since the root-finding algorithm of Section 4.6.3 must be executed for each mesh point in the shell, increasing the number of points in the beamlet shell could make computation of all quantities highly impractical. Fortunately, all the quantities, as evidenced in Figure 4.24, seem to be well behaved and vary slowly. This lends the computation to the use of interpolation. After computing for a mesh with a relatively small number of points, the relevant quantities can be interpolated to a finer mesh of the same beamlet shell through bilinear- or another 2D-interpolation method. This provides essentially no limit to the number of particles we can simulate, and thus can supply a sufficient number of particles to each energy range to significantly reduce statistical noise. The

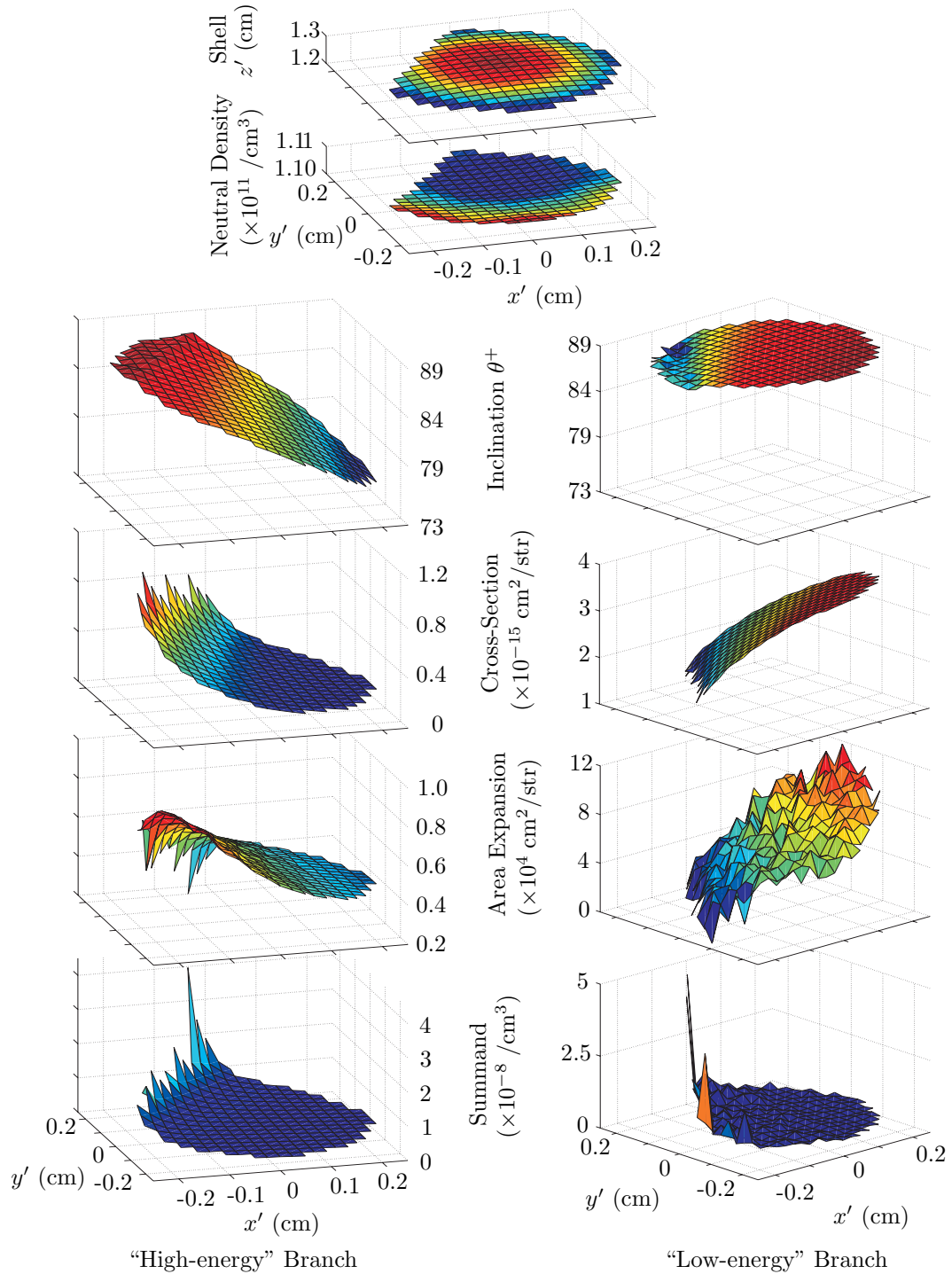


Figure 4.25: Beamlet-shell summand quantities. Mesh points within the beamlet shell example that contribute to the CEX-ion flux are shown in the top figure. The neutral atom density at each contributing point in the shell is shown in the second figure from the top. The left and right columns correspond to the lower- and upper-inclination scattering angle solution branches (see Figure 4.24). Differential cross-sections corresponding to the scattering angle solutions and the area expansion $dA/d\Omega$ quantities are shown in the second and third figures from the top of each column, respectively. The contributions to the summand of Equation 4.45 are shown in the bottom figures.

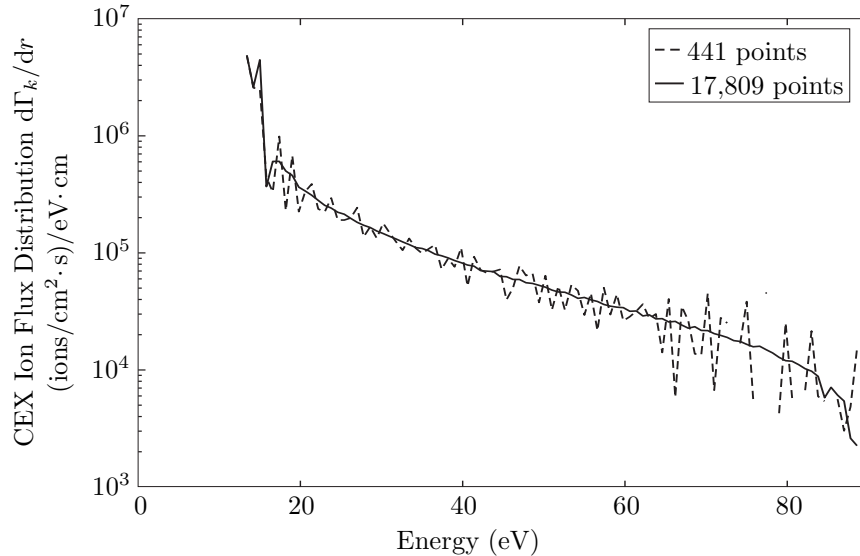


Figure 4.26: Beamlet-shell contribution to the CEX-ion flux distribution. The contribution to the CEX-ion flux energy distribution, per unit shell radius, from the sample beamlet shell of Figure 4.25, is found from evaluating the sum of Equation 4.52. Increasing the number of mesh points in the beamlet shell can improve the resolution of the energy distribution and reduce statistical noise. The 17,809 points used to compute the distribution corresponding to the solid line were obtained using bilinear interpolation of the quantities of the original 441 mesh points (see Figure 4.24). The shell radius is $r = 1.293$ cm.

effectiveness of interpolation from a coarse to a finer mesh for the shell used in our example (see Figures 4.24 and 4.25) is demonstrated in Figure 4.26.

The dotted line presents the contribution to the CEX-ion flux energy distribution, per unit shell radius, computed using only the original $J = 441$ mesh points (see Figure 4.24). The statistical noise is evident. Bilinear interpolation was used to interpolate the values for $J = 17,809$ scattering mesh points representing the same original shell. The solid line shows the resulting energy distribution contribution computed from using this increased number of mesh points. The total distribution was obtained using contributions calculated from both scattering branches (high- and low-energy). The vast majority of the contribution for energies below $E = 16$ eV is from the low-energy branch, whereas the high-energy branch is solely responsible for all contributions above $E = 16$ eV.

4.7.3 Example: Sputtering Rate Contribution from One NSTAR Beamlet

The full energy distribution, as a function of both shell radius and CEX-ion energy, for the hole and beamlet used in the previous example is shown in Figure 4.27, and was obtained by evaluating Equation 4.52 for multiple beamlet-shell radii. The distribution of Figure 4.26 corresponds to the line in Figure 4.27, at a constant radius of $r = 1.293$ cm. The apparent jaggedness of the forefront edge of the surface is due to the fact that the flux drops to zero at this edge, which cannot be depicted well in graphical form on a logarithmic plot. More frequent sampling by reducing the increments in both the shell radius and ion energy would smooth the jaggedness of the edge.

It is evident that the most energetic ions originate from shells close to the grid surface. It is also apparent that, in all shells, the largest flux comes from ions with energies less than approximately 20 eV. This is anticipated, for these low-energy ions come from collisions where the scattering-angle solution is very close to 90° , and the majority of the ion energy is obtained from the potential difference between the scattering location and target point (see Equation 2.18). The cross-section is largest for scattering angles close to 90° , and thus explains the largest flux at low energies. For this example, we can see that the contribution to the flux from shells with a radius greater than approximately 11 cm drops to zero.

The complete contribution to the CEX-ion distribution at the target point from all collisions that occur within one beamlet is obtained by integrating Equation 4.52, at constant energy, over all shell radii, i.e., (using Equation 4.47)

$$\Gamma_k|_E = \int_{r_{\min}}^{\infty} \left. \frac{d\Gamma_k}{dr} \right|_{E,r} dr = \int_{r_{\min}}^{\infty} \left. \frac{\partial^2 F_k}{\partial E \partial r} \right|_{E,r} dr. \quad (4.53)$$

The lower limit of the integration, r_{\min} , corresponds to the radius for which the shell is at the surface of the grid. Using Equation 4.6,

$$r_{\min} = |\mathbf{y}_k - \mathbf{y}'_k| = R \cotan \vartheta_k. \quad (4.54)$$

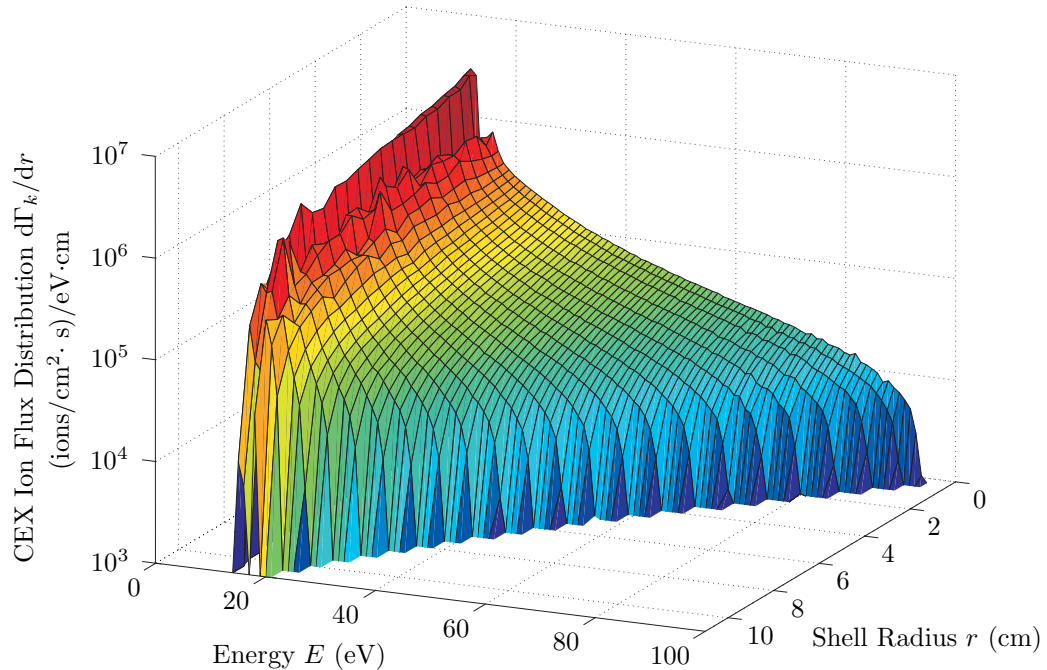


Figure 4.27: Beamlet contribution to the CEX-ion flux distribution. Evaluating Equation 4.52 for multiple beamlet-shell radii, yields a surface parameterized by the CEX-ion energy E and shell radius r . The distribution of Figure 4.26 corresponds to the line at constant shell radius, $r = 1.293$ cm. The vast majority of the flux is from ions with energies less than approximately 20 eV. The highest-energy ions originate from collisions in beamlet shells closest to the grid surface. The contribution from this beamlet to the energy distribution of CEX-ions at the target point, Γ_k , can be obtained by integrating, at constant energy, over the shell radius.

In practice, the upper infinite limit of the integration can be replaced by the maximum shell radius, r_{\max} , from which any contribution is made. There is no closed-form solution to find this radius and it must be found by trial and error. In the case of this example, Figure 4.27 indicates a maximum shell radius of approximately $r_{\max} = 11$ cm.

The energy distribution for the beamlet and target point used in this example, integrated over shell radius using Simpson integration, is shown in Figure 4.28. An interesting fact to note is that, even though there are significantly fewer ions at the high energies than at the lowest energies (3 to 4 orders of magnitude difference), the noise seems to be significant at the low energies. The primary source of this noise is expected to be from the computation of the streamtube expansion. It was discussed earlier, and seen in Figure 4.25, that an accurate and relatively noise-free computation of $dA/d\Omega$ becomes difficult for low-energy ions.

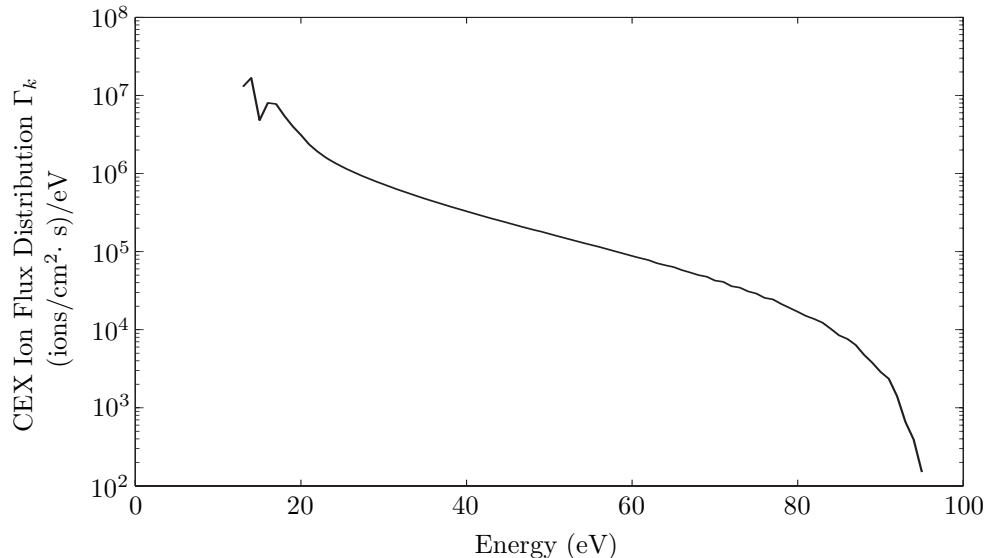


Figure 4.28: Spatially integrated beamlet contribution to the flux distribution. Simpson integration of the lines at constant E of Figure 4.27, over shell radius, yields the contribution to the CEX-ion flux energy distribution from the beamlet of our example. This is equivalent to evaluating Equation 4.53. Further integration over energy yields the total flux contribution from the entire beamlet to the sample target point, F_k .

Another contributing factor to the noise is the rapid increase of flux from points in the beamlet shells where the streamtube expansion gets very small. We discussed in the 2D example of Section 4.6 how, mathematically, an infinite flux can arise, without violating mass conservation, due to focussing of the streamtube by the electric field ($dA/d\Omega \rightarrow 0$). However, regardless of mathematical correctness, large flux contributions can be difficult to handle accurately in a computational algorithm, where we approximate infinitesimal quantities with finite values, i.e., $dV \rightarrow \delta V$.

We are now at a point that we can compute the total CEX-ion density at the target point. By Equation 2.33, integration of the energy distribution over the CEX-ion energy E yields the scalar value of the total CEX-ion density contribution at the target point from the entire beamlet chosen in our example:

$$n_{s,k} = \int_0^\infty v^{-1} \Gamma_k dE. \quad (4.55)$$

The total CEX-ion density at the target point is obtained by summing the contributions from all

the grid beamlets:

$$n_s = \sum_{k=1}^K n_{s,k}. \quad (4.56)$$

When discussing how we obtain the plume potential, from which we could determine ion trajectories, we had to make an assumption about the form of the potential (see Sections 4.1 and 4.2). The ability to determine the density at various target points is very desirable, for doing so closes the loop in the path to computing ion trajectories and a potential that are self-consistent. The original potential used can be compared to the one obtained here, and, if necessary, the potential can be modified to recompute the densities.

As was seen in the shell contribution (see Figure 4.26), the vast majority of CEX ions arriving at the target point from this beamlet have energies less than approximately 20 eV. This being the case, the average CEX-ion energy would be expected to be in the vicinity of 20 eV — of the order of the potential difference between the main beam interior and spacecraft surface. This is in agreement with the assumption (discussed in Section 1.2) that others have used in their simulations of the CEX-ion plume environment: they assume all CEX ions scatter at 90° , with zero initial energy [15, 16].

Unfortunately, due to the large amount of noise present in the flux distribution (Figure 4.28) at low energies, the resulting computation of the density from numerical integration of the distribution would be suspect. Resolving the aforementioned issues that cause the large amount of noise would need to be resolved before confidence could be placed in the densities obtained through this method. That being stated, integration of the distribution in Figure 4.28 yields a total density contribution to the target point from this beamlet of $n_{s,k} = 1.67 \times 10^4 / \text{cm}^3$. The energy below which 5% of the total contribution is made occurs at approximately 14 eV. Similarly, 10%, 90%, and 95% of the total density are from ions below approximately 15, 28, and 36 eV, respectively.

If we were to assume that this beamlet is typical of all the holes in the grid, we could obtain an estimate of the total density at the target point. There are 14,845 holes in the grid, thus the total density would be estimated to be approximately $n_s = 2.5 \times 10^8 / \text{cm}^3$. The density at this same point computed from the CEX-ion densities used to obtain the initial plume potential (see Section

4.2.2) is approximately $n_s = 1.1 \times 10^7 / \text{cm}^3$, about an order of magnitude less than our estimated value.

For several reasons, the difference in the two computed values of the CEX-ion density at the chosen target point is not unexpected. First, the assumption that this particular beamlet is typical is not accurate. It was described earlier that the total beamlet current depends on the location of the hole with respect to the grid axis. With the beamlet current profile used (Equation 4.12), 21.8% of the total beam current comes from the inner 11.1% of the total grid area, or all the holes within the first third of the total radius. Conversely, 32.4% of the total beam current comes from the outer 55.5% of the grid area, or all holes in approximately the outer third of the radius. In other words, there are a large number of beamlets with a total current greater than the current of the beamlet from our example, and an even larger number of beamlets with less total current. Second, the hole used in our example, located at $\mathbf{y}_k = (3.11, 8.07, 1.34)$, is in the half of the grid closest to the target point, and has a normal vector partially directed towards the target point. Many of the holes located in the other half of the grid, with normal vectors pointed away from the target point, will contribute very little or nothing to the ion density. Additionally, there are other factors which make direct comparison of our computed density with that obtained from the other computation difficult. There are many specific parameters used in each computation that are not directly used in the other. Assumptions and conversions must be made in order to make the two computations loosely correspond with the same operating conditions. For example, the upstream neutral density, while specified in this model, is not an explicit parameter of the other.

For the purposes of this work, while computing the total CEX-ion density at any point is desirable, our primary goal is to know how much sputtering we can expect at the target point. Using the form for the sputtering yield presented earlier (Equation 4.29), the integrand of Equation 4.48 is shown, as a function of energy and shell radius, in Figure 4.29. The data for this figure was obtained by multiplying the value at each point in the surface of Figure 4.27 with the value of the sputtering yield evaluated at the corresponding energy. One of the most important results to note from this figure is that the entire low-energy ion population has been all but wiped out, due to the high sensitivity of

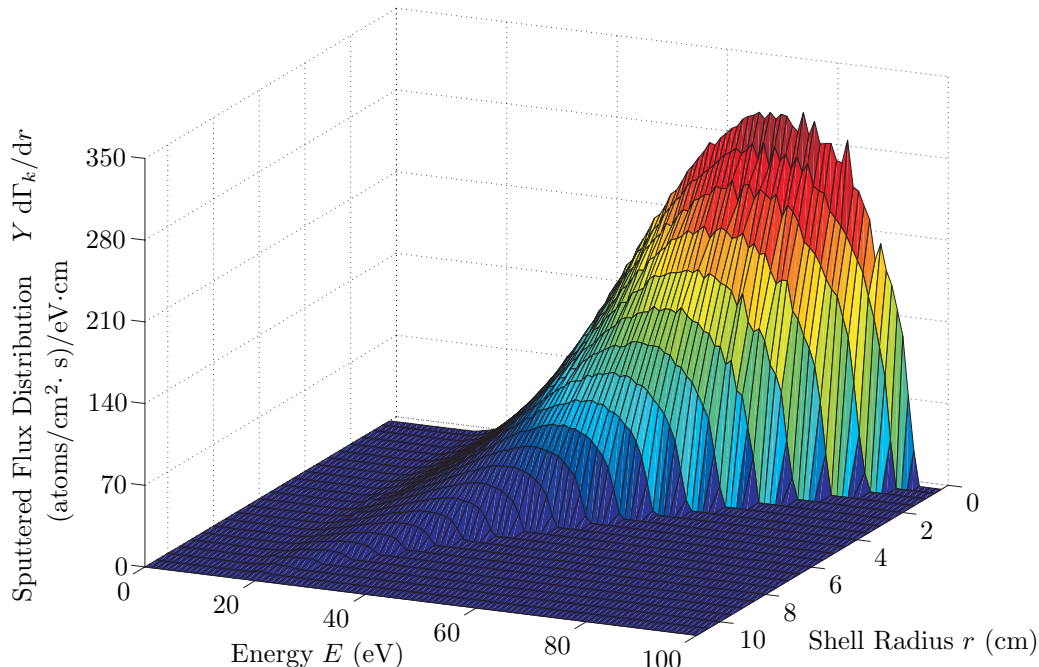


Figure 4.29: Beamlet contribution to the sputtering rate. Multiplying the sputter yield with the distribution contribution from each beamlet shell of Figure 4.27, results in a surface depicting the sputtering rate parameterized by the CEX-ion energy E and beamlet shell radius r . The beamlet of this example contributes an amount equal to the volume under the surface to the sputtering rate at the target point. The high sensitivity of the sputter yield to energy results in a very minor sputtering contribution from the dominant population of low-energy ions.

the sputter yield to energy. The total sputtering rate, per unit area, due to CEX ions originating in this sample beamlet is obtained by integrating over both shell radius and energy (equivalent to the volume under the surface). Thus we see that, though the low-energy ions are the most populous, they make a very small contribution to the sputtering integral. Additionally, the significant noise we found associated with our computation of the flux of the low-energy ions will have an insignificant impact on the computed value for the sputtering.

In a manner similar to how we obtained the CEX-ion flux energy distribution of Figure 4.28, the distribution of sputtered atoms, integrated over shell radius, is shown as a solid curve (left axis) in Figure 4.30, i.e.,

$$\left. \frac{d\Upsilon_k}{dE} \right|_E = \int_{r_{\min}}^{\infty} Y(E) \left. \frac{d\Gamma_k}{dr} \right|_{E,r} dr. \quad (4.57)$$

The curve can be obtained from the product of the sputter yield with the energy distribution (see

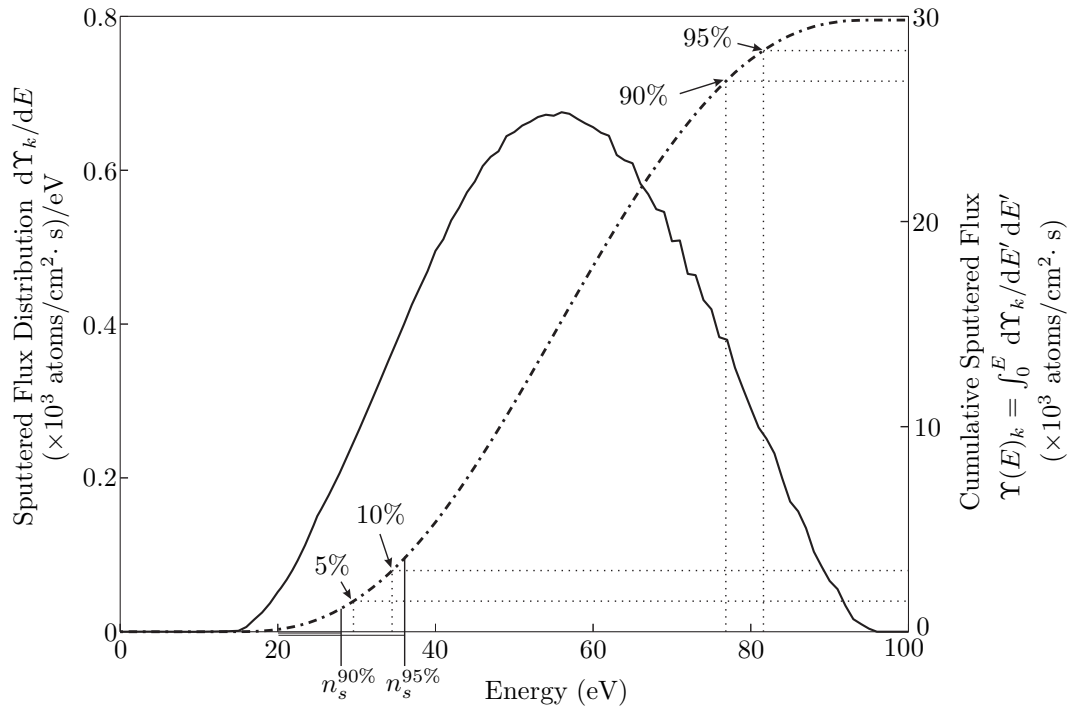


Figure 4.30: Integrated beamlet sputtering contribution. The solid line (left axis) is obtained from the product of the sputter yield with the energy distribution of Figure 4.28, or by integrating Figure 4.29, at constant E , over all beamlet radii. The dashed line (right axis) is the cumulative integral, over energy, of the quantity represented by the solid line. The CEX-ion energies below which 5%, 10%, 90%, and 95% of the total sputtering contribution from this beamlet are indicated. For reference, the energies below which 90% and 95% of the total density contribution from this beamlet are also shown. The most energetic ions (upper 5%) are responsible for nearly 90% of the total sputtering from this beamlet.

Figures 4.11 and 4.28), or by integrating, at constant E , the data of Figure 4.29 over shell radius. Note that the energy E of both Figures 4.28 and 4.29 is the CEX-ion energy, *not* the energy of the sputtered atom. The quantity of Equation 4.57 is the rate that atoms are sputtered from the surface, per unit area, per unit *CEX-ion energy*, due to all the CEX ions originating from the beamlet of our example and colliding with the surface with energies between E and $E + dE$. The dash-dot line in Figure 4.30 is the cumulative integral (right axis), over energy, of the sputtering rate (solid line):

$$\Upsilon(E)_k = \int_0^E \frac{d\Upsilon_k}{dE'} dE'. \quad (4.58)$$

Ions with energies less than approximately 30 eV are responsible for 5% of the total sputtering contribution from this beamlet, as indicated in the figure. Similarly, 10%, 90%, and 95% of the total

sputtering is due to ions with energies less than approximately 35, 77, and 82 eV, respectively. The energies at which the computed density reaches 90% and 95% of the contribution are also indicated, for reference. As can be seen, 95% of the density contribution, composed of CEX ions with energies less than approximately 36 eV, only accounts for a little more than 10% of the total sputtering contribution: nearly 90% of the sputtering is due to the 1-in-20 ions with energies more than 36 eV. The largest contribution to the sputtering rate originates from CEX ions with energies in the vicinity of 56 eV.

The average potential drop between points within the beamlet and the target point is approximately 13 eV. Assuming this to be a typical value for $\Delta\Phi$, CEX ions arriving at the target point with energies of $E = 36$ eV, 56 eV, and 82 eV would have scattering angles of $\theta^+ = 81.7^\circ, 78.6^\circ$, and 75.5° , respectively. These results seem to provide a very strong case for the argument that CEX collision dynamics, while it only has a minor effect on the CEX-ion density at any point, plays a very important role in determining the sputtering rate of surfaces within the vicinity of the thruster. Other models, which assume all CEX ions emerge from collisions with zero initial energy ($\theta^+ = 90^\circ$), do not account for the dynamics of these collisions.

We must keep in mind the role that the sputter yield plays in these calculations. The results obtained in our one-beamlet example are dependent on the sensitivity of the sputter yield to CEX-ion energy. The data we used to obtain the sputter yield was from measurements made from xenon colliding with molybdenum. While previous ion engine grids have been made using molybdenum, current designs frequently use carbon-fiber material, which is much more resistant to sputtering. Additionally, since we are looking at locations surrounding the engine, and not the grid surface itself, there are many other materials which may be used to construct different spacecraft components, such as solar arrays, which are of concern to those designing the craft. All these different materials may be more- or less-sensitive to sputtering overall. More importantly, however, is the sensitivity of the sputtering to the energy of the impinging ions. Materials with sputter yields that do not have such a dramatic decline in sputtering with decreasing energy, compared to molybdenum, may not have the same results as found here: the low-energy ions may not only dominate the density, but

the sputtering as well.

It took approximately 30 minutes on a modern desktop computer to do the entire computation required to obtain the data contained in Figure 4.30. The large majority of this time was spent executing the root-finding algorithm which determines the scattering-angle solutions. This execution time is impractical, for, to obtain the final expected sputtering rate at a specific point around any particular grid, the computations shown in this example must be repeated for all of the nearly 15,000 holes. Some savings in time could be made by both reducing the number of mesh points ($J = 441$ in this example), and reducing the number of shells computed in each beamlet (some beamlets may also not require as many shells as others, due to a small contribution). Additionally, since the model is based on the superposition of individual beamlets, the model is amenable to parallel computing methods which, given the required computing resources, could significantly decrease the time required.

All of these time-saving methods make little difference in an optimization problem, as we are attempting to do. Incorporating this model into an optimization routine requires computing the sputtering rate for multiple grids, not only the multiple holes of one grid. In order to implement an optimization routine using this model, we must reduce the computational time required. In Chapter 5 we discuss some time-reducing simplifications made.

4.8 Chapter Summary

In this chapter we developed the means to compute the remaining quantities required in order to evaluate the CEX-ion flux and sputtering integrals derived in Chapter 2. The primary-ion flux is modeled as mono-energetic ions originating from point emission sources located behind each grid hole. Superposition of the density contributions from each hole yields the total main-beam ion density at any individual point in space. The barometric law is assumed to model the plume potential, from which we obtain the electric field, which relates the potential to the logarithm of the total ion density. For the sole purpose of computing the potential, an unchanging CEX-ion density map is assumed, and was obtained from previous simulations of the NSTAR plume. Individual ion

trajectories through the plume are calculated using a time-adaptive velocity-Verlet algorithm.

Both the charge-exchange differential cross-section and the sputter yield were obtained from physical measurements, which were parameterized by applying simple curve-fits. The differential cross-section data was from scattering measurements of xenon ions, with an energy of 1100 eV, colliding with stationary (thermal) neutral xenon atoms. The data for the sputter yield was obtained from measurements of xenon ions impinging on a molybdenum surface.

A two-dimensional problem was analyzed from which information was obtained that assists both in developing the model, as well as in interpreting results from the full three-dimensional problem. It was found that, from any small scattering volume, there may be multiple scattering angle solutions, which result in CEX ions passing through the specified target point, associated with any primary ion velocity vector. The presence of multiple solutions imply that there are certain “turn around” angles where the streamtube of ions scattered at these angles gets focussed. Scattering-angle solutions that approach one of these “turn around” angles result in a very large flux through the target point, due to the focussing effect, $dA/d\Omega \rightarrow 0$. A Gauss-Newton root-finding algorithm was developed in order to locate the scattering-angle solutions for any primary-ion velocity vector passing through a specified point in space.

In order to facilitate numerical integration of the ion flux and sputtering rate equations, the idea of a beamlet shell and mesh were introduced. As an implementation example, one beamlet shell within an NSTAR beamlet was modeled. It was demonstrated how all the required quantities are computed for mesh points in the beamlet shell, and from which the numerical integral was computed. An example was also shown of how the sputtering rate contribution from one beamlet is obtained by integration over multiple beamlet shell radii. The vast majority of CEX ions were found to have energies comparable to the potential difference between the scattering point and the target point $\Delta\Phi$. This is in agreement with the assumption made in other models: most CEX ions receive very little energy from the charge-exchange collision process. Though the calculated CEX-ion density was found to be within the range of values computed by other models, it was determined that the current model inadequately treats the lowest-energy ions. Since the low-energy ions are the most

populous, density calculations from this model are unreliable.

Despite the inadequacies of the model in its treatment of low-energy ions, it was found that the majority of the sputtering is due to collisions involving CEX ions that have significantly more energy than $\Delta\Phi$. This is a direct result of the sensitivity of the sputter yield to energy. Since the sputtering contribution from the low-energy ions was found to be so small, it was determined that the errors in computing the number of these ions have little impact on the computed sputtering rate. It was found that the highest-energy CEX ions originate from a region very close to the grid surface. These ions are the products of ion-atom encounters involving collision angles smaller than 90° , and were found to have values in the low 80° s or lower. This finding is in disagreement with other models, where the assumption is that collision dynamics play a minor role in sputtering, due to the vast majority of low-energy ions.

Implementation of the model, as presented in this chapter, was found to be a formidable task, due to the large amount of time required. If the computation was to be done for only one grid, parallel computing methods could be used to reduce the required time to a reasonable amount. However, incorporating the model into an optimization routine, for which computation of multiple grids would be required, is impractical. We compare, in Chapter 5, the results obtained using some simplifications with those obtained using the full computational description discussed in this chapter.

Chapter 5

Approximation Technique

In order to obtain the complete energy distribution at any particular point due to CEX ions, the computation described in Chapter 4 must be done for every hole in the mesh modeling the grid. The time required to do this computation for all of the approximately 15,000 holes is impractical, and thus an approximating technique was sought to reduce the amount of time to compute the energy distribution, yet still yield approximately the same results.

5.1 LOS Approximation Method

5.1.1 Description of the Approximation

One of the simplest approximations is to assume that the plume potential has no effect on the trajectories of the CEX ions; i.e., upon scattering, an ion will follow an asymptotically straight, line-of-sight (LOS) trajectory from the scattering point. This approximation makes computing the scattering angle required for any ion to scatter to the target point relatively simple: it is the angle between the primary-ion velocity vector, and the vector from the scattering point to the target point,

$$\cos \theta_{\text{LOS}} = \frac{\hat{\mathbf{u}} \cdot (\tilde{\mathbf{x}} - \mathbf{x})}{|\tilde{\mathbf{x}} - \mathbf{x}|}. \quad (5.1)$$

This is significantly faster to compute than integrating the equations of motion! Additionally, as discussed in the previous chapter, an ensemble of such trajectories will have a streamtube area expansion equal to R_s^2 ; the expansion coefficient defined in Equation 4.51 has a value of unity

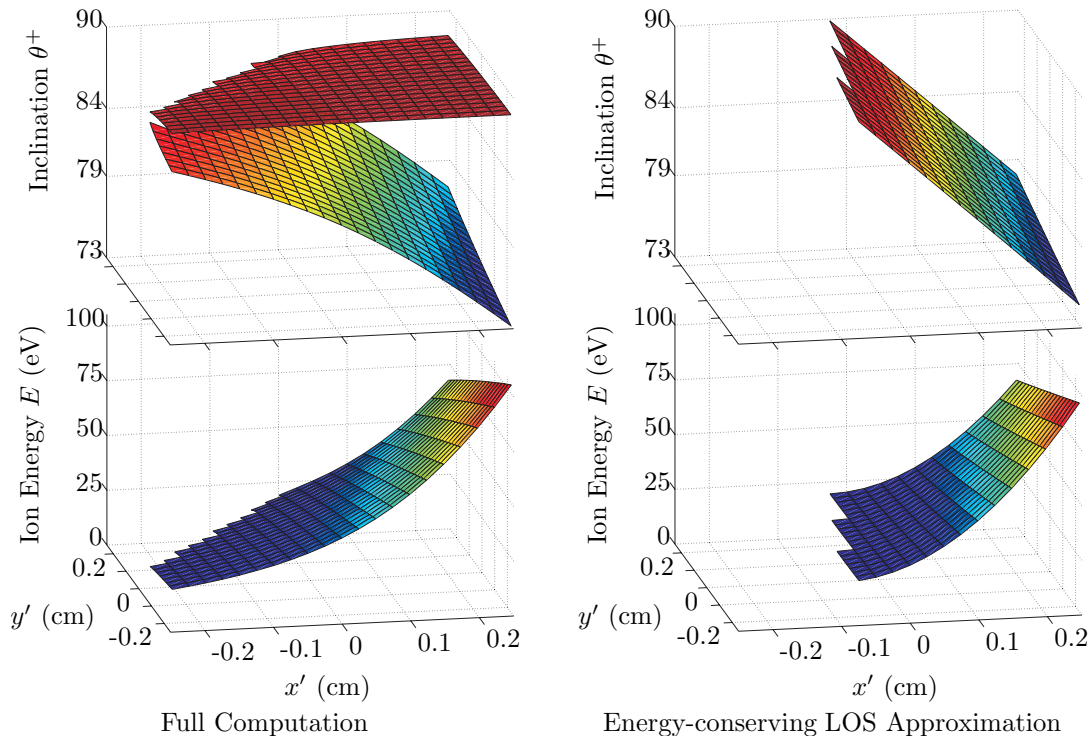


Figure 5.1: Beamlet shell mesh scattering solution quantities: LOS approximation method. The figures in the left column show the scattering angle solutions and ion energies of the “high-energy” solution branch (lower), from points in one beamlet shell computed using the full-trajectory method (from Figure 4.24). Only mesh points that contribute to the CEX-ion distribution at the target point are shown ($D_{\min} = 0$). The right column of figures shows the same properties computed using the energy-conserving LOS scattering approximation. Only mesh points with physically possible scattering angles ($\theta_{\text{LOS}} \leq 90^\circ$) are shown.

everywhere.

A different approximation that can improve on the above, that is also relatively simple to compute, is to enforce conservation of energy for each particle. In general, there is a potential drop between any scattering center located in the main beam and the target point, which results in the scattered ion having more kinetic energy (and velocity) at the target point. In this approximation, Equation 2.18 is still satisfied:

$$E = E_0 \cos^2 \theta_{\text{LOS}} - \Delta\Phi. \quad (5.2)$$

A comparison of some of the beamlet-shell scattering properties found through full computation, and the energy-conserving LOS assumptions, are shown in Figure 5.1. The top figure on the left side shows both scattering-angle solution branches found through the full trajectory computation

(see Figure 4.24). Those points in the beamlet shell for which there is no contributing solution have been removed. Immediately below this figure is the corresponding energy of each ion upon arrival at the target point (also reproduced from Figure 4.24). Only the energy of those ions scattered from the “high-energy” branch (lower) are shown. The top figure on the right side shows the scattering angle found simply based on the LOS assumption. Using the full computation method of Chapter 4, an ion scattered from a point in the beamlet shell was determined to contribute to the CEX-ion distribution at the target point if the scattered ion passed through the target point (i.e., $D_{\min} = 0$). The LOS method has no way to determine the accuracy of the assumed scattering angle θ_{LOS} , nor how close any trajectory scattered at such an angle actually comes within the vicinity of the target point, if it were to actually pass through the electric field. Under the LOS-scattering assumption, the only means by which to decide whether a particle contributes to the CEX-ion distribution at the target point is by whether the angle is physically possible. Therefore for LOS scattered ions, only those scattered at angles less than the physical limit of 90° are shown and considered to have trajectories passing through the target point. The lower-right plot of Figure 5.1 shows the energy the particle has upon arriving at the target point, if energy conservation is enforced (see Equation 5.2).

Significant differences and similarities can be found between the inclination angles computed using the two methods. The first significant difference between the two methods is the simple fact that the LOS method only yields, at most, one solution whereas we showed earlier that the full trajectory analysis yields, in general, multiple solutions. Comparison of the scattering angles shows that the LOS trajectories are similar to the lower branch of scattering-angle solutions, corresponding to the ions scattered with more energy than those from the upper branch. These “high-energy” ions are less susceptible to the effects of the plume potential, than those ions scattered from the upper branch, and thus have straighter trajectories, which are more similar in nature to the trajectories assumed in the LOS approximation. The contributing area of the beamlet shell to the ion distribution at the target point is smaller for the LOS method than for the full-trajectory analysis method.

Though it may be difficult to tell from the figure, the LOS scattering-angle solution is greater than the angle computed using the full-trajectory analysis at every point in the beamlet shell. Insight

into the reason for this (and exceptions) can be obtained by examining the situation presented in Figure 4.2. In this case, the LOS trajectory is represented by Path 1, and the ion trajectory computed using the full analysis is represented by Path 3. As we saw earlier in Figure 4.13, the effect of the plume potential on the scattered ions generally tends to deflect the ions back towards the engine or spacecraft. Thus, an ion scattered at the LOS angle θ_{LOS} will take a trajectory passing further upstream if the electric field is considered (Path 2) than if it is not (Path 1). The ion for which the effect of the electric field is considered (in the full trajectory analysis) must scatter at an angle smaller than the LOS angle in order to pass through the same target point (compare Paths 1 and 3). Of course, also demonstrated by Figures 4.13 and 4.14, is that this is only the case for ions scattered at angles less than the critical “turn-around” scattering angle, where the ions begin to drift downstream due to lack of sufficient energy or momentum to overcome the increasing relative impact of the electric field inside the main beam. This suggests that an even more accurate approximation would include not only a correction to the ion energy (through $\Delta\Phi$), but also a correction to the LOS scattering angles, to account for the deflection of the trajectories due to the plume potential.

There are different possible methods one could use to implement this correction. The simplest would be to add or subtract a constant value to the LOS angles, in order to make the computed angle and LOS angle match at one point in the shell; knowledge of only one angle, computed using the full-trajectory analysis, in each shell is required. Another method could, in addition to matching the scattering angle at one point in the shell, also match the gradient of the surface at one point; a minimum of three angles, again computed using the full-trajectory analysis, would be required for this procedure. Progressively more sophisticated approximations could be made such as to conform the shape of the beamlet shell LOS scattering-angle surface (upper-right plot of Figure 5.1) function closer to that of the surface obtained from full computation (lower branch, upper-left plot of Figure 5.1). Such approximations would also require increasingly more information about the shape of the surface. Due to the time required to compute each correct scattering angle through the full-trajectory analysis, we choose to implement the simplest method here — adding or subtracting a constant value to the LOS solution angles.

How to choose the position in the shell at which to make the two beamlet scattering-angle solution surfaces match is arbitrary, and depends on which region of the surface the most accuracy is desired. The results from the complete computation outlined in the previous chapter demonstrated how the largest amount of sputtering is expected from the energetic ions. Since we are concerned about sputtering for this work, it was decided to match the maximum ion energy for each beamlet shell. Since we have already assumed to implement energy conservation through inclusion of $\Delta\Phi$, matching the maximum ion energy is equivalent to matching the smallest scattering angle.

Beamlet-shell functions like those shown in Figure 4.24 were computed for various beamlet-shell radii, and for holes at different locations on the NSTAR grid model. In all those computed, it was found that the scattered ion with the most energy from any particular beamlet shell originated from the beamlet-shell edge nearest to the target point. For example, the highest-energy ions scattering from the beamlet shell in Figure 4.24 originate from the edge at $x' \approx 0.23$ cm, and the target point is located in the vicinity of $x' \approx 57$ cm. We are confident that this is generally the case, and thus implementation of matching the smallest scattering angle only requires computation of the scattering angle using the full-trajectory analysis at points along that edge. Of the points computed, the minimum scattering-angle solution is found, and the minimum LOS scattering angle solution is made to match:

$$\theta_{\text{LOS}}^* = \theta_{\text{LOS}} - \theta_{\text{LOS},\text{min}} + \theta_{\text{min}}^+ \quad (5.3)$$

While the minimum-scattering-angle-corrected, energy-conserving LOS angles provide an approximation to the lower branch of actual scattering-angle solutions, an approximation to the second branch is still missing. The previous chapter demonstrated that the ions coming from the second scattering branch typically scatter at angles close to 90° , and so have very little energy. Since it was found that the low-energy particles contribute very little to the sputtering, it was decided to neglect the second scattering branch in this approximation. Based on the analysis of Chapter 4, omission of this branch is justified for purposes of computing sputtering rates; however, this approximation would be inappropriate for computing the CEX-ion density at the target point. The majority of the the density contribution originates from the low-energy scattering events characteristic of the upper

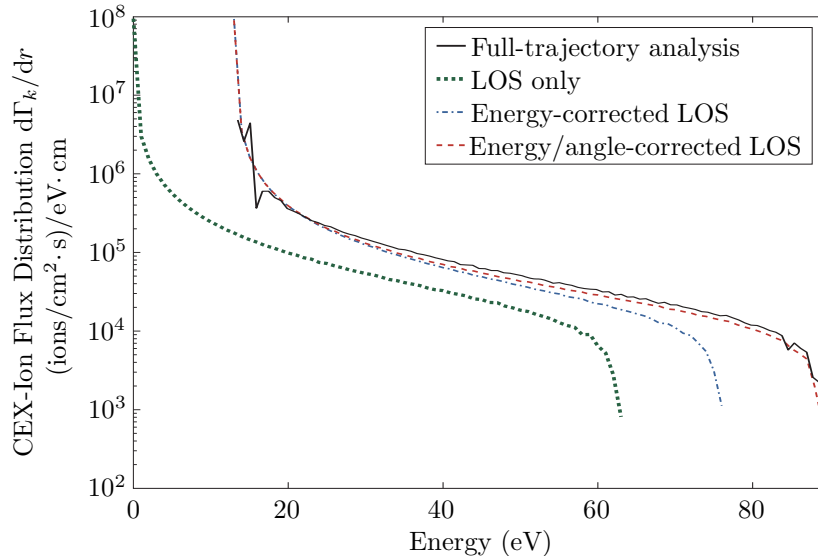


Figure 5.2: Beamlet-shell contribution to the CEX-flux distribution: Approximations. Contributions from the same beamlet shell from the example in Section 4.7.2 were computed using different simplifying approximations. The line-of-sight (LOS) only approximation assumes the CEX ions scatter directly to the target point and does not take account of the change in potential $\Delta\Phi$. The energy-corrected LOS approximation also assumes the CEX ions scatter directly to the target point, but accounting for the change in potential between the scattering and target points is also made. The energy- and angle-corrected LOS approximation adjusts all LOS scattering angles such that the maximum ion energy matches that from the distribution obtained by full trajectory analysis (from Figure 4.26).

scattering angle solution branch.

5.1.2 Comparison of Results with the Full Trajectory Analysis

To judge the appropriateness of the assumptions, distributions obtained using only LOS trajectories, LOS trajectories with energy conservation, and angle-corrected, energy-conserving LOS trajectories were obtained for the same beamlet shell used in the example from Chapter 4. In Figure 5.2, the CEX-ion flux distribution computed using the full-trajectory analysis (see Figure 4.26) is compared with the distributions obtained using these different approximations.

The distribution obtained using only LOS trajectories (dotted line) is seen to be very different from the actual distribution obtained from the complete trajectory computation (solid line). The distribution obtained by enforcing particle energy conservation (dash-dotted line) has approximately the same minimum energy as the actual distribution, however the maximum energy of the approxi-

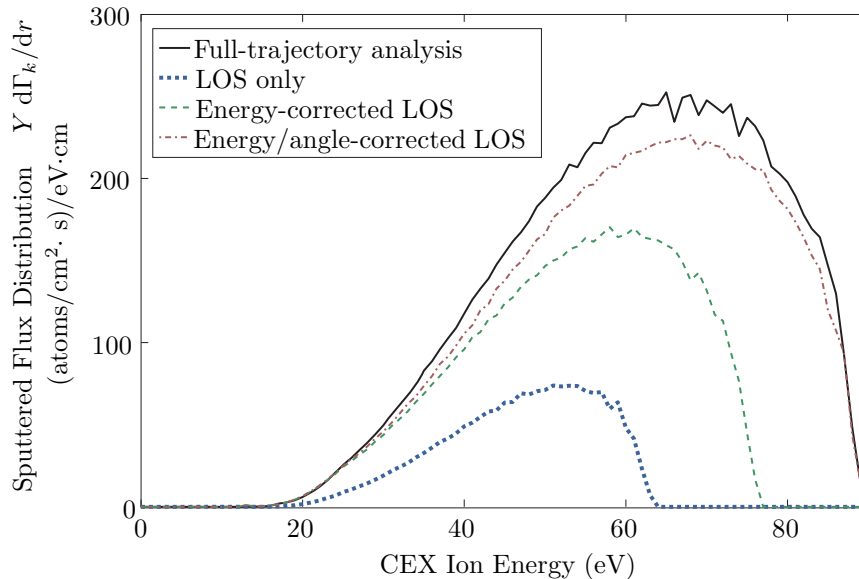


Figure 5.3: Sputtering-rate-distribution contribution comparison. Contributions, $Y(E) d\Gamma_k/dr$, from the same beamlet shell from the example in Section 4.7.2 were computed using different simplifying approximations. The expected sputtering is obtained from the flux distributions in Figure 5.2.

mate distribution is significantly less. When the scattering angle is corrected to match the maximum energy, the approximation yields a distribution (dashed line) very similar to the actual distribution. At the lowest energies, we can do little in the way of comparison, for as we found in our analysis in Chapter 4, even the complete-trajectory computation method is inaccurate at these energies. Since the majority of the CEX ions populate the low-energy region, as anticipated, integration of each of these functions yields vastly different results for the total density contribution from this particular beamlet shell.

Our ultimate goal is to predict the amount of sputtering expected. For each distribution resulting from the different approximations, the expected sputtered flux from ions originating from this shell is shown in Figure 5.3. As we found for the ion flux distribution, the sputtering rate expected using only LOS trajectories is very different from the rate predicted by the complete trajectory computation. Even enforcing energy conservation is insufficient to produce a distribution similar to the full-trajectory analysis. On the other hand, the sputtering rate distribution obtained using both the energy and scattering-angle corrections to the LOS approximation is very similar to the distribution computed using complete-trajectory analysis, however it still predicts a lower rate.

To obtain a better idea of how well the energy- and angle-corrected LOS approximation does in duplicating the results obtained using the full-trajectory analysis, the sputtering rate contributions from three entire NSTAR beamlets were computed using both methods, and compared. The results for each of the beamlets are shown in Figures 5.4 through 5.6. The contributions to the CEX-ion flux distribution from each beamlet are shown at the top of each figure. The inset depicts a representative inclination scattering-angle solution surface for one of the shells in the beamlet. The lower-left plot in each figure shows the contribution to the flux distribution (left axis), integrated over the beamlet-shell radii, and the sputtered flux distribution (right axis), also integrated over the beamlet-shell radii. The solid lines correspond to the solutions found based on the full-trajectory analysis and the dashed lines correspond to the solutions found using the energy- and angle-corrected LOS approximation. The lower-right plot in each figure shows the contribution to the sputtering rate (left axis), integrated over CEX-ion energy, as a function of the beamlet-shell radii, and the cumulative integral of the sputtering rate (right axis), integrated over the beamlet-shell radii. Again, the solid lines correspond to the solutions found based on the full-trajectory analysis, and the dashed lines correspond to the solutions found using the energy- and angle-corrected LOS approximation.

The total contributions to the sputter rate, Υ_k , due to the approximating method in the first and second examples shown (Figures 5.4 and 5.5) are less than that predicted using the full-trajectory analysis by approximately 10%. The beamlet in the first example originated from the hole located at $(x, y)_k = (-0.111, 5.96)$ cm, which is nearly on the axis transverse to the axis on which the target point was located ($S(\tilde{\mathbf{x}}) = (60, 0, 3)$), and at approximately a third of the grid radius from the center of the grid ($R_g = 15$ cm). The beamlet in the second example originated from the hole located at $(x, y)_k = (5.994, 0)$ cm, which is on the same axis as the target point, and also approximately a third of the grid radius from the center of the grid.

It is interesting to note from the second example the presence of the “valley” in the CEX-ion flux distribution at energies around 30 eV for shell radii less than approximately 4 cm. As the shell radii increase, the valley disappears, indicating a merging of two separate populations (“high”- and “low”-energy). The reason for this is apparent from the scattering-angle solutions shown in the

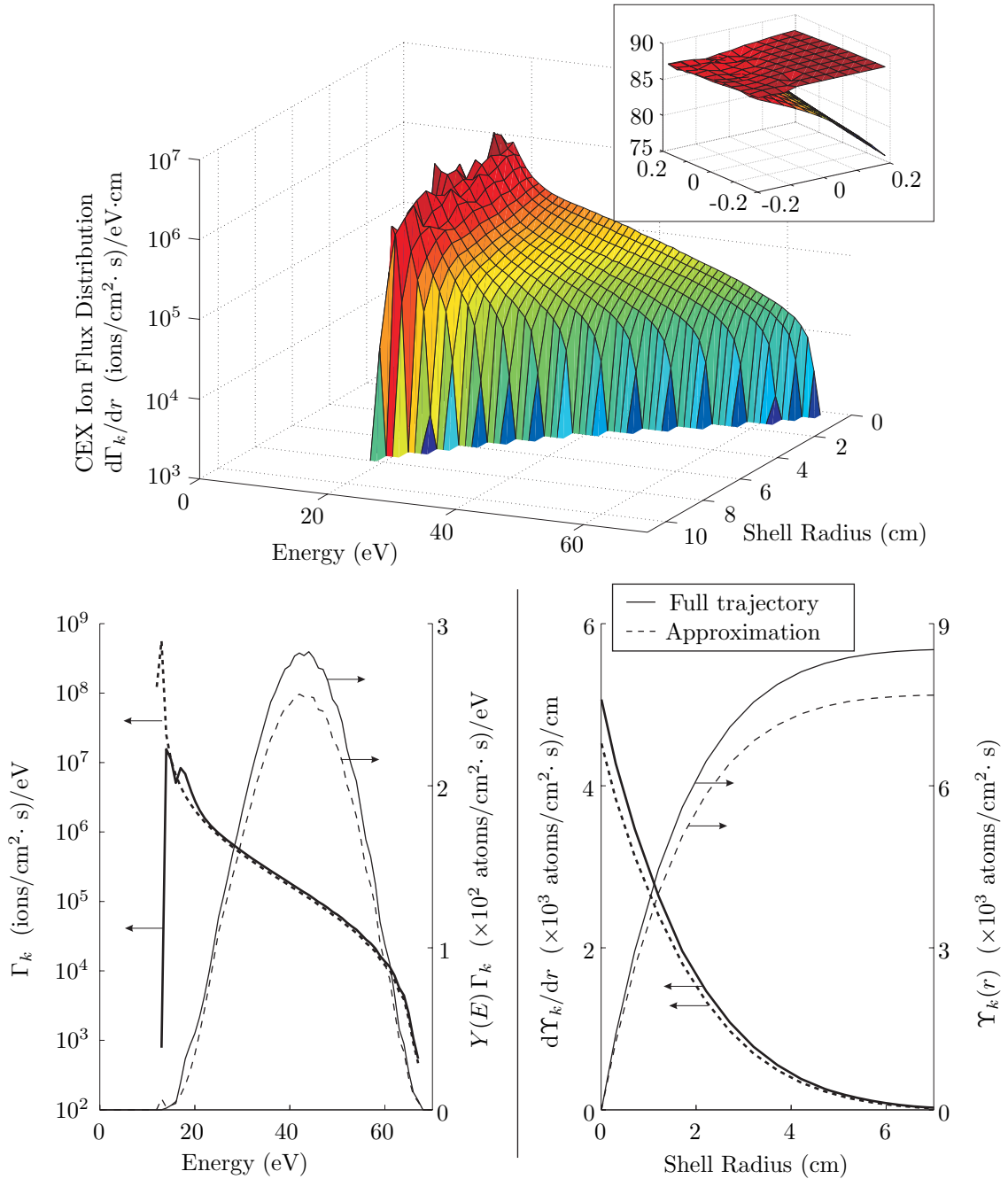


Figure 5.4: Full-beamlet approximation comparison: Hole $(x, y)_k = (-0.111, 5.96)$ cm. **Top:** The contribution to the CEX-ion energy distribution, as a function of energy and beamlet shell radius, computed using the full-trajectory analysis. The inset displays a characteristic inclination scattering-angle solution surface. **Lower-left:** The total beamlet contribution to the (1) CEX-ion energy distribution (left axis), integrated over beamlet-shell radii, and (2) sputtering rate (right axis), as a function of CEX-ion energy. **Lower-right:** The total beamlet contribution to the sputtering rate (1) as a function of beamlet-shell radius (left axis), and (2) integrated (cumulative) over beamlet-shell radius (right axis). Solid lines indicate results obtained using the full-trajectory analysis. Dashed lines indicate results obtained using the energy- and angle-corrected LOS approximation.

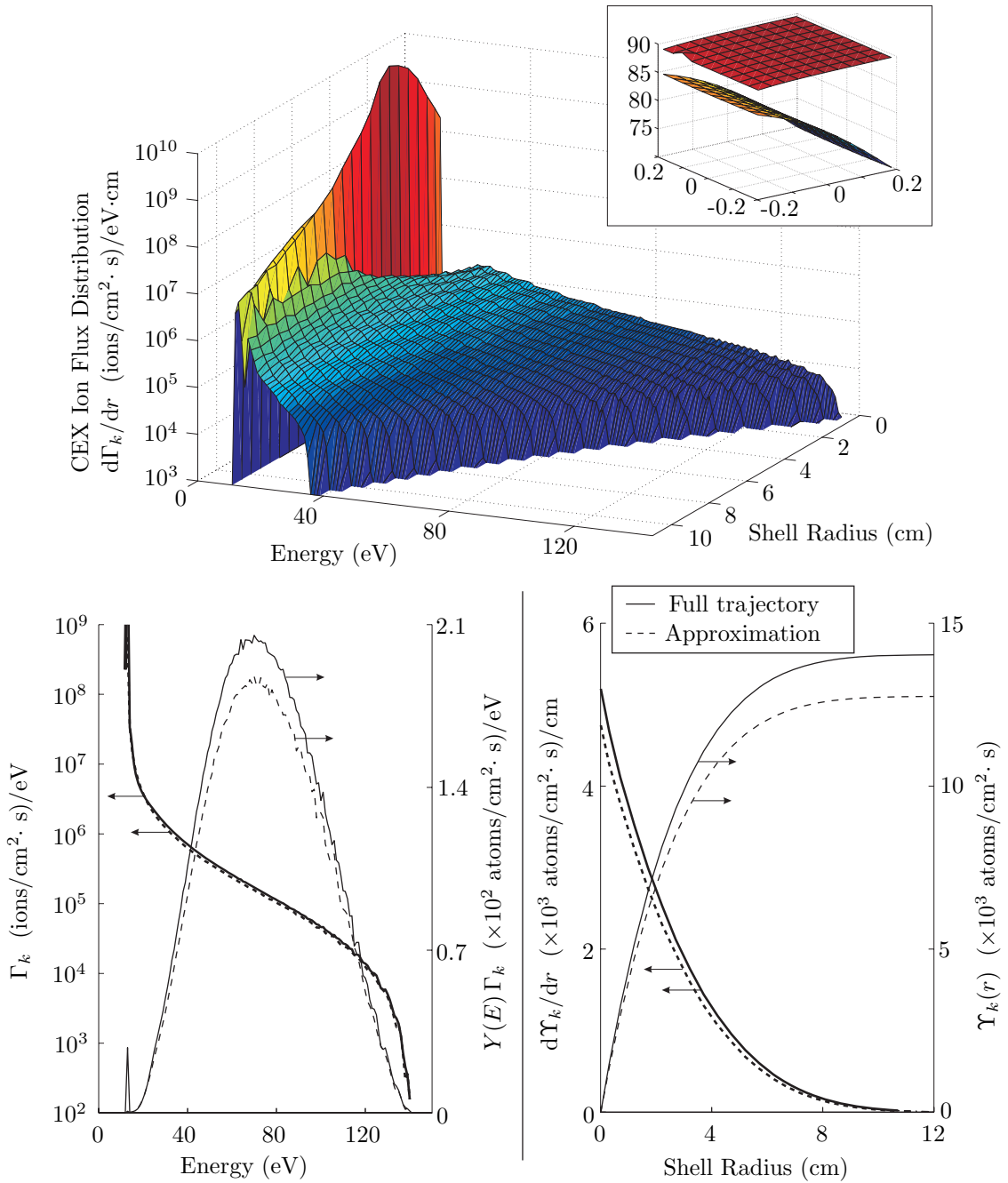


Figure 5.5: Full-beamlet approximation comparison: Hole $(x, y)_k = (5.994, 0)$ cm. **Top:** The contribution to the CEX-ion energy distribution, as a function of energy and beamlet shell radius, computed using the full-trajectory analysis. The inset displays a characteristic inclination scattering-angle solution surface. **Lower-left:** The total beamlet contribution to the (1) CEX-ion energy distribution (left axis), integrated over beamlet-shell radii, and (2) sputtering rate (right axis), as a function of CEX-ion energy. **Lower-right:** The total beamlet contribution to the sputtering rate (1) as a function of beamlet-shell radius (left axis), and (2) integrated (cumulative) over beamlet-shell radius (right axis). Solid lines indicate results obtained using the full-trajectory analysis. Dashed lines indicate results obtained using the energy- and angle-corrected LOS approximation.

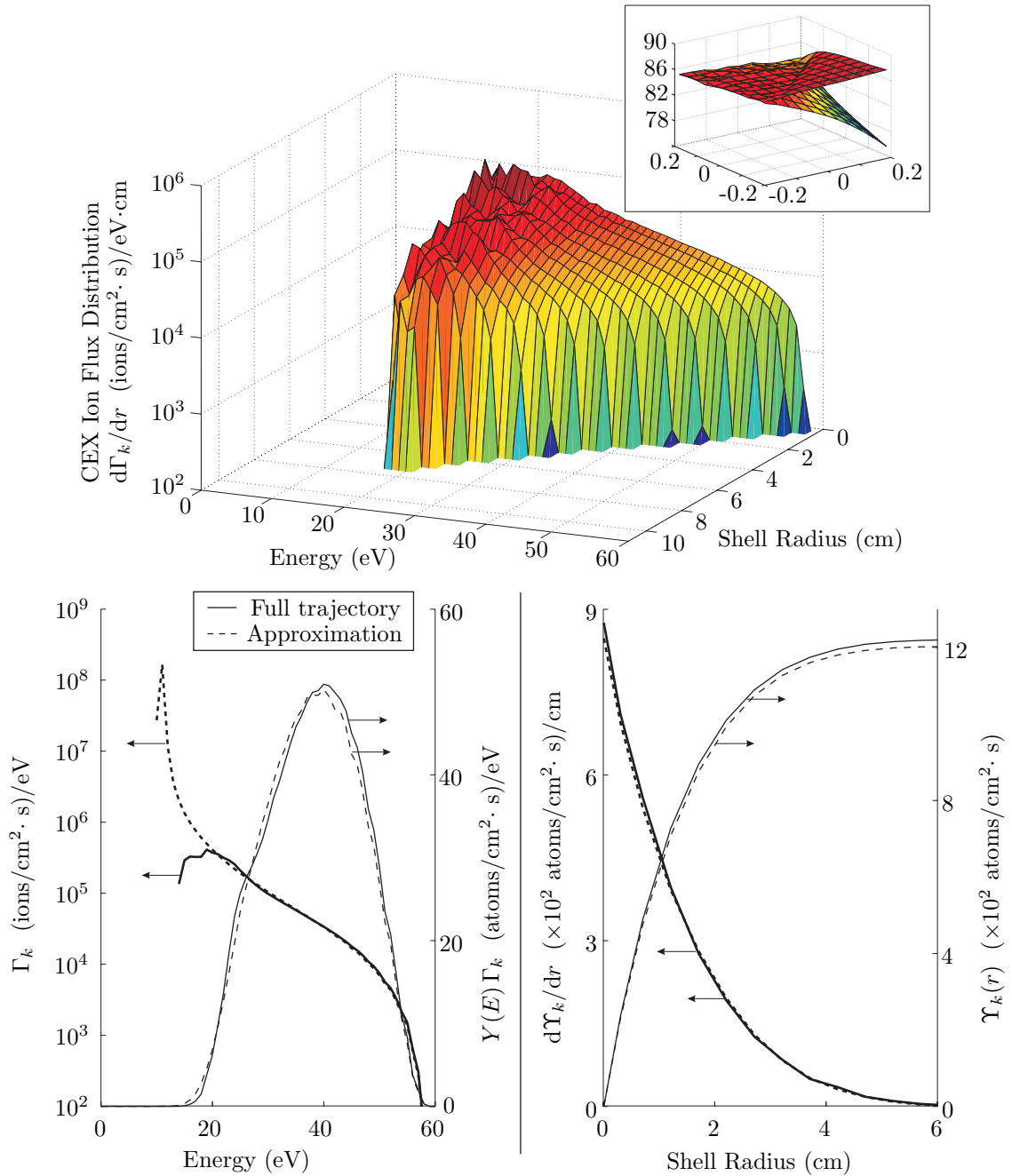


Figure 5.6: Full-beamlet approximation comparison: Hole $(x, y)_k = (0, 11.92)$ cm. **Top:** The contribution to the CEX-ion energy distribution, as a function of energy and beamlet shell radius, computed using the full-trajectory analysis. The inset displays a characteristic inclination scattering-angle solution surface. **Lower-left:** The total beamlet contribution to the (1) CEX-ion energy distribution (left axis), integrated over beamlet-shell radii, and (2) sputtering rate (right axis), as a function of CEX-ion energy. **Lower-right:** The total beamlet contribution to the sputtering rate (1) as a function of beamlet-shell radius (left axis), and (2) integrated (cumulative) over beamlet-shell radius (right axis). Solid lines indicate results obtained using the full-trajectory analysis. Dashed lines indicate results obtained using the energy- and angle-corrected LOS approximation.

top inset. For shell radii less than approximately 4 cm, all points within the beamlet shell have scattering events that contribute CEX ions to the target point. Additionally, all of the contributing points within the shell fall within Case II: there are multiple scattering-angle solutions. For these small shell radii, there are no points where Case III arises: a situation where the multiple solutions merge to a single solution and $d\tilde{A}/d\Omega \rightarrow 0$. Thus, there is a range of energy which no CEX ions originating from these beamlet shells close to the grid can have. The eventual merging of the two CEX-ion populations at larger beamlet shell radii is due to the scattering-angle solutions eventually becoming more like that shown previously in Figure 4.24 or the inset of Figure 5.4: the two solution branches merge at some point within the beamlet shell, and some points within the shell make no contribution to the CEX-ion population at the target point.

The total contribution to the sputter rate, Υ_k , due to the approximating method in the third example (Figure 5.6) is also less than that predicted using the full-trajectory analysis, but only by approximately 1%¹. The beamlet in this last example originated from the hole located at $(x, y)_k = (0, 11.92)$ cm, which is on the axis transverse to the axis on which the target point was located, and at nearly 80% of the grid radius from the center of the grid. Note that the contributions from each of the beamlets in these examples have values ranging over two orders of magnitude. The contribution from the third beamlet is an order of magnitude less than that from the first beamlet, which, in turn, is less by another order of magnitude than the contribution from the second beamlet.

The three examples shown indicate that the approximations made — LOS trajectories corrected for energy conservation with an adjustment to the scattering angles to match the maximum CEX-ion energy — give a good approximation of the results expected from the full-trajectory analysis, with an error within the range of 10%. These approximations reduce the computations required by limiting the number of scattering-angle solutions that need to be found to only a few mesh points, instead of all the mesh points within any beamlet shell. The computational time saved is exceptional,

¹The large difference in error between this example and the previous two (10%) is now thought to be attributed to the expected contributing area of the beamlet shell. Figure 5.2 indicates that the LOS approximation reduces the contributing area, since the gradient of the surface is larger for the LOS solutions than for those found using the full-trajectory analysis. If effort was made to match the surface gradients as well, it is expected that the contributing area from the LOS approximation would increase, and yield better agreement with the full analysis. In the case of this third example, the contributing area is already small (see inset of Figure 5.6), so it is expected the differing surface gradients do not have as much impact as for the others. We arrived at this line of thought after the work was completed, and therefore were not able to test it further.

since the majority of the computation during the full-trajectory analysis is spent on locating the scattering-angle solutions using the Gauss-Newton search algorithm of Section 4.6.

The pseudo-code outlining the procedure for adjusting the scattering-angle solutions is presented next. Section 5.2 addresses the case where the grid is not axisymmetric. In such cases, the computational time required can substantially increase, since the electric field cannot be expected to be axisymmetric either.

5.1.3 Pseudo-Code: Adjusting the Scattering Angle

The following pseudo-code outlines the procedure used to determine the adjustment made to the scattering-angle solution calculated using the line-of-sight approximation. The adjustment changes all LOS-angle solutions within a beamlet shell, such that the maximum ion energy is the same as that computed using the full-trajectory analysis detailed in Chapter 4. The code was implemented using Matlab.

1. Let \mathbf{y}'_k and $\tilde{\mathbf{x}}$ be the locations of the emission point of hole k and the target point, respectively.
2. Define the square beamlet scattering mesh with J scattering points, $\{\mathbf{x}_1 \dots \mathbf{x}_J\}$.
3. $j = 1$.
4. Find the radial emission primary ion velocity unit vector, $\hat{\mathbf{u}}_{k,j} = (\mathbf{x}_j - \mathbf{y}'_k) / \|\mathbf{x}_j - \mathbf{y}'_k\|$.
5. Compute the unit vector between the target point and scattering point, $\hat{\mathbf{R}}_j = (\tilde{\mathbf{x}} - \mathbf{x}_j) / \|\tilde{\mathbf{x}} - \mathbf{x}_j\|$.
6. Compute $\theta_{\text{LOS},k,j} = \cos(\hat{\mathbf{u}}_{k,j} \cdot \hat{\mathbf{R}}_j)$.
7. If $j < J$, $j = j + 1$, go to step 4; otherwise go to step 8.
8. Compute the required scattering angle for each of the scattering points at the corners and midpoint of the mesh edge located closest to the target point, $\theta_{1,2,3}^+$.
9. Find $\theta_{\text{LOS},\min} = \min\{\theta_{\text{LOS},k,j}\}$.
10. Find $\theta_{\min} = \min\{\theta_{1,2,3}^+\}$.

11. Compute $\Delta\theta = \theta_{\text{LOS,min}} - \theta_{\text{min}}$.
12. Output adjusted LOS scattering angles, $\theta_{\text{LOS},j}^* = \theta_{\text{LOS},j} - \Delta\theta$.

5.2 In the Case of Grid-Shape Asymmetry

In general, the spacecraft we intend to place an ion engine on is not cylindrically symmetric. Since there will be asymmetries in the shape of the craft, we can expect there will be certain regions around the engine that are more sensitive to sputtering than others. As a result, an optimum engine grid shape could, in all likelihood, be asymmetric also. Unlike the axisymmetric NSTAR grid shape, which has a corresponding axisymmetric plume potential (Figure 4.7), the plume obtained using the procedure outlined in the previous chapter will be asymmetric for any arbitrary grid shape. While the procedure for integrating the equations of motion change very little between a 2D-axisymmetric and 3D-asymmetric plume, obtaining a fully three-dimensional plume of sufficient resolution could be impractical; to complete an optimization calculation, a new plume is required to be computed at each new grid configuration from each iteration. It would be preferable if an approximating method could be found such that the need for finding the complete three dimensional potential is eliminated, but that still gives sufficiently accurate trajectories and results.

It was hypothesized that approximating the potential as axisymmetric, despite the asymmetry of the grid shape, could yield sufficiently correct results. A sensible candidate for the two-dimensional potential assumed to be axisymmetric would be the potential in the radial plane that the target point falls on. This hypothesis was tested using a highly asymmetric grid shape considered to be at the engineering limits of the asymmetry possible to construct. The shape of the grid was that of a “barrel vault” and is shown in Figure 5.7. The radius of curvature in the second principal axis is that of the NSTAR — 50.8 cm. The two-dimensional potentials occurring in the two radial planes along each of the principal axes are shown in Figure 5.8.

The contribution to the CEX-ion energy distribution at the target point (60,0,3) was computed for this grid shape using both a full asymmetric-3D plume potential as well as the axisymmetric

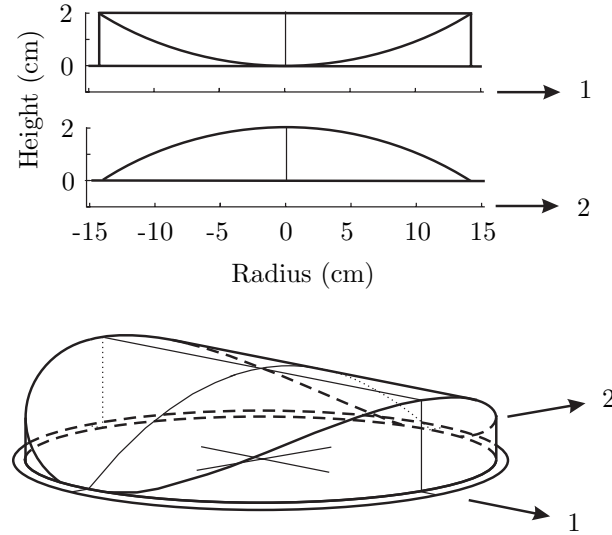


Figure 5.7: Barrel-vault grid shape. Shape chosen to represent an asymmetric grid. The radius of curvature in the direction of the second axis is the same as for NSTAR — 50.8 cm. For this example, Axis 1 corresponds to the x -axis. The target point is again located at $S(\vec{x}) = (60, 0, 3)$.

extension of the 2D potential that lies in the same plane as the target point and the grid axis ($x - z$ plane). For this comparison, the x -axis corresponded to the first principal axis and the y -axis corresponded to the second principal axis. For both cases, both the full-trajectory as well as the energy- and angle-corrected LOS methods were used. The resulting contributions from three different beamlets are shown in Figures 5.9 through 5.11. The estimated contributions from the 2D approximation is shown for both the full-trajectory analysis assuming a 2D potential, as well as for the LOS energy- and angle-corrected approximation. The contributions predicted using all three methods are similar for the first two beamlets. The approximations for the first beamlet under-estimate the sputtering rate contribution predicted using a full asymmetric plume by approximately 20% and 27%, for the 2D full-trajectory analysis and the LOS energy- and angle-corrected approximations, respectively. The maximum energy predicted by both the 2D and 3D plumes are approximately the same, at 72 eV and 75 eV, respectively.

For the second beamlet, the 2D full-trajectory approximation over-estimates the sputter rate contribution by approximately 11%, and the 2D energy- and angle-corrected approximation under-estimates the contribution by approximately 9%. The maximum energy predicted by both the 2D

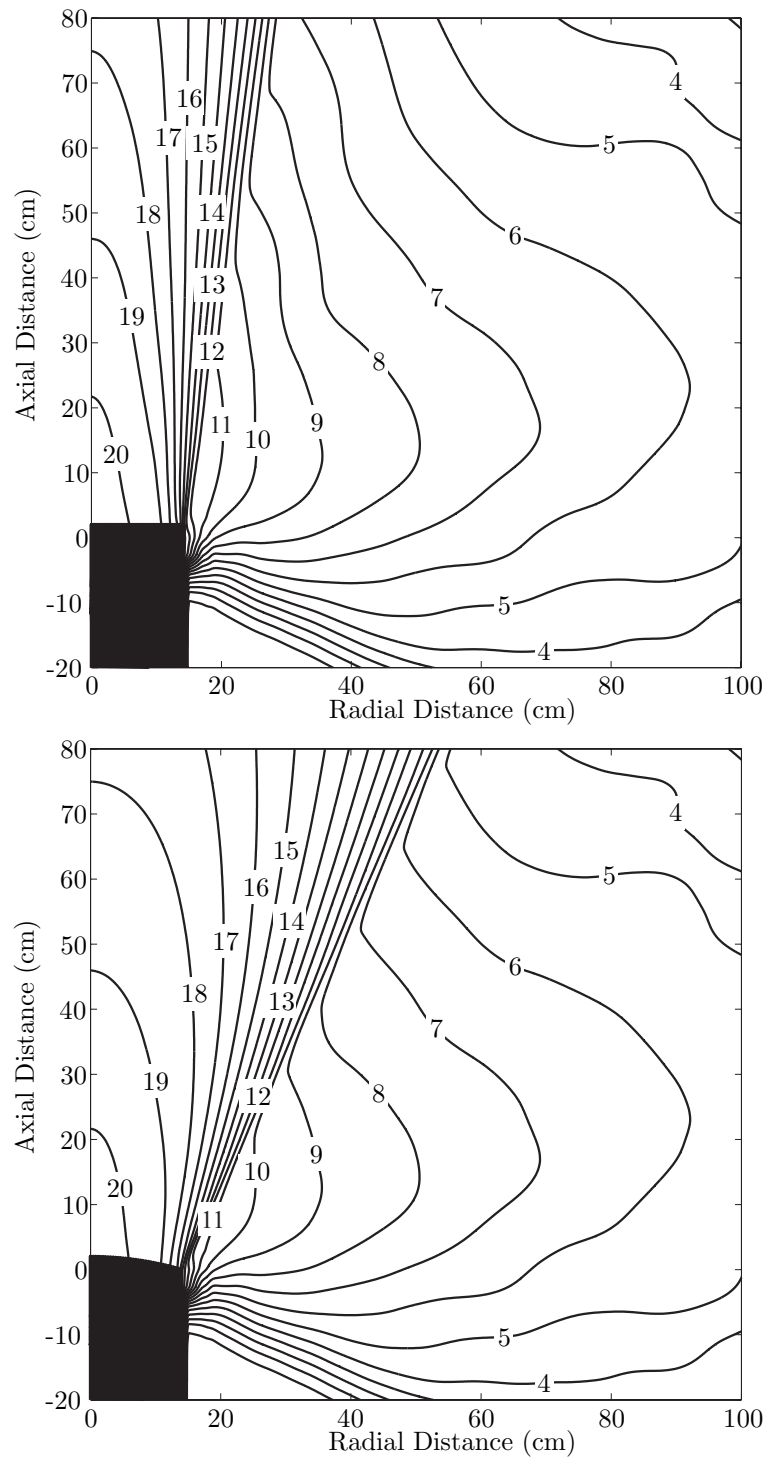


Figure 5.8: Barrel-vault plume potentials. Two examples of the asymmetry of the plume due to the shape of the barrel-vault grid. **Top figure:** Plume potential of Axis 1 from Figure 5.7. **Bottom figure:** Plume potential of Axis 2 from Figure 5.7.

and 3D plumes were identical at 69 eV. Note that though the hole from which this beamlet originates is located on the plane from which the 2D plume was obtained, the contributions are not the same. This is a result of the fact that the scattering centers located within the beamlet itself are not restricted to this same plane.

The 2D approximation was inadequate for estimating the contribution from the third beamlet shown in Figure 5.11. Though the 2D energy- and angle-corrected approximation yielded a result similar to the full-trajectory analysis using the 2D plume, both of these methods under-estimated the contribution by more than 75%. The maximum energy estimated by the 2D approximation was 45 eV, 10 eV less than the maximum energy predicted using the full 3D plume.

Though this analysis indicates that approximating an asymmetric plume by the symmetric extension of the 2D plume corresponding to the plane in which the target point is located is inaccurate, it must be considered that the total predicted sputtering rate contribution from the third beamlet is two orders of magnitude less than that from the first beamlet. Though the 2D approximation yields inaccurate values for the third beamlet, the error contribution is small. Though the 2D approximation is not an ideal approximation to make, we proceeded with using this approximation for ease of implementing the model into a grid shape optimization which we discuss further in Chapter 7.

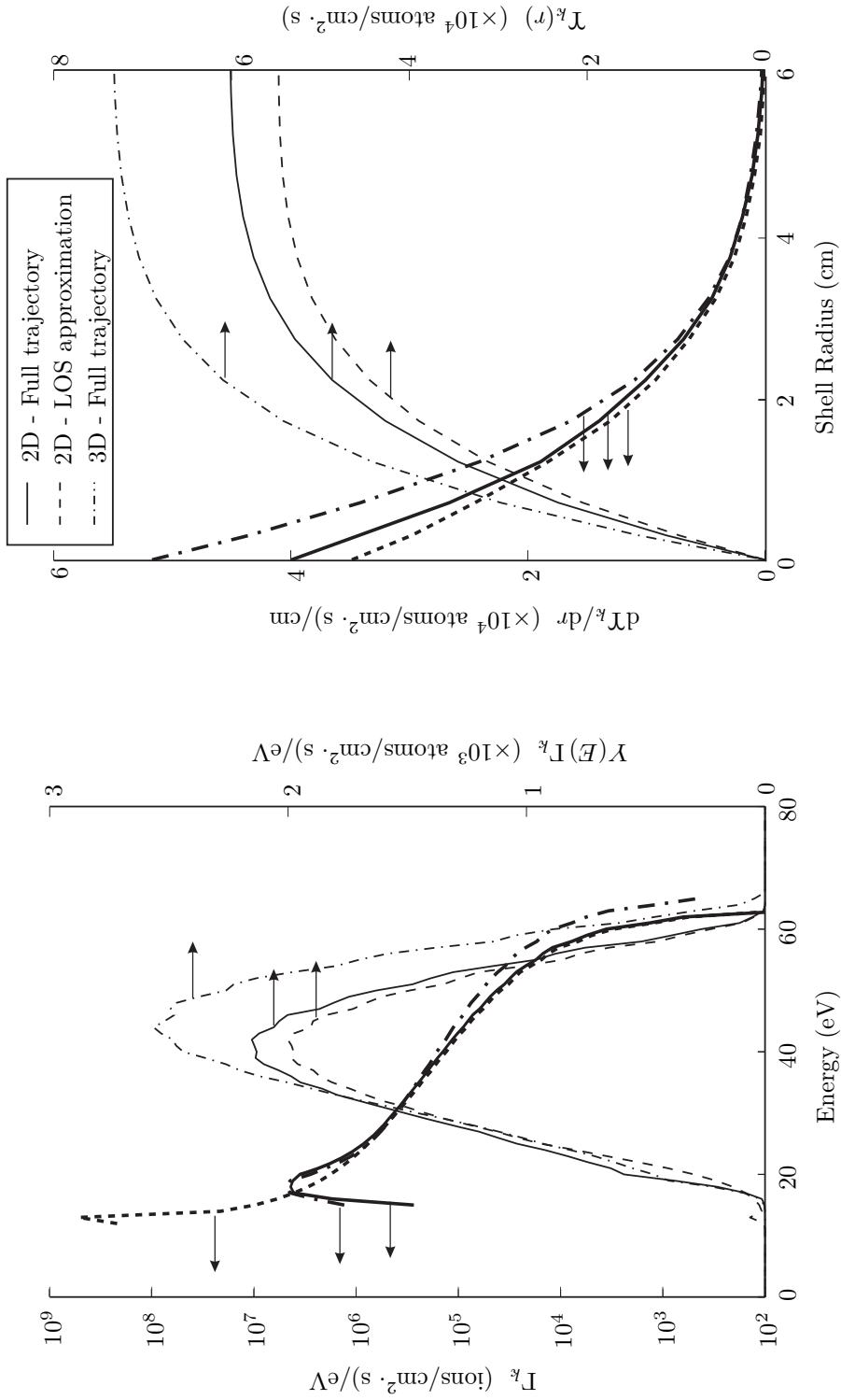


Figure 5.9: Full-beamlet 3D approximation comparison: Hole $(x, y)_k = (-0.111, 5.96)$. Left figure is the spatially integrated energy distribution (left axis) and energy-differentiated sputtering contribution (right axis). Right figure is the energy-integrated sputtering contribution (left axis) and cumulative integral over beamlet-shell radius of the sputtering contribution (right axis). The solid line indicates the correct computation using the full 3D potential to compute trajectories. The dashed line is the correct computation using the 2D-potential assumption. The dash-dot line is the energy- and angle-corrected LOS assumption using a 2D potential.

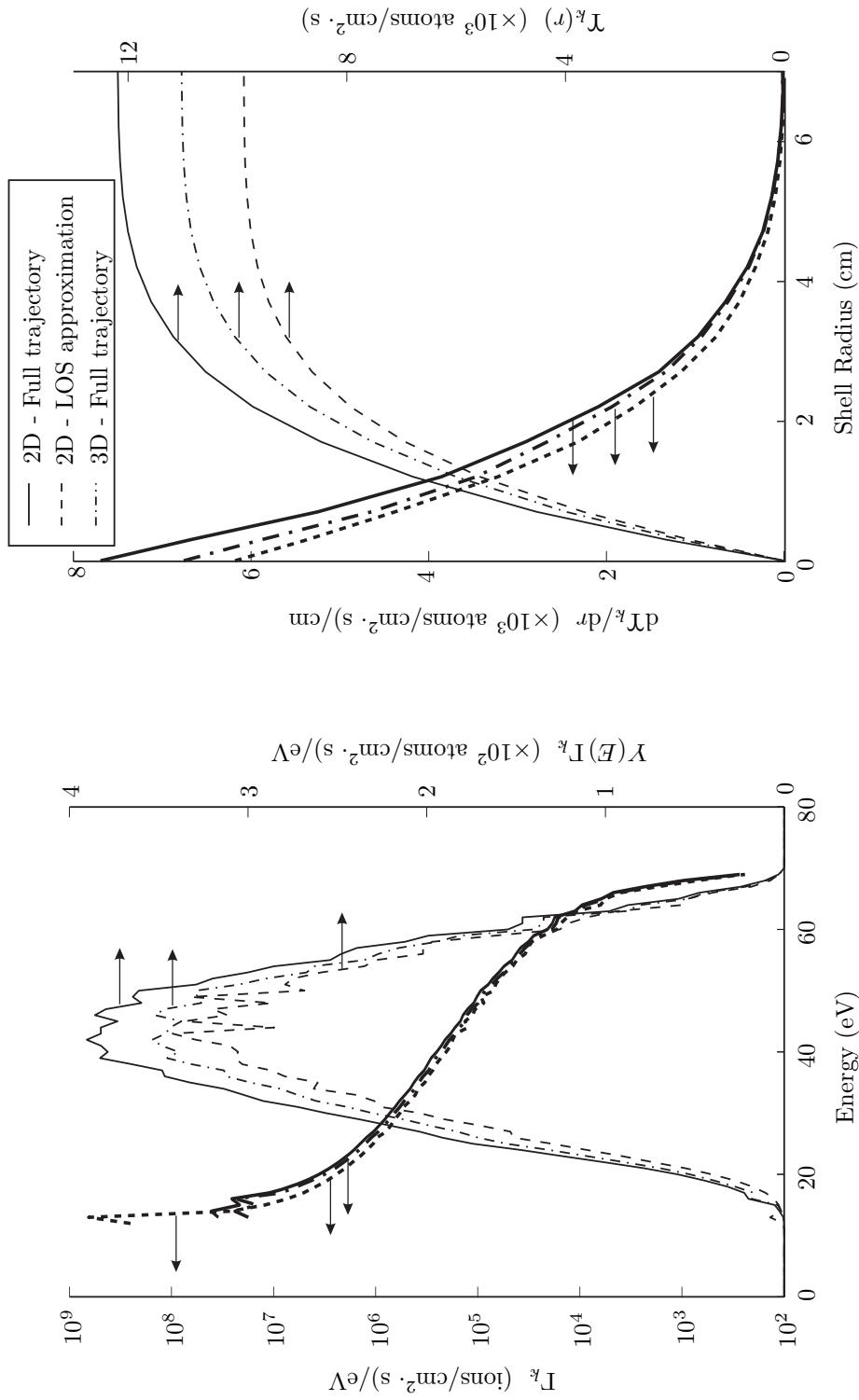


Figure 5.10: Full-beamlet 3D approximation comparison: Hole $(x, y)_k = (5.994, 0)$. Left figure is the spatially integrated energy distribution (left axis) and energy-differentiated sputtering contribution (right axis). Right figure is the energy-integrated sputtering contribution (left axis) and cumulative integral over beamlet-shell radius of the sputtering contribution (right axis). The solid line indicates the correct computation using the full 3D potential to compute trajectories. The dashed line is the correct computation using the 2D-potential assumption. The dash-dot line is the energy- and angle-corrected LOS assumption using a 2D potential.

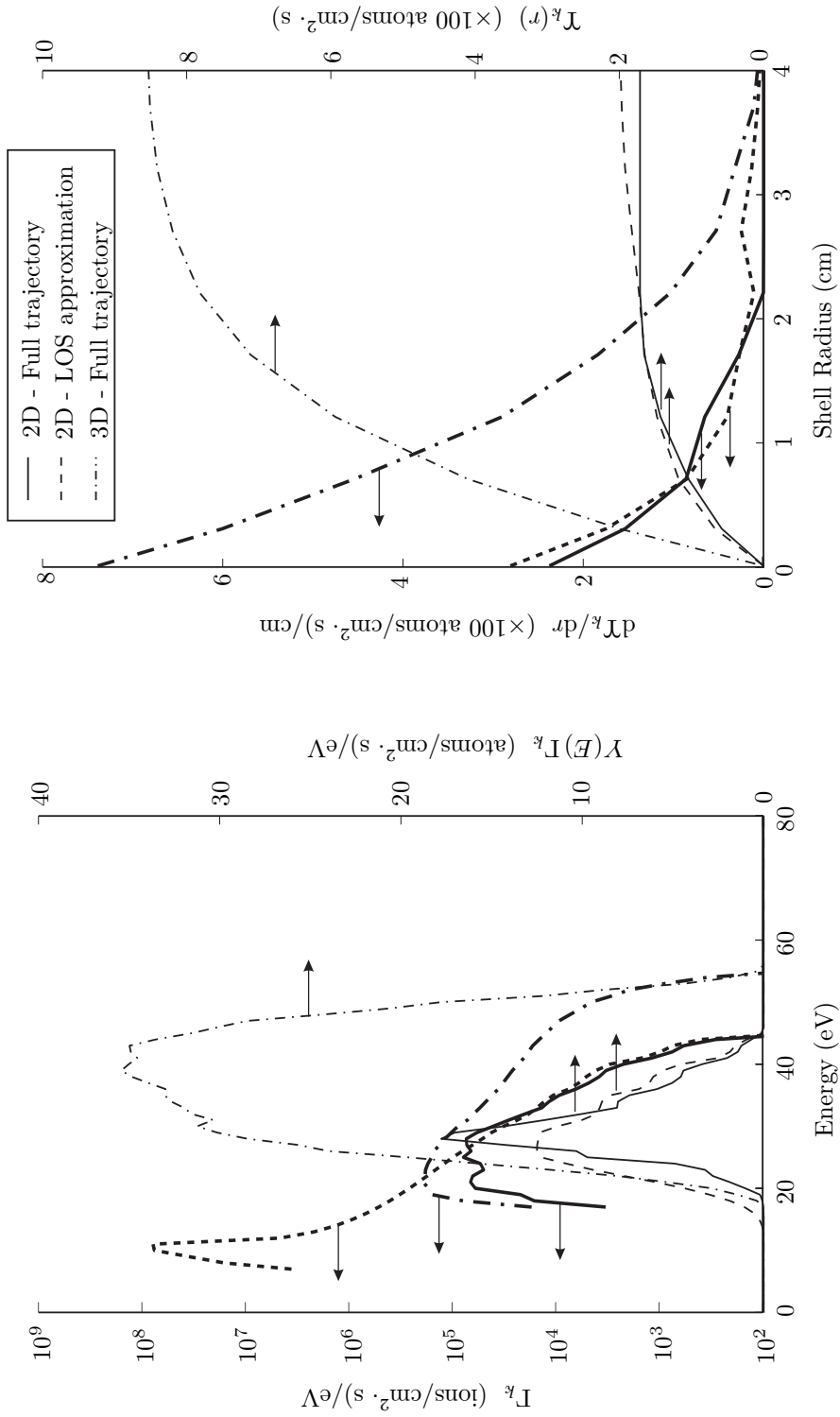


Figure 5.11: Full-beamlet 3D approximation comparison: Hole $(x, y)_k = (0, 11.92)$. Left figure is the spatially integrated energy distribution (left axis) and energy-differentiated sputtering contribution (right axis). Right figure is the energy-integrated sputtering contribution (left axis) and cumulative integral over beamlet-shell radius of the sputtering contribution (right axis). The solid line indicates the correct computation using the full 3D potential to compute trajectories. The dashed line is the correct computation using the 2D-potential assumption. The dash-dot line is the energy- and angle-corrected LOS assumption using a 2D potential.

Chapter 6

Perforated Shell Structure Analysis

Both thin and thick plate theory is well understood. Even if exact analytical expressions cannot be found for any particular plate under a specified loading, there are a multitude of finite-element software packages available, which do an excellent job at modeling even very complex problems. Computational modeling of any specific problem can get extremely time consuming if the number of elements defining the structure gets large. Modeling a shell containing many thousands of holes could become too time consuming for application to an optimization problem requiring repeated computation. This chapter will discuss the concept of equivalent elastic properties commonly used when dealing with perforated structures, which significantly simplifies analysis. Section 6.1 will present both theoretical and experimental work done in the past in attempts to determine these effective properties for flat plates of varying thickness and hole pattern. Discussion of applicability of these properties to shells that are not flat will follow in Section 6.2. The chapter will end with a brief presentation, in Section 6.3, of some simulations done of both flat plates and NSTAR-shaped grids, and how these results affect the implementation of the structural analysis into the optimization discussed in Chapter 7.

6.1 Previous Results

Research into the response of flat plates with periodically drilled hole patterns, commonly referred to as tubesheets, came into prominence in the 1950s. Interest in such structures was highly motivated by application to pressure vessels and heat exchangers — especially those in the newly emerging nuclear

reactor technology [60]. Without exact theoretical solutions for the displacements and stresses occurring within a tubesheet under some specified load, Gardner [61] introduced the concept of an equivalent solid plate with elastic properties such that, under the same load, this solid plate would undergo the same displacements as the tubesheet. Stress concentration factors then assist in predicting the maximum stress that occurs at the hole edges [60]. Research since then has focussed on measurements and theories that predict these equivalent elastic properties. A thorough review of the historical development of tubesheet theory and experimentation can be found in [62].

One of the seminal works in tubesheet theory was the thesis by Meijers [63]. In this work, Meijers primarily dealt with determining analytical solutions for the equivalent elastic properties of doubly-periodic perforated plates. The plane stress condition is typically only encountered when there are in-plane loads acting on a thin plate. A plate is considered to be thin when $t/L \ll 1$, where t is the thickness of the plate and L is any characteristic dimension of the plate. Plane strain conditions, on the other hand, are typically encountered when dealing with thick plates under the influence of in-plane loading. Conversely, a thick plate is one for which $t/L \gg 1$, and traditionally has been defined to be any plate for which $t/L \geq 2$ [64].

In the past, researchers [65] have asserted, and Duncan [66] demonstrated, that the equivalent elastic properties are very similar for thick perforated plates in tension or under bending loads. Meijers argued that, while this assertion may be supported by experimental data, the reasoning is not soundly based in theory. He then proceeded to derive approximate relations between the effective elastic constants applicable to thick plates under plane stress and bending. Using these relations, effective elastic properties for perforated plates in the bending state could be found in the two limits: thin and thick. Figure 6.1 shows the effective properties, under bending, found from Meijers' theory for the triangular hole pattern (see Figure 3.2) in thin and thick plates. Data obtained by Duncan [66] for thick perforated plates ($t/R = 2.29$) is also shown. The results are plotted as a function of the total open-area fraction, Θ . For a triangular hole pattern,

$$\Theta = \frac{\sqrt{3}\pi}{6} \left(\frac{R}{p/2} \right)^2, \quad (6.1)$$

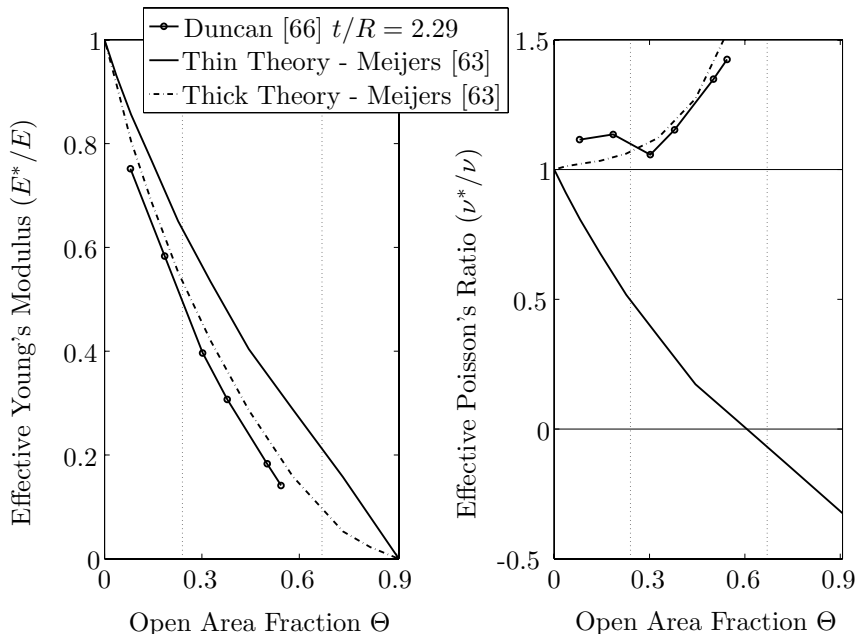


Figure 6.1: Effective moduli as a function of open-area fraction. Effective moduli predicted from theory and measured from experiments for varying open area fractions of plates in the thin ($t/R \ll 1$) and thick ($t/R \gg 1$) limits. Poisson's ratio used to obtain the data from theory is $\nu = 0.3$. Poisson's ratio for the material used in the physical experiments is $\nu = 0.27$. The open-area fractions of the NSTAR screen and accel grids, $\Theta_s = 0.67$ and $\Theta_a = 0.24$, are indicated.

where R is the hole radius and p is the pitch. The open-area fraction has a maximum value of $\Theta_{\max} = 0.907$ for this hole pattern. With $R_a = 0.57$ mm, $R_s = 0.955$ mm, and $p = 2.22$ mm, the open-area fractions of the NSTAR accel and screen grids are $\Theta_a = 0.24$ and $\Theta_s = 0.67$, respectively. The NSTAR open-area fractions are indicated in the figure.

It can be seen that theory predicts a large difference in the effective properties depending on whether the plate is considered to be thin or thick. Note that for thick plates under bending, the effective Poisson's ratio, ν^* , is expected to be larger than the undrilled bulk value, ν , for all open-area fractions. Duncan's results seem to verify this. On the other hand, the effective Poisson's ratio for thin plates under bending is expected to always be less than the undrilled bulk value, and may even be negative for sufficiently large open-area fractions.

While Meijers' initial work is useful in the situation of dealing with perforated plates that are within either of the two limits, it provides no information in cases where the thickness is of the same order as the other dimensions in the plate, such as $t/R \sim 1$. Later work of his [67] extended the

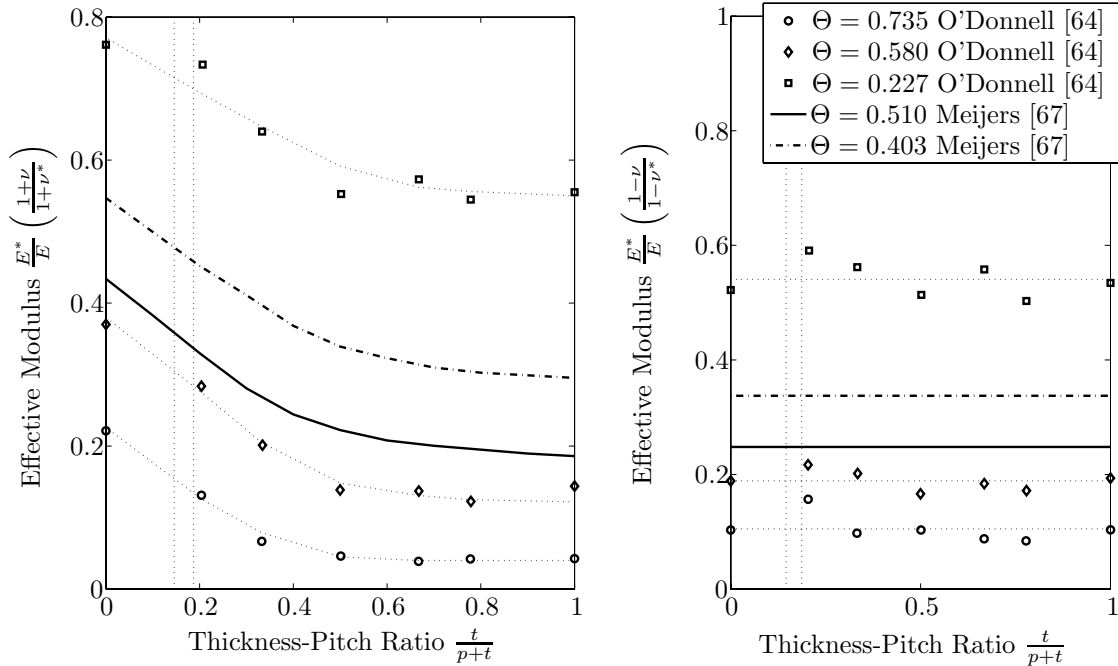


Figure 6.2: Effective moduli as a function of plate thickness. Effective moduli predicted from theory and measured from experiments for various open-area fractions. Poisson’s ratio used to obtain the data from theory is $\nu = 0.3$. Poisson’s ratio for the material used in the physical experiments is $\nu = 0.33$. The data points for $t/(p+t) = 0$ and $t/(p+t) = 1$ in the measured data sets were not obtained by measurement but from theory. The thickness-pitch ratios of the NSTAR screen and accel grids, $t/(p+t) = 0.15$ and $t/(p+t) = 0.19$, respectively, are indicated. Dotted lines through the measured data sets are simply to guide the eye.

previous to include terms of $O(t/R)$, which, in addition to yielding the limit values for $t/R = 0$ and $t/R \rightarrow \infty$, allows for computation of the effective properties as $t/R \rightarrow 0$. If the effective properties are viewed as a function of t/R , the additional analysis yields the slope of this function at $t/R = 0$. Using finite element analysis, Meijers was able to fill in the range between the two limits for all possible values of t/R . Physical experiments were carried out by O’Donnell [64] on perforated metal plates of varying thickness under bending. The effective properties found by theory, finite element analysis, and experiment are shown in Figure 6.2. The first quantity shown is the first Lamé constant, normalized by the undrilled bulk value, or shear modulus. It has been argued [64, 67] that, under equi-biaxial bending, the quantity $(1 - \nu)/E$ should be relatively constant for all plate thicknesses. It is this quantity, again normalized by the bulk value, shown in the second figure. The limit values for the experimental data are taken from [64], which originally were obtained from Miegers’ theory [63]. The NSTAR accel and screen grids have thicknesses of $t = 0.51$ mm and $t = 0.38$ mm, yielding

thickness-pitch ratios, $t/(p+t)$, of 0.19 and 0.15, respectively. The NSTAR thickness-pitch ratios are indicated in the figure. Figure 6.2 enables us to interpolate the effective elastic constants, E^* and ν^* , for a plate of any thickness, and with an open-area fraction $0.227 \leq \Theta \leq 0.735$.

6.2 Shallow Shells vs. Flat Plates

The entire discussion in the previous section referred to flat plates under bending loads. Unfortunately, the grids we are concerned with are not usually flat. For example, the NSTAR grids are spherically dished, with a radius of 51 cm. With a diameter of 30 cm, a thickness of 0.51 mm, and a height of approximately 2 cm, the accel grid can hardly be considered to be a flat plate. The measurements, and all theory from which the data in the previous section was obtained were based on flat plate theory where the kinematic equations reduce to a two-dimensional problem. Do we have any reason to believe the effective elastic properties obtained from the previous section can be applied to shells that are not flat?

Much theoretical work has been done on deriving the full three-dimensional equations for shells, and, like the Airy potential for flat plates, can be reduced to the solution of a pair of differential equations involving the displacements and a stress function or potential [68, 69, 70]. There has also been some work in attempting to model shallow shells with periodically spaced holes [71]. Despite this work, the author is unaware of simple reductions that can be made for perforated arbitrary shaped shells like those made for flat plates in the previous section. It would seem that full analysis of these types of structures remains only within the realm of computer modeling. With no other option available to us that we are aware of, we will assume that the effective elastic properties found for a flat plate with a certain pitch-to-thickness ratio and open-area fraction are also, at least approximately, applicable to a perforated shell of the same dimensions.

As stated in the previous section, the whole purpose for finding effective elastic properties is to simplify the analysis of an otherwise complex problem. Our desire is to mesh the plume model developed in Chapters 4 and 5 with structural modeling of an engine grid, to optimize the sputtering under certain structural constraints. As the method for finding a solution to a particular optimization

set will be manifest in multiple evaluations of both the plume and structural quantities, we wish to be able to do the structural analysis of any particular grid shape rapidly. This would not be possible if we attempted to model a shell with all 15,000 holes. Thus, we use the effective elastic properties.

A finite element analysis tool tailored specifically for thin-shell analysis developed at Caltech was used for doing the structural analysis. Details pertaining to the operation of this code can be found elsewhere [72, 73, 74].

6.3 The Loading

The stress on the grids due to acceleration while in operation in space is negligible, and is not considered to be one of the limiting factors on the effective lifetime of the spacecraft; the NSTAR engine produces 92.67 mN of thrust at the highest throttle level, TH15 [9]. However, in order for the spacecraft to have an opportunity to successfully fulfill its mission, it must survive the few minutes it takes to place the spacecraft in orbit. Depending on the launch vehicle used, the entire spacecraft will be subjected to acceleration forces, vibrations in a large range of frequencies, as well as possibly impulsive shocks from the ignition of explosive bolts [18]. If the engine grids fracture, either from excessive stress or from a mutual collision, the entire mission could be jeopardized due to an ineffective or inoperable engine.

In order to safeguard against such catastrophic failures, all components of a spacecraft must meet certain random vibration specifications [75, 76]. Ideally for this work, we would like to be able to simulate the effects of this same stress test on a model of any candidate grid geometry, and analyze both the expected stresses and displacements achieved in such a test. If the stress is too great, such as to expect the grid to fracture, or if the displacements are too large, such that the two grids would be expected to collide with each other, the candidate geometry would be deemed inadequate.

The finite-element modeling software used in this study, to be discussed further in Chapter 7, has been shown to be capable of dynamic loading [77]. Once again we face the issue of being able to model the structural response of the grid rapidly. Unfortunately time-dependent loading was deemed to require too much time to be implemented into the current optimization problem, and

it was decided to limit the current study to static loading of the grid under simulated constant acceleration.

Since we have chosen to only simulate static loads, it is unclear as to what an appropriate simulated load would be to, at the very least, provide insight into which grid shapes are optimal. Not only is the magnitude of the load an unknown quantity, but the direction in which this load should be applied to the grid is unclear. Depending on the specific craft and launch vehicle, the engine grid could have any orientation with respect to the direction of travel during launch. With nothing to give us preference to one loading direction over another, it was decided to apply the load in the direction opposite to the engine thrust vector.

In order to first gain some confidence in the structural analysis code, simulations for circular flat plates, with the same diameter and thickness as the NSTAR accel grid, under a range of uniformly distributed transverse loads were performed. The effective elastic properties were used, assuming the plate was made from molybdenum and perforated in the same hole pattern as the NSTAR accel grid. The elastic properties were found in the following way: The two effective quantities from Figure 6.2 were interpolated for a thickness-pitch ratio of 0.19, corresponding to the NSTAR accel grid, on all five curves shown. From these five values, corresponding to the five indicated open-area fractions, the quantities were interpolated for an NSTAR accel grid open area-fraction of 0.24. The following values were found:

$$\frac{E^*}{E} \left(\frac{1 + \nu}{1 + \nu^*} \right) = 0.682, \quad \text{and} \quad \frac{E^*}{E} \left(\frac{1 - \nu}{1 - \nu^*} \right) = 0.540.$$

Using a value of $\nu = 0.30$ for molybdenum [78], solving these two equations for the effective Young's modulus and Poisson's ratio yields

$$\frac{E^*}{E} = 0.625, \quad \text{and} \quad \nu^* = 0.201.$$

The Young's modulus of molybdenum is $E = 329$ GPa, which yields an effective modulus of $E^* = 196.7$ GPa.

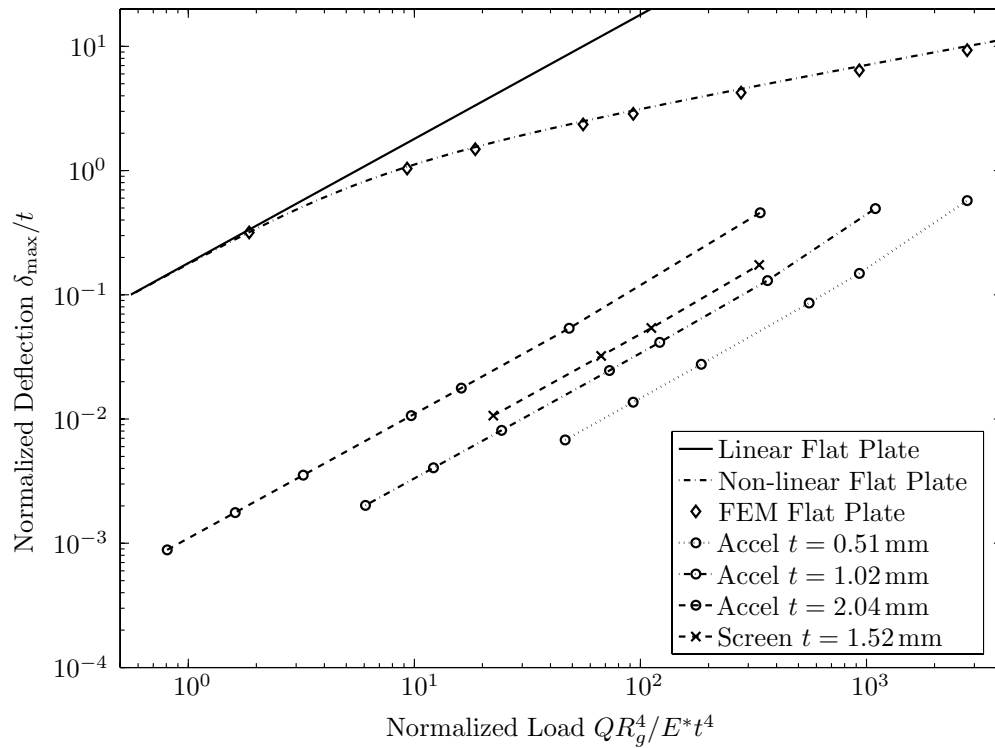


Figure 6.3: Theoretical- and FEM-deflection comparison. Comparison of deflections computed from FEM analysis of a flat plate under large deflection is shown to have less than 8% difference from the deflections predicted by non-linear large-deflection plate theory. NSTAR accel and screen grids of various thicknesses were analyzed using the FEM code. The effective moduli were computed by interpolation of the data of Figure 6.2, and summarized in Table 6.1. The radius of the plate was specified to be $R_g = 15$ cm.

The maximum displacements, δ_{\max} , predicted by the code for various loads, Q , were compared with those predicted by large-displacement flat plate theory [79]. The normalized results are shown in Figure 6.3. The displacements obtained from the simulations were systematically less than theory, where the difference increased with increasing load. The results differed by no more than 8% over a range of loads spanning three orders of magnitude.

To obtain an idea of the magnitudes of the expected displacements from different loads, the NSTAR grids were modeled in a similar manner to the flat plates above. Grids with 1x, 2x, and 4x the accel grid thickness, and 4x the screen grid thickness were all modeled under a range of transverse static loads. The results are also shown in Figure 6.3. The effective properties used for each are shown in Table 6.1.

Table 6.1: Effective properties for simulated NSTAR grids of different thickness: Obtained from interpolation from Figure 6.2

Grid	Thickness (mm)	Thick-Pitch Ratio $\frac{t}{p+t}$	Open-Area Fraction	$\frac{E^*}{E} \left(\frac{1+\nu}{1+\nu^*} \right)$	$\frac{E^*}{E} \left(\frac{1-\nu}{1-\nu^*} \right)$	$\frac{E^*}{E}$	ν^*
Accel (1x)	0.51	0.187	0.239	0.682	0.540	0.625	0.201
Accel (2x)	1.02	0.315	0.239	0.634	0.540	0.598	0.226
Accel (4x)	2.04	0.479	0.239	0.576	0.540	0.563	0.281
Screen (4x)	1.52	0.406	0.671	0.102	0.147	0.114	0.457

It was found that as the thickness of the simulated grid decreased, the time required to complete the computational analysis increased, and was less likely to converge to a solution. To avoid possible issues of non-convergence during the optimization procedure outlined in Chapter 7, we decided in some situations to increase the thickness of the simulated grid. The data from Figure 6.3 will be used to obtain scaling factors for the expected displacements. The constraint on our optimization will be that the maximum grid deflection must not exceed a certain value under a specified loading. Since increasing the thickness of the grid makes it more resistant to deflection, the scaling factors obtained from Figure 6.3 will enable us to scale the allowable maximum displacement of the thickened grid appropriately, such that both the grid of correct thickness and the artificially thickened grid will violate the displacement constraint under approximately the same load.

Chapter 7

Optimization Procedure and Results

We started this work with two goals in mind: (1) develop a model that accounts for the energy and momentum transfer process during charge-exchange collisions for purposes of predicting the amount of sputtering that one would expect at any particular point around an ion engine, and (2) to implement a constrained optimization problem that adjusted the shape of the grids in order to minimize the sputtering rate at specified points while meeting certain constraints on the structural strength. The first goal, the model, was developed in Chapters 3 through 5. We now tackle the second goal.

In any constrained optimization problem, as outlined in Section 2.2, there are three quantities required. The first quantity is the objective function, Υ , which we wish to minimize. In our problem, the objective function is the sputtering rate at specified points. The CEX-ion model developed in the previous chapters provides us with the value of this objective function. The second quantity that is required is the set of all optimization parameters, ξ , that define the value of the objective function. Since the goal is to adjust the grid shape to minimize the sputtering, the parameters required are all quantities that can parameterize and fully define any grid surface shape. The procedure followed for obtaining a parameterized surface, a subdivision technique used within the structure code, will be discussed in Section 7.1. The third, and final, quantity needed to execute an optimization procedure is the set of constraints on either the optimizing parameters, or on the objective function itself. In this problem, we have chosen the constraints to be those quantities that determine and limit

the physical strength of the grid. The Matlab function used to execute the optimization, *fmincon*, will be discussed in Section 7.2 as will how the constraints are chosen in our implementation of the optimization procedure. The chapter will end in Section 7.3 with a presentation of the results obtained from various optimization runs.

7.1 Control Mesh and Limit Surface Construction

The tool used to conduct the finite-element analysis on the grid structure was a code ideally suited for thin, shell-like structures and is discussed at length elsewhere [73, 72]. The geometry of the shell structure in question is input to the code in the form of a mesh defining the shape of the surface. The mesh is composed of the coordinates of numerous points, and the surface is formed by the set of triangular areas created by vectors joining the points within the mesh.

The nature of the hole layout on the NSTAR grid, an equilateral triangular pattern (see Figure 3.2), would seem to imply that the mesh defining the location of all the holes on the grid is a natural choice for input to the finite-element code. However, with nearly 15,000 holes in the grid, the number of triangular elements formed by the vectors joining the points representing the positions of these holes would be of the order of 60,000. This number of holes and points in the input mesh is troublesome for at least two reasons. First, the time required to model the response to even a static load imposed on a surface represented by a mesh with so many elements would make optimization impractical. The mesh that we ended up using had nearly 5,000 elements, and simulation of a steady load took anywhere between five and fifteen minutes. In an optimization procedure, where we may need to compute hundreds of different grid shapes, times much longer than this make the computation too expensive. Second, we must be able to parameterize the surface in some way in order to execute an optimization based on the shape of the surface, which is exactly what we wish to do. Though the coordinates of 15,000 points located on the surface (defined by the locations of the hole centers) provides one parameterization of the surface, this also means that the optimization parameter vector, ξ , has at least 15,000 elements. Minimizing a function of 15,000 variables is no easy task, and could prove to be nearly impossible in a computational optimization algorithm [80].

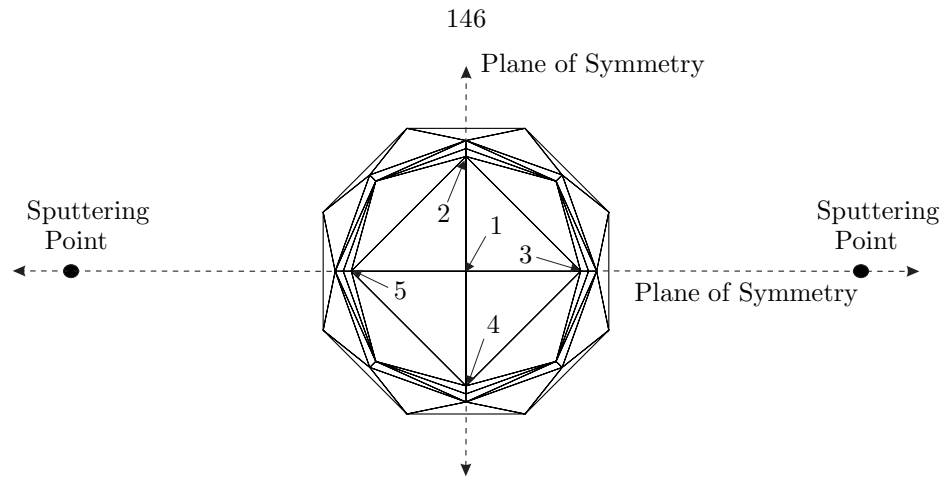


Figure 7.1: Control mesh and imposed symmetry. Requiring that any grid considered must conform to the current mounting systems of existing ion engines restricts the free parameters to the locations of the five labeled points (1-5). All unlabeled points always have zero height. Two diametrically opposed sputtering locations impose two planes of symmetry on the shape of the grid, and thus points 2 & 4 and points 3 & 5 must have identical heights. The optimizing parameters are the heights of points 1, 2, and 3: $\xi = \{z_1, z_2, z_3\}$.

Rather than using the mesh defining the locations of the 15,000 holes in the grid as the input to the finite-element code, we need a mesh with many fewer points and elements. Doing so will enable us to parameterize the surface with relatively few variables, and the time to compute the response to a static load will not yield the procedure as impractical. The method of subdivision allows for the specification of a limited number of design parameters, through a control mesh composed of a few points, that fully parameterize a surface. Additionally, subdivision provides the means for which a finite-element mesh, with an appropriate number of elements, can be obtained from the control mesh. As the name implies, the subdivision technique subdivides all the elements in the control mesh into smaller elements through the addition of more mesh points. The positions of these new mesh points are calculated based on the positions of the original control mesh points. Iterative subdivision of the resulting mesh can produce a final mesh with any number of points and elements. The algorithm by which the positions of consecutive mesh points are calculated is determined such that, in the limit of an infinite number of subdivision iterations, a limit surface is obtained where every point on the surface is defined. A discussion of the use of the subdivision technique for the problem of optimization of surfaces can be found in Reference [74].

The control mesh developed for this work is shown in Figure 7.1. It was assumed that any

candidate grid shape should be required to conform to the current mounting system used in existing ion engines. This requirement forces the edges of the grid to have no height nor any slope. Based on the algorithm used for subdivision, any limit surface will meet these requirements if all unlabeled points in the control mesh always have a height equal to zero. There is no restriction on the heights of the labeled points (1-5) imposed by these requirements. For simplicity, it was assumed for this work that there were two diametrically opposing points, S , where we wished to minimize the sputtering. Such an assumption creates two planes of symmetry within the grid shape. Thus, by symmetry, points 2 and 4 must have the same height and points 3 and 5 must have the same height. There remain only three free parameters which define the geometry of any limit surface derivable from this control mesh, and any combination of values for the heights of these points fully parameterizes a unique limit surface. Consequently, the heights of these three points are the optimization parameters: $\xi = \{z_1, z_2, z_3\}$.

Each time a mesh is subdivided, each element is divided into four new elements. The large variation in control mesh element size would result in a large concentration of very small elements in some regions after subdivision. In order to even out the distribution of elements within the finite element mesh, a series of subdivision and element-removal steps was implemented every time a new grid shape was created (by the specification of new values for ξ). The same procedure was followed for each grid to keep the evolution of the control mesh to the finite element mesh, and eventually the limit surface, consistent. The progression of subdivision steps and element removal is shown in Figure 7.2. It is the last mesh with 661 points and 1248 elements that is defined to be the finite element mesh, and is that which is input into the analysis software. The shell code subdivides the input mesh once in order to separate irregular vertices [72], resulting in a final mesh with 2569 points and 4992 elements.

Further subdivision of the mesh results in a finer mesh that approaches a limit surface which defines the location of every point in the shell. Though it requires an infinite number of subdivisions to actually obtain the limit surface, in practice only a few subdivisions yields a mesh that nearly conforms to the limit surface [72]. The same mesh with 661 points that is used as input to the shell

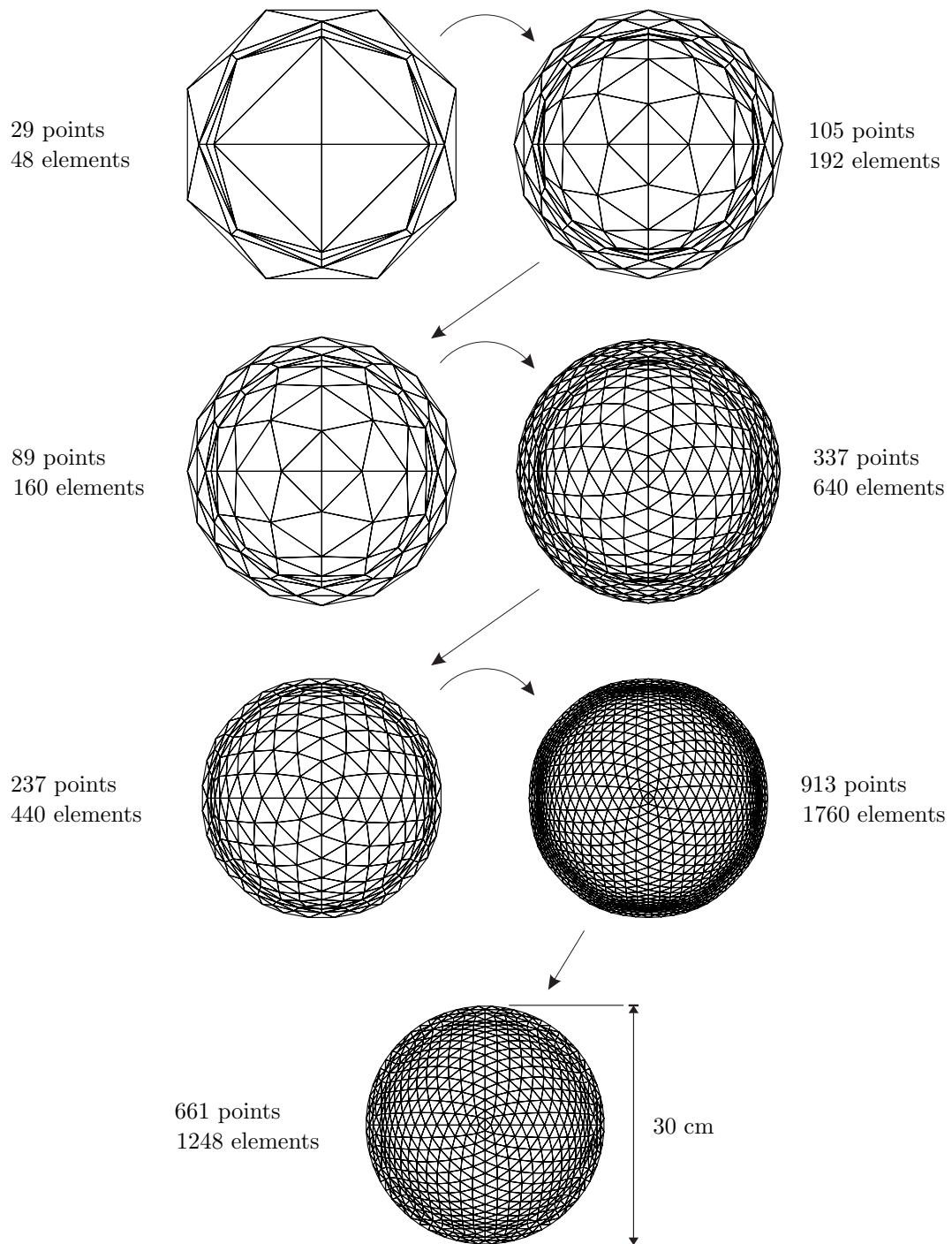


Figure 7.2: Creating the finite-element mesh. The finite-element mesh is produced by a repeated series of subdivision and element-removal, beginning with the control mesh. Arrows from left-to-right indicate a subdivision step. Rows advancing down a row indicate a step where the smallest elements are removed from the mesh. The finite-element code subdivides one further time before computing the load response. An approximation to the limit surface, from which hole coordinates and normal vectors are computed, is obtained by three further subdivisions of the last mesh shown.

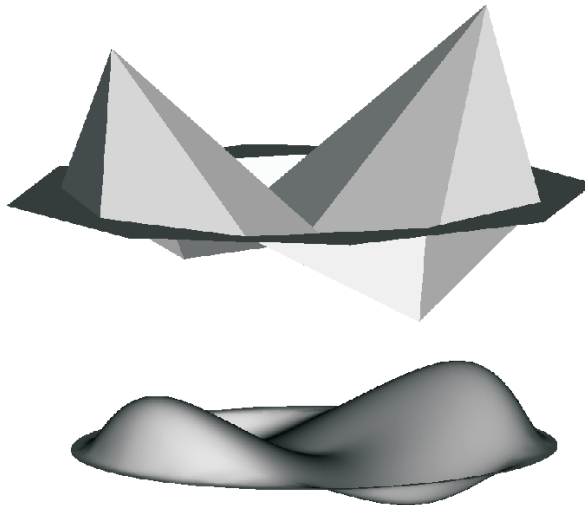


Figure 7.3: Sample of a control mesh and resulting limit surface. Following the subdivision and element-removal procedure shown in Figure 7.2 with three additional subdivisions yields an approximation to the limit surface (lower figure), represented by a control mesh (upper figure). For easier visualization, the height of the grid has been increased significantly and is larger than that encountered in any optimizations.

code is subdivided three more times, to obtain a mesh with 40225 points and 79872 elements. An example of a control mesh, and the surface obtained using the procedure outlined above, is shown in Figure 7.3. For purposes of visualization, the height of the grid is significantly larger in this example than we will encounter in our problem.

The locations of the grid holes are interpolated from this subdivided mesh using 2D spline interpolation. The Matlab function *griddata* is used to do the interpolation. The pitch, or distance between holes, is measured along the surface of the grid. Since we are dealing with shallow shells where the shape changes relatively slowly, the pitch is very nearly $p = \sqrt{(\Delta x)^2 + (\Delta y)^2 + (\Delta z)^2}$. We assume that $(\Delta z)^2 \ll (\Delta x)^2 + (\Delta y)^2$, and thus keep the (x, y) locations of the holes constant, regardless of the grid shape, and simply interpolate for the height. Under this assumption, the pitch between any two adjacent holes is only precisely correct if they are of the same height.

Table 7.1: Optimization procedure (*fmincon*) input and output arguments**Output**

<i>param_opt</i>	vector containing the values of the parameters found to minimize the objective function
<i>optvalue</i>	the scalar value of the objective function at the constrained minimum

Input

<i>obj_fun</i>	the function that evaluates the objective for the input parameters <ul style="list-style-type: none"> • has one scalar output
<i>param_init</i>	vector containing the initial guess at the values of the optimizing parameters (\mathbf{x})
<i>A</i>	matrix expressing the equations of the linear inequality constraints: NULL
<i>b</i>	vector of the values of the inequality constraints: NULL ($\mathbf{A} \mathbf{x} \leq \mathbf{b}$)
<i>A_eq</i>	matrix expressing the equations of the linear equality constraints: NULL
<i>b_eq</i>	vector of the values of the equality constraints: NULL ($\mathbf{A}_{eq} \mathbf{x} = \mathbf{b}_{eq}$)
<i>param_min</i>	vector of minimum values the optimization parameters can have
<i>param_max</i>	vector of maximum values the optimization parameters can have
<i>nonlincon_fun</i>	function that evaluates the nonlinear parameter constraints <ul style="list-style-type: none"> • must return two vectors
<i>nonlincon_eq</i>	all values must equal zero at the minimum solution: NULL
<i>nonlincon_ineq</i>	all values must be less than zero at the minimum solution
<i>options</i>	a structure specifying various parameters used in the optimization routine
<i>DiffMinChange</i>	minimum amount to change the optimization parameters for determining objective function derivatives
<i>DiffMaxChange</i>	maximum amount to change the optimization parameters for determining objective function derivatives
<i>TolX</i>	tolerance value on the objective function for determining convergence and termination of optimization
<i>TolCon</i>	tolerance value on the constraints

7.2 Setting Up the Problem

7.2.1 The Optimization Routine

The Matlab function *fmincon* was used to execute the optimization. The syntax used for this function is the following:

$$[param_opt, optvalue] = \mathbf{fmincon}(obj_fun, param_init, A, b, A_eq, b_eq, \dots, param_min, param_max, nonlincon_fun, options).$$

The input and output arguments are summarized in Table 7.1.

Some of the inputs do not apply to our specific problem, and therefore must be specified as null

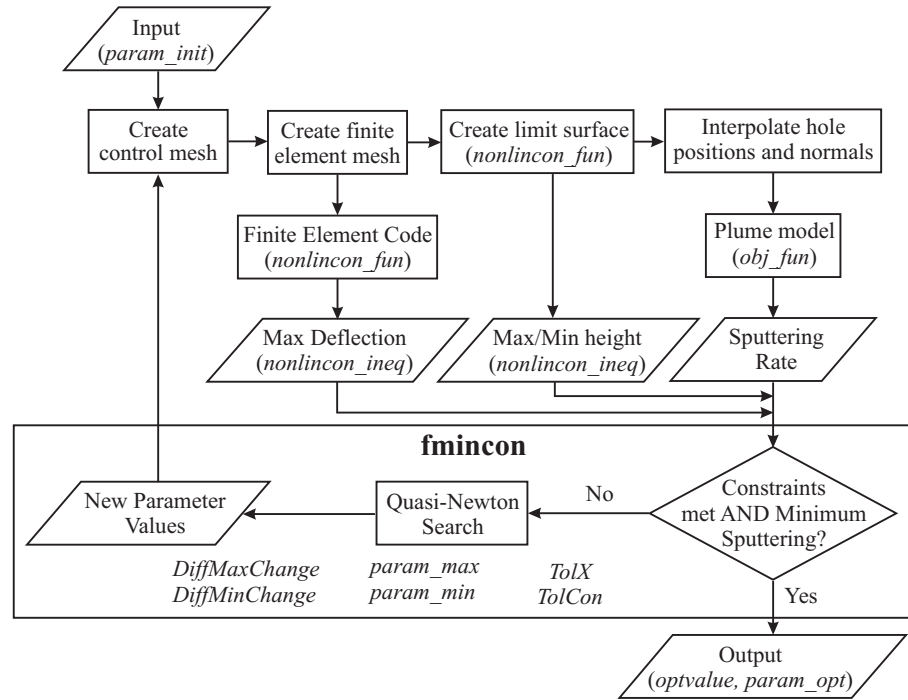


Figure 7.4: Optimization procedure flowchart

vectors. As discussed in the following section, the only constraints present are (1) the maximum displacement of the grid under a specified load, and (2) the maximum and minimum height the grid can have. All three of these constraints are nonlinear inequality constraints. Thus the input arguments A , b , A_{eq} , b_{eq} , and $nonlincon_{eq}$ are null, or zero vectors for our application. In the first optimizations attempted $param_min$ and $param_max$ were not specified either, however, it was found that large derivatives could be cause for large step sizes and result in unreasonable values of the three control point positions. Following this discovery, $param_min$ and $param_max$ were specified in every optimization run. A flowchart for the optimization procedure is shown in Figure 7.4.

7.2.2 The Load and Constraints

The issue of time-dependent loading for the shell structure analysis was discussed in Chapter 6. Due to the significantly larger amount of time needed, it was decided to only model the grid response to a steady load similar to that of constant acceleration. The question remains as to what magnitude of load is appropriate. The grid separation for the NSTAR engine is 0.66 mm [9]. It was decided to

choose the load such that the maximum deflection of the correct thickness accel grid is approximately half of the grid separation. The finite-element code did not output the resulting stresses in the shell due to loading, so we have limited the constraints on our optimization to only the maximum allowable displacement of the grid.

From Figure 6.3, it was found that an NSTAR grid with a thickness of 0.51 mm has a maximum deflection of approximately $\delta_1^{\text{NSTAR}} = 0.293$ mm under a normalized load of $\bar{Q} = 2806$. Applying Newton's First Law to a small element of the shell with a surface area, δA , and thickness, t , yields

$$Q = \frac{\delta F}{\delta A} = \frac{1}{\delta A} \int_0^t \int_{\delta A} \tilde{\rho} \, dA' \, dt', \quad (7.1)$$

where a is the acceleration of the element, and $\tilde{\rho}$ is the average material density. Thus, the normalized load is

$$\bar{Q} = \frac{QR^4}{E^*t^4} = \frac{(1 - \Theta)\rho a R_g^4}{E^*t^3}, \quad (7.2)$$

where the average density, $\tilde{\rho}$, has been replaced with the expression using the bulk density, ρ , using the definition of the open area fraction, Θ . With a grid radius, $R_g = 15$ cm, and using the results from Table 6.1, we find that the constant acceleration corresponding to the normalized load of $\bar{Q} = 2806$ for the NSTAR accel grid is $a = 1.93 \times 10^4$ m/s², or $a = 1.97 \times 10^3$ g.

It was found that using a correct thickness for the accel grid of $t = 0.51$ mm was cause for convergence issues with the finite-element shell code. It was observed that for grid shapes other than the NSTAR, the applied force often caused buckling, or snap-through, of the grid. In these instances, the shell code would often terminate, due to reaching the maximum allowable number of iterations before convergence was reached.

Some success was met by increasing the thickness of the grid. Using the corresponding effective elastic properties (Table 6.1) and the same acceleration of $a = 1.97 \times 10^3$ g, normalized loads for twice and four times the actual thickness were found to be $\bar{Q} = 367$ and $\bar{Q} = 48.7$, or $Q = 1.54$ kPa and $Q = 3.09$ kPa, respectively. Under these loads the maximum deflection of the NSTAR accel grid with twice and four times the actual thickness is predicted to be (Figure 6.3) $\delta_2^{\text{NSTAR}} = 0.133$

mm and $\delta_4^{\text{NSTAR}} = 0.110$ mm, respectively. It was decided to assume that the maximum deflection any grid could undergo was approximately twice that of the NSTAR grid under the same load.

In addition to the deflection constraint, two constraints on the grid shape were imposed such that the maximum and minimum heights of the grid could not exceed specified values. These were imposed in consideration of the limitations on manufacturing the grids [76, 81]. The values chosen for all optimizations were a maximum height of 3 cm and a minimum height no less than -1 cm.

7.3 Optimization Results

In this section we present the results of the optimization runs executed. The sensitivity of the results to changing different optimization input variables (see Table 7.1) was tested and the results are sorted according to each of these studies.

7.3.1 Sensitivity: *param_init*

Due to concerns about global convergence of the optimization routine, the first optimization runs varied the values of the initial parameters, *param_init*, to see how the starting point affected the end result. The optimization input variable *param_init* specifies the initial values of the optimization parameters ξ . Optimizations using both twice and four times the NSTAR accel grid thickness were done. For all cases, except those noted otherwise, *options*, *param_min*, and *param_max* were held constant:

$$\begin{aligned} \textit{DiffMinChange} &= 0.01, & \textit{TolX} &= 0.05, \\ \textit{DiffMaxChange} &= 0.5, & \textit{TolCon} &= \text{N/A}, \\ \textit{param_min} &= [-2, -2, -2], & \textit{param_max} &= [10, 10, 10]. \end{aligned}$$

The two diametrically opposed points for which the sputtering was minimized were located at $S(\tilde{\mathbf{x}}) = (-60, 0, 3)$ and $(60, 0, 3)$, and the load was $a = 1.97 \times 10^3$ g as discussed in the previous section. The input parameters and the results are summarized in Table 7.2. Runs in italics indicate optimization runs for which either no optimizing solution (due to non-convergence or a constraint violation) was found. Constraint violations are indicated in bold.

Table 7.2: Optimization results demonstrating dependence on *param_init*

$$\Upsilon^{\text{NSTAR}} = 7.36 \times 10^8 \text{ atoms/cm}^2\cdot\text{s}$$

$$\delta_2^{\text{NSTAR}} = 0.133 \text{ mm}$$

$$\delta_4^{\text{NSTAR}} = 0.110 \text{ mm}$$

Run #	<i>t</i> (mm)	<i>param_init</i>	δ_{max} (mm)	<i>param_opt</i>	δ (mm)	<i>optvalue</i> $\times 10^8$ (ratio)
42	1.02	3.0, 3.0, 3.0	0.30	3.22, 2.28, 3.12	0.300	9.02 (1.23)
49	1.02	3.5, 3.5, 3.5	0.30	2.80, 0.69, 3.29	0.310	6.05 (0.82)
54	1.02	3.0, 1.4, 1.4	0.30	2.69, 0.77, 1.63	0.298	5.63 (0.76)
63	1.02	3.0, 1.4, 1.4	0.30	2.66, 0.84, 1.59	0.300	5.74 (0.78)
72	1.02	2.25, 1.0, 1.0	0.30	2.70, 1.27, 0.92	0.281	6.43 (0.87)
<i>43</i>	<i>1.02</i>	<i>0, 0, 0</i>	<i>0.30</i>	<i>-1.35, -0.60, -0.59</i>	0.596	<i>5.38 (0.73)</i>
<i>46</i>	<i>1.02</i>	<i>2.5, 2.5, 2.5</i>	<i>0.30</i>	<i>N/A</i>	<i>N/A</i>	<i>N/A</i>
<i>48</i>	<i>1.02</i>	<i>2.8, 2.8, 2.8</i>	<i>0.30</i>	<i>N/A</i>	<i>N/A</i>	<i>N/A</i>
<i>52</i>	<i>1.02</i>	<i>2.8, 2.8, 2.8</i>	<i>0.30</i>	<i>N/A</i>	<i>N/A</i>	<i>N/A</i>
<i>65</i>	<i>1.02</i>	<i>1.5, 0.7, 0.7</i>	<i>0.30</i>	<i>N/A</i>	<i>N/A</i>	<i>N/A</i>
44	2.04	3.0, 3.0, 3.0	0.15	3.46, 1.04, 2.47	0.149	7.32 (0.99)
47	2.04	2.5, 2.5, 2.5	0.15	3.40, 1.67, 1.07	0.150	8.72 (1.18)
50	2.04	2.8, 2.8, 2.8	0.15	3.17, 1.57, 1.75	0.150	7.83 (1.06)
51	2.04	3.5, 3.5, 3.5	0.15	3.32, 0.89, 3.54	0.150	6.54 (0.89)
55	2.04	3.0, 1.4, 1.4	0.15	3.12, 1.35, 1.52	0.150	7.32 (0.99)
57	2.04	3.0, 1.4, 1.4	0.22	2.64, 1.02, 1.46	0.207	5.94 (0.81)
61	2.04	3.0, 1.4, 1.4	0.22	2.62, 0.96, 1.48	0.217	5.80 (0.79)
67	2.04	3.0, 1.4, 1.4	0.22	2.75, 0.84, 1.97	0.221	5.37 (0.73)
68	2.04	-2.0, -1.0, -1.4	0.22	-2.42, -0.93, -1.40	0.220	9.92 (1.35)
<i>45</i>	<i>2.04</i>	<i>0, 0, 0</i>	<i>0.15</i>	<i>-1.44, -0.58, -0.61</i>	0.518	<i>5.51 (0.75)</i>

[†] *TolCon* = 0.002 mm

[‡] *DiffMinChange* = 0.002 *DiffMaxChange* = 0.1

* *param_min* = [0, 0, 0]

** *param_min* = [-4, -4, -4]

Note: Runs in italics indicate runs for which either no solution was found or a constraint violation occurred. Violations are indicated in bold.

The thickness, *t*, of the grid under question is shown in the second column, and the initial values of the three control points, *param_init*, are listed in the third column. The height of point 1 (see Figure 7.1) is specified by the first value, and similarly point 2 by the second, and point 3 by the third. By symmetry, the height of point 4 is the same as 2, and the height of point 5 is the same as 3. The maximum allowed displacement due to the steady load, δ_{max} , is specified in the fourth column. For grids with twice the thickness of the NSTAR accel grid, *t* = 1.20 mm, the maximum displacement was specified to be 0.30 mm — a factor of 2.26 larger than the NSTAR grid under the same load, $\delta_2^{\text{NSTAR}} = 0.133$ mm.

Initially (Runs 44-55), for grids with four times the NSTAR accel grid thickness, $t = 2.04$ mm, the maximum displacement was 0.15 mm — a factor of 1.36 larger than the NSTAR grid. The convergence to a solution occurred sporadically for these optimizations, which was thought to be a result of the limited degrees of freedom that are available to altering the grid shape. Since the NSTAR shape can not be identically replicated with the specific control mesh used, it was thought that a maximum displacement factor of only 1.36 was too restrictive. After Run 55, δ_{\max} was increased to twice the displacement of the NSTAR grid, $\delta_4^{\text{NSTAR}} = 0.110$ mm.

The fifth column displays the optimizing parameter values found to optimize the sputtering rate within the constraints, ξ^* . Except for Runs 47 and 72, point 3 was found to always have a height larger than point 2; and except for Runs 49 and 51, point 1 was always found to have a height larger than both of the other points. This trend that the solutions take corresponds to grids similar in shape to the barrel vault, with the axis of curvature (Axis 2, Figure 5.7) occurring on the axis transverse to that on which the target point lies.

Especially for the $t = 1.02$ mm grids, the optimization would often not converge to a solution when the initial control points were all of the same height. The resulting grid from such parameter values has a flat top, and was found to often buckle under the load. This seemed to cause the Quasi-Newton search algorithm, used by the Matlab function *fmincon*, problems in determining a direction and step size to take at the next iteration. Grids from subsequent iterations were often found to be unstable in regards to the structure analysis, and would not converge to a solution, as evidenced by multiple entries containing N/A. Though the NSTAR shape cannot be reproduced exactly with only the five points in the control mesh, a shape similar to the NSTAR can be constructed by specifying the control mesh point values to be [3, 1.4, 1.4]. The probability of convergence was found to significantly improve if the initial parameters were set to those that approximate the NSTAR shape.

The sixth column of Table 7.2 lists the maximum displacement of the grid, δ , at the solution point. The final column lists both the computed sputtering rate, in atoms/cm²·s, at the solution, followed in parentheses by the ratio of this value to that computed for the NSTAR grid. For target points located at $S(\bar{\mathbf{x}}) = (-60, 0, 3)$ and $(60, 0, 3)$, the NSTAR is computed to have a sputtering

rate of $\Upsilon^{\text{NSTAR}} = 7.36 \times 10^8$ atoms/cm²·s. All of the runs, except for Runs 42, 47, 50, and 68, were found to have solutions that decreased the sputtering over the NSTAR shape. The greatest decrease in sputtering was found to occur in Run 67, where the solution yielded an expected sputtering rate that was only 73% of that expected by the NSTAR.

The grid cross-section for the NSTAR grid, the initial state, and the optimized state from Run 67 are shown in the top figure of Figure 7.5. The bottom two figures show the CEX-ion flux distribution and the contributions to the sputtering from each energy range and shell radius.

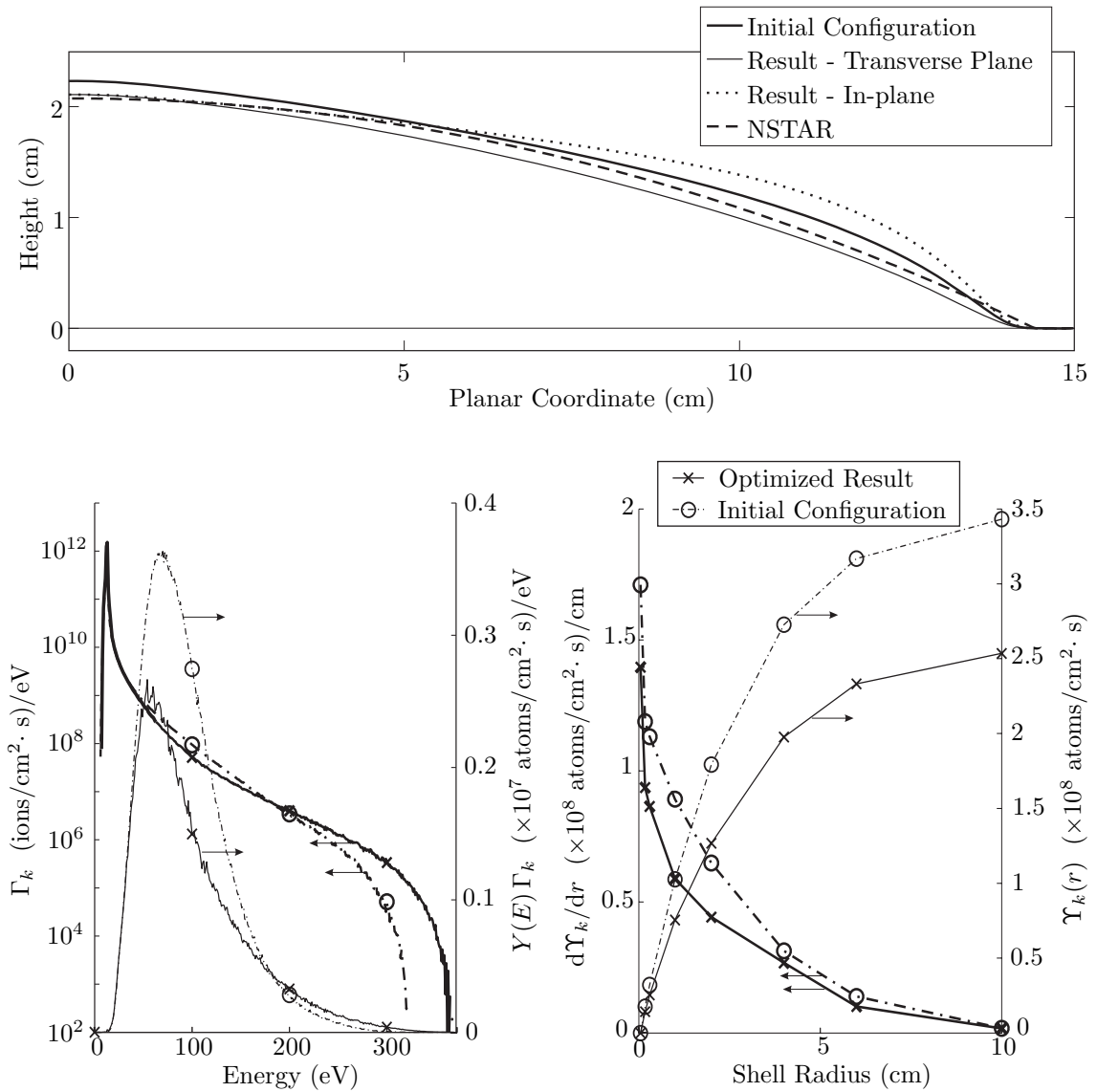


Figure 7.5: Sample optimization results for Run 67. The top figure shows the cross-sections of the NSTAR, axisymmetric initial state, and of the optimized result in the two symmetry planes. The in-plane cross-section is that of the symmetry plane passing through the sputtering points (horizontal plane in Figure 7.1). The transverse plane is that running perpendicular to the other. The lower-left figure shows the energy distribution of CEX ions, at the sputtering point at the initial state and optimized solution (left axis) and at the sputtering contribution at each energy (right axis). The lower-right figure shows the contributions to the sputtering from each shell radius (left axis), and the cumulative integral over radius (right axis).

7.3.2 Sensitivity: Evaluation Points

The sensitivity of the optimization routine to the choice in location of the target point $S(\bar{\mathbf{x}})$ was tested. If the two diametrically opposed target points are located at $(60,0,\bar{z})$ and $(-60,0,\bar{z})$, the effect on the optimization result was tested for both small and large changes in the value of \bar{z} . For all cases, except those noted otherwise, *options*, *param_min*, and *param_max* were held constant:

$$\begin{aligned} \textit{param_init} &= [3.0, 1.4, 1.4], \\ \textit{DiffMinChange} &= 0.01, & \textit{TolX} &= 0.05, \\ \textit{DiffMaxChange} &= 0.5, & \textit{TolCon} &= 0.002 \text{ mm}, \\ \textit{param_min} &= [-2, -2, -2], & \textit{param_max} &= [10, 10, 10]. \end{aligned}$$

The steady load corresponded to $a = 1.97 \times 10^3$ g. The input parameters and the results are summarized in Table 7.3.

The thickness, t , of the grid under question is shown in the second column, and the height of the target point, \bar{z} , is listed in the third column. The maximum allowed displacement due to the steady load, δ_{\max} , is specified in the fourth column, followed by the optimizing parameter values found to optimize the sputtering rate in column five. The sixth column tabulates the maximum displacement of the grid computed at the solution point. The final column lists both the computed sputtering rate, in atoms/cm²·s, at the solution, followed in parentheses by the ratio of this value to that computed for the NSTAR grid *at the specified target location* (if available).

$$\Upsilon(1.5)^{\text{NSTAR}} = 5.19 \times 10^8 \text{ atoms/cm}^2 \cdot \text{s},$$

$$\Upsilon(3.0)^{\text{NSTAR}} = 7.36 \times 10^8 \text{ atoms/cm}^2 \cdot \text{s}.$$

In all cases, the height of point 1 was greater than the heights of both points 2 and 3, and the height of point 3 was greater than that of point 2. Additionally, between all runs, the height of point 1 at the solution varied little, with a minimum value in Run 62 of $z_1 = 2.61$ cm and a maximum value in Run 58 of $z_1 = 2.76$ cm. Between all runs, the height of point 2 at the solution varied a bit more, with a minimum value in Run 54 of $z_2 = 0.77$ cm and a maximum value in Run 60 of $z_2 = 1.08$ cm. If

Table 7.3: Optimization results demonstrating dependence on evaluation point location

Run #	t (mm)	Height \tilde{z} (cm)	δ_{\max} (mm)	$param_opt$	δ (mm)	$optvalue$ $\times 10^8$ (ratio)	
54	1.02	3.0	0.30	2.69, 0.77, 1.63	0.298	5.63 (0.76)	†,*
58	1.02	2.9	0.30	2.76, 0.82, 1.44	0.289	5.57	†
63	1.02	3.0	0.30	2.66, 0.84, 1.59	0.300	5.74 (0.78)	*
57	2.04	3.0	0.22	2.64, 1.02, 1.46	0.207	5.94 (0.81)	†
59	2.04	2.9	0.22	2.63, 1.00, 1.33	0.210	5.75	†
60	2.04	1.5	0.22	2.65, 1.08, 1.35	0.200	4.14 (0.80)	†
61	2.04	3.0	0.22	2.62, 0.96, 1.48	0.217	5.80 (0.79)	
62	2.04	1.5	0.22	2.61, 0.98, 1.54	0.217	3.86 (0.74)	
67	2.04	3.0	0.22	2.75, 0.84, 1.97	0.221	5.37 (0.73)	‡
83	2.04	0	0.22	2.62, 0.93, 1.52	0.221	2.60	‡
84	2.04	6.0	0.22	2.63, 0.88, 2.21	0.220	10.75	‡

† $TolCon = N/A$

‡ $DiffMinChange = 0.002$ $DiffMaxChange = 0.1$

* $param_min = [0, 0, 0]$

the runs for which $TolCon$ was not specified are removed, the variation decreases, with a minimum value in Runs 63 and 67 of $z_2 = 0.84$ cm and a maximum value in Run 62 of $z_2 = 0.98$ cm. Between all runs, the height of point 3 at the solution varied between a minimum value of $z_3 = 1.33$ cm in Run 59 and a maximum value of $z_3 = 2.21$ cm in Run 84. For all cases for which the sputtering rate was computed for the NSTAR grid, the optimized solution yielded sputtering rates between 73% and 81% of the expected NSTAR rate.

7.3.3 Sensitivity: *Options*

The first optimization cases (Runs 42-60) did not have a tolerance limit on the constraint values, *TolCon*. For all runs after this, the constraint tolerance was specified. Pairs of runs are listed in Table 7.4 that compare results from identical conditions except for the specification of the constraint tolerance. The last pair compares the results obtained from specifying different values for *DiffMinChange* and *DiffMaxChange*. These option values specify the minimum and maximum amount, respectively, that the control mesh point parameters are changed in order to compute finite difference derivatives used for the Quasi-Newton search in the Matlab function *fmincon*. In all cases, except where noted, the following were kept constant:

$$\begin{aligned} param_init &= [3.0, 1.4, 1.4], & TolX &= 0.05, \\ param_min &= [-2, -2, -2], & param_max &= [10, 10, 10]. \end{aligned}$$

The steady load corresponded to $a = 1.97 \times 10^3$ g.

The thickness, t , of the grid under question is shown in the second column and the height of the target point, \tilde{z} , is listed in the third column. The *option* values are specified in the fourth column, followed by the control mesh point heights found to optimize the sputtering rate in column five. The sixth column tabulates the maximum displacement of the grid computed at the solution point. The final column lists both the computed sputtering rate, in atoms/cm²·s, at the solution, followed in parentheses by the ratio of this value to that computed for the NSTAR grid *at the specified target location*.

$$\begin{aligned} \Upsilon(1.5)^{NSTAR} &= 5.19 \times 10^8 \text{ atoms/cm}^2 \cdot \text{s}, \\ \Upsilon(3.0)^{NSTAR} &= 7.36 \times 10^8 \text{ atoms/cm}^2 \cdot \text{s}. \end{aligned}$$

In all cases, the height of the point 1 was greater than the heights of both points 2 and 3, and the height of point 3 was greater than that of point 2. The largest change in the solution occurred when *TolCon* was changed from N/A for a target point height $\tilde{z} = 1.5$ cm (Runs 60 and 62).

Table 7.4: Optimization results demonstrating dependence on algorithm parameters

 $DiffMinChange = 0.01$ $DiffMaxChange = 0.5$

Run #	t (mm)	Height \tilde{z} (cm)	$TolCon$ (mm)	$param_opt$	δ (mm)	$optvalue$ $\times 10^8$ (ratio)
54	1.02	3.0	N/A	2.69, 0.77, 1.63	0.298	5.63 (0.76)
63	1.02	3.0	0.002	2.66, 0.84, 1.59	0.300	5.74 (0.78)
57	2.04	3.0	N/A	2.64, 1.02, 1.46	0.207	5.94 (0.81)
61	2.04	3.0	0.002	2.62, 0.96, 1.48	0.217	5.80 (0.79)
60	2.04	1.5	N/A	2.65, 1.08, 1.35	0.200	4.14 (0.80)
62	2.04	1.5	0.002	2.61, 0.98, 1.54	0.217	3.86 (0.74)

* $param_min = [0, 0, 0]$ $TolCon = 0.002$

Run #	t (mm)	Height \tilde{z} (cm)	$DiffMin$ / $DiffMax$	$param_opt$	δ (mm)	$optvalue$ $\times 10^8$ (ratio)
61	2.04	3.0	0.01 / 0.5	2.62, 0.96, 1.48	0.217	5.80 (0.79)
67	2.04	3.0	0.002 / 0.1	2.75, 0.84, 1.97	0.221	5.37 (0.73)

When the restriction on $DiffMinChange$ and $DiffMaxChange$ were made stricter, the height of points 1 and 3 increased and the height of point 2 decreased, thus increasing the asymmetry of the grid shape. Additionally, the stricter restrictions on $DiffMinChange$ and $DiffMaxChange$ resulted in a larger decrease in the expected sputtering, compared to the NSTAR: the expected sputtering dropped from 79% of that expected by the NSTAR shape to 73% of the expected NSTAR sputtering rate.

7.3.4 Sensitivity: Neutral-Density Effects

The effect of the distribution function used to calculate the neutral density was tested. Optimization runs were performed using both the cosine distribution and that obtained for a single aperture in an infinite plane to calculate the neutral density downstream. The results are given in Table 7.5. In all cases, except where noted:

$$\begin{aligned}
 param_init &= [3.0, 1.4, 1.4], & \delta_{max} &= 0.22 \text{ mm}, \\
 DiffMinChange &= 0.01, & TolX &= 0.05, \\
 DiffMaxChange &= 0.5, & TolCon &= 0.002 \text{ mm}, \\
 param_min &= [-2, -2, -2], & param_max &= [10, 10, 10].
 \end{aligned}$$

The steady load corresponded to $a = 1.97 \times 10^3$ g, and all were computed for the target points $S(\bar{\mathbf{x}}) = (60, 0, 3)$ and $(-60, 0, 3)$.

The thickness, t , of the grid under question is shown in the second column. The distribution used to compute the neutral density (cosine or single aperture) are listed in the third column. The control mesh point heights found to optimize the sputtering rate are shown in column four. The fifth column tabulates the maximum displacement of the grid computed at the solution point, and the final column lists both the computed sputtering rate, in atoms/cm²·s, at the solution, followed in parentheses by the ratio of this value to that computed for the NSTAR grid *using the given neutral distribution*.

$$\Upsilon_{\cos}^{\text{NSTAR}} = 7.95 \times 10^8 \text{ atoms/cm}^2 \cdot \text{s},$$

$$\Upsilon_{\text{ap}}^{\text{NSTAR}} = 7.36 \times 10^8 \text{ atoms/cm}^2 \cdot \text{s}.$$

In all cases, the height of the point 1 was greater than the heights of both points 2 and 3, and the height of point 3 was greater than that of point 2. The solutions for Run 61 (aperture) and Run 70 (cosine) vary little. The heights of the control mesh points are nearly identical, and the reduction in the sputtering rate, compared to the NSTAR rate (using the given neutral distribution) is the same for both, 79%. When the restrictions on *DiffMinChange* and *DiffMaxChange* were made stricter,

Table 7.5: Comparison of optimization results from different neutral densities

Run #	t (mm)	Distribution	$param_opt$	δ (mm)	$optvalue$ $\times 10^8$ (ratio)
61	2.04	aperture	2.62, 0.96, 1.48	0.217	5.80 (0.79)
67	2.04	aperture	2.75, 0.84, 1.97	0.221	5.37 (0.73)
70	2.04	cosine	2.59, 0.95, 1.46	0.220	6.26 (0.79)

[‡] $DiffMinChange = 0.002$ $DiffMaxChange = 0.1$

the expected sputtering rate using the neutral distribution of a single aperture dropped to 73% of the expected NSTAR rate.

7.3.5 Sensitivity: Sputter-Yield Effects

In all the previous computations the sputter yield for xenon on molybdenum (Section 4.5) was used. One of the simplifying assumptions made in Chapter 5, in order to reduce the computational time required, was based on the fact that the sputter yield is orders of magnitude larger for high-energy ions than for low-energy ions, and has a dramatic drop-off for energies less than approximately 30 eV. Though the majority of the ions have energies less than this value, the drop-off allowed for us to neglect them because of their insignificant contribution to the predicted sputtering. We were thus able to ignore the “low-energy” solution branch which we had no way to compute other than using the full-trajectory analysis developed in Chapter 4.

Measurements have shown that not all materials, such as C_2 [26], have such a dramatic decrease in sputter yield for low energies. For such materials, the assumptions made in Chapter 5 may not be valid. To investigate the effect of the sputtering yield on the optimization results, two artificial sputter yields were created by modifying the sputter yield of xenon on molybdenum. Though neither of these sputter yields are derived from any measurements on actual materials, they were constructed such as to place emphasis on one energy range or the other: “low” or “high.” The first artificial sputter yield increases the effect of ions with energies below 60 eV, compared to the Mo-Xe⁺ yield, but is the same as xenon on molybdenum for energies higher than 60 eV. Conversely, the second artificial sputter yield increases the effect of ions with energies above 60 eV, compared to the Mo-Xe⁺ yield, but is identical to the xenon on molybdenum yield for energies less than 60 eV. Both sputter

Table 7.6: Coefficients for low-energy emphasis sputter yield

	α	β	γ	δ
$\hat{E} < 1.778$	0	0	3.316	-8.024
$1.778 \leq \hat{E} < 1.803$	0	-3.608	16.147	-19.432
$1.803 \leq \hat{E} < 2.3$	0	-2.236	11.105	-14.802
$2.3 \leq \hat{E}$	0	0	0.8203	-2.975

Table 7.7: Coefficients for high-energy emphasis sputter yield

	α	β	γ	δ
$\hat{E} < 1.384$	30.679	-144.55	231.39	-128.71
$1.384 \leq \hat{E} < 1.778$	0	-3.608	16.147	-19.432
$1.778 \leq \hat{E}$	0	0	3.316	-8.024

yields were made such that the value and slope at 60 eV is continuous.

As for the original curve fit from Section 4.5, a cubic curve (4.29) was used to represent the data for both constructed sputter yields and is reproduced here:

$$\log_{10} Y(E) = \alpha \hat{E}^3 + \beta \hat{E}^2 + \gamma \hat{E} + \delta,$$

where $\hat{E} = \log_{10}(E/\text{eV})$. The coefficients of the polynomial for the yield with low-energy emphasis are listed in Table 7.6. The coefficients of the polynomial for the yield with high-energy emphasis are listed in Table 7.7. The original sputter yield and the two artificial yields are shown in Figure 7.6.

In all other regards, the optimization parameters were identical to that of Run 67:

$$\begin{aligned} param_init &= [3.0, 1.4, 1.4], & \delta_{\max} &= 0.22 \text{ mm}, \\ DiffMinChange &= 0.002, & TolX &= 0.05, \\ DiffMaxChange &= 0.1, & TolCon &= 0.002 \text{ mm}, \\ param_min &= [-2, -2, -2], & param_max &= [10, 10, 10]. \end{aligned}$$

The steady load corresponded to $a = 1.97 \times 10^3$ g, and all were computed at the target points $S(\tilde{\mathbf{x}}) = (60, 0, 3)$ and $(-60, 0, 3)$.

The optimization using the low-energy emphasis curve did not converge. After 94 iterations, the solution was found to have made no progress and was oscillating about the initial control point

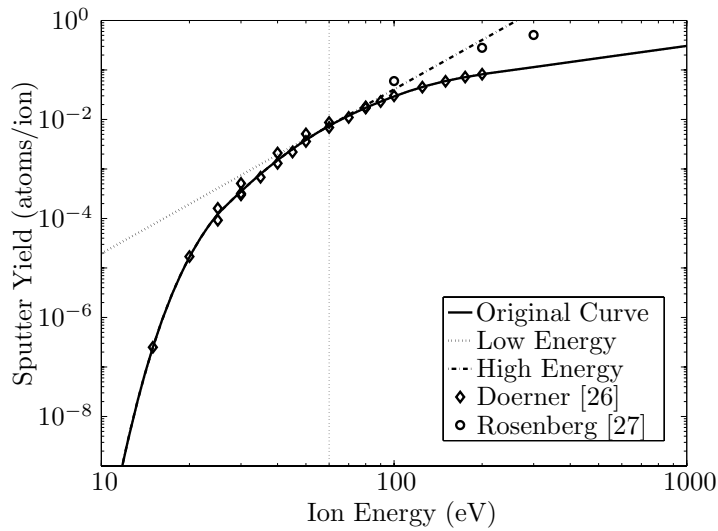


Figure 7.6: Original and constructed low/high energy emphasis sputter yields. The low energy emphasis sputter yield has increased yield, over the original yield (Figure 4.11), for energies less than 60 eV. The high energy emphasis sputter yield has increased yield for energies greater than 60 eV. Both the low and high energy emphasis have yields identical to the original for energies higher(lower) than 60 eV.

values.

For the sputter yield with emphasis on the high-energy ions, the NSTAR grid was found to have a sputtering rate $\Upsilon^{\text{NSTAR}} = 11.16 \times 10^8$ atoms/cm²-s. The grid shape optimization was found to converge to the solution at $\text{param_opt} = [2.57, 0.97, 1.26]$, with an optimum sputtering rate of $\text{optvalue} = 8.11 \times 10^8$ atoms/cm²-s, yielding a ratio of 0.73. In comparison, the solution using the original sputter yield (Run 67) was found to be $\text{param_opt} = [2.75, 0.84, 1.97]$, with a sputtering rate of $\text{optvalue} = 5.37 \times 10^8$ atoms/cm²-s, or a ratio to the NSTAR of 0.73. It is seen that, in comparison, the high-energy emphasis sputter yield resulted in a lower height of both control mesh points 1 and 3, however point 1 was still higher than the other two, and point 3 was still higher than point 2.

7.3.6 Thickness Effects

The optimization of thinner grids was found to be more stable at smaller acceleration loads. The load was reduced to that of a 25 g acceleration, and all three grid thicknesses — 1x, 2x, and 4x (the

Table 7.8: Comparison of optimization results for different grid thickness

Run #	t (mm)	δ_{\max} ($\times 10^{-3}$ mm)	$param_opt$	δ ($\times 10^{-3}$ mm)	$optvalue$ $\times 10^8$ (ratio)
85	0.51	6.94	2.62, 1.08, 1.99	6.93	6.10 (0.83)
86	1.02	4.12	2.90, 0.83, 1.87	4.12	6.03 (0.82)
87	2.04	3.61	2.80, 0.78, 1.98	3.59	5.34 (0.73)

NSTAR accel grid thickness) — were optimized. In all three cases the maximum deflection allowed was specified to be twice that of an NSTAR grid of the same thickness under the same load. The results are shown in Table 7.8. The optimization parameters were as follows:

$$\begin{aligned}
 param_init &= [3.0, 1.4, 1.4], \\
 DiffMinChange &= 0.002, & TolX &= 0.05, \\
 DiffMaxChange &= 0.1, & TolCon &= 2 \times 10^{-5} \text{ mm}, \\
 param_min &= [-2, -2, -2], & param_max &= [10, 10, 10].
 \end{aligned}$$

The thickness, t , of the grid under question is shown in the second column. The maximum allowable deflection (twice the NSTAR deflection under the same load) is listed in the third column. The control mesh point heights found to optimize the sputtering rate are shown in column four. The fifth column tabulates the maximum displacement of the grid computed at the solution point, and the final column lists both the computed sputtering rate, in atoms/cm²·s, at the solution, followed in parentheses by the ratio of this value to that computed for the NSTAR grid.

In all cases, the height of the point 1 was greater than the heights of both points 2 and 3, and the height of point 3 was greater than that of point 2. Additionally, the sputtering rate at the target points decreased as the grid thickness increased.

Chapter 8

Discussion of Results and Conclusions

8.1 Summary of Work Done and Discussion of Results

A plume model describing the energy distribution of charge-exchange (CEX) ions at any point — particularly at points located at large angles with respect to the ion engine thrust axis and beyond the main ion beam — has been developed. Other models that have been developed for this same purpose have typically used Direct Simulation Monte Carlo (DSMC) and Particle-in-Cell (PIC) methods for solving for the electric fields, particle trajectories, and densities [14, 45, 46]. These methods simulate the motion of a pre-determined number of “macro-particles” through a time-iterative computation. At each time step, the electric field is found through application of Poisson’s equation from which the motion of each particle until the next time step is computed. All properties — such as density, average particle energy, and the electric field — are obtained through weighting factors which determine the number of atoms that each macro-particle represents. The restriction on the number of particles that can be simulated due to availability of computing resources or time can lead to an issue of “shot” noise in these simulations. As a result, obtaining a highly resolved energy or velocity distribution of ions at any particular point in space is difficult, at best. This difficulty can be apparent especially in cases where the number of ions with one energy is orders of magnitude larger or smaller than the number with another energy. Obtaining relative sputtering contributions due to ions of different energies is thus made difficult when an accurate distribution

can not be computed [11].

Despite the inability to obtain highly resolved ion energy distributions, these models are generally successful in predicting total ion densities and average ion energies at positions surrounding the engine. The reason behind this is the assumption made in these models: the assumption that there is no transfer of energy in a charge-exchange collision and that an ion emerges from a collision with the neutral atom thermal velocity. As the results of this work support, the majority of charge-exchange collisions involve little to no energy transfer between the primary ion and neutral atom. Thus, the assumption made is applicable to most ions and these models are successful at predicting the dynamics of these particular ions which are the most populous.

In this work, we have not made the same assumption. Assuming elastic collisions, the model developed in this thesis accounts for the collision dynamics during the charge-exchange process, permitting the primary ion to transfer energy and for the CEX ion to be scattered at all available scattering angles as determined by conservation of energy and momentum. In addition, the method chosen to solve the model equations is different than the DSMC-PIC methods chosen by others. In this work, a continuum approach is used where the properties of the scattered CEX ions are assumed to vary smoothly and continuously. Though individual ion trajectories are computed, it is assumed that an ensemble of ions with similar initial conditions behave similarly, and so the properties of any ion can be interpolated based on the behavior of a select few representative ions. It is in this way that this model differs from the discretized method used by PIC models where a specific number of “macro-particles” are simulated, each of which represents a certain number of real ions.

The neutral atoms are assumed to be a cold gas and have zero velocity before the collision. The probability of finding a CEX ion at any specific angle is determined by the differential cross-section for charge-exchange and is obtained from a curve fit to previously measured data. To find an accurate estimate of the neutral atom density at any point where CEX collisions may occur, simulations of the diffusion of a rarefied gas through a two-hole aperture were performed using the Direct-Simulation Monte Carlo method. The flows through a single aperture in an infinite plane and one hole of a pseudo-periodic hole pattern were simulated. The farfield distribution for points

far from the aperture, compared to the hole radius, was found for both cases and compared to the modified cosine distribution used frequently in current models. The effective Clausing factor, which relates the flux compared to that from an infinitely flat hole, for both aperture configurations was also found.

The modified cosine distribution and the neutral-density distribution obtained for a single aperture in an infinite plane were used to compute the total neutral-atom density at any point downstream of the engine grid by superposition of the contributions from all grid holes. Comparisons of the densities computed using both distributions were made. It was found that the density in the region up to approximately 13 cm downstream of the grid surface dropped off more quickly for the cosine distribution than for the aperture distribution. Beyond approximately 13 cm and to the sides of the engine the density dropped off more slowly for the cosine distribution. Since the contribution to the CEX-ion density at any point is proportional to the neutral density within the volume where collisions occur, these results can have an impact on the relative contributions to the ion density from different regions within the main beam. For target points located at large angles with respect to the grid axis, it was found that the majority of the CEX-ion contribution came from the region within a few centimeters of the grid surface. Thus, a model using the cosine distribution would be expected to yield higher sputtering rates, due to the larger neutral density in this region, than a model incorporating a beamed neutral distribution such as that from the simulations of an NSTAR aperture.

In order to predict the motion of the CEX ions downstream of the engine, a method for computing the plasma potential and electric field was sought. The Boltzmann distribution, or barometric potential model, for computing the plasma potential downstream of an ion engine was presented in Chapter 4. Assuming the neutralizing electrons are in thermal equilibrium, this model permits computation of the plume potential at any point with knowledge of the total ion density and electron temperature only. The primary ions were assumed to emit isotropically from a point source behind each grid hole into a cone of specified divergence angle. The superposition of the contributions from all grid holes enabled us to compute the primary-ion density at any point. To overcome the

issue of needing both the ion density and plume potential simultaneously at any point in order to compute the other, the CEX-ion density, for purposes of computing the electric field, was assumed to be unaffected by the grid shape. The CEX-ion density at any point was found from the results of previous simulations using a different model. Comparison showed that the plume potential computed in this manner was qualitatively similar to the potential obtained from self-consistent Particle-in-Cell computations. It was proposed that the potential could be corrected and updated by repetitive iteration of the model presented to recompute the CEX-ion density at a series of points, though it was found that doing so would require extensive computational resources and an improvement to the method for computing the contributions from the lowest energy (and most populous) ions.

A scattering event was defined to be all possible collisions between primary ions with a specific velocity vector passing through a small volume and the neutral atoms contained within the same volume. One, initially unexpected, result in developing the model was the possible existence of multiple scattering angle solutions from any particular scattering event that could result in a CEX ion passing through any specified target point. Not only that, but it was found that for most scattering events, if a solution exists, there are two or more solutions. The reason for this was found to be the following. The most energetic CEX ions, which are scattered at relatively small angles, are affected little by the electric field and follow asymptotic trajectories along vectors of motion similar to their initial asymptotic scattering vectors. The effect of the electric field on a CEX ion increases as the scattering angle increases, since less energy is imparted to the ion from the collision. Passing through the main beam edge results in a CEX ion being swept farther upstream as the initial energy of the ion decreases. Additionally, as the initial energy of the CEX ion decreases, the electric field within the main beam has an increasing influence and results in sweeping the CEX ion some distance downstream before the ion encounters the upstream-directed electric field of the beam edge. The net result is that, at some critical scattering angle, the effect of the electric field within the main beam overcomes that of the beam edge: increasing the scattering angle further results in a CEX ion travelling farther downstream than an ion scattered at a smaller angle. Thus it is possible for multiple scattering angles from any scattering event that result in an ion passing through the target

point.

The presence of two possible scattering-angle solutions leads to an unexpected, but potentially significant, contribution to the CEX-ion density at any point. The streamtube area expansion $d\tilde{A}/d\Omega$ expresses the divergence of a streamtube formed by the trajectories of an ensemble of ions scattered within a small solid angle about the same scattering angle. An expansion approaching a value of zero describes a focussing situation where ions scattered within a finite range of angles all pass through a vanishing area. Such an occurrence happens when the scattering angle approaches the critical scattering angle at which the interior electric field begins to dominate the trajectory of the ion, and typically results in relatively low-energy ions. In situations when the scattering angle solution approaches this critical angle, ions scattered within a small range of the solution get focussed into a vanishingly small area at the target point and results in a large contribution to the flux of ions through that point.

Thus, it was found that the CEX ions from any scattering event that passed through any specified target point could be divided into four different cases:

- (I) One pair of scattering angles, (θ^+, ϕ^+) , results in the scattered ion passing through the target point; the streamtube area at the target point is greater than zero ($d\tilde{A}/d\Omega > 0$).
- (II) Multiple pairs of scattering angles result in a scattered ion passing through the target point.
- (III) One pair of scattering angles results in the scattered ion passing through the target point; the streamtube area at the target point is equal to zero ($d\tilde{A}/d\Omega = 0$).
- (IV) No ion from this scattering event passes through the target point.

Unfortunately, the infinite contributions from scattering events where the the streamtube is focussed ($d\tilde{A}/d\Omega \rightarrow 0$) present a computational problem. It was discussed in Chapter 4 that, though these events contribute an infinite CEX-ion flux through the point, conservation of mass bounds the total flux through any finite area surrounding the target point. The model was developed to compute the flux through a vanishingly small area (point) rather than a finite area surrounding the target point, and thus presented difficulty in computing accurate contributions from these events. Since

these events occur when the interior electric field begins to dominate the ion trajectory, the ion energy is typically low. Thus, error in the distribution was found to increase for lower energy ions. There is no precise definition for “low” and “high” energy, however, in the cases presented here where the target point was located at a large angle with respect to the thrust axis, “low” energy was typically found to apply to those ions with energies less than approximately 30-40 eV.

Except for situations where the CEX ions are focussed (Case III), the streamtube area expansion was found, for the high-energy ions, to approach the value of uniform divergence in a force-free region, i.e., $d\tilde{A}/d\Omega = R^2$. The streamtube area expansion was found to be larger for low-energy ions, or equivalently, was found to be larger for large scattering-angle solutions. This is simply due to the increasing effect the electric field has on ions of decreasing energy. Conversely, the differential cross-section is largest for the low-energy ions. Thus, the effects of a large divergence and a large cross-section of the low-energy ions tend to counteract each other when computing the flux. However, whereas the divergence of low-energy ions may typically be an order of magnitude larger than that for the higher-energy ions, the differential cross-section is multiple orders of magnitude larger for low-energy ions than for high-energy ions. The net result is that the low-energy ions still make the largest contribution to the CEX-ion density. Since the ions of Case III have relatively low energy as well, the issues presented by these ions due to a computed infinite flux do not affect this result: The low-energy ions make the largest contribution to the CEX-ion density. This result supports the hypothesis made in the development of other CEX models: The majority of the CEX ion density at any point is from low energy ions. These other models assume that all CEX ions scatter with the minimum energy, i.e. $\theta^+ = 90^\circ$.

The difficulties and inaccuracies in computing the energy distribution at the low energies, due to the issue of a computed infinite flux, lead to a problem with verifying the assertion made when computing the potential. Without a priori knowledge of the CEX-ion density it was assumed that the densities computed from another model could be used and were assumed not to change with changing grid shape. It was hypothesized that the initial guess at the potential could be corrected and updated by iterative computation of the densities. Since the greatest contribution to the density

was found to come from the low-energy ions, until the distribution of these ions can be computed more accurately, iterative correction of the potential is not feasible. However, the results here support the assumption made in other charge-exchange models: the largest density contribution comes from low-energy ions. Therefore, it is reasonable to assume that the densities computed by these other models are adequate for determining the potential, and that further iteration of this model, were it corrected for low-energy ions and computationally feasible, will yield little change.

In order to solve for the scattering angle solutions associated with any particular scattering event, the scattering target interception sphere was introduced. Any CEX ion scattered from a specific scattering event was parameterized by the chord length $D(\phi^+, \theta^+)$ between the target point and the point on the surface of this sphere through which the ion passed. A Gauss-Newton root-finding algorithm was developed which allowed for determination of the scattering-angle solution pairs (ϕ^+, θ^+) that minimize the chord length $D(\phi^+, \theta^+)$ (solutions for which $D_{\min} = 0$ apply to one of Cases I, II, or III, and solutions for which $D_{\min} > 0$ apply to Case IV).

The concept of a beamlet shell was then introduced, which allowed for simple evaluation of the integral equations derived in Chapter 2. It was demonstrated how the beamlet shell uniquely defines all scattering events within any shell, of a specific radius, within the primary ion beamlet emission cone of each hole. The scattering angle solutions, (ϕ^+, θ^+) , required to scatter a CEX ion into a trajectory passing through a specific target point, for the scattering event defined by each point within a beamlet shell were found by minimization of the chord length $D(\phi^+, \theta^+)$. For each solution the streamtube expansion, $d\tilde{A}/d\Omega$, and the energy of the ion as it passes through the target point were found. Using the beamlet shell approach had the result of making these quantities amenable to interpolation to a much greater number of scattering mesh points within the shell due to the smooth and slowly varying nature of these quantities over the surface of the shell. Such an interpolation allowed for highly resolved evaluation, by numerical integration, of the contribution to the CEX ion energy distribution at the target point from each shell.

It was demonstrated how the contributions from shells of various radii, spanning the entire beamlet emission cone, could be numerically integrated to obtain the entire contribution to the

CEX-ion energy distribution at the target point due to the beamlet. It was found that the greatest contribution to the density came from ions scattered at angles corresponding to the upper scattering-angle solution branch (“low-energy”, Case II) and from the case where the streamtube area expansion was equal to zero (Case III). Similarly, the total sputtering rate of material at the target point due to the CEX ions from each beamlet was shown to be the CEX-ion energy distribution, multiplied by the sputter yield, integrated over all space and ion energy. For xenon on molybdenum, it was found that the sputter yield dropped off at energies lower than approximately 30 eV, such that the ions with energies less than this contributed very little to the total sputtering rate. This is fortunate, for the model is not ideally suited for computing the distribution of ions at these low energies, due to the reasons stated earlier. For this reason, the validity of the sputtering rates computed by this model, and subsequent optimizations based on the sputtering rate, is critically dependent on the specific material being sputtered. The sputtering yield for molybdenum used in this work was found to drop off dramatically for low ion energies, and allowed for the inaccuracies of the energy distribution at energies less than approximately 30 eV to be ignored. If a different material with a sputter yield that does not drop off as dramatically for low ion energies is chosen, attention must again be given to correcting the inaccuracies of the distribution at these energies.

Reducing the sputtering rates of sensitive surfaces on the spacecraft is highly desirable, since it may lengthen the lifetime of the craft. It was a further goal of this work to implement the charge-exchange model into an optimization algorithm that minimizes the sputtering rate at specified surfaces by modifying the shape of the engine grids. It was found that complete computation of the CEX-ion energy distribution and sputtering rate due to all beamlet shells was found to be too computationally demanding for application to a grid shape optimization routine. Chapter 5 presented several simplifying assumptions made to the model, developed in Chapter 4, to reduce the number of required computations. Based on the results of xenon on molybdenum, it was chosen to disregard the larger of the two possible scattering-angle solutions since these were found to typically have energies less than approximately 30 eV and contributed very little to the quantity of interest, the sputtering rate. The quantities associated with the “high”-energy scattering-angle solution

were compared to the line-of-sight (LOS) scattering solutions for ions that scattered directly to the target point with no electric field acting on them. It was found that the two solutions yielded similar CEX-ion energy distributions and sputtering rates if the LOS scattering-angle solutions were adjusted by matching the energies of the highest-energy ion originating from the beamlet shell. Further improvement could be made by making further approximations that conform the surfaces created under the LOS assumption to those computed using the full-trajectory analysis. The uniform streamtube area expansion characteristic of trajectories scattered in a region free of electric forces ($d\tilde{A}/d\Omega \propto R^2$) was used for all scattering events in the LOS approximation.

Computation of a fully three-dimensional plume potential was also found to be computationally demanding when applied to an optimization routine. It was hypothesized that the computed CEX-ion energy distribution would not be greatly affected if the potential was assumed to be axisymmetric where the two-dimensional potential in the same radial plane as the target point was used as the axisymmetric potential. The distributions computed using an asymmetric three-dimensional potential as well as the axisymmetric approximation were compared. Of the beamlets compared, the general shape of the energy distribution and sputtered distribution were found to be similar for most, however, the total sputtering rate was found to differ by as much as 77%. This provides motivation for further work in improving the computational efficiency of the model, or the introduction of different approximations and simplifications within the model to deal with three-dimensional plumes.

Though the goal was to minimize the sputtering rate at specified surfaces by modifying the grid shape, structural constraints on the strength of the grids does not allow for completely arbitrary alteration of the shape. All grid shapes that minimize the sputtering may not be suitable for practical application to a flight mission, due to concern of the grids not surviving the launch environment. A method for estimating the response of any candidate minimizing grid shape to a specified loading was sought.

Finite-element modeling of the perforated grids (15,000 holes in the case of NSTAR) is computationally impractical, so the practice of implementing effective elastic properties was implemented. The effective elastic properties of a perforated plate were defined in Chapter 6. Theory and mea-

measurements have found the effective properties to vary as a function of not only the open-area fraction of the plate, but as a function of the relative thickness to the characteristic dimension of the hole pattern. Results from theory and measurements were compiled from which the effective properties for plates of the same thickness and hole pattern as the NSTAR grids could be found. For verification purposes, the software for analyzing the structural response of shells was used to simulate the response of a flat plate to various uniform static loads and compared to the non-linear theory for large displacements. Displacements computed from the simulations were found to agree within approximately 5% of those predicted by theory. The effective properties for a flat plate were assumed to be the same for shallow shells with the same bulk properties and hole pattern. A parameter study was performed for NSTAR-shaped grids of varying thickness under numerous uniform static loads and compared to the displacements of flat plates under identical loads. As expected, the NSTAR grids suffered significantly less deflection than a flat plate under the same load, and the deflection decreased for increasing grid thickness. It was found that difficulties with convergence were often encountered when executing the finite-element code for very thin grids under large loads. The results from this parameter study provided information for approximate scaling of loads so that thicker grids could be simulated to avoid the convergence issues often encountered.

A development of the optimization method used for minimizing the sputtering rate at a specific point by altering the grid shape was presented in Chapter 7. The grid surface was parameterized by the specification of the height of 3 node points in a control mesh. A process including subdivision and the removal of small elements yielded a mesh representing the grid surface that contained an adequate number of node points and elements for finite-element analysis. An approximation to the limit surface, corresponding to the physical shape of the parameterized surface, was also obtained by further subdivision. A triangular pattern of holes, like that of the NSTAR, were overlaid onto the limit surface. The coordinates of the simulated holes, as well as the surface normal vectors at the locations of the holes, were then computed which were used for implementing the charge-exchange model.

The sensitivity of the optimized shape to the (1) neutral density, (2) sputter yield, (3) initial

grid shape, (4) location of the target point, and (5) grid thickness were tested. The results of the optimizations were compared to the shape and sputtering rate predicted for the NSTAR grid and, in most cases, were found to reduce the sputtering.

As expected by the nature of the different neutral distributions investigated in Chapter 3, the sputtering rates predicted using the cosine distribution were higher than for rates predicted using the NSTAR aperture distribution computed from the DSMC simulations. This is a result of the higher neutral density expected in the region immediately downstream of the grid surface using the cosine distribution. The majority of the CEX ions that reach the target point originate from this region. The optimizing grid shapes obtained under the same initial conditions for both neutral density distributions were very similar and both predicted a reduction of the sputtering rate of approximately 20% over the NSTAR grid.

The sensitivity of the optimization results to the sputter yield was tested by altering the yield to emphasize both the low-energy and the high-energy ions respectively. The optimization using the sputter yield that emphasized the low-energy ions more than the original sputter yield did not converge to a minimizing solution. This is not unexpected, for sputtering rates computed using this sputter yield will be more sensitive to the inaccuracies of the model in dealing with the low energy ions. Since the computed flux of low energy ions has a large amount of noise, this noise will be reflected in the sputtering rates. Such noise can result in discontinuities of the hypersurface describing the function being minimized. The Newton search method used by the optimizing algorithm requires both the function and the gradients of the function to be continuous in order to locate a minimum.

The optimization using the sputter yield that emphasized the high-energy ions more than the original sputter yield did converge to a minimizing solution. As expected, the total predicted sputtering rate was higher due to the increase sputtering activity of the energetic ions. The minimizing grid for the high-energy yield was flatter than the minimizing grid for the original yield, as evidenced by the reduced difference between the heights of all three control mesh points. This is not surprising, for in flattening the grid, the normals of the surface are inclined at larger angles with respect to

the line-of-sight vectors pointing to the target point, and thus typically require larger scattering angles, which are less energetic. Intuitively, this makes sense, for a flat grid would be expected to do less sputtering damage to a surface located at a large angle with respect to the grid axis than a domed grid such as used on the NSTAR which has holes emitting primary ions directed more towards the target point. The minimizing surfaces obtained for both the high-energy yield and the original yield were both predicted to reduce the sputtering rate at the target point by approximately 27% compared to the NSTAR grid shape.

The extent to which optimization solutions are global minimums of the sputtering rate hypersurface was tested by varying the initial values of the optimizing parameters. It was found that, for many initial values, the optimization algorithm failed to locate any minimizing solution. Such cases were usually associated with initial parameters that created grid surfaces that had a plateau-like quality. These grid shapes were domed, but with a large flat area at the center. From the structural analysis, it was found that often these grids buckled under the imposed load, and are believed to have thus created discontinuities in the optimizing constraints. A minimizing solution must meet the condition that the gradient of the Lagrangian, as defined in Chapter 2, must equal zero, and the Hessian of the Lagrangian must be positive-definite. Since the Lagrangian includes the constraint conditions through use of Lagrange multipliers, discontinuities in the constraint conditions can render the problem unsolvable using a numerical algorithm.

It was found that the minimizing solution was dependent on the values of the initial optimization parameters. Not all solutions were found to reduce the sputtering rate compared to the NSTAR, but rather had greater predicted rates. The expected sputtering rates of the minimizing solutions were found to be as great as 135% and as little as 73%, the rate predicted for the NSTAR grid shape. However, nearly all cases had similar characteristics in the values of optimization parameter solutions. With the exception of a few cases, the height of the first control mesh point (at the center of the mesh) was the greatest. Similarly, the third control mesh point (located in the same plane as the target point) was almost always greater than the second (located in the plane transverse to that which the target point is on). Such a configuration of control mesh point heights results in a grid

shape reminiscent of the barrel vault shape discussed in Chapter 5.

The location of the target point was found to have little impact on the shape of the optimally shaped grid. For all target points within a few centimeters of the original point, the optimum shape had the same characteristics: (1) the height of the first control mesh point was the greatest, and (2) the height of the third control mesh point was always greater than the second. The values of the optimum control mesh point heights also changed relatively little indicating that the same shape would be effective at reducing the sputtering over an extended area located around the target point instead of only at the target point itself. The results from varying the grid thickness were very similar. In all cases, the optimal grid shape reduced the sputtering in comparison to the NSTAR shape by as much as 27%.

The two goals of this work were: (1) to develop a model that accounts for the energy and momentum transfer process during charge-exchange collisions and can predict the amount of sputtering that one would expect at any particular point around an ion engine due to impacts from the CEX ions, and (2) to combine both the charge-exchange dynamics model and structural strength analysis into an optimization problem based on the shape of the grid, such that the sputtering rate at specified locations is minimized under imposed structural constraints. The model enabled high resolution of the expected energy distribution of CEX ions, especially those with energies greater than approximately 30 eV, which can only be accounted for if the energy and momentum transfer process of charge-exchange collisions is included. Results indicated that the density of CEX ions is due in most part to the slowest ions, which receive little to no energy from the collision. This supports the approximations used currently in other Particle-in-Cell models of the CEX-ion environment, where all CEX ions are assumed to emerge from the charge-exchange collisions with zero energy.

In a departure from what is currently thought, the results indicated that the significantly smaller population of high-energy ions, created due to transfer of energy during charge-exchange collisions, may be responsible for the majority of the sputtering at locations around the engine and at high angles with respect to the grid axis. Though this was demonstrated, it was also found that this result is highly dependent on the material being sputtered and its attendant sputter yield. In cases

where there is a less significant difference in the yield from high-energy ions as from low-energy ions, this result may not apply.

A limited application of the model to a grid shape optimization procedure was demonstrated. All results indicated that alteration of the grid shape can result in reduced sputtering of certain surfaces and the reduction can be expected to be of the order of 20-30% compared to the sputtering expected when using the NSTAR grid.

8.2 Future Work

Further work could be pursued in improving the accuracy of the CEX-ion energy distribution and sputtering rates predicted by the CEX-ion model, and in improving the integration of the CEX-ion model into an optimization problem for enhancing engine grid design. There are many ways in which the work can be expanded, but here we provide recommendations for extensions that could reap obvious benefits.

As stated in the previous section, difficulties were encountered in computing the density contributions from scattering events where the streamtube area expansion approaches zero at the target point. This could likely be resolved by computing the average energy distribution over a small but finite area, instead of an infinitesimal target point. Such an approach would eliminate the computational issues due to infinite contributions from infinitesimal volumes, and enable more accurate determination of the CEX-ion distribution over all energies. This would enable one to compute more accurate CEX-ion densities, which would then permit calculation of a self-consistent potential by iterative computation. Additionally, a CEX-ion distribution accurate over all energies would also yield more reliable sputtering rates in the cases when the sputter yield does not decrease rapidly for small energies.

This work could also benefit from additional consideration of methods for speeding up the computation. Currently, iterative computation of the potential, computation of an asymmetric potential, and inclusion of all scattering-angle solutions (high- and low-energy branches) is practically infeasible without the use of supercomputing resources.

Accounting for the reduction in the flux of the primary ions due to depletion from CEX collisions could also be implemented, however in Chapter 2 we found that the depletion of the primary ions due to collisions (at least in space-based applications) is minimal. This would likely only make a difference of a couple of percent in the predicted sputtering rate. Though the effects were assumed to be negligible, secondary CEX collisions between the CEX ions and neutrals can also occur. The significant increase in computational requirements to include these secondary processes would have to be considered against the expected gain offered by doing so. Since the majority of the CEX ions are found to originate from within the region extending a few centimeters downstream of the grid surface, a more in-depth study of the CEX ion behavior near the grid as a CEX ion passes between beamlets, or gets absorbed by the negatively charged accel grid, could be performed.

With regard to practical implementation of the model into an optimization problem, increasing the number of control mesh points could yield more flexibility in terms of the achievable shapes of the optimum grid. In this work, only three control points were used, which significantly limited the shapes available. Of course, increasing the number of control points also has its attendant problems of possible convergence instability, and manufacturability of the grid. Including the grid stresses within the constraints and extension to time-dependent loading could also yield results more applicable to the particular mission under consideration.

Any effort invested in continuing this work will have to be considered in terms of the balance between the extra computational time or resources required and the expected improvement in the results.

References

- [1] R.E. Wirz. *Discharge Plasma Processes of Ring-Cusp Ion Thrusters*. PhD thesis, California Institute of Technology, 2005.
- [2] S.R. Oleson, R.M. Myers, C. Kluever, J.P. Riehl, and F.M. Curran. Advanced propulsion for geostationary orbit insertion and north-south station keeping. In *31st AIAA/ASME/SAE/ASEE Joint Propulsion Conference and Exhibit*, San Diego, CA, 1995.
- [3] J. Polk, J.R. Kakuda, J. R. Anderson, and J.R. Brophy. Performance of the NSTAR ion propulsion system on the Deep Space One mission. In *39th AIAA Aerospace Sciences Meeting and Exhibit*, Reno, NV, 2001.
- [4] R.C. Fernandez. SMART-1: Europe reaches the moon. In *55th International Astronautical Congress of the International Astronautical Federation*, Vancouver, Canada, 2004.
- [5] J.S. Sovey, V.K. Rawlin, and M. J. Patterson. Ion propulsion development projects in U.S.: Space Electric Rocket Test I to Deep Space 1. *Journal Of Propulsion And Power*, 17(3), 2001.
- [6] P.J. Wilbur, V.K. Rawlin, and J.R. Beattie. Ion thruster development trends and status in the United States. *Journal Of Propulsion And Power*, 14(5):708–715, 1998.
- [7] S.R. Oleson. Electric propulsion technology development for the Jupiter Icy Moons Orbiter project. In *Space 2004 Conference and Exhibit*, San Diego, CA, 2004.
- [8] D.E. Hedges and J.S. Meserole. Demonstration and evaluation of carbon-carbon ion optics. *Journal Of Propulsion And Power*, 10(2):255–261, 1994.

- [9] J. Brophy. NASA's Deep Space 1 ion engine (plenary). *Review of Scientific Instruments*, 73(2):1071 – 1078, 2002.
- [10] V. Davis, I. Katz, M. J. Mandell, D. Brinza, M. Henry, J. Wang, and D. T. Young. Ion engine generated charge exchange environment: Comparison between NSTAR flight data and numerical simulations. In *36th AIAA/ASME/SAE/ASEE Joint Propulsion Conference*, Huntsville, Alabama, 2000.
- [11] I. Katz. A Hall Effect thruster plume model including large-angle elastic scattering. In *37th AIAA/ASME/SAE/ASEE Joint Propulsion Conference and Exhibit*, Salt Lake City, Utah, 2001.
- [12] I. G. Mikellides, I. Katz, R. A. Kuharski, and M. J. Mandell. Elastic scattering of ions in electrostatic thruster plumes. *Journal Of Propulsion And Power*, 21(1):111–118, 2005.
- [13] J. Wang, D. E. Brinza, D. T. Young, J. E. Nordholt, J. E. Polk, M. D. Henry, R. Goldstein, J. J. Hanley, D. J. Lawrence, and M. Shappirio. Deep Space One investigations of ion propulsion plasma environment. *Journal Of Spacecraft And Rockets*, 37(5):545–555, 2000.
- [14] I. G. Mikellides, G. A. Jongeward, I. Katz, and D. H. Manzella. Plume modeling of stationary plasma thrusters and interactions with the Express-A spacecraft. *Journal Of Spacecraft And Rockets*, 39(6):894–903, 2002.
- [15] J. Wang, D. Brinza, and M. Young. Three-dimensional particle simulations of ion propulsion plasma environment for Deep Space 1. *Journal Of Spacecraft And Rockets*, 38(3):433–440, 2001.
- [16] J. Wang, J. Polk, J. Brophy, and I. Katz. Three-dimensional particle simulations of ion-optics plasma flow and grid erosion. *Journal Of Propulsion And Power*, 19(6):1192–1199, 2003.
- [17] R. I. S. Roy, D. E. Hastings, and N. A. Gatsonis. Ion-thruster plume modeling for backflow contamination. *Journal Of Spacecraft And Rockets*, 33(4):525–534, 1996.

- [18] J. Polaha, N. Meckel, B. Welander, N. Juhlin, and T. Haag. Random and sine-spectrum vibration testing of pyrolytic graphite ion optics. In *41st AIAA/ASME/SAE/ASEE Joint Propulsion Conference and Exhibit*, Tucson, AZ, 2005.
- [19] J.H. Jeans. *The Dynamical Theory of Gases*. Cambridge University Press, 1904.
- [20] S. Chapman and T.G. Cowling. *The Mathematical Theory of Non-Uniform Gases*. Cambridge University Press, Cambridge, 1970.
- [21] E.A. Guggenheim. *The International Encyclopedia of Physical Chemistry and Chemical Physics*. Pergamon Press, New York, 1960.
- [22] E.H. Kennard. *Kinetic Theory of Gases*. McGraw-Hill Book Company, New York, 1938.
- [23] F. Reif. *Fundamentals of Statistical and Thermal Physics*. McGraw-Hill Book Company, New York, 1965.
- [24] G.N. Patterson. *Molecular Flow of Gases*. John Wiley & Sons, Inc., New York, 1956.
- [25] M. Allis. *Cross Section Measurements and Numerical Model for Ion Thruster*. Senior project, California Institute of Technology, 2003.
- [26] R.P. Doerner, D.G. Whyte, and D.M. Goebel. Sputtering yield measurements during low energy xenon plasma bombardment. *Journal of Applied Physics*, 93(9):5816–5823, 2003.
- [27] D. Rosenberg and G.K. Wehner. Sputtering yields for low energy He⁺, Kr⁺, and Xe⁺-ion bombardment. *Journal of Applied Physics*, 33(5):1842–1845, 1962.
- [28] Y. Yamamura and H. Tawara. Energy dependence of ion-induced sputtering yields from monatomic solids at normal incidence. *Atomic Data and Nuclear Data Tables*, 62:149–253, 1996.
- [29] J.M. Fife, M.R. Gibbons, D. B. Van Gilder, and D.E. Kirtley. Initial use of a 3-d plasma simulation system for predicting surface sputtering and contamination by hall thrusters. In *33rd Plasmadynamics and Lasers Conference*, Maui, Hawaii, 2002.

- [30] M.M. Jakas. Transport theories of sputtering. *Philosophical Transactions of the Royal Society of London*, 362:139–156, 2004.
- [31] M. Tartz, D. Manova, and H. Neumann. Sputter investigation of ion thrusters grid materials. In *41st AIAA/ASME/SAE/ASEE Joint Propulsion Conference and Exhibit*, Tucson, AZ, 2005.
- [32] J.B. Marion. *Classical Dynamics of Particles and Systems*. Academic Press, New York, second edition, 1970.
- [33] P. Sigmund. Theory of sputtering. I. Sputtering yield of amorphous and polycrystalline targets. *Physical Review*, 184(2):383–416, 1969.
- [34] K. Kannenberg, V. Khayms, B. Emgushov, L. Werthman, and J. Pollard. Validation of Hall thruster plume sputter model. In *37th Joint Propulsion Conference*, Salt Lake City, Utah, 2001.
- [35] P.Y. Papalambros and D.J. Wilde. *Principles of Optimal Design*. Cambridge University Press, Cambridge, second edition, 2000.
- [36] M. Knudsen. *Ann. Phys., Lpz*, 28:75–130, 1909.
- [37] I. D. Boyd, D. B. Van Gilder, and X. M. Liu. Monte Carlo simulation of neutral xenon flows in electric propulsion devices. *Journal Of Propulsion And Power*, 14(6):1009–1015, 1998.
- [38] W. Steckelmacher. Knudsen flow 75 years on: The current state of the art for flow of rarefied gases in tubes and systems. *Rep. Prog. Phys.*, 49:1083–1107, 1986.
- [39] P. Clausing. The flow of highly rarefied gases through tubes of arbitrary length. *The Journal of Vacuum Science and Technology*, 8(5):636–646.
- [40] P. Clausing. *Z. f. Physik*, 66:471–476, 1930.
- [41] B.B. Dayton. Gas flow patterns at entrance and exit of cylindrical tubes. In *National Symposium on Vacuum Technology Transactions*, 1956.
- [42] G.A. Bird. <http://ourworld.compuserve.com/homepages/gabird/ds2g.htm>, accessed September 1, 2006.

- [43] G.A. Bird. *Molecular Gas Dynamics*. Oxford University Press, London, 1976.
- [44] F.F. Chen. *Introduction to Plasma Physics and Controlled Fusion*, volume 1. Plenum Press, New York, 2 edition, 1984.
- [45] I. D. Boyd. Hall thruster far field plume modeling and comparison to Express flight data. In *AIAA 40th Aerospace Sciences Meeting*, Reno, NV, 2002.
- [46] D. Y. Oh, D. E. Hastings, C.M. Marrese, J.M. Haas, and A.D. Gallimore. Modeling of Stationary Plasma Thruster-100 thruster plumes and implications for satellite design. *Journal Of Propulsion And Power*, 15(2):345–357, 1999.
- [47] M. Celik, M. Santi, S. Cheng, M. Martinez-Sanchez, and J. Peraire. Hybrid-PIC simulation of a Hall thruster plume on an unstructured grid with DSMC collisions. In *International Electric Propulsion Conference*, Toulouse, France, 2003.
- [48] C.K. Birdsall and A.B. Langdon. *Plasma Physics Via Computer Simulation*. Bristol, 1991.
- [49] J.W. Emhoff, I. D. Boyd, and S.P. Shepard. Numerical analysis of NEXT ion thruster optics. In *International Electric Propulsion Conference*, Toulouse, France, 2003.
- [50] J. R. Anderson. Private communication, 2005.
- [51] M. J. Mandell, I. G. Mikellides, L. K. Johnson, and I. Katz. A high power ion thruster plume model. In *40th AIAA/AASME/SAE/ASEE Joint Propulsion Conference and Exhibit*, Fort Lauderdale, Florida, 2004.
- [52] I. G. Mikellides, R. A. Kuharski, M. J. Mandell, and B. M. Gardner. Assessment of spacecraft systems integration using the Electric Propulsion Interactions Code (EPIC). In *38th AIAA/ASME/SAE/ASEE Joint Propulsion Conference and Exhibit*, Indianapolis, Indiana, 2002.
- [53] I. G. Mikellides. Private communication, 2005.

- [54] L. Verlet. Computer “experiments” on classical fluids. I. Thermodynamical properties of Lennard-Jones molecules. *Physical Review*, 159(1):98–103, 1967.
- [55] R.D. Richtmyer and K.W. Morton. *Difference Methods for Initial Value Problems*. John Wiley, Hoboken, 2 edition, 1967.
- [56] J. L. Delcroix. *Plasma Physics*. Wiley, 1965.
- [57] R.L. Liboff. *Kinetic Theory: Classical, Quantum, and Relativistic Descriptions*. Springer-Verlag, New York, 2003.
- [58] R. Dressler and S. Pullins. Ion dynamics in Hall Effect and ion thrusters: Xe⁺ + Xe symmetric charge transfer. In *38th Aerospace Sciences Meeting and Exhibit*, Reno, NV, 2000.
- [59] R. Kolasinski. *Fundamental Ion-Source Interactions in Plasma Thrusters*. PhD thesis, California Institute of Technology, 2006.
- [60] R. Bailey and R. Hicks. Behaviour of perforated plates under plane stress. *Journal of Mechanical Engineering Science*, 2(2):143–161, 1960.
- [61] K.A. Gardner. Heat-exchanger tubesheet design. *ASME Journal of Applied Mechanics*, 70:377–385, 1948.
- [62] V. G. Ukadgaonker, P. A. Kale, N. A. Agnihotri, and R. S. Babu. Review of analysis of tube sheets. *International Journal Of Pressure Vessels And Piping*, 67(3):279–297, 1996.
- [63] P. Meijers. *Doubly-Periodic Stress Distributions in Perforated Plates*. Phd, Technische Universiteit Delft, 1967.
- [64] W. J. O’Donnell. Effective elastic-constants for bending of thin perforated plates with triangular and square penetration patterns. *Journal Of Engineering For Industry-Transactions Of The Asme*, 95(1):121–128, 1973.
- [65] T. Slot and W. J. O’Donnell. Effective elastic constants for thick perforated plates with square and triangular penetration patterns. *Journal Of Engineering For Industry*, 93(4):935–942, 1971.

- [66] J.P. Duncan and R.W. Upfold. Equivalent elastic properties of perforated bars and plates. *Journal of Mechanical Engineering Science*, 5(1):53–65, 1963.
- [67] P. Meijers. Refined theory for bending and torsion of perforated plates. *Journal of Pressure Vessel Technology*, 108:423–429, 1986.
- [68] V.V. Novozhilov. *The Theory of Thin Shells*. P. Noordhoff Ltd., Groningen, 2 edition, 1959.
- [69] E. Reissner. Stresses and small displacements of shallow spherical shells. I. *Journal Of Mathematics And Physics*, 25(2):80–85, 1946.
- [70] E. Reissner. On derivation of theory of thin elastic shells. *Journal Of Mathematics And Physics*, 42(4):263–277, 1963.
- [71] L. E. Hulbert and F. A. Simonen. Analysis of stresses in shallow spherical shells with periodically spaced holes. *Journal Of Engineering For Industry*, 92(4):834–840, 1970.
- [72] F. Cirak, M. Ortiz, and P. Schroder. Subdivision surfaces: A new paradigm for thin-shell finite-element analysis. *International Journal for Numerical Methods in Engineering*, 47:2039–2072, 2000.
- [73] F. Cirak and M. Ortiz. Fully C^1 -conforming subdivision elements for finite deformation thin-shell analysis. *International Journal for Numerical Methods in Engineering*, 51:813–833, 2001.
- [74] F. Cirak, M.J. Scott, E.K. Antonsson, M. Ortiz, and P. Schroder. Integrated modeling, finite-element analysis, and engineering design for thin-shell structures using subdivision. *Computer Aided Design*, 34:137–148, 2002.
- [75] T. Haag and G.C. Soulas. Performance and vibration of 30 cm pyrolytic ion thruster optics. In *39th AIAA/ASME/SAE/ASEE Joint Propulsion Conference and Exhibit*, Huntsville, Alabama, 2003.
- [76] N. Meckel, J. Polaha, and N. Juhlin. Structural analysis of pyrolytic graphite optics for the HiPEP ion thruster. In *40th AIAA/ASME/SAE/ASEE Joint Propulsion Conference and Exhibit*, Fort Lauderdale, Florida, 2004.

- [77] F. Cirak, M. Ortiz, and A. Pandolfi. A cohesive approach to thin-shell fracture and fragmentation. *Computer Methods in Applied Mechanics and Engineering*, 194:2604–2618, 2005.
- [78] M. Winter. <http://www.webelements.com/webelements/elements/text/mo/phys.html>, accessed September 12, 2006.
- [79] W.C. Young and R.G. Budynas. *Roark's Formulas for Stress and Strain*. McGraw-Hill, 7 edition, 2002.
- [80] R.T. Haftka and R.V. Grandhi. Structural shape optimization – a survey. *Computer Methods in Applied Mechanics and Engineering*, 57:91–106, 1986.
- [81] J. Mueller, J. Brophy, and D.K. Brown. Design, fabrication, and testing of 30-cm dia. dished carbon-carbon ion engine grids. In *32nd AIAA/ASME/SAE/ASEE Joint Propulsion Conference and Exhibit*, Buena Vista, Florida, 1996.